UNIWERSYTET ŚLĄSKI
W KATOWICACH

Uniwersytet Śląski w Katowicach

Wydział Nauk Ścisłych i Technicznych

Instytut Chemii

PRACA DOKTORSKA

Badanie dynamiki i oddziaływań molekularnych w zasocjowanych substancjach aktywnych i ich pochodnych tworzących struktury supramolekularne w różnych warunkach termodynamicznych

mgr Paulina Jesionek-Ratka

Promotorzy:

prof. dr hab. Kamil Kamiński

prof. dr hab. n. farm. Ewa Ozimina-Kamińska

Chorzów 2025

Z całego serca pragnę podziękować
prof. dr hab. n. farm. Ewie Oziminie – Kamińskiej
i prof. dr hab. Kamilowi Kamińskiemu
za nieocenione wsparcie, inspirujące wskazówki
oraz cierpliwe towarzyszenie mi na każdym
etapie pracy nad rozprawą doktorską.
Ich merytoryczna wiedza, otwartość na dyskusję
i motywacja do poszukiwania nowych rozwiązań
były dla mnie nieustannym źródłem inspiracji.

Panu dr Dawidowi Heczko –
za nieustanną pomoc, życzliwość i poświęcony czas.

Składam serdeczne podziękowania
Koleżankom i Kolegom z zespołu
za codzienne wsparcie, inspirujące rozmowy,
motywację oraz wspólnie spędzony czas.

Pracę dedykuję Mężowi, Rodzicom i Teściom.

NARODOWE CENTRUM NAUKI

Badania przeprowadzone na potrzeby niniejszej pracy doktorskiej były finansowane przez Narodowe Centrum Nauki w ramach projektu OPUS 21 pt. „*Korelacje między strukturą supramolekularną, dynamiką molekularną, stabilnością fizyko-chemiczną i rozpuszczalnością w czystych farmaceutycznych substancjach aktywnych (APIs) oraz systemach binarnych API-substancja pomocnicza*” o numerze 2021/41/B/NZ7/01654.

Spis treści

Wykaz skrótów 7

Wykaz rycin i tabel 10

I. Wprowadzenie 11

1.1. Otrzymywanie szkieł 11

1.2. Badania dielektryczne na substancjach szklistych z wiązaniami wodorowymi, w tym amorficznych APIs 13

1.3. Kryształy orientacyjnie nieuporządkowane. Badania na pochodnych adamantanu 15

1.4. Cel pracy 18

II. Omówienie i dyskusja otrzymanych wyników 22

2.1. Badania wysokociśnieniowe silnie zasocjowanej substancji aktywnej – tikagreloru w fazie cieczy przechłodzonej i szklistej 22

2.2. Zmiana objętości aktywacji jako wskaźnik różnic w zjawisku klasteryzacji indukowanym przez wiązania wodorowe i oddziaływania F-Π *stacking* w enancjomerach flurbiprofenu i ich mieszaninie racemicznej 26

2.3. Badania nad naturą, ewolucją ciśnieniową i kinetyką przejść fazowych w pochodnych ADM 30

III. Treści artykułów stanowiących podstawę pracy doktorskiej wraz z oświadczeniami współautorów 38

IV. Podsumowanie i wnioski 129

V. Literatura 132

Wykaz skrótów

1-NH_2-ADM – 1-adamantyloamina (amantadyna)

1-OH-ADM – 1-adamantanol

3-NH_2-1-OH-ADM – 3-amino-1-adamantanol

ADM – adamantan

API/APIs – farmaceutyczna/e substancja/e aktywna/e (ang. *Active Pharmaceutical Ingredient/s*)

BCS – system klasyfikacji biofarmaceutycznej (ang. *Biopharmaceutics Classification System*)

BDS – szerokopasmowa spektroskopia dielektryczna (ang. *Broadband Dielectric Spectroscopy*)

C_p – ciepło właściwe

DFT – obliczenia kwantowo-mechaniczne (ang. *Density Functional Theory*)

DSC – różnicowa kalorymetria skaningowa (ang. *Differential Scanning Calorimetry*)

DSE – Debye'a-Stokes'a-Einstein'a (równanie)

dT_g/dp – współczynnik ciśnieniowy temperatury przejścia szklistego

E_a – energia (bariera) aktywacji

E_{int} – energia wiązania (tutaj wodorowego)

E_p – energia aktywacji przy stałym ciśnieniu

Eq. – skrót od słowa *Equation* (równanie)

E_V – energia aktywacji przy stałej objętości

ε^* – zespolona przenikalność dielektryczna

ε' – dyspersja dielektryczna

ε'' – straty dielektryczne

f – częstotliwość

F – fluor

Fig. – skrót od słowa *Figure* (rysunek)

FTIR – spektroskopia w podczerwieni z transformacją Fouriera (ang. *Fourier Transform Infrared Spectroscopy*)

G – funkcja Gibbsa

H – entalpia

HN – Havriliaka-Negami (funkcja)

JG – Johari-Goldstein

KWW – Kohlrauscha-Williamsa-Wattsa (funkcja)

OC – kryształ uporządkowany (ang. *ordinary crystal*)

ODIC – kryształy orientacyjnie nieuporządkowane (ang. *orientationally disordered crystals*)

p – ciśnienie

PC – plastyczne kryształy (ang. *plastic crystals*)

PDG – ciśnieniowo zagęszczone szkło (ang. *pressure densified glass*)

p_g – ciśnienie zeszklenia

p_k – ciśnienie krystalizacji

R-FLP – *R*-flurbiprofen

RS-FLP – *RS*-flurbiprofen

RTV – rytonawir

Rys. – rysunek

S – entropia

s – wykładnik w równaniu ułamkowym Debye'a-Stokes'a-Einstein'a (DSE)

S-FLP – *S*-flurbiprofen

t – czas

T – temperatura

T_g – temperatura zeszklenia

TICA – tikagrelor

T_k – temperatura krystalizacji

T_m – temperatura topnienia

TOP – (ang. *Two Order Parameter*)

TPS – superpozycja temperaturowo-ciśnieniowa (ang. *temperature-pressure superpositioning*)

V – objętość

VFT – Vogela-Fulchera-Tammanna (funkcja)

XRD – dyfrakcja rentgenowska

Z – liczba atomowa

α,β – procesy relaksacyjne

β_{KWW} – parametr kształtu, wykładnik funkcji Kohlrausha-Williamsa-Wattsa

ΔH_β – entalpia aktywacji procesu β

ΔS_β – entropia aktywacji procesu β

ΔV – zmiana objętości w temperaturze przejścia fazowego

ΔV_α – objętość aktywacji procesu α

ΔV_β – objętość aktywacji procesu β

η – lepkość

μ – moment dipolowy

σ_{DC} – przewodnictwo stałoprądowe

τ – czas relaksacji

τ_α, τ_β, τ_γ, – czasy relaksacji α, β i γ

Wykaz rycin i tabel

Rys. 1. Uzyskanie fazy szklistej na drodze witryfikacji (panel a) i izotermicznej kompresji cieczy (panel b). T_{g1} i T_{g2} oznaczają temperatury przejść szklistych dla dwóch różnych szybkości chłodzenia $T_1>T_2$, T_k to temperatura krystalizacji. Obszar pomiędzy T_k i T_g oraz p_k i p_g to tzw. faza cieczy przechłodzonej. 13

Rys. 2. Schematyczne przedstawienie możliwych przejść cieczy do fazy stałej: szkła strukturalnego, szkła orientacyjnego (poprzez fazę plastycznego kryształu) oraz kryształu uporządkowanego [35]. 15

Rys. 3. Superpozycja widm TICA (a) i RTV (b) zebranych w różnych warunkach T i p w pobliżu i powyżej T_g. Panele (c) i (d) przedstawiają widma FTIR zmierzone w temperaturze pokojowej odpowiednio dla OG i PDG TICA oraz RTV [89]. 23

Rys. 4. Porównanie znormalizowanych widm dielektrycznych zmierzonych w różnych warunkach T i p, blisko T_g dla *R*-, *S*- i *RS*-FLP (a). Panel (b) przedstawia T_g wykreślone w funkcji p_g, zaś (c) zależność objętości aktywacji α-procesu (ΔV_α) od T_g/T (c). W panelu (d) pokazano histogram rozkładu klastrów połączonych wiązaniami wodorowymi w *S*- i *RS*-FLP. 28

Rys. 5. Termogramy DSC uzyskane podczas ogrzewania i chłodzenia trzech pochodnych ADM: 1-NH_2-ADM (a), 1-OH-ADM (b) i 3-NH_2-1-OH-ADM (c). W panelach (d), (e) i (f) przedstawiono zależności ε' ($f = 10^5$ Hz) vs. T w ciśnieniu atmosferycznym. 31

Rys. 6. Ewolucje czasowe znormalizowanego przewodnictwa stałoprądowego dla pomiarów przeprowadzonych w wybranych T oraz zależności logarytmu stałej szybkości od $1/T$ (wstawki) dla 3-NH_2-1-OH-ADM (a) i 1-NH_2-ADM (b). 36

Tabela 1. Struktury chemiczne oraz nazwy substancji badanych w ramach pracy doktorskiej 21

I. Wprowadzenie

Przejście szkliste to jedno z najbardziej intrygujących i wciąż nie do końca poznanych zjawisk w fizyce materii skondensowanej. Od kilkudziesięciu lat, jego natura/pochodzenie jest przedmiotem licznych debat wśród naukowców. Pomimo wielu prac eksperymentalnych i teoretycznych prowadzonych na różnych grupach substancji (niskocząsteczkowych związkach organicznych i nieorganicznych, polimerach, cieczach jonowych, itd. [1–5]), wiele kwestii, w tym gwałtowny wzrost lepkości w okolicy przejścia szklistego, czy dynamika molekularna w bliskim otoczeniu i poniżej punktu zeszklenia, wciąż nie zostały w pełni poznane i wyjaśnione.

1.1. Otrzymywanie szkieł

Rys. 1a obrazuje dwa możliwe scenariusze otrzymywania postaci stałej na drodze schładzania ciekłej substancji. Pierwszy z nich to przejście do fazy krystalicznej (przejście fazowe pierwszego rodzaju wg Ehrenfesta) w temperaturze T_k, któremu towarzyszy nagła, nieciągła zmiana objętości (V) i entropii (S). Z uwagi na to, iż powstawanie kryształów i ich późniejszy wzrost wymaga czasu, możliwe jest jego ominięcie poprzez zastosowanie dostatecznie szybkiego tempa schładzania (różnego dla różnych substancji, zwykle jest to kilka Kelwinów na minutę). Wówczas w temperaturze zeszklenia, T_g (*ang. glass transition temperature*) przechłodzona ciecz przechodzi do fazy szklistej (**Rys. 1a**). Istotnym faktem jest, iż w okolicy tej temperatury, parametry takie jak lepkość (η) czy czas relaksacji strukturalnej (τ_α) wzrastają o kilkanaście rzędów wielkości (w T_g η~10^{13} P i τ_α~100 s) [6,7]. Skutkuje to silnym spowolnieniem ruchliwości molekuł [8]. Co ważne, przejście ciecz-szkło przypomina termodynamiczne przejście fazowe drugiego rodzaju wg Ehrenfesta. Zachowany jest bowiem pierwszy warunek dotyczący ciągłości pierwszych pochodnych funkcji Gibbsa (G) względem ciśnienia i temperatury (tj. objętości V i entropii S) w pobliżu T_g. Jednak drugi warunek, zakładający skokowe/nieciągłe zmiany drugich pochodnych G, np. ciepła właściwego (C_p) pozostaje niespełniony – skok w zależności $C_p(T)$ w punkcie zeszklenia nie tworzy pionowej nieciągłości [9]. Ponadto, ze względu na to, że T_g bezpośrednio zależy od szybkości chłodzenia – im wolniejsze schładzanie, tym niższa temperatura zeszklenia – oraz fakt, że wszystkie właściwości fizyczne zmieniają się z czasem, formowanie szkła nie jest rozpatrywane jako klasyczne, termodynamiczne przejście fazowe, a raczej kinetyczne „zamrożenie" ruchów molekularnych w skali czasowej eksperymentu (przejście z układu równowagowego $>T_g$ do stanu nierównowagowego $<T_g$) [8]. W ostatnich latach opracowano liczne teorie próbujące wyjaśnić zjawisko przejścia szklistego. Wśród nich wyróżnić można model TOP (ang. *Two Order Parameter*) stworzony przez Hajimę Tanakę [10], modele oparte na koncepcji objętości

swobodnej, np. model Cohena-Gresta [11], czy też wiążące przejście szkliste z efektami entropowymi (teoria Adama-Gibbsa [12]).

Warto dodać, iż uzyskane na drodze szybkiego schładzania, czyli witryfikacji, szkło (zwane także amorfikiem lub ciałem bezpostaciowym) nie wykazuje na poziomie molekularnym dalekozasięgowego (translacyjnego i orientacyjnego) uporządkowania charakterystycznego dla struktury krystalicznej, lecz cechuje się chaotycznym rozkładem cząstek, zbliżonym do tego spotykanego w cieczy [9]. Porządek bliskozasięgowy, występujący także w krysztale, jest jednak zachowany.

Z uwagi na to, iż witryfikacją jest najprostszym sposobem otrzymania fazy amorficznej, większość badań mających na celu uzyskanie wglądu w procesy relaksacyjne zachodzące w fazie ciekłej/ciekłej przechłodzonej i szklistej substancji nisko- i wielkocząsteczkowych jest prowadzona w funkcji temperatury, w warunkach ciśnienia atmosferycznego (0.1 MPa). Chociaż dostarczają one istotnych informacji, nie pozwalają na pełne scharakteryzowanie analizowanych układów (z uwagi na zmiany gęstości i energii kinetycznej cząsteczek). Dlatego kluczowe jest zastosowanie alternatywnej metody pozwalającej na uzyskanie stanu szklistego, tj. izotermicznej kompresji cieczy, gdzie poprzez dobór tempa przeciśnieniowania i temperatury możliwe jest ominięcie krystalizacji (zachodzącej w ciśnieniu p_k), i uzyskanie szkła w ciśnieniu zeszklenia (p_g) (**Rys. 1b**). Ze względu na fakt, iż obniżenie temperatury, jak również kompresja prowadzą do tego samego efektu - „zamrożenia" dynamiki molekularnej - mogą być uważane za równoważne parametry termodynamiczne. Niemniej jednak, oddziałują na materię w różny sposób. Obniżenie temperatury wpływa na rotacyjne i wibracyjne stany energetyczne układu, zmieniając energię kinetyczną molekuł, natomiast wywieranie ciśnienia zmniejsza odległości między cząsteczkami (oddziałuje na energię potencjalną), a tym samym zwiększa upakowanie molekularne. Dlatego szkło uzyskane metodą izotermicznej kompresji cieczy charakteryzuje się wyraźnie większą gęstością w porównaniu do tego otrzymanego na drodze witryfikacji [13].

Warto też wspomnieć, iż technikami, które także, choć rzadziej wykorzystuje się celem uzyskania substancji w formie amorficznej, są m.in. ekstruzja topliwa, suszenie rozpyłowe, liofilizacja czy mielenie w temperaturze pokojowej lub ciekłego azotu, tj. 77 K. W tym miejscu należy podkreślić, iż pojęcie szkło (używane zamiennie z określeniem amorfik) jest zarezerwowane wyłącznie dla materiałów amorficznych produkowanych metodami szybkiego przechłodzenia i izotermicznej kompresji cieczy.

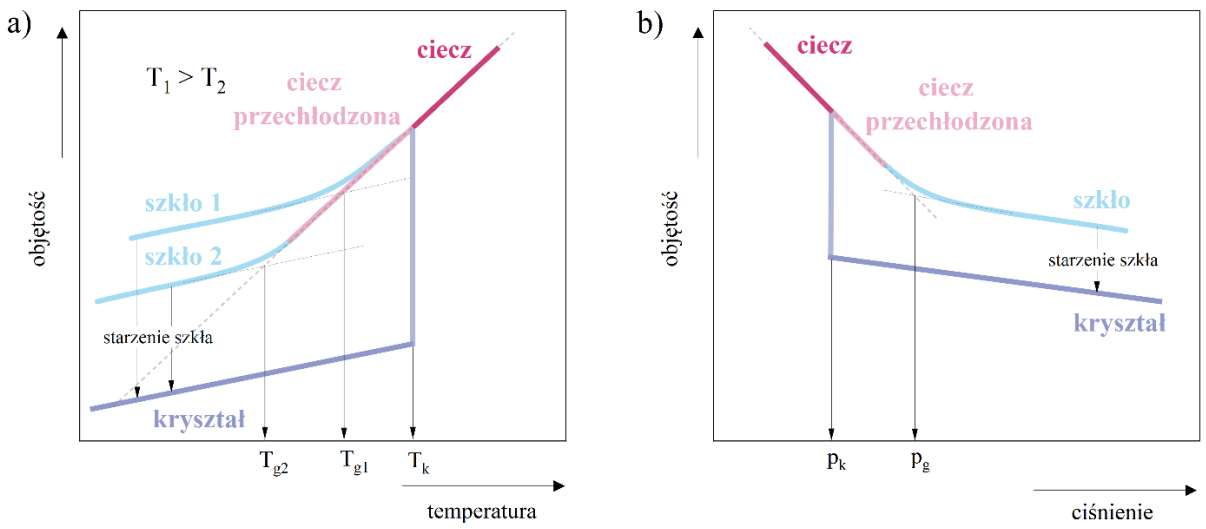

Rys. 1. Uzyskanie fazy szklistej na drodze witryfikacji (panel a) i izotermicznej kompresji cieczy (panel b). T_{g1} i T_{g2} oznaczają temperatury przejść szklistych dla dwóch różnych szybkości chłodzenia T_1>T_2, T_k to temperatura krystalizacji. Obszar pomiędzy T_k i T_g oraz p_k i p_g to tzw. faza cieczy przechłodzonej.

1.2. Badania dielektryczne na substancjach szklistych z wiązaniami wodorowymi, w tym amorficznych APIs

Prowadzenie eksperymentów z wykorzystaniem metody szerokopasmowej spektroskopii dielektrycznej (ang. *Broadband Dielectric Spectroscopy*, BDS) na szkłach/amorfikach z różnym charakterem/typem oddziaływań międzymolekularnych (siły van der Waalsa, wiązanie wodorowe, oddziaływania jonowe, itp.) otrzymanych na drodze witryfikacji i izotermicznej kompresji, umożliwia wnikliwą ocenę wrażliwości na temperaturę (T) i ciśnienie (p) obserwowanych na widmach dielektrycznych procesów relaksacyjnych. Szczególnie istotne są badania BDS układów zasocjowanych, dla których populacja wiązań wodorowych, ich architektura, są zależne od obu tych zmiennych termodynamicznych. Zasadniczo, obecność tych wiązań (co pokazano m.in. na przykładzie wody [6,14], alkoholi [15], itp.) skutkuje wysokimi wartościami temperatur przejść fazowych. Co więcej, kompresja ma na nie, jak również przejście szkliste, istotny wpływ. Zostało to dobrze udokumentowane zwłaszcza na przykładzie współczynnika ciśnieniowego temperatury przejścia szklistego (dT_g/dp), który informuje, o ile zwiększy się T_g materiału, na który wywierane jest ciśnienie o wartości 1 GPa. Stanowi więc parametr umożliwiający ocenę wrażliwości dynamiki globalnej/strukturalnej na kompresję (zmiany gęstości). Okazuje się, że jest on znacznie niższy dla układów zasocjowanych, np. glukozy czy glicerolu (dT_g/dp~60 K/GPa) [16], w porównaniu do systemów, w których dominują oddziaływania van der Waalsa (dT_g/dp>200 K/GPa) [8,17].

Warto jednak wspomnieć, że dla niektórych substancji, np. ibuprofenu [18] czy ketoprofenu [19], mających zdolność do formowania struktur dimerycznych lub trimerycznych, stabilizowanych wiązaniami wodorowymi, wartości dT_g/dp są zbliżone do tych oszacowanych dla związków van der Waalsowskich. Ponadto, systematyczne badania dynamiki strukturalnej układów zasocjowanych wyraźnie pokazują, że jest ona w głównej mierze determinowana przez zmiany temperatury. Zależność tę można określić ilościowo poprzez stosunek E_v/E_p, gdzie E_v i E_p oznaczają odpowiednio energię aktywacji przy stałej objętości i ciśnieniu. Przyjmuje się, że jeśli stosunek ten jest bliski jedności, jak w przypadku np. glicerolu i sorbitolu [8], dynamika molekularna układu jest kontrolowana przez temperaturę (dla odmiany dla układów van der Waalsa oraz licznych polimerów stosunek ten wynosi ~0.4–0.6 [8,20], wskazując, że gęstość i energia termiczna mają porównywalny wpływ na proces relaksacji strukturalnej w pobliżu przejścia szklistego). Warto też nadmienić, że obowiązująca dla większości systemów van der Waalsowskich fundamentalna reguła superpozycji temperaturowo-ciśnieniowej (ang. *temperature pressure superpositioning,* TPS), mówiąca o niezmienności kształtu/szerokości procesu relaksacji strukturalnej (α) dla określonej wartości czasu relaksacji (τ_α), niezależnie od kombinacji temperatury i ciśnienia [21], w przypadku substancji zasocjowanych nie jest spełniona [8,22–24]. Przyczyną takiego zachowania są zmiany w rozkładzie czasów relaksacji α na skutek modyfikacji w sile i populacji wiązań wodorowych wywołanych kompresją, a także fluktuacji gęstości w różnych warunkach termodynamicznych. Należy jednak dodać, że najnowsze eksperymenty przeprowadzone na wybranych układach formujących struktury dimeryczne, trimeryczne, a nawet sieci z wiązaniami wodorowymi [18,19,25], wskazały odmienne zachowanie (obowiązywanie reguły TPS podobnie jak w systemach van der Waalsa) co sugeruje, że wpływ obecności tych wiązań na kształt dyspersji α jest bardziej złożonym, zależnym od innych czynników zagadnieniem, które wymaga dodatkowych badań.

Należy też wspomnieć, iż charakterystyka dynamiki molekularnej z wykorzystaniem metody BDS, w szczególności w ciśnieniu podwyższonym, ma także istotne znaczenie w przypadku szklistych/amorficznych farmaceutycznych substancji aktywnych (ang. *Active Pharmaceutical Ingredients*, APIs). Co istotne, układy te cechują się wyższą wartością energii swobodnej Gibbsa względem swoich krystalicznych odpowiedników, co bezpośrednio wpływa na ich większą rozpuszczalność [26], szybkość wchłaniania/rozpuszczania [27–30], a tym samym lepszą dostępność biologiczną. Dotyczy to głównie APIs z II i IV grupy systemu klasyfikacji biofarmaceutycznej (ang. *Biopharmaceutics Classification System*, BCS). Niestety, mimo licznych zalet amorficznych farmaceutyków, poważnym wyzwaniem pozostaje ich wysoka niestabilność fizykochemiczna, która objawia się silną tendencją do rekrystalizacji,

chemicznej degradacji, czy przemian izomerycznych i polimorficznych zachodzących w różnych warunkach termodynamicznych [27,31–34]. Warto zaznaczyć, że większość badań na amorficznych APIs jest prowadzona w ciśnieniu atmosferycznym, bez uwzględnienia wpływu wysokiej kompresji, która odgrywa ważną rolę w formulacjach farmaceutycznych (substancje aktywne w procesie tabletkowania są poddawane naprężeniom mechanicznym w zakresie ciśnień 50-400 MPa). Dlatego wykorzystanie techniki BDS umożliwiającej generowanie ciśnień podobnego rzędu (tym samym odzwierciedlenie warunków podczas tabletkowania), pozwala na kontrolowanie/przewidywanie przejść fazowych czy przemian chemicznych związanych np. ze zmianami konformacyjnymi, izomerią *E-Z*, zachodzących w badanej substancji, a także jej stabilności chemicznej, co w rezultacie może znacząco wpłynąć na skuteczność terapeutyczną i bezpieczeństwo finalnego produktu/preparatu z amorficzną API w tabletce.

1.3. Kryształy orientacyjnie nieuporządkowane. Badania na pochodnych adamantanu

Co istotne, kluczem do zrozumienia natury przejścia szklistego jest dogłębne poznanie mechanizmów prowadzących do spowolnienia dynamiki molekularnej cząsteczek podczas zeszklenia. Tradycyjne materiały szkłotwórcze, jak wspomniano wyżej, charakteryzują się nieporządkiem dalekozasięgowym: translacyjnym i orientacyjnym, w konsekwencji znaczną liczbą stopni swobody. Jednym z podejść do lepszego poznania zjawiska zeszklenia i dynamiki reorientacyjnej substancji tworzących fazę szklistą, jest analiza układów o ograniczonej liczbie stopni swobody. Odpowiednim modelem do takich badań są kryształy orientacyjnie nieuporządkowane (*ang. orientationally disordered crystals*, ODIC), powszechnie określane jako plastyczne kryształy (*ang. plastic crystals*, PC, **Rys. 2**). Układy te, ze względu na unikalne właściwości fizykochemiczne, w tym wyjątkową plastyczność oraz możliwość odwracalnego przejścia ze stanu nieuporządkowanego do uporządkowanego/ nieuporządkowanego stały się w ostatnich latach atrakcyjne dla wielu technologii, w tym przemysłu farmaceutycznego [35–44]. Co istotne, większość PC jest

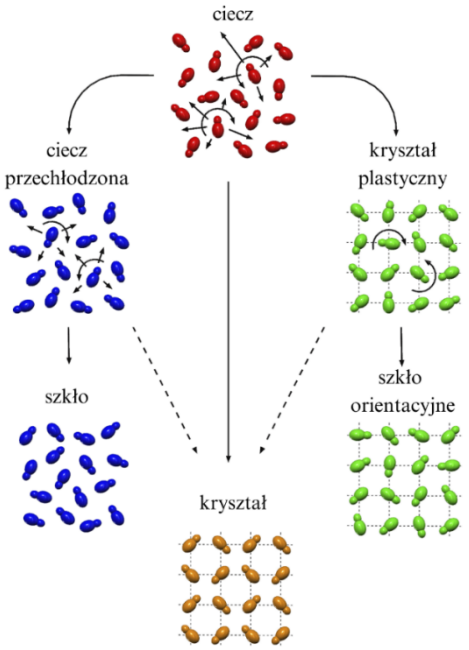

Rys. 2. Schematyczne przedstawienie możliwych przejść cieczy do fazy stałej: szkła strukturalnego, szkła orientacyjnego (poprzez fazę plastycznego kryształu) oraz kryształu uporządkowanego [35].

tworzonych przez cząsteczki o kształcie globularnym (prawie sferycznym) [35], które charakteryzują się dynamicznym nieporządkiem orientacyjnym (podobnym do tego, jaki występuje w cieczy), przy jednoczesnym uporządkowaniu translacyjnym (co odróżnia je od tradycyjnych materiałów szklistych, a upodabnia do kryształów), z tendencją do tworzenia wysoce symetrycznych sieci krystalicznych: sześciennych, quasi-sześciennych lub romboedrycznych [45,46]. Warto podkreślić, że ze względu na duże podobieństwo we właściwościach termodynamicznych czy dynamice molekularnej do klasycznych materiałów amorficznych, PC mają kluczowe znaczenie dla wyjaśnienia zachowania tych bardziej złożonych, nieuporządkowanych układów, zachodzących w nich przejść fazowych/przejścia szklistego oraz ich mikroskopowego pochodzenia [35,45,47,48].

W szczególności, w wielu przypadkach zastosowanie odpowiedniego tempa chłodzenia związków znajdujących się w fazie plastycznej prowadzi do przejścia do fazy szklistego kryształu (ang. *glassy crystal*), inaczej nazywanego szkłem orientacyjnym (ang. *orientational glass*, **Rys. 2**) [35,49]. Wówczas dynamika tych układów spowalnia o wiele rzędów wielkości, co przypomina zachowanie typowe dla materiałów szklistych. Ponadto, zarówno PC i konwencjonalne szkła charakteryzują się wyraźnym odchyleniem od Arrheniusowskiego zachowania czasów relaksacji strukturalnej (τ_α) od temperatury, a rozkład τ_α (szerokość dyspersji α) jest często opisywany funkcją Kohlrauscha-Williamsa-Wattsa (KWW) [50,51], gdzie wartości parametru kształtu, β_{KWW}, są znacznie mniejsze od jedności (odpowiedź nie-Debye'owska). Chociaż przejścia fazowe w ODIC/PC były intensywnie badane dla wielu, różnego typu związków, np. orto-, para- i meta-karboranów [52,53], anhydrosacharydów [42,54], cyklicznych alkoholi [35,55,56], etanolu [35], czy heksa-podstawionych benzenów [57,58], towarzyszący im charakter zmian w strukturze, oddziaływaniach między- i wewnątrzmolekularnych, czy właściwościach termicznych, dynamicznych, wciąż budzą ciekawość i zainteresowanie środowiska naukowego.

W ostatnich 20-30 latach, adamantan (ADM) i jego pochodne, ze względu na unikalne właściwości strukturalne, sztywność molekularną, czy tendencję do formowania wielu form polimorficznych, stanowią jedną z najintensywniej badanych grup związków formujących fazy ODIC/PC [59–68]. W literaturze istnieje wiele doniesień naukowych poświęconych wpływowi podstawienia jednego/dwóch atomów wodoru w cząsteczce ADM, atomami halogenu (np. -Cl, -Br, -I, -F) [63,69–73], czy grupami funkcyjnymi (np. -OH, $-NH_2$, -CN) [35,59,74–76], na właściwości fizykochemiczne tych układów. Wiele z nich wykazało zwiększenie polarności systemu, zniekształcenie symetrycznego kształtu cząsteczki, czy zmiany w układzie wiązań wodorowych na skutek podstawienia [74,76–79]. Warto również dodać, iż wspomniane

modyfikacje w strukturze chemicznej związku nie skutkują tłumieniem przejścia z uporządkowanej fazy krystalicznej (ang. *ordinary crystal*, OC) do fazy PC, ale mogą wpływać na sieć krystaliczną, czy też temperaturę, w której to przejście występuje [64,69,74]. Są również doniesienia wskazujące na istnienie zależności pomiędzy temperaturą przejścia OC-PC a liczbą atomową (Z) halogenu (-F, -Cl, -Br) przyłączonego do cząsteczki ADM – $T_{OC\text{-}PC}$ rośnie ze wzrostem Z [62]. Część artykułów naukowych poświęcona jest stricte badaniom spektroskopowym na zasocjowanych pochodnych ADM. Przykładowo, Harvey i wsp., na przykładzie wyników pomiarów podczerwonych wykonanych dla 1-OH-ADM ujawnili, że w wysokotemperaturowej fazie ODIC występują wolne grupy hydroksylowe, co wskazuje na zmniejszony stopień asocjacji molekuł w tej fazie względem OC [80]. Natomiast badania przeprowadzone dla innej pochodnej ADM – 2-metylo-2-adamantanolu – wykazały istnienie w fazie krystalicznej tego związku silnych wiązań wodorowych (z przewagą struktur dimerycznych) [81]. Jednak podczas przejścia fazowego OC-PC siła tych wiązań malała, czego efektem było występowanie zarówno połączeń dimerycznych, jak i niezasocjowanych cząsteczek 2-metylo-2-adamantanolu w fazie plastycznej. Dokonując przeglądu literaturowego można zauważyć, iż większość badań właściwości termodynamicznych czy pomiarów spektroskopowych (podczerwonych, Ramana, dielektrycznych) na pochodnych ADM jest prowadzonych w ciśnieniu otoczenia [35,68,75,82–84]. Znaleźć można nieliczne prace, w których zaprezentowano wyniki eksperymentów przeprowadzonych w warunkach wysokiej kompresji [60,62,63,85–88]. Głównie koncentrowały się one na charakterze przejść fazowych w badanych związkach i ich właściwościach mechanicznych. Dlatego kluczowe jest wypełnienie luki w tym obszarze badań, w celu uzyskania wglądu w strukturę, dynamikę molekularną oraz mechanizmy przejść fazowych w PC. Informacje w tym temacie pozwolą nie tylko lepiej poznać fundamentalne właściwości układów tworzących fazy PC, ale także umożliwią zrozumienie zachowania nieuporządkowanych dalekozasięgowo materiałów szklistych, ze szczególnym naciskiem na naturę przejścia szklistego.

1.4. Cel pracy

Głównym założeniem niniejszej rozprawy doktorskiej było scharakteryzowanie własności termicznych, struktury atomowej, oddziaływań międzycząsteczkowych i dynamiki molekularnej wybranych zasocjowanych amorficznych/tworzących fazy plastyczne substancji aktywnych oraz ich pochodnych (tj. tikagreloru, enancjomerów flurbiprofenu i ich racemicznej mieszaniny i trzech pochodnych adamantanu - 1-adamantylaminy (amantadyny), 1-adamantanolu oraz 3-amino-1-adamantanolu), w różnych warunkach termodynamicznych (T,p). Ważnym aspektem badań były wysokociśnieniowe eksperymenty dielektryczne, które umożliwiły wgląd w dynamikę strukturalną i lokalną, charakter/naturę przejść fazowych występujących w badanych układach (zwłaszcza tych formujących fazy plastyczne), jak również, w oparciu o dodatkową analizę parametrów takich jak kształt dyspersji α czy ΔV, pośrednio w siłę i populację wiązań wodorowych podczas kompresowania/zagęszczania.

Struktury chemiczne oraz nazwy (pełne i skrócone) wszystkich badanych substancji przedstawiono w **Tabeli 1**.

Rezultaty wszystkich przeprowadzonych eksperymentów zostały opublikowane w międzynarodowych czasopismach naukowych z listy filadelfijskiej o łącznej punktacji Impact Factor **(IF)=16.2** oraz łącznej punktacji **MNiSW=520**:

P1. P. Jesionek, D. Heczko, B. Hachuła, K. Kamiński, E. Kamińska, ***High-pressure studies in the supercooled and glassy state of the strongly associated active pharmaceutical ingredient—ticagrelor***, Sci. Rep. 13 (**2023**) 8890. **IF=3.8, MNiSW=140 pkt.**

P2. P. Jesionek, B. Hachuła, K. Jurkiewicz, P. Włodarczyk, M. Hreczka, K. Kamiński, E. Kamińska, ***Variation of Activation Volume as an Indicator of the Difference in Clusterization Phenomenon Induced by H-Bonding and F−Π Stacking Interactions in Enantiomers and a Racemate of Flurbiprofen***, J. Phys. Chem. B. 128 (**2024**) 4021–4032. **IF=2.8, MNiSW=140 pkt.**

P3. P. Jesionek, B. Hachuła, D. Heczko, T. Lamrani, K. Jurkiewicz, M. Tarnacka, M. Książek, K. Kamiński, E. Kamińska, ***Studies on the nature and pressure evolution of phase transitions in 1-adamantylamine and 1-adamantanol,*** Spectrochim. Acta Part A Mol. Biomol. Spectrosc. 299 (**2023**) 122794. **IF=4.3, MNiSW=140 pkt.**

P4. P. Jesionek, B. Hachuła, M. Tarnacka, K. Jurkiewicz, K. Kamiński, E. Kamińska, ***Comparative studies on the nature and kinetics of phase transitions in plastic crystals: Hydrogen-bonded adamantane derivatives***, J. Mol. Liq. 413 (**2024**) 125907. **IF=5.3, MNiSW=100 pkt.**

Treści powyższych publikacji stanowiących podstawę niniejszej pracy doktorskiej są załączone w **Rozdziale III**. Rezultaty przeprowadzonych eksperymentów zostały zaprezentowane przeze mnie na wymienionych poniżej konferencjach naukowych:

1. 65. Zjazd Naukowy Polskiego Towarzystwa Chemicznego. „*Badania wysokociśnieniowe silnie zasocjowanej substancji aktywnej – tikagreloru*". Toruń, 2023.
2. IV Seminarium Ogólnoakademickie. „*Badania charakteru i ciśnieniowej ewolucji przejść fazowych w 1-adamantyloaminie i 1-adamantanolu*". Sosnowiec, 2023.
3. V Seminarium Ogólnoakademickie. "*Calorimetric, structural and dielectric studies on active substances forming plastic crystal phases*". Sosnowiec, 2024.
4. 12th BDS Conference. *"Variation of Activation Volume as an Indicator of the Change in Clusterization Phenomenon in Flurbiprofen enantiomers and the racemate*". Lizbona, 2024.
5. 66. Zjazd Naukowy Polskiego Towarzystwa Chemicznego. „(*Nie)rozróżnialne związki chiralne: porównanie właściwości termicznych, strukturalnych oraz dielektrycznych enancjomerów flurbiprofenu i ich mieszaniny racemicznej*". Poznań, 2024.
6. VI Seminarium Ogólnoakademickie. *"Indistinguishable or not? A comprehensive studies of flurbiprofen enantiomers and their racemic mixture"*. Sosnowiec, 2025.

Ponadto jestem współautorką 4 artykułów naukowych, które nie zostały włączone do rozprawy doktorskiej:

1. D. Heczko, **P. Jesionek**, B. Hachuła, K. Jurkiewicz, J. Grelska, M. Tarnacka, K. Kamiński, M. Paluch, E. Kamińska, ***Variation in the local ordering, H-bonding pattern and molecular dynamics in the pressure densified ritonavir,*** J. Mol. Liq. 351 (**2022**) 118666,
2. **P. Jesionek**, B. Hachuła, D. Heczko, K. Jurkiewicz, M. Tarnacka, M. Zubko, M. Paluch, K. Kamiński, E. Kamińska, ***The impact of H/D exchange on the thermal and structural properties as well as high-pressure relaxation dynamics of melatonin***, Sci. Rep. 12 (**2022**) 14324,
3. T. Lamrani, **P. Jesionek**, M. Tarnacka, D. Zakowiecki, P. Włodarczyk, M. Zubko, E. Kamińska, K. Kamiński, K. Jurkiewicz, ***Generation of nematic order in itraconazole by cryo-milling***, J. Mol. Liq. 414 (**2024**) 126106,

4. **P. Jesionek-Ratka**, B. Hachuła, M. Tarnacka, T. Lamrani, K. Jurkiewicz, K. Kamiński, E. Kamińska, ***Insights into the nature of phase transitions and relaxation dynamics in memantine – An active substance forming orientationally disordered crystals***, Spectrochim. Acta Part A Mol. Biomol. Spectrosc. 341 (**2025**) 126427,

jak również 1 zgłoszenia patentowego pt. ***„Sposób otrzymywania itrakonazolu w stabilnej fazie nematycznej”*** (Numer: P.447909, data zgłoszenia: 1 marzec 2024). Co więcej, zostałam Laureatką XVII edycji Konkursu Wyróżnień Jego Magnificencji Rektora Uniwersytetu Śląskiego, co stanowi szczególne uhonorowanie moich osiągnięć naukowych oraz zaangażowania podczas kształcenia w Szkole Doktorskiej.

Dodatkowo, wyniki badań nad melatoniną i jej deuterową pochodną zostały zaprezentowane na poniższych konferencjach:

1. XV Kopernikańskie Seminarium Doktoranckie. *„Badania nad melatoniną i jej deuterowaną pochodną pod kątem ich farmaceutycznego zastosowania”.* Toruń, 2022.
2. 2nd Interdisciplinary Conference on Drug Science ACCORD. "*The influence of H/D exchange on the thermal and structural properties as well as molecular dynamics (at ambient and high pressure) of the selected active pharmaceutical ingredient*". Warszawa, 2024.

Tabela 1. Struktury chemiczne oraz nazwy substancji badanych w ramach pracy doktorskiej

Struktura chemiczna	Nazwa	Skrót
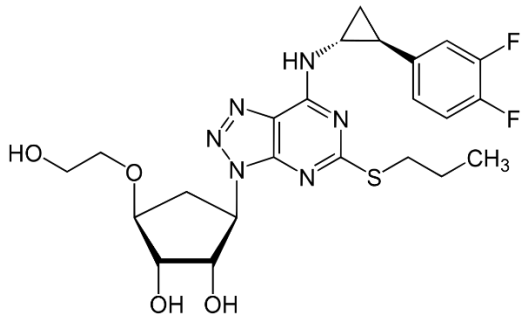	tikagrelor	TICA
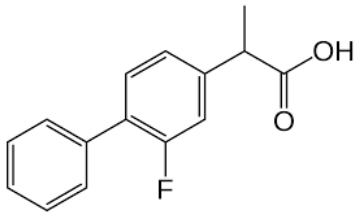	flurbiprofen	FLP (R-FLP, S-FLP, RS-FLP)
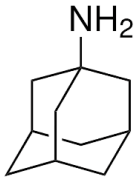	1-adamantylamina (amantadyna)	1-NH_2-ADM
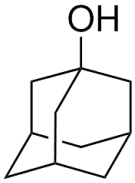	1-adamantanol	1-OH-ADM
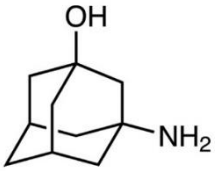	3-amino-1-adamantanol	3-NH_2-1-OH-ADM

II. Omówienie i dyskusja otrzymanych wyników

2.1. Badania wysokociśnieniowe silnie zasocjowanej substancji aktywnej – tikagreloru w fazie cieczy przechłodzonej i szklistej

Jak wspomniano w podr. 1.2., zrozumienie wpływu różnych warunków termodynamicznych (T i p) na szerokość α-dyspersji w związkach tworzących wiązania wodorowe stanowi wymagające wyzwanie. Celem badań wykonanych w publikacji P1 było w szczególności znalezienie odpowiedzi na pytanie, czy istnieje bezpośredni związek między siłą/populacją/schematem wiązań wodorowych a kształtem procesu strukturalnego? Aby uzyskać wgląd w to zagadnienie, wykonano eksperymenty na szkle zagęszczonym (ang. *pressure densified glass*, PDG), jak również witryfikowanym (ang. *ordinary glass*, OG) silnie zasocjowanej API stosowanej w profilaktyce i leczeniu chorób sercowo-naczyniowych - tikagreloru (TICA). Uzyskane wyniki zestawiono i dyskutowano z tymi otrzymanymi dla rytonawiru (RTV).

W pierwszej kolejności TICA poddano badaniom z wykorzystaniem techniki różnicowej kalorymetrii skaningowej (ang. *Differential Scanning Calorimetry,* DSC) celem uzyskania pełnej charakterystyki termicznej badanej API. Na termogramie zmierzonym podczas ogrzewania krystalicznej próbki TICA (Fig. 1a w P1) uwidocznił się pojedynczy proces endotermiczny, odpowiadający zjawisku topnienia. Dalsze chłodzenie, a następnie ogrzewanie zeszklonej substancji (OG) ujawniło endotermiczny skok w temperaturowej zależności przepływu ciepła związany z przejściem do fazy szklistej, na podstawie którego wyznaczono (jako punkt przegięcia) wartość T_g równą 325 K oraz obliczono zmianę ciepła właściwego w T_g (ΔC_p=0.464 J/g·K).

W kolejnym kroku przeprowadzono badania dynamiki molekularnej witryfikowanego TICA w ciśnieniu atmosferycznym, w szerokim zakresie T. Zarejestrowane w fazie cieczy przechłodzonej ($T>T_g$) widma strat dielektrycznych rozpatrywanej API wskazały na obecność dwóch charakterystycznych procesów. Pierwszym z nich było przewodnictwo stałoprądowe (σ_{DC}), stanowiące wypadkową dwóch efektów: transportu jonów oraz przeskoku protonów (ang. *proton hopping*) wzdłuż sieci wiązań wodorowych – warunkowanego obecnością wielu grup hydroksylowych w strukturze TICA (Tabela 1). Natomiast drugim procesem, zlokalizowanym przy wyższych częstotliwościach (f), była relaksacja strukturalna (α), wywodząca się z kooperatywnych ruchów wszystkich cząsteczek w próbce (Fig. 1b w P1). Z kolei w fazie szklistej ($T<T_g$), na widmach ε" vs. f uwidoczniły się dwie relaksacje drugorzędowe: β i γ.

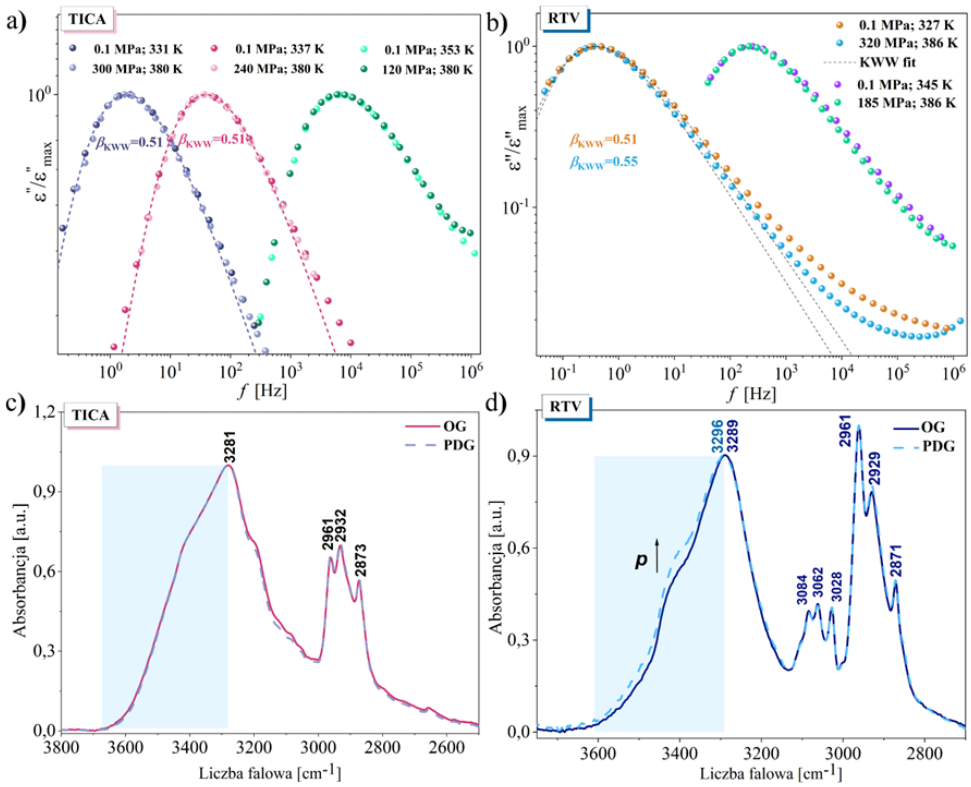

Rys. 3. Superpozycja widm TICA (a) i RTV (b) zebranych w różnych warunkach T i p w pobliżu i powyżej T_g. Panele (c) i (d) przedstawiają widma FTIR zmierzone w temperaturze pokojowej odpowiednio dla OG i PDG TICA oraz RTV [89].

Następnie analizie poddano zachowanie badanej API w warunkach wysokiej kompresji. Podobnie jak w przypadku danych uzyskanych w $T>T_g$ w ciśnieniu otoczenia, na widmach dielektrycznych TICA zmierzonych podczas wysokociśnieniowych eksperymentów izobarycznych i izotermicznych, widoczne było σ_{DC} oraz proces relaksacji α (Fig. 2 w P1). Co ciekawe, porównanie wybranych widm BDS zebranych w różnych T i p w pobliżu T_g pokazało, iż szerokość α-dyspersji pozostaje stała niezależnie od zastosowanych kombinacji obu zmiennych termodynamicznych (spełniona jest reguła TPS), co potwierdziła jednakowa wartość współczynnika β_{KWW} (=0.51) uzyskana z dopasowania do danych funkcji Kohlrausch-Williamsa-Wattsa, KWW (**Rys. 3a** oraz Fig. 3a w P1, Eq. 1). Wynik ten był bardzo zaskakujący, biorąc pod uwagę prawdopodobieństwo tworzenia silnych wiązań wodorowych przez cząsteczki TICA. Tym samym oczekiwano, że zastosowanie wysokich T i p znacząco wpłynie na populację i siłę tych oddziaływań, co z kolei znajdzie odzwierciedlenie w kształcie α-procesu. Aby lepiej zrozumieć powyższe zachowanie, przeprowadzono badania na szkle zagęszczonym/przeciśnieniowanym (PDG) badanej API z wykorzystaniem spektroskopii w podczerwieni z transformacją Fouriera (ang. *Fourier Transform Infrared Spectroscopy*, FTIR). Należy podkreślić, iż takie podejście pozwala „zamrozić" strukturę skompresowanej substancji i uzyskać informacje na temat specyficznych oddziaływań w podwyższonym ciśnieniu.

Co istotne, uzyskany dla PDG profil widmowy w zakresie liczb falowych odpowiadających drganiom rozciągającym grup OH i NH nie różnił się od tego uzyskanego dla OG (**Rys. 3c** oraz Fig. 3c w P1), co wskazywało na dalece podobne uporządkowanie związanych wodorowo cząsteczek w obu próbkach. Mogło to również sugerować, że w warunkach wysokiej kompresji, wpływ T i p na te oddziaływania wzajemnie się kompensuje. W konsekwencji, kształt α-procesu pozostaje niezmieniony w warunkach izochronicznych (τ_α=const.). Otrzymane wyniki porównano do tych uzyskanych dla innej, słabiej zasocjowanej API – RTV, dla której z kolei obserwowano zwężenie α-dyspersji w podwyższonym ciśnieniu [89] (**Rys. 3b** oraz Fig. 3b w P1). Co ważne, w przypadku tej substancji, profil widmowy pasm odpowiadających drganiom rozciągającym grup OH i NH zmieniał się znacząco pod wpływem p (**Rys. 3d** oraz Fig. 3d w P1), co utożsamiono z rosnącą populacją słabszych wiązań wodorowych w PDG. Na podstawie omawianych przypadków (TICA i RTV) stwierdzono, że istnieje ścisła zależność między kształtem procesu α a schematem wiązań wodorowych w warunkach wysokiej kompresji.

Dalsza dogłębna analiza widm dielektrycznych zarejestrowanych dla TICA w $T>T_g$ w różnych warunkach termodynamicznych z użyciem funkcji Havriliaka-Negami, HN (Eq. 2 w P1), umożliwiła wyznaczenie czasów relaksacji strukturalnej (τ_αs), a następnie wykreślenie ich w funkcji T i p. Uzyskane trójwymiarowe zależności zostały zanalizowane z wykorzystaniem zmodyfikowanego równania Avramova (Fig. 4 w P1) [90]. Następnie otrzymane ze wzoru (Eq. 3 w P1) wartości T_g wykreślono w funkcji ciśnienia, co pozwoliło oszacować współczynnik ciśnieniowy temperatury zeszklenia (dT_g/dp) w granicy p=0.1 MPa, który wyniósł 163 K/GPa. Relatywnie wysoka wartość tego parametru (nieco niższa niż ta odnotowana dla RTV (~200 K/MPa) [89]) wskazywała na silny wpływ kompresji na relaksację strukturalną w TICA. Należy podkreślić, iż dT_g/dp~160-200 MPa uzyskane dla obu APIs było wyraźnie wyższe niż wartości raportowane dla innych niskocząsteczkowych związków z silnymi wiązaniami wodorowymi, np. D-sorbitolu, glicerolu (dT_g/dp<80 K/GPa) [16].

Dodatkowo postanowiono sprawdzić, czy istnieje korelacja/sprzężenie (ang. *coupling*) między σ_{DC} a τ_α w różnych warunkach termodynamicznych zgodnie z prawem Debye'a-Stokes'a-Einstein'a (DSE) (Eq. 4 w P1). Okazało się, że wykresów zależności $\log_{10}\sigma_{DC}$ vs. $\log_{10}\tau_\alpha$ (dane izobaryczne i izotermiczne) nie można opisać funkcją liniową z nachyleniem równym 1. Konieczne więc do opisu danych jest użycie ułamkowego równania DSE ($0<s<1$), w którym wykładnik s odpowiada nachyleniu ww. prostej (Eq. 5 w P1). Co ważne, parametr s praktycznie nie zmieniał się ze wzrostem T i p (Fig. 4c w P1), co powiązano ze stabilnym schematem wiązań wodorowych w warunkach wysokiej kompresji (takie zachowanie potwierdziły badania FTIR wykonane na PDG TICA). Najprawdopodobniej zatem, zmienne warunki termodynamiczne nie wpływają na zjawisko *proton hopping*, które ma znaczący wkład

do σ_{DC}. Należy podkreślić także, iż wyraźnie mniejsze od 1 wartości parametru s (~0.6–0.7) oszacowane z analizy danych izotermicznych i izobarycznych (Fig. 4c w P1), wskazywały na wyraźne rozprzężenie między przewodnictwem stałoprądowym i dynamiką strukturalną.

W kolejnym etapie scharakteryzowano wpływ wysokiej kompresji na dynamikę molekularną TICA w stanie szklistym ($T<T_g$). W przeciwieństwie do danych dielektrycznych uzyskanych w ciśnieniu atmosferycznym (gdzie widoczne były dwa procesy drugorzędowe: β oraz γ), w podwyższonym p zaobserwowano tylko β-relaksację (Fig. 5 w P1). Wyznaczone przy użyciu funkcji HN czasy relaksacji τ_β oraz τ_γ (p=0.1 MPa), wraz z uprzednio otrzymanymi wartościami τ_α, wykreślono w funkcji T_g/T (Fig. 6 w P1). Następnie zależności $\log_{10}\tau_\beta$ i $\log_{10}\tau_\gamma$ vs. T_g/T zanalizowano przy użyciu równania Arrheniusa celem określenia bariery aktywacji (E_x, gdzie x=β i γ) tych procesów (Eq. 6 w P1). Dla β-relaksacji zauważono wzrost E_β wraz ze wzrostem ciśnienia (E_β=66, 73 i 81 kJ/mol odpowiednio w 0.1, 170 i 340 MPa). Natomiast E_γ uzyskana w p=0.1 MPa (=38 kJ/mol) była wyraźnie niższa w porównaniu do E_β oszacowanej w tym samym ciśnieniu. Istotnym faktem jest, iż τ_β otrzymane w p=0.1, 170 i 340 MPa oraz zaprezentowane względem T_g/T idealnie się nakładały (Fig. 6 w P1), co wskazywało na silną wrażliwość procesu β na kompresję. Dodatkowym argumentem potwierdzającym ten wniosek była wyjątkowo wysoka wartość objętości aktywacji tego procesu (ΔV_β=43 cm^3/mol), oszacowana na podstawie analizy danych izotermicznych (Eq. 7 w P1). Na podstawie uzyskanych wyników stwierdzono, że relaksacja β w TICA jest typu Johari-Goldstein (JG) i pochodzi od niekooperatywnych, lokalnych ruchów całych cząsteczek. Z kolei szybszy proces γ ma charakter wewnątrzcząsteczkowy i jest związany z reorientacją jedynie fragmentu cząsteczki TICA. Ponadto, stały stosunek $\tau_\alpha/\tau_{JG\text{-}\beta}$ dla danych otrzymanych w p=0.1 i 170 MPa wskazywał na spełnienie reguły izochronicznej superpozycji czasów relaksacji α i JG-β.

Na koniec, używając równania Eyringa (Eq. 8 w P1), obliczono entropię i entalpię aktywacji dla procesu β-relaksacji (odpowiednio ΔS_β i ΔH_β) w ciśnieniu otoczenia i warunkach wysokiej kompresji. Oba parametry rosły ze wzrostem p. Co istotne, ΔS_β miała wartość dodatnią (co sugerowało międzycząsteczkową kooperatywność tego procesu) i nieznacznie zwiększała się z kompresją, od 105 J/mol·K w 0.1 MPa do 108 J/mol·K w 340 MPa, co powiązano z niewielkimi zmianami konformacyjnymi/ molekularnymi cząsteczek TICA w wysokim p.

2.2. Zmiana objętości aktywacji jako wskaźnik różnic w zjawisku klasteryzacji indukowanym przez wiązania wodorowe i oddziaływania F-Π *stacking* w enancjomerach flurbiprofenu i ich mieszaninie racemicznej

Celem badań przeprowadzonych w publikacji P2 było określenie różnic w organizacji molekularnej, wynikających z obecności wiązań wodorowych, pomiędzy enancjomerami (*R* i *S*) a racematem flurbiprofenu (FLP) – API należącej do grupy niesteroidowych leków przeciwzapalnych, zarówno w stanie krystalicznym, jak i w fazie cieczy przechłodzonej. Istotnym aspektem było także zweryfikowanie, czy struktura atomowa, właściwości termiczne oraz dynamika molekularna czystych izomerów *R*- i *S*-FLP są podobne do tych obserwowanych dla *RS*-FLP w różnych warunkach termodynamicznych. Warto podkreślić, że badania wysokociśnieniowe odgrywają kluczową rolę w przypadku enancjomerów substancji aktywnych, które mogą istotnie różnić się pod względem aktywności biologicznej, toksyczności oraz właściwości farmakokinetycznych [91–93]. Jak wskazano w podr. 1.2., warunki wysokiej kompresji mogą determinować konformację cząsteczek APIs, co może mieć istotny wpływ na ich działanie farmakologiczne.

Komplementarne badania rozpoczęto od dokładnej charakterystyki struktury atomowej *R*-FLP, *S*-FLP i *RS*-FLP z wykorzystaniem techniki dyfrakcji rentgenowskiej (ang. *X-ray diffraction,* XRD). Analiza zarejestrowanych dyfraktogramów wykazała różnice między strukturą krystaliczną obu enancjomerów i mieszaniny racemicznej (układ trójskośny w przypadku *RS*-FLP i ortorombowy dla *R*- i *S*-FLP), które mogą wynikać z przestrzennej organizacji molekuł oraz ich oddziaływań poprzez wiązania wodorowe (Fig. 1a w P2). Co istotne, po stopieniu, różnice pomiędzy obydwoma enancjomerami a racematem nie były zauważalne (Fig. 1b w P2).

Różnice w przestrzennym ułożeniu cząsteczek w sieci krystalicznej *R*-, *S*- i *RS*-FLP znajdowały także odzwierciedlenie w parametrach spektralnych (strukturze subtelnej) pasm widm podczerwonych, szczególnie w obszarach liczb falowych odpowiadających drganiom grup zaangażowanych w proces asocjacji, tj. drganiom rozciągającym grupy hydroksylowej, karbonylowej, karboksylowej, alifatycznej, jak również pozapłaszczyznowym deformacjom grupy OH (Fig. 1c w P2). Na podstawie dokładnej analizy widm FTIR form krystalicznych badanych substancji stwierdzono, że cząsteczki racematu tworzą typowe struktury dimeryczne, natomiast molekuły czystych enancjomerów FLP formują długie, wodorowo związane łańcuchy. Zauważono, podobnie jak w przypadku badań XRD, że wszystkie różnice spektralne zanikają po stopieniu próbek, czego efektem są identyczne widma podczerwone trzech badanych układów (Fig. 1d w P2).

Analiza termogramów DSC zarejestrowanych dla *R*-, *S*- i *RS*-FLP wskazała, że każdy z badanych układów ma zdolność do formowania fazy amorficznej, co potwierdziła obecność skoku endotermicznego odpowiadającego przejściu szklistemu, widocznemu podczas ogrzewania uprzednio stopionych, a następnie przechłodzonych próbek. Warto zaznaczyć, że wartości T_g oraz ΔC_p były zbliżone dla wszystkich analizowanych związków (Fig. 2 w P2).

W kolejnym kroku wnikliwie zbadano dynamikę molekularną obu enancjomerów i mieszaniny racemicznej FLP w ciśnieniu atmosferycznym, w szerokim zakresie *T*. Zmierzone w fazie cieczy przechłodzonej zależności $\varepsilon''(f)$ dla wszystkich próbek ujawniły dwa charakterystyczne procesy: σ_{DC} oraz relaksację α. W fazie szklistej ($T<T_g$) stwierdzono natomiast występowanie procesu drugorzędowego β (Fig. 3a-c w P2). Uzyskane z dopasowania funkcji HN do widm dielektrycznych zarejestrowanych w $T>T_g$ czasy relaksacji strukturalnej (τ_αs) wykreślone w funkcji $1/T$ analizowano następnie z użyciem funkcji Vogela-Fulchera-Tammana (VFT, Fig. S2 w P2), co umożliwiło wyznaczenie dla każdego z układów wartości T_g (definiowanej jako *T* w której τ_α=100 s). Co istotne, nie różniły się one znacząco od siebie (T_g=263.1, 263.4 oraz 261.9 K, odpowiednio dla *R*-, *S*-, i *RS*-FLP) i były niewiele niższe od tych oszacowanych techniką DSC.

Następnym, ważnym etapem badań były wysokociśnieniowe (izobaryczne i izotermiczne) pomiary BDS. Widma strat dielektrycznych zmierzone w stałym *p* i $T>T_g$, jak również w stałej *T* i $p<p_g$ (gdzie p_g jest ciśnieniem zeszklenia), ujawniły, podobnie jak w przypadku badań w *p*=0.1 MPa, obecność σ_{DC}, a także dwóch relaksacji: α i β. Istotnym faktem jest, że porównanie znormalizowanych widm dielektrycznych *R*-, *S*- i *RS*-FLP, zarejestrowanych w stałym i podwyższonym *p* oraz $T\sim T_g$, przy ustalonej częstotliwości maksymalnej α-procesu (~1 Hz), ujawniły spełnienie reguły izochronicznej superpozycji czasów relaksacji α i β. Co również ważne, w przypadku enancjomerów FLP (w szczególności dla *R*-FLP), zaobserwowano poszerzenie lewego zbocza α-dyspersji wraz ze wzrostem *p*, co wskazywało na złamanie reguły superpozycji temperaturowo-ciśnieniowej (TPS). Natomiast dla *RS*-FLP, z uwagi na brak zmian w szerokości procesu α w różnych warunkach *T* i *p* powyższa reguła była spełniona. (**Rys. 4a**, Fig. 3d w P2).

W dalszej kolejności, czasy τ_αs uzyskane z dopasowania do widm BDS zmierzonych w warunkach izotermicznych i izobarycznych funkcji HN, wykreślono względem *T* i *p* i poddano analizie z użyciem zmodyfikowanego równania Avramova (Eq. 4 w P2). Następnie, T_gs obliczone na podstawie Eq. 7 w P2, zostały przedstawione w funkcji *p,* a na podstawie otrzymanych zależności oszacowano wartości dT_g/dp (w granicy *p*=0.1 MPa). Wyniosły one odpowiednio 240, 247 i 248 K/GPa dla *R*-, *S*- i *RS*-FLP, a więc były zbliżone (**Rys. 4b**, Fig. 6a w P2). Wskazywały jednak na silną wrażliwość relaksacji strukturalnej na ciśnienie w każdym

z układów. Ponadto, wyznaczono jeszcze inny parametr wskazujący jak wrażliwy na kompresję jest procesu α, tj. objętość aktywacji (ΔV_α, Eq. 8 w P2). Co ciekawe, obliczone w T_g wartości ΔV_α dla czystych enancjomerów były zbliżone - wyniosły 377 i 385 cm^3/mol dla *R*- i *S*-FLP. Z kolei, ΔV_α uzyskana dla mieszaniny racemicznej była wyraźnie niższa (ΔV_α=337 cm^3/mol) w porównaniu do ΔV_α oszacowanych dla izomerów (**Rys. 4c**, Fig. 6b w P2). Ten zaskakujący wynik (zważywszy na zbliżone wartości dT_g/dp dla trzech badanych układów) sugerował, że lokalny układ molekuł badanych substancji w stanie ciekłym może być inny.

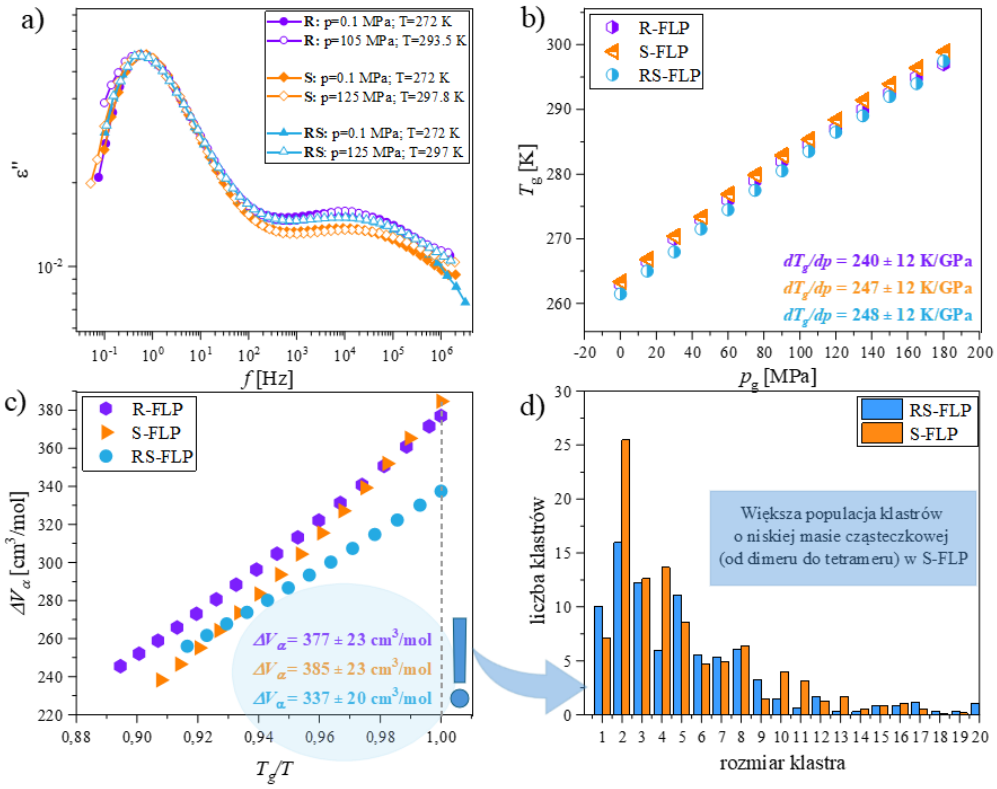

Rys. 4. Porównanie znormalizowanych widm dielektrycznych zmierzonych w różnych warunkach *T* i *p*, blisko T_g dla *R*-, *S*- i *RS*-FLP (a). Panel (b) przedstawia T_g wykreślone w funkcji p_g, zaś (c) zależność objętości aktywacji α-procesu (ΔV_α) od T_g/T (c). W panelu (d) pokazano histogram rozkładu klastrów połączonych wiązaniami wodorowymi w *S*- i *RS*-FLP.

Aby zweryfikować tę hipotezę, przeprowadzono szczegółowe symulacje dynamiki molekularnej w przechłodzonym stanie ciekłym *S*- i *RS*-FLP. Na podstawie analizy uzyskanych wyników w pierwszej kolejności wykazano, że klastry połączone wiązaniami wodorowymi występują w większej ilości (o 0.5% jeśli chodzi o ich ogólną liczbę) w enancjomerze niż w racemacie FLP. Istotniejsze różnice uwidoczniły się natomiast w ich rozkładzie/dystrybucji. W przypadku *S*-FLP stwierdzono większą (na poziomie 56%) populację klastrów o niskiej masie molowej (od dimerów do tetramerów), w racemacie było ich 44% (**Rys. 4d**, Fig. S3 w P2). W obu układach występowała także niewielka populacja cyklicznych dimerów i trimerów

(Fig. 7 w P2). Na podstawie otrzymanych rezultatów symulacji wnioskowano, że wyższa w porównaniu do *RS*-FLP wartość ΔV_α uzyskana z pomiarów BDS dla *R*- i *S*-FLP wynika najprawdopodobniej z większej populacji struktur di-, tri- i tetramerycznych w enancjomerach. Aby odpowiedzieć na pytanie, co stanowi główną siłę napędową do tworzenia większych klastrów w czystym enancjomerze, obliczono energię wiązania wodorowego OH---O (E_{int}) między dwoma cząsteczkami jednakowych (układ *S*-*S*) oraz dwóch różnych izomerów (*R*-*S*). Uzyskane wartości E_{int}, równe odpowiednio 105 i 100 kJ/mol, były wysokie biorąc pod uwagę tworzenie wiązania OH---O tylko między dwoma molekułami. Tłumaczono to występowaniem dodatkowych oddziaływań typu Π-*stacking* (warunkowanych obecnością pierścieni aromatycznych) w konformacji dwóch liniowo połączonych cząsteczek FLP. Ponadto, dzięki obecności atomu fluoru (F) połączonego z pierścieniem stwierdzono, że oddziaływanie to może być wzmocnione przez specyficzny przypadek Π-*stackingu*, tzw. F-Π. Co istotne, dalsze symulacje pokazały, że istnieją dwie możliwości Π-s*tackingu* – tworzenie uporządkowanych struktur równoległych i antyrównoległych, w sytuacji, gdy odpowiednio oba pierścienie aromatyczne z atomem F są ułożone względem siebie równolegle i antyrównolegle. Zaobserwowano, że w przypadku *RS*-FLP licznie występują oba ustawienia, a z kolei w czystym enancjomerze jedynie struktury równoległe.

Dodatkowo, zoptymalizowane metodą funkcjonału gęstości (ang. *density functional theory*, DFT) struktury dimerów *R*-*S* i *S*-*S*, połączone wyłącznie siłami Π-*stacking*, zobrazowano w postaci gęstości elektronowej z odwzorowanym potencjałem elektrostatycznym (Fig. 8 w P2). Zauważono, że struktura połączeń *R*-*S* charakteryzuje się idealną symetrią, co skutkuje zerowym momentem dipolowym (μ=0 D), podczas gdy konformacja *S*-*S* wykazuje zniekształcenia w rozkładzie ładunku i symetrii, czego efektem jest μ równy 1.33 D. Energia oddziaływań F-Π wyniosła 55 kJ/mol w układzie *R*-*S* i 50 kJ/mol w systemie *S*-S. W przypadku *S*-FLP, stwierdzono, iż brak możliwości tworzenia symetrycznych struktur F-Π sprawia, że układ jest bardziej zdominowany przez wiązania wodorowe, co prowadzi do odmiennej struktury krystalicznej (ortorombowej dla tego enancjomeru). Ponadto, ponieważ energia oddziaływań F-Π jest porównywalna z energią wiązań wodorowych OH---O, energia wiązania dimeru liniowego, w których występują oba typy oddziaływań, jest zbliżona do energii dimeru cyklicznego. To stanowiło wyjaśnienie, dlaczego w obu przechłodzonych układach (*R*-*S* i *S*-*S*) dominują liniowe klastry, a nie pozornie stabilniejsze cykliczne dimery.

2.3. Badania nad naturą, ewolucją ciśnieniową i kinetyką przejść fazowych w pochodnych ADM

Jak zaznaczono w podr. 1.3., układy tworzące fazy PC (ODIC), ze względu na ich ograniczoną liczbę stopni swobody, stanowią modele w badaniach nad naturą przejścia szklistego i mechanizmami prowadzącymi do „zamrożenia" dynamiki molekularnej cząsteczek podczas zeszklenia. Celem dwóch kolejnych prac wchodzących do cyklu artykułów (P3 i P4) było poznanie natury przejść fazowych w trzech zasocjowanych pochodnych ADM – 1-adamantylaminie (1-NH_2-ADM), inaczej amantadynie (API stosowanej w leczeniu choroby Parkinsona), 1-adamantanolu (1-OH-ADM) i 3-amino-1-adamantanolu (3-NH_2-1-OH-ADM) - substancji będącej substratem do produkcji wildagliptyny, API o działaniu przeciwcukrzycowym. W tym celu wykonano pomiary z wykorzystaniem metod DSC, XRD oraz spektroskopii: w podczerwieni, Ramana i dielektrycznej. Dodatkowo, w przypadku 1-NH_2-ADM i 1-OH-ADM analizie poddano również ciśnieniową ewolucję tych przejść.

Badania kalorymetryczne przeprowadzone dla 1-NH_2-ADM ujawniły podczas pierwszego cyklu grzania dwa wyraźne procesy endotermiczne (w T=324 i T=458 K), z których ten ujawniający się w wyższej T był związany ze zjawiskiem sublimacji (**Rys. 5a**, Fig. 1a w P3). Na termogramach zarejestrowanych podczas chłodzenia (do 160 K) nowej próbki, tym razem po uprzednim jej ogrzaniu od 293 do 353 K (celem uniknięcia sublimacji) uwidoczniły się dwa przejścia fazowe, w T=282 i T=245 K, dla których zmiana entropii (ΔS) wyniosła odpowiednio 16.61 i 8.65 J/mol·K (sumaryczna ΔS=25.3 J/mol·K była bardzo zbliżona do wartości oszacowanej przez Bazylevę i wsp. [76], $\sum \Delta S$=25.8 J/mol·K, którzy zasugerowali, uwzględniając także plastyczność tej substancji, iż mogą to być przejścia między fazami PC). Co istotne, podczas ponownego ogrzewania od 160 do 353 K, na krzywych DSC także uwidoczniły się dwa procesy endotermiczne, choć w nieco wyższych temperaturach (T=248 i T=288 K). Jednakże nie zaobserwowano przejścia fazowego w T=324 K, co sugerowało, że początkowa faza I nie została odtworzona po wszystkich wykonanych cyklach termicznych. Termogramy uzyskane podczas pierwszego ogrzewania 1-OH-ADM wykazały, analogicznie jak w przypadku 1-NH_2-ADM, obecność dwóch procesów endotermicznych w T=362 K i T=493 K (**Rys. 5b**, Fig. 1b w P3), z których drugi powiązano ze zjawiskiem sublimacji. Podczas schładzania nowej próbki substancji (uprzednio ogrzanej od 293 do 393 K) wykryto jedno przejście fazowe w T=343 K, z ΔS równą 34.96 J/mol·K, a więc znacznie przewyższającą wartości uzyskane dla dwóch przejść w 1-NH_2-ADM. Co ważne, było ono również widoczne podczas ponownego ogrzewania 1-OH-ADM, jednak w znacznie wyższej T (=362 K). Z kolei krzywe DSC zarejestrowane w czasie ogrzewania wyjściowej próbki 3-NH_2-1-OH-ADM ujawniły obecność szerokiego procesu endotermicznego w T=352 K, która była odpowiednio

wyższa i niższa w stosunku do temperatury przejścia w T=324 K (w 1-NH_2-ADM) oraz T=362 K (w 1-OH-ADM), **Rys. 5c**, Fig. 1a w P4. W przeciwieństwie do tych dwóch związków, dla których, jak pokazano na **Rys. 5a,b** widoczne były przejścia fazowe związane z sublimacją, dla 3-NH_2-1-OH-ADM nie wykryto tego zjawiska, co wynikało z temperatury zapłonu próbki (T=383 K), a tym samym uniemożliwiło wykonanie pomiarów w wyższych T. Podczas cyklu chłodzenia zaobserwowano natomiast dwa efekty egzotermiczne w T=309 K i T=293 K (analogicznie do przypadku 1-NH_2-ADM, **Rys. 5a**, Fig. 1b w P4), zaś podczas ponownego ogrzewania uwidoczniło się tylko jedno przejście fazowe w T=341 K (**Rys. 5c**, Fig. 1a w P4).

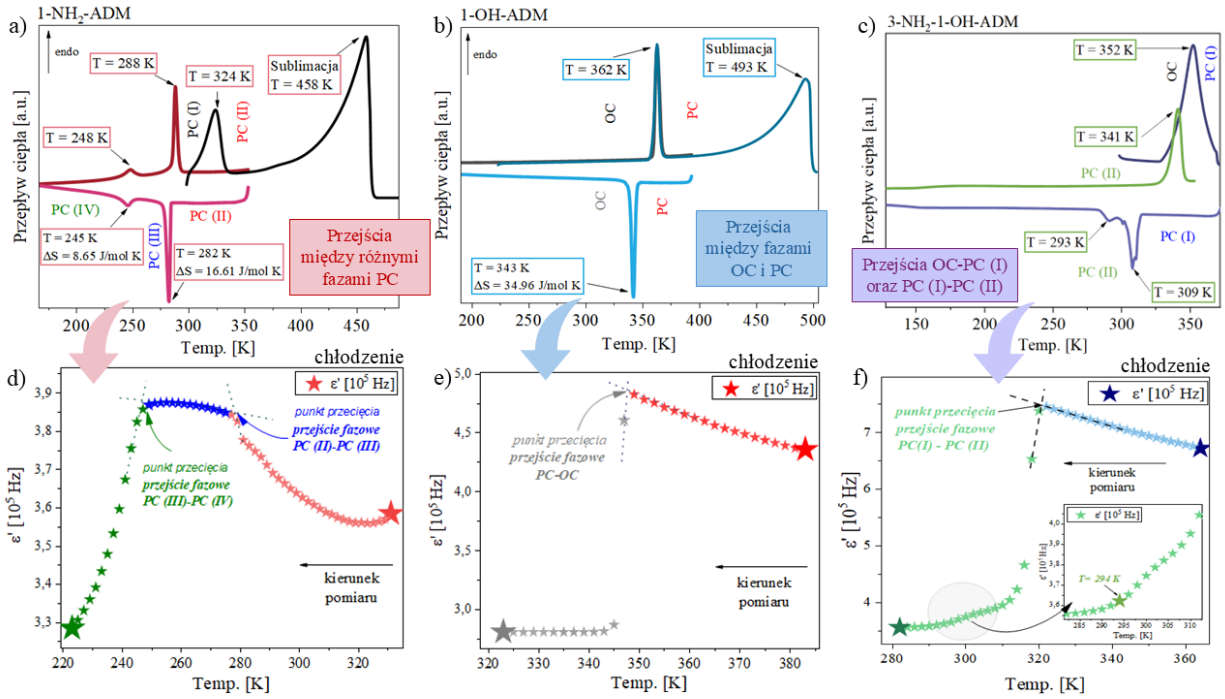

Rys. 5. Termogramy DSC uzyskane podczas ogrzewania i chłodzenia trzech pochodnych ADM: 1-NH_2-ADM (a), 1-OH-ADM (b) i 3-NH_2-1-OH-ADM (c). W panelach (d), (e) i (f) przedstawiono zależności ε' (f = 10^5 Hz) vs. T w ciśnieniu atmosferycznym.

Aby określić naturę obserwowanych na termogramach przejść fazowych, przeprowadzono badania techniką XRD. Wykazały one, że 1-OH-ADM przechodzi z wyjściowej, krystalicznej fazy I (układ tetragonalny) do fazy II, wykazującej wyższą symetrię (układ sześcienny) w T=362 K. Takie zachowanie, zgodnie z doniesieniami Charapennikau i wsp [74], jest charakterystyczne dla przemiany OC-PC. Po ochłodzeniu próbki z T>362 K do 343 K, widoczne było odwrotne przejście z fazy II (PC) do fazy I (OC). Co ważne, zmiany zarejestrowane na dyfraktogramach w obu cyklach termicznych następowały w T zbliżonych do temperatur przejść obserwowanych w pomiarach DSC. Z kolei 1-NH_2-ADM wykazywał bardziej złożone zachowanie – w czasie ogrzewania, w T=324 K, a więc podobnej do T występowania efektu endotermicznego w badaniach kalorymetrycznych, zaobserwowano

przejście z fazy I (dyfraktogram tej fazy był typowy dla sferycznych cząsteczek tworzących fazy PC) do fazy wykazującej wyższą symetrię. Stwierdzono zatem, iż powyżej 324 K, 1-NH_2-ADM tworzy inną fazę PC (fazę II). W czasie schładzania próbki od T>324 K do T=282 K, widoczne było kolejne przejście fazowe, ale w odróżnieniu do 1-OH-ADM, nie było to przejście do wyjściowej fazy I, ale do innej fazy (oznaczonej jako III) różniącej się pozycją i intensywnością pików braggowskich. Dalsze ochładzanie ujawniło jeszcze jedno przejście, widoczne jako niewielka zmiana strukturalna, w T=245 K, a więc w T bliskiej występowania procesu na termogramie DSC. Komórka elementarna tej fazy (oznaczonej jako IV) była zbliżona do fazy III. Co istotne, poniżej T=245 K, dyfraktogramy wskazywały na zachowaną ruchliwość molekularną układu, co sugerowało, że pozostaje on w fazie plastycznej. Badania XRD wykonane natomiast na 3-NH_2-1-OH-ADM wykazały, iż w T~353 K, z uwagi na wzrost symetrii układu i osłabienie maksimów pików dyfrakcyjnych przy wyższych kątach rozpraszania, następuje, tak jak miało to miejsce dla 1-OH-ADM, przejście badanej substancji z fazy I (OC) do fazy II (PC). Po ochłodzeniu fazy II, w T=313 K widoczne było kolejne przejście fazowe, lecz w przeciwieństwie do 1-OH-ADM, nie następował powrót do fazy I. Nowo powstała faza III wykazywała niższą symetrię, jednak podobnie jak w przypadku 1-NH_2-ADM zachowane w niej zostało osłabienie maksimów pików dyfrakcyjnych w szerokim zakresie kątów rozpraszania, co sugerowało, że jest to faza PC (była ona stabilna zarówno podczas dalszego chłodzenia do T=173 K, jak i po ponownym ogrzaniu do T=293 K). Co więcej, zaobserwowano nietypowe zachowanie amplitudy najbardziej intensywnego maksimum piku dyfrakcyjnego w pobliżu 5.7°, która systematycznie malała wraz ze spadkiem T w zakresie temperatur, w którym na termogramie mierzonym podczas chłodzenia w T=293 K widoczny był niewielki efekt egzotermiczny (**Rys. 5c**, Fig. 2a w P4).

Aby zweryfikować rezultaty pomiarów XRD, przeprowadzono badania z wykorzystaniem spektroskopii FTIR i Ramana. Widma podobnie jak w pomiarach XRD rejestrowano w cyklach grzania i chłodzenia. W przypadku 1-OH-ADM, dane FTIR, w szczególności znaczne poszerzenie pasm odpowiadających drganiom rozciągającym grup OH oraz zanik rozszczepienia pasm związanych z drganiami rozciągającymi grup CH (charakterystycznego dla fazy krystalicznej) na widmach, wskazywały na przejście z fazy OC do fazy PC w T~362 K. Odwrotne zachowanie obserwowano w czasie schładzania próbki do 349 K (przejście PC-OC). W przypadku 1-NH_2-ADM, analiza widm FTIR zarejestrowanych podczas ogrzewania z 293 do 343 K, a następnie schładzania z 343 do 203 K, ujawniła, iż wyraźne zmiany w pozycji analizowanych pasm (związanych m.in. z drganiami grup NH zaangażowanych w tworzenie wiązań wodorowych, czy drganiami rozciągającymi grup CH), a także ich intensywności oraz szerokości połówkowej, wskazujące na fluktuacje w

reorganizacji molekuł tej substancji, zachodzą w okolicy temperatur 331 K i 277 K, odpowiadającym przejściom między fazami I i II oraz II i III wykrytymi na termogramach. Co szczególnie istotne, pasma związane z drganiami grup NH i CH nie wykazywały rozszczepienia w T=293 K i T=343 K, co w świetle danych literaturowych [86,94] mogło wskazywać na przejście między dwoma fazami PC (fazą I i II) w T~331 K. Jednocześnie, pozwoliło stwierdzić, iż 1-NH_2-ADM faktycznie tworzy fazę PC(I) w T=293 K. Wyraźnych różnic w widmach FTIR nie zaobserwowano w T~245 K, co oznaczało, że przejście z fazy III do IV może wiązać się z niewielkimi zmianami w strukturze sieci krystalicznej i organizacji molekuł. Dodatkowe badania z użyciem spektroskopii Ramana wykonane wyłącznie na aminowej pochodnej ADM wykazały jedynie niewielkie fluktuacje parametrów spektralnych (pozycja pasma, intensywność integralna) z temperaturą, występujące w zakresie niskich liczb falowych. Sugerowało to, że przejściom między różnymi fazami PC w 1-NH_2-ADM towarzyszy głównie subtelna reorganizacja strukturalna, a nie duże zmiany w dynamice molekularnej. Z kolei eksperymenty z wykorzystaniem obu technik spektroskopowych wykonane na 3-NH_2-1-OH-ADM ujawniły liczne rozszczepienia pasm na widmach zarejestrowanych w T=293 K (faza I), charakterystyczne dla uporządkowanej fazy OC. Wraz ze wzrostem T, pasma te stawały się szersze i mniej wyraźne, a ich rozszczepienie zanikało, co wskazywało na przejście do orientacyjnie nieuporządkowanej fazy II (PC) w T=353 K. Podczas chłodzenia z fazy II do 313 K, widoczne były tylko niewielkie zmiany na widmach FTIR i Ramana, w tym modyfikacje kształtu pasma OH/NH oraz dodatkowe rozszczepienia pasm występujących w zakresie drgań CH i NH, co sugerowało reorganizację orientacyjną cząsteczek (faza III). W dalszym etapie chłodzenia do 288 K, obserwowane zmiany były subtelne, a widma nie różniły się od tych zmierzonych w fazie III w 313 K (Fig. 3 w P4). Dodatkowe cykle chłodzenia i ogrzewania w zakresie T 253-293 K nie spowodowały istotnych zmian na widmach, co potwierdziło stabilność fazy III. Ogólny przebieg przejść fazowych 3-NH_2-1-OH-ADM wykazywał podobieństwo do 1-OH-ADM, który także ulegał przemianie OC-PC. Jednak w przeciwieństwie do tej pochodnej, widma zmierzone w fazie III 3-NH_2-1-OH-ADM były bardziej zbliżone do tych zarejestrowanych w fazie II (PC) niż w początkowej fazie I (OC) 1-OH-ADM. Zasadniczo, brak wyraźnych zmian na widmach mierzonych w cyklu chłodzenia sugerował plastyczny charakter faz II i III w 3-NH_2-1-OH-ADM, co przypominało zachowanie obserwowane w przypadku czterech faz PC w 1-NH_2-ADM.

Podsumowując, w oparciu o uzyskane wyniki badań strukturalnych i spektroskopowych (FTIR i Raman), a w przypadku 1-NH_2-ADM i 1-OH-ADM, także otrzymane z pomiarów kalorymetrycznych wartości zmian entropii ΔS (dla dwóch przejść w aminowej i jednego przejścia w hydroksylowej pochodnej ADM) termiczne efekty obserwowane na krzywych DSC

1-NH_2-ADM, 1-OH-ADM i 3-NH_2-1-OH-ADM zostały przypisane odpowiednio przejściom fazowym między czterema fazami PC: PC(I)-PC(II), PC(II)-PC(III), PC(III)-PC(IV), przejściu OC-PC i przejściom OC-PC oraz PC(I)-PC(II).

Dalsze badania dynamiki molekularnej w ciśnieniu otoczenia przeprowadzone dla wszystkich badanych pochodnych ADM wykazały ewolucję odpowiedzi dielektrycznej wraz z temperaturą, zarówno w czasie ogrzewania, jak i chłodzenia próbek. W przypadku 1-NH_2-ADM, w zależnościach ε" vs. f uwidocznił się pojedynczy proces relaksacyjny podczas cyklu grzania, mający prawdopodobnie swe źródło we fluktuacjach w obrębie grupy NH_2 (Fig. 7a w P3). Co istotne, powyżej T=323 K (odpowiadającej maksimum efektu endotermicznego na krzywej DSC i przejściu z fazy I do fazy II) wspomniany proces był systematycznie przykrywany przez wkład σ_{DC}. Natomiast podczas chłodzenia, stawał się on ponownie widoczny w okolicy 280 K. W T=249 K, odpowiadającej drugiemu efektowi egzotermicznemu na termogramie, zmiany na widmie strat dielektrycznych były zbyt małe, by można je było odpowiednio zinterpretować. W przypadku 1-OH-ADM odpowiedź dielektryczna była nieco inna niż dla 1-NH_2-ADM, bowiem nie zaobserwowano procesu relaksacyjnego na widmach podczas cyklu grzania (wyraźna dominacja σ_{DC}), Fig. 7b w P3. Natomiast w czasie schładzania następowała wyraźna zmiana w zależności ε"(f) poniżej 347 K, co sugerowało przejście do fazy OC. Z kolei widma strat dielektrycznych zmierzone dla 3-NH_2-1-OH-ADM podczas ogrzewania, ujawniły subtelny proces relaksacyjny, związany najprawdopodobniej z lokalnymi fluktuacjami termicznymi grup OH (Fig. 4a w P4). W T=352 K, odpowiadającej maksimum szerokiego zjawiska endotermicznego na krzywej DSC i przejściu fazowemu OC-PC(I), odpowiedź dielektryczna była niemal całkowicie zdominowana przez σ_{DC}, którego źródłem był transport ładunków jonowych oraz *proton hopping* wzdłuż sieci wiązań wodorowych, warunkowany obecnością grup OH i NH_2 w cząsteczce 3-NH_2-1-OH-ADM. Podczas chłodzenia, proces relaksacyjny ponownie stawał się widoczny, szczególnie w okolicach T=316 K (bliskiej T przejścia z fazy II do fazy III na krzywej DSC). Natomiast w T=294 K, zmiany w zależności ε" vs f były niewielkie (Fig. 4b w P4).

Co istotne, zauważalne różnice w okolicach T pojawiania się charakterystycznych efektów egzotermicznych w pomiarach DSC, były także widoczne na wykresach dyspersji dielektrycznej (ε') w funkcji f zarejestrowanych dla trzech badanych pochodnych ADM (Figs. 8a,b w P3, Fig. 5a w P4). Aby zweryfikować te obserwacje, dodatkowo przeanalizowano zależności ε' (przy stałej f=10^5 Hz) oraz $d\varepsilon'/dT$ od T (**Rys. 5d,e,f** oraz Figs. 8c,d w P3, Fig. 5b,c w P4), a także wykres σ_{DC} vs. T (3-NH_2-1-OH-ADM, Fig. S9 w P4), potwierdzając wyraźne fluktuacje dyspersji dielektrycznej i σ_{DC} (3-NH_2-1-OH-ADM), związane z przejściami fazowymi. Warto podkreślić, że widoczne zmiany w ε' stanowią odzwierciedlenie zmian w

ruchliwości molekuł. Można tym samym uznać je, po uwzględnieniu rezultatów uzyskanych z innych technik eksperymentalnych, za wiarygodny wskaźnik charakteru faz w badanym układzie. Pomiary BDS wykonane w p=0.1 MPa uwidoczniły przejścia między różnymi fazami PC w 1-NH_2-ADM, oraz przejścia PC-OC i PC-PC (podczas chłodzenia) odpowiednio w 1-OH-ADM i 3-NH_2-1-OH-ADM. Warto jeszcze dodać, iż w przypadku 3-NH_2-1-OH-ADM, w T~294 K (odpowiadającej T występowania procesu egzotermicznego na termogramie DSC) wykryto subtelne fluktuacje w zależnościach ε'[10^5 Hz] i σ_{DC} vs. T, odzwierciedlające zmienną ruchliwość molekularną w próbce/zmiany w nieporządku orientacyjnym badanej substancji.

Ważnym etapem badań było określenie wpływu wysokiej kompresji na przejścia fazowe w rozpatrywanych pochodnych ADM. Wysokociśnieniowe eksperymenty dielektryczne wykonano dla 1-NH_2-ADM i 1-OH-ADM (P3). Wszystkie pomiary izotermiczne przeprowadzono w szerokim zakresie p, rozpoczynając od T>323 K dla 1-NH_2-ADM i T>363 K dla 1-OH-ADM. Analogicznie do wyników uzyskanych w ciśnieniu otoczenia, widma strat dielektrycznych obu związków były zdominowane przez wkład od σ_{DC} i ewoluowały z kompresją. Ponownie, w przypadku aminowej pochodnej, proces relaksacyjny stawał się bardziej wyraźny przy pewnej wartości ciśnienia. Ponadto w pobliżu p=60 MPa i p=220 MPa (dane izotermiczne, T=291 K) zaobserwowano zmiany w kształcie widm absorpcyjnych, które przypisano dwóm przejściom fazowym: PC(II)-PC(III) oraz PC(III)-PC(IV) (Fig. 9a w P3). Natomiast dla 1-OH-ADM, w zależnościach ε" vs. f, podobnie jak w p=0.1 MPa, nie zarejestrowano procesu relaksacyjnego, a jedynie wyraźny wkład od σ_{DC} (Fig. 9b w P3). Niemniej jednak, w odpowiedzi dielektrycznej były widoczne zmiany wskazujące na przejście PC-OC w p=160 MPa i T=371 K. Analiza ε' vs. f wykazała gwałtowny spadek ε' w p=160 MPa dla tej pochodnej ADM, jak również w p=220 MPa dla pochodnej aminowej, co przypominało zmiany obserwowane w T~347 K i T~249 K (**Rys. 5c,d**, Fig. 9c,d w P3). Warto zauważyć, że zależności ε' (przy stałej f=10^5 Hz) oraz pochodnej $d\varepsilon'/dp$ od p ujawniły podobne zmiany do tych widocznych w p=0.1 MPa w funkcji T dla obu układów (**Rys. 5e,f**, Fig. 9e,f w P3). Dodatkowo, uzyskane wyniki umożliwiły określenie wartości ciśnienia, w których występują przejścia fazowe. Tym samym, przeprowadzone eksperymenty wysokociśnieniowe również wskazały na obecność dwóch przejść fazowych (PC(II)-PC(III) i PC(III)-PC(IV)) oraz jednego przejścia PC-OC odpowiednio w 1-NH_2-ADM oraz 1-OH-ADM.

Analizując następnie zależności temperatur przejść fazowych od ciśnienia dla obu układów, określono ich wrażliwość na kompresję (Fig. 10 w P3). Wykres $T_{PC(II)-PC(III)}$ od p dla aminowej pochodnej miał charakter liniowy, stąd do jego analizy zastosowano funkcję liniową. Natomiast wykresy $T_{PC(III)-PC(IV)}$ (1-NH_2-ADM) oraz T_{PC-OC} (1-OH-ADM) vs. p, z uwagi na przebieg logarytmiczny, analizowano z użyciem funkcji Anderssona-Anderssona (Eq. 1 w P3). W

oparciu o wartość nachylenia funkcji liniowej, a także stosunku parametrów k_1/k_3 oszacowano dT_x/dp_x dla każdego z przejść fazowych. W przypadku 1-NH_2-ADM, uzyskane wartości (tj. $dT_{PC(II)-PC(III)}/dp_{PC(II)-PC(III)}$=0.236 K/MPa i $dT_{PC(III)-PC(IV)}/dp_{PC(III)-PC(IV)}$=0.219 K/MPa) wskazywały, że przejście PC(II)-PC(III) jest nieco bardziej wrażliwe na ciśnienie niż przejście PC(III)-PC(IV). Natomiast dla 1-OH-ADM, wartość dT_{PC-OC}/dp_{PC-OC} wyniosła 0.193 K/MPa. Dodatkowo dla obu związków porównano zmiany objętości w temperaturach przejść fazowych (ΔV) wyznaczone z równania Clausiusa-Clapeyrona (Eq. 2 w P3). Uzyskano następujące wartości ΔV: 0.0259 cm³/g i 0.0125 cm³/g dla przejść PC(II)-PC(III) oraz PC(III)-PC(IV) w 1-NH_2-ADM, oraz 0.0443 cm³/g dla przejścia PC-OC w 1-OH-ADM, stwierdzając, że przejście PC(III)-PC(IV) w 1-NH_2-ADM powoduje zmianę objętości, która jest dwa razy mniejsza niż w przypadku przejścia fazowego PC(II)-PC(III). Z kolei dla 1-OH-ADM, ΔV podczas przejścia fazowego PC-OC była znacznie większa, nawet w porównaniu do ΔV towarzyszącej przejściu PC(II)-PC(III) w 1-NH_2-ADM.

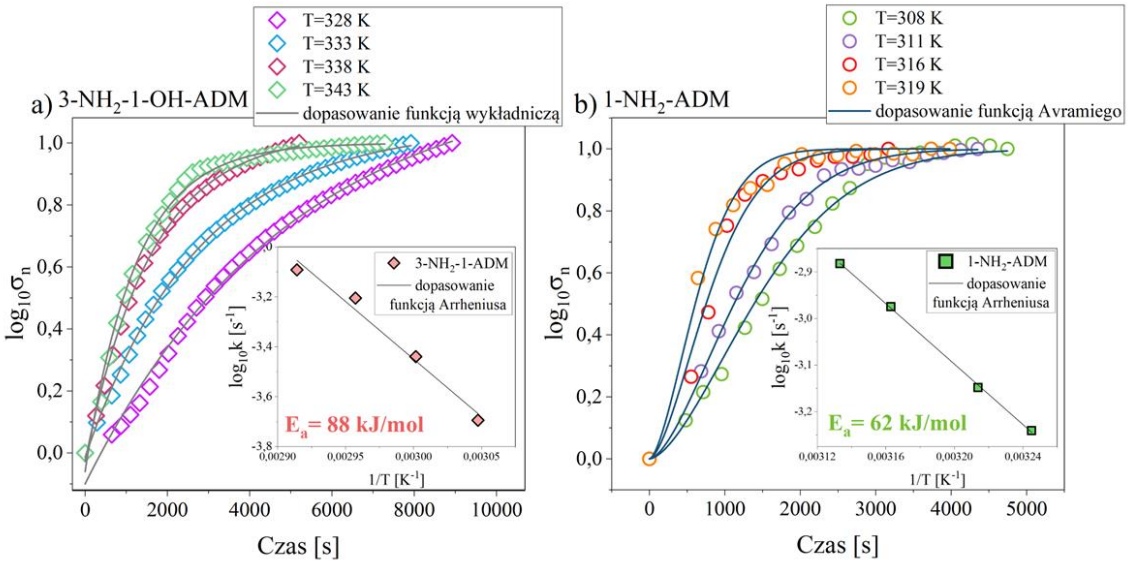

Rys. 6. Ewolucje czasowe znormalizowanego przewodnictwa stałoprądowego dla pomiarów przeprowadzonych w wybranych T oraz zależności logarytmu stałej szybkości od $1/T$ (wstawki) dla 3-NH_2-1-OH-ADM (a) i 1-NH_2-ADM (b).

Co więcej, aby lepiej zrozumieć charakter przejścia fazowego OC-PC(I) w 3-NH_2-1-OH-ADM, jak również przejścia PC(I)-PC(II) w 1-NH_2-ADM, widocznego na termogramach DSC w postaci bardzo szerokiego procesu endotermicznego odpowiednio w okolicy 352 K i 324 K (**Rys. 5a,c**, Fig. 1a,b w P4), przeprowadzono izotermiczne pomiary BDS w T<352 K i T<324. K. Co ciekawe, zauważono, że odpowiedź dielektryczna 3-NH_2-1-OH-ADM i 1-NH_2-ADM zmienia się w czasie. W przypadku 3-NH_2-1-OH-ADM, efekt ten był bardziej wyraźny, a widma dielektryczne ewoluowały z czasem w stronę wyższych f (Fig. 6 w P4), w przeciwieństwie do 1-NH_2-ADM, dla której obserwowano zmienność czasową widm ku

niższym *f* (Fig. S10 w P4). Dodatkowo, subtelny proces relaksacyjny widoczny dla 3-NH_2-1-OH-ADM na początku pomiarów, był stopniowo zakrywany przez σ_{DC}.

Warto zaznaczyć, że podobny efekt, tj. występowanie szerokiego procesu termicznego (związanego z przejściem z metastabilnej fazy I (PC) do fazy II (OC)) zaobserwowano także dla kofeiny [95]. Na podstawie izotermicznych badań XRD i BDS wykazano, że przejście to (PC-OC) zachodzi w czasie, czyli jest zjawiskiem fizycznym o charakterze procesu kinetycznego. Analogicznie, kształt procesu termicznego w okolicach 352 K i 324 K odpowiednio dla 3-NH_2-1-OH-ADM oraz 1-NH_2-ADM sugerował, że przejścia fazowe OC-PC(I) oraz PC(I)-PC(II) w tych związkach mogą mieć podobny charakter do tego występującego w kofeinie.

Celem zbadania kinetyki tych przemian, dokonano analizy czasowej ewolucji znormalizowanych wartości σ_{DC} dla przejść fazowych OC-PC(I) w 3-NH_2-1-OH-ADM oraz PC(I)-PC(II) w 1-NH_2-ADM. Wykazała ona, że oba procesy ulegają spowolnieniu wraz z obniżaniem temperatury (**Rys. 6a,b**, Fig. 7a,b w P4). Aby ilościowo określić ten efekt oraz wyznaczyć stałe szybkości (k), zależności $\log_{10}\sigma_{DC}^{n}$ vs. t w przypadku 3-NH_2-1-OH-ADM analizowano z wykorzystaniem funkcji wykładniczej (dobre dopasowanie do danych wskazywało na kinetykę pierwszego rzędu dla przejścia OC-PC(I)), a w przypadku 1-NH_2-ADM użyto równania Avramiego (Eq. 4 w P4). Dopasowując następnie funkcję Arrheniusa do zależności $\log_{10}k$ vs. $1/T$ (Eq. 5 w P4) oszacowano barierę aktywacji (E_a) dla obu przemian fazowych. Okazało się, że przejście OC-PC(I) w 3-NH_2-1-OH-ADM charakteryzuje się wyższą E_a (=88 kJ/mol) niż przejście PC(I)-PC(II) w 1-NH_2-ADM (E_a=62 kJ/mol), wstawki na **Rys. 6a,b** i Fig. 7a,b w P4. Dodatkowo, aby potwierdzić wyniki badań BDS, przeprowadzono także dla 3-NH_2-1-OH-ADM zależne od czasu pomiary FTIR (w T=348 K) oraz analizę synchronicznych i asynchronicznych widm korelacyjnych 2D-IR. Ujawniły one istotne zmiany w zakresie pasm odpowiadających drganiom rozciągającym CH (sygnał przy 2883 cm^{-1} zanikał, a ten w okolicach 2903 cm^{-1} ulegał wzmocnieniu), które świadczyły o występowaniu przejścia OC-PC(I). Ponadto, intensywność szerokiego pasma związanego z drganiami rozciągającymi grup OH/NH zmniejszała się w czasie, i pasmo to stawało się bardziej rozmyte. Warto też dodać, że analiza asynchronicznych widm 2D-IR jednoznacznie wykazała, że w trakcie przejścia fazowego OC-PC(I), oprócz zmian σ_{DC} (obserwowanych w badaniach BDS), dochodzi również do modyfikacji dynamiki wewnątrzcząsteczkowej grup CH, NH i OH. Co istotne, najszybsze fluktuacje zachodziły w obrębie grup CH, które wyprzedzały reorientację polarnych ugrupowań OH oraz NH_2 w momencie rozpoczęcia przejścia fazowego.

III. Treści artykułów stanowiących podstawę pracy doktorskiej wraz z oświadczeniami współautorów

3.1. **Publikacja 1 (P1):** *High-pressure studies in the supercooled and glassy state of the strongly associated active pharmaceutical ingredient—ticagrelor*, Sci. Rep. 13 (**2023**) 8890.

Autorzy: P. Jesionek, D. Heczko, B. Hachuła, K. Kamiński, E. Kamińska.

DOI: 10.1038/s41598-023-35772-7

Impact Factor czasopisma z roku opublikowania pracy: 3.8

Liczba punktów ministerialnych MNiSW czasopisma z roku opublikowania pracy: 140

Mój udział w pracy polegał na zebraniu danych literaturowych, współtworzeniu hipotezy badawczej, przygotowaniu próbek, wykonaniu pomiarów dielektrycznych tikagreloru w ciśnieniu otoczenia oraz w warunkach wysokiej kompresji, analizie otrzymanych danych, dyskusji uzyskanych wyników, przygotowaniu rysunków do pracy, udziale w redagowaniu tekstu manuskryptu, jak także przygotowaniu odpowiedzi dla recenzentów i wykonaniu koniecznych poprawek w manuskrypcie.

www.nature.com/scientificreports

scientific reports

Check for updates

OPEN

High-pressure studies in the supercooled and glassy state of the strongly associated active pharmaceutical ingredient—ticagrelor

Paulina Jesionek[1,2]✉, Dawid Heczko[3], Barbara Hachuła[1], Kamil Kamiński[4] & Ewa Kamińska[2]✉

In this paper, the molecular dynamics at different thermodynamic conditions of hydrogen-bonded (H-bonded) active pharmaceutical ingredient—ticagrelor (TICA) have been investigated. Extensive high-pressure (HP) dielectric studies revealed surprising high sensitivity of the structural (α)-relaxation to compression. They also showed that unexpectedly the shape of the α-peak remains invariable at various temperature (*T*) and pressure (*p*) conditions at constant α-relaxation time. Further infrared measurements on the ordinary and pressure densified glasses of the examined compound indicated that the hydrogen-bonding pattern in TICA is unchanged by the applied experimental conditions. Such behavior was in contrast to that observed recently for ritonavir (where the organization of hydrogen bonds varied at high *p*) and explained the lack of changes in the width of α-dispersion with compression. Moreover, HP dielectric measurements performed in the glassy state of TICA revealed the high sensitivity of the slow secondary (β)-relaxation (Johari–Goldstein type) to pressure and fulfillment of the isochronal superpositioning of α- and JG-β-relaxation times. Additionally, it was found that the activation entropy for the β-process, estimated from the Eyring equation (a high positive value at 0.1 MPa) slightly increases with compression. We suggested that the reason for that are probably small conformational variations of TICA molecules at elevated *p*.

Glass-forming materials have been the subject of intensive research in recent decades[1–4]. A special attention is paid to the molecular understanding of the vitrification process and phenomena occurring in the vicinity of the glass transition. It is worth mentioning that intensive studies carried out on various types of glass-formers, i.e., polymers, low-molecular-weight (LMW) organic and inorganic compounds, ionic liquids, etc.[5–9], have revealed two characteristic features of these systems. The first one is the continuous and rapid increase of the structural relaxation time (τ_α) from values of the order of picoseconds (typical for liquids) up to hundreds of seconds near the glass transition temperature (T_g), while the second one is a non-exponential (in a time-domain) or non-Debye (in a frequency domain) character of the relaxation function. It should be mentioned that according to the literature data, the width of the α-dispersion close to the T_g (reflected in the stretched exponent of the Kohlrausch–Williams–Watts (KWW) function, β_{KWW}) is considered as either an inherent feature of supercooled liquids or the measure of the heterogeneity in the investigated systems[4]. Thus, with regard to this claim, the response relaxation function of the materials in the vicinity of the T_g consists of the series of Debye relaxations characterized by different relaxation rates. Recently, an important step forward in understanding the asymmetric shape of the structural (α)-process in supercooled liquids has been made. In ref.[10], it was shown that the polarity of the molecules is a key parameter that may have a strong impact on the breadth of the α-mode.

[1]Institute of Chemistry, Faculty of Science and Technology, University of Silesia in Katowice, Szkolna 9, 40-007 Katowice, Poland. [2]Department of Pharmacognosy and Phytochemistry, Faculty of Pharmaceutical Sciences in Sosnowiec, Medical University of Silesia in Katowice, Jagiellonska 4, 41-200 Sosnowiec, Poland. [3]Department of Statistics, Department of Instrumental Analysis, Faculty of Pharmaceutical Sciences in Sosnowiec, Medical University of Silesia in Katowice, Ostrogorska 30, 41-200 Sosnowiec, Poland. [4]Institute of Physics, Faculty of Science and Technology, University of Silesia in Katowice, 75 Pulku Piechoty 1, 41-500 Chorzow, Poland. ✉email: paulina.jesionek@us.edu.pl; ekaminska@sum.edu.pl

The authors analyzed over 180 van der Waals materials and concluded that along with the increasing dipole moment/ dielectric relaxation strength, the narrowing of the α-loss peak is noted. What is more, the observed phenomenon was correlated with the anharmonicity of the potential well describing intermolecular interactions in examined systems. Having that in mind, it would be valuable to confront this supposition with high-pressure investigations that induce strong densification of the sample and consequently change the shape as well as the depth of the potential well. Interestingly, the vast majority of the data collected for the purely van der Waals systems indicated that the width of α-dispersion is solely governed by the relaxation times and remains unchanged regardless of different thermodynamic conditions[4,11–16]. This means the fulfillment of the very important rule called temperature–pressure superpositioning (TPS)[11]. However, there are some substances having silyl/acetyl units in their chemical structures, for which the above rule is not satisfied. Herein, one can briefly mention LMW non-associated compounds, such as tris(dimethylsiloxy)phenylsilane (TDMSPS)[17], octa(trimethyl)silyl and octaacetyl trehalose (silTRE and acTRE)[18], where the narrowing of the α-loss peak under elevated pressure is observed. Another family of compounds where the TPS law is not obeyed are strongly associating liquids forming extensive H-bonded networks, i.e., *m*-fluoroaniline[19], polyalcohols (glycerol, xylitol, threitol)[20], di-, tri-propylene glycols[21]. Importantly, in these materials, the broadening of the α-dispersion with compression is noted. Such a finding was explained by the researchers as resulting from the variations in the strength and population of hydrogen bonds (H-bonds) as well as density fluctuations at extreme thermodynamic conditions, thereby causing the changes in the physical structures[11]. However, it turns out that there are a few H-bonded compounds where the influence of T and p on the width of the structural relaxation peak is not observed[22–25]. Thus, the question arises, why in some compounds forming H-bonds, there is a pronounced impact of thermodynamic conditions on the shape of the α-dispersion, while in others—it is not. To gain some insight into this problem, we decided to study the behavior of pressure densified glasses made of two active pharmaceutical ingredients (APIs): ticagrelor and ritonavir (for comparison). As can be shown in this paper, the change in the population of H-bonds has, in fact, an impact on the variation in the shape of the structural process at various T and p conditions.

Results and discussion

Differential scanning calorimetry (DSC) data. At first, we have carried out calorimetric measurements to entirely characterize the thermal properties of TICA. In panel (a) of Fig. 1, DSC curves recorded on heating (10 K/min) the crystalline and glassy TICA are presented. As can be seen, there is one endothermic event in the thermogram of the crystalline sample at $T_m = 413$ K, corresponding to the melting process. Further cooling, followed by heating of the vitrified TICA, reveals the presence of a well-visible heat capacity jump at $T_g = 325$ K ($\Delta C_p = 0.464$ Jg^{-1} K^{-1}), associated with the glass transition phenomenon. It should be mentioned that similar values of ΔC_p parameter (i.e., change in heat capacity at T_g) have been reported for other H-bonded APIs, such as bisoprolol ($\Delta C_p = 0.510$ Jg^{-1} K^{-1})[26], posaconazole ($\Delta C_p = 0.480$ Jg^{-1} K^{-1})[27], ezetimibe ($\Delta C_p = 0.470$ Jg^{-1} K^{-1})[28], indapamide ($\Delta C_p = 0.490$ Jg^{-1} K^{-1})[28], indomethacin ($\Delta C_p = 0.466$ Jg^{-1} K^{-1})[29] or valsartan ($\Delta C_p = 0.420$ Jg^{-1} K^{-1})[30]. Note that they exceeded those determined for, e.g., terconazole, ketoconazole, and itraconazole ($\Delta C_p = 0.391$, 0.366, 0.260 Jg^{-1} K^{-1}, respectively)[27], as well as for griseofulvin ($\Delta C_p = 0.272$ Jg^{-1} K^{-1})[31], which are typical van der Waals systems.

Broadband dielectric spectroscopy (BDS) data. In the next step, we have performed molecular dynamics BDS studies on the supercooled/vitrified (ordinary glass, OG) of TICA at ambient pressure, in a wide

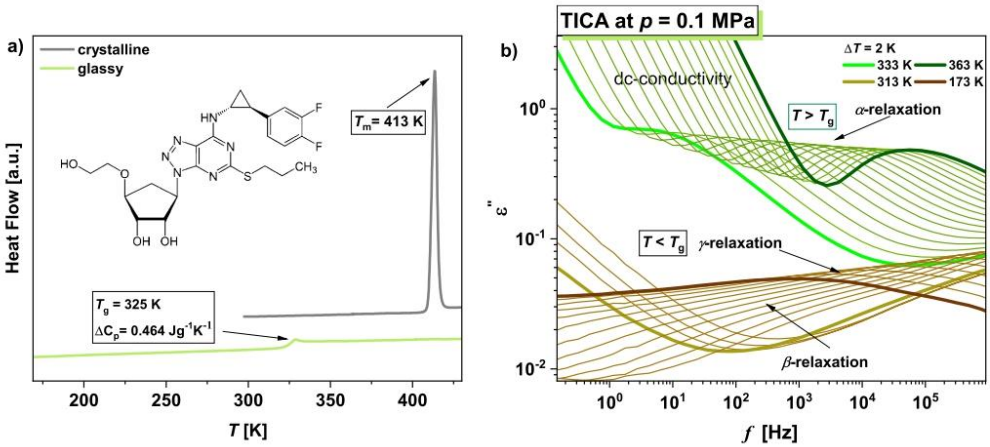

Figure 1. DSC thermogram obtained during heating of the crystalline and vitrified TICA at the rate of 10 K/min (**a**). In the inset, the chemical structure of the examined API is presented. Panel (**b**) presents dielectric loss spectra measured for TICA at ambient pressure in the indicated temperature (T) ranges.

range of T, both above and below the glass transition temperature (T_g). Dielectric loss spectra obtained from these investigations are illustrated in panel (b) of Fig. 1. In the supercooled liquid phase ($T > T_g$) of the examined compound, one can distinguish two characteristic processes in the spectra. The first one is the dc-conductivity, connected to the charge transport of ionic impurities and also, due to the presence of many hydroxyl groups in the TICA structure, to the proton hopping. Consequently, the measured conductivity is a result of both types of effects. In turn, the second one, located at higher frequencies (f), is the structural (α)-relaxation associated with the cooperative motions of all molecules and responsible for the glass transition. As illustrated, both processes shift towards lower f with decreasing T. In turn, in the glassy state ($T < T_g$), two secondary relaxations with small amplitude (labeled as β and γ) are observed in dielectric loss spectra.

Having ambient pressure dielectric spectra of TICA described qualitatively, we shift our attention to the behavior of this API at varying thermodynamic conditions. The results of isobaric and isothermal experiments performed at indicated thermodynamic conditions are presented in Fig. 2. Panels (a) and (c) of this figure demonstrate representative dielectric loss spectra measured at constant p and various $T > T_g$, while panels (b) and (d) present the analogical data obtained at constant T and different $p < p_g$ (where p_g means the glass transition pressure). As in the case of ambient pressure data, besides the dc-conductivity, a single structural (α)-relaxation peak is apparent in the loss spectra of the studied API at elevated compression. Its maximum shifts toward lower f with decreasing T or increasing p. The subsequent stage of our investigations was to compare the normalized dielectric spectra collected for TICA at various thermodynamic conditions in the vicinity of the T_g, see panel (a) of Fig. 3. It should be mentioned that the dc-conductivity part was subtracted from the spectra to better visualize the shape of the α-relaxation peak.

As illustrated, the width of the α-dispersion remains unchanged regardless of combinations of T and p, which indicates the fulfillment of the TPS rule[11]. This is confirmed by the outcomes of fitting the normalized spectra to the one-sided Fourier transform of the KWW function (dashed lines)[33,34]:

$$\Phi_{KWW}(t) = \exp[-(t/\tau_\alpha)^{\beta_{KWW}}]. \quad (1)$$

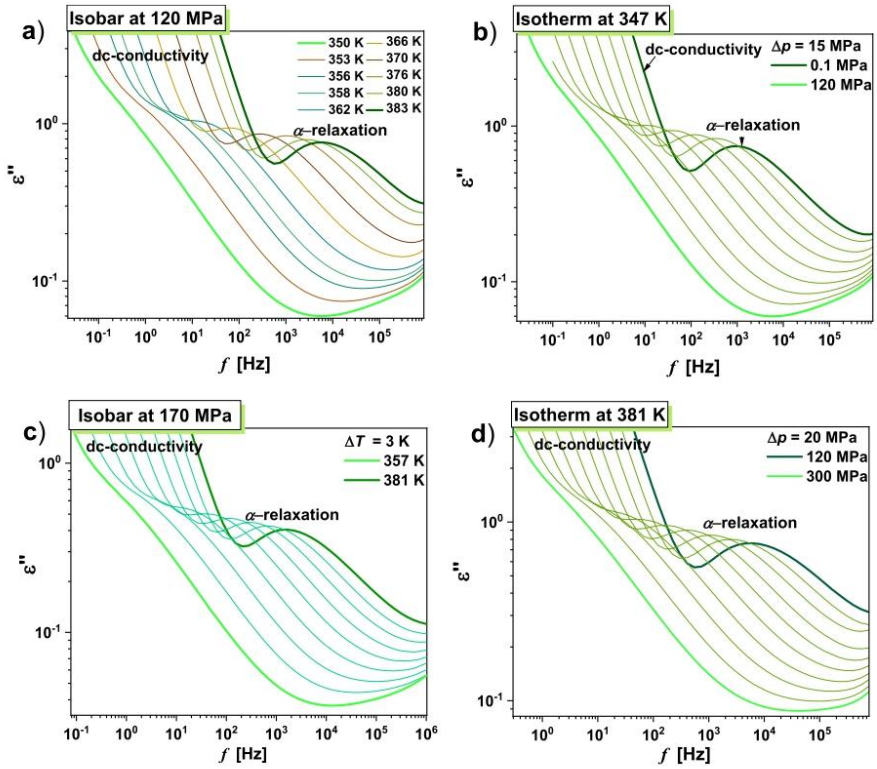

Figure 2. Representative dielectric loss spectra measured for TICA at isobaric (panels (**a**) and (**c**)) and isothermal (panels (**b**) and (**d**)) conditions.

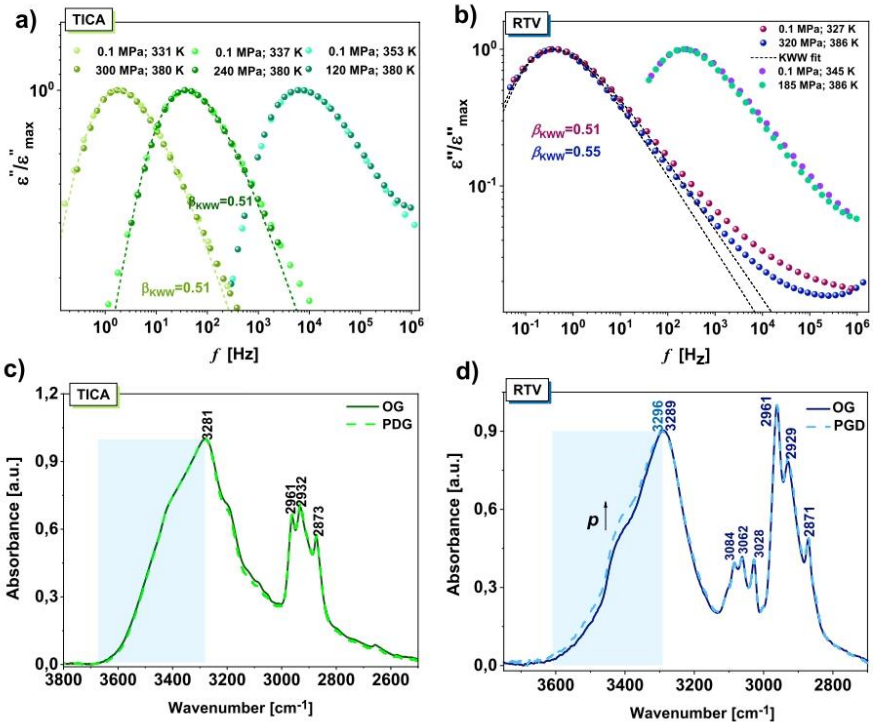

Figure 3. A superpositioning of TICA (**a**) and RTV[32] (**b**) spectra collected at three (two) different thermodynamic conditions close and far above the T_g. The spectra were normalized with respect to the maximum of dielectric loss (ε''_{max}). The dashed lines represent KWW fits. Panels (**c**) and (**d**) present FTIR spectra measured at 298 K for the OG as well as PDG of TICA and RTV[32], respectively.

The obtained value of the stretched exponent (β_{KWW}) was the same, equal to 0.51. This result is very surprising considering the presence of three O–H and one N–H groups in the TICA molecule (and hence the probability of formation of strong H-bonds/extensive H-bonded networks). In such a situation, it is highly expected that the application of high T and p should affect the population and strength of these specific interactions, which further should be reflected in the variation in the dielectric response function, as it was previously reported for many H-bonded systems[19–21,35]. Therefore, a question arises, is there a direct connection between the H-bonding pattern and the shape of the structural process, or maybe alternatively, pressure and temperature effects compensate (consequently, there is a marginal impact of thermodynamic conditions applied in our experiments on the strength of H-bonds)? To verify which of these theses is the true one, complementary Fourier-transform infrared spectroscopy (FTIR) investigations at high p must be done. Unfortunately, at the moment, we do not have access to such equipment. To overcome these limitations, we decided to carry out FTIR studies on the pressure densified glass (PDG) of TICA. Herein, one can mention that the above approach allows us to freeze the higher density and structure of the compressed sample and potentially obtain a valuable insight into specific interactions at high pressure[36]. In order to produce the PDG, as a first, the sample of TICA was compressed up to $p = 400$ MPa at $T = 385$ K. Next, it was cooled to $T = 283$ K (much below the T_g), and then the pressure was released. Just after decompression, the PDG of API was measured by means of FTIR spectroscopy to avoid any significant effect of equilibration/ physical aging.

In panel (c) of Fig. 3, the infrared spectra measured at room temperature for the PDG, as well as the OG of TICA are presented. As illustrated, the spectral profile corresponding to the stretching vibrations of the O–H and N–H groups in the densified glass (PDG) remains unchanged with respect to the OG. This indicates a stable distribution of H-bonds in both samples and thus confirms that, most likely, there is a compensating effect of densification and higher thermal energy on the strength of this kind of interactions at high p. As a consequence, at isochronal conditions (τ_α = const.), the shape of the structural process remains unchanged. Herein, one can refer to our recent paper, where a similar methodology has been applied to understand a peculiar narrowing of the width of the structural process in ritonavir (RTV) at high compression[32]. In panel (d) in Fig. 3, infrared spectra of OG and PDG of this active substance are shown. As can be seen, the spectral profile of the O–H and N–H

stretching vibration bands varies significantly due to compression. The observed changes indicate the increasing population of the weaker H-bonds in the PDG. This phenomenon was reflected in the variation of the shape of the structural process (its narrowing) at constant structural relaxation time (see Fig. 3b). Both mentioned examples (TICA and RTV) suggest that, in fact, there is a relationship between the shape of the structural process and the H-bonding pattern at high pressure.

Subsequently, we performed a comprehensive analysis of dielectric spectra determined for TICA from isobaric to isothermal measurements. First of all, the loss spectra collected at various thermodynamic conditions in the liquid/supercooled liquid state were fitted to the Havriliak–Negami (HN) function with the conductivity term (Eq. 2)[37]:

$$\varepsilon(\varpi)'' = \frac{\sigma_{dc}}{\varepsilon_0 \varpi} + \varepsilon_\infty + \frac{\Delta\varepsilon}{[1 + (i\overline{\omega}\tau_{HN})^\alpha]^\gamma}, \tag{2}$$

where σ_{dc} is the dc-conductivity, ε_0 is the vacuum permittivity, $\overline{\omega}$ is an angular frequency ($\overline{\omega} = 2\pi f$), ε_∞ is the high-frequency limit permittivity, $\Delta\varepsilon$ is the dielectric relaxation strength, τ_{HN} is the HN relaxation time, α and γ are the shape parameters representing the breadth and asymmetry of given relaxation peaks. Then, in panel (a) of Fig. 4, we plotted the obtained α-relaxation times , τ_α (firstly recalculated from τ_{HN} using the formula given in ref. [38]) versus temperature and pressure. Next, these τ_α (T, p) dependencies, which created two-dimensional surfaces within the considered T and p range, were analyzed using the modified Avramov expression[39] given in the Supplementary Information, SI (equation S1). Note that the accuracy of the Avramov fits is illustrated in Fig. S1 presenting the separate isobars and isotherms determined for TICA together with the fits using equation S1.

Afterwards, the values of T_g obtained from the following formula proposed by Avramov[40]:

$$T_g(p) = T_g(p_0)\left(1 + \frac{p}{\Pi}\right)^{\beta / \alpha_0 \left(1 - \frac{C}{C_{p_0}}\left(\ln\left(1 + \frac{p}{\Pi}\right)\right)\right)}, \tag{3}$$

with the same parameters (Π, β, α_0, and C_{p_0}) as those in equation S1 were plotted versus pressure (see Fig. 4b). From this dependence, we estimated the pressure coefficient of the glass transition temperature (dT_g/dp)—a parameter reflecting the sensitivity of the structural dynamics to compression. Its value in the limit of ambient pressure (= 163 K/GPa) indicates a relatively strong influence of pressure on the α-relaxation in TICA. Note that a similar but quite higher value of dT_g/dp has been reported for RTV (~200 K/GPa)[32] and some weakly associated pharmaceuticals, such as droperidol[24], ibuprofen[41], or curcumin[42]. Importantly, the values in the

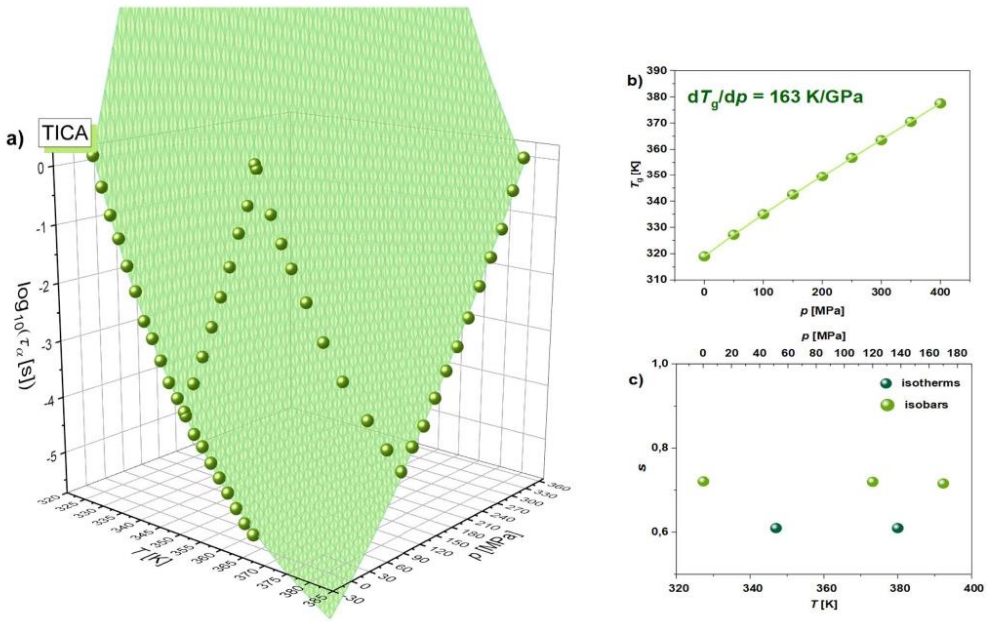

Figure 4. Structural (α)-relaxation times plotted as a function of T and p for TICA (**a**). The green area represents surface fits to equation S1. T_g versus p plot (**b**) and the dependence of the parameter s from Eq. (5) as a function of T and p (**c**).

range 160–220 K/GPa significantly exceed those determined for the other LMW compounds ($dT_g/dp < 70$ K/GPa)[20,22], which, similarly to TICA, are strongly H-bonded systems.

Additionally, we have decided to check whether for TICA there is a correlation between the dc-conductivity, σ_{dc} (associated with the charge transport and proton hopping) and α-relaxation times, τ_α (reorientation dynamics) according to the Debye–Stokes–Einstein (DSE) law:

$$\sigma_{dc}\tau_\alpha = const, \tag{4}$$

Due to the fact that the above relation is very often not fulfilled, another form of Eq. (4), which is called the fractional DSE law (FDSE), has been applied[43]:

$$\sigma_{dc}^{s}\tau_\alpha = const(0 < s < 1), \tag{5}$$

where s is the fractional exponent describing the slope of dependency σ_{dc} versus τ_α; see Fig. S2a,b in the SI). It should be mentioned that when $s \sim 1$, there is a coupling between σ_{dc} and τ_α, while its lowering (to values closer to 0) suggests the increase of decoupling between both quantities. In panel (c) of Fig. 4, we plotted the values of s (determined from the linear fitting of the isobaric and isothermal data shown in Fig. S2 in the SI) versus pressure and temperature. As can be seen, the fractional exponent practically does not vary with increasing p and T. This experimental observation might be related to the unchanged H-bonding pattern at higher compression as deduced from FTIR investigations on the PDG of TICA. As a consequence, proton hopping—an important factor contributing to the overall dc-conductivity of the sample, is most likely not affected by the thermodynamic conditions applied in our experiments. Nevertheless, it should be stressed that there is a clear decoupling between σ_{dc} and structural dynamics in the examined sample at each investigated isotherm and isobar ($s \approx 0,6 - 0,7$). It is an expected result since we deal with the H-bonded liquid, where proton hopping strongly contributes to the measured dc-conductivity. It is worth noting that a pronounced decoupling between σ_{dc} and τ_α has been also reported in the case of another associated API, curcumin (s =0.87 at p = 0.1 MPa)[42]. However, for this substance, the fractional exponent, s, changed in a slightly wider range, from 0.87 to 0.73 and from 0.7 to 0.63 with increasing p and T, respectively. A similar scenario has been also found for the anhydrosaccharide—1,6-anhydro-D-glucose[22]. Herein, the value of s varied from 0.95 (p = 0.1 MPa) to 0.68 at p = 255 MPa.

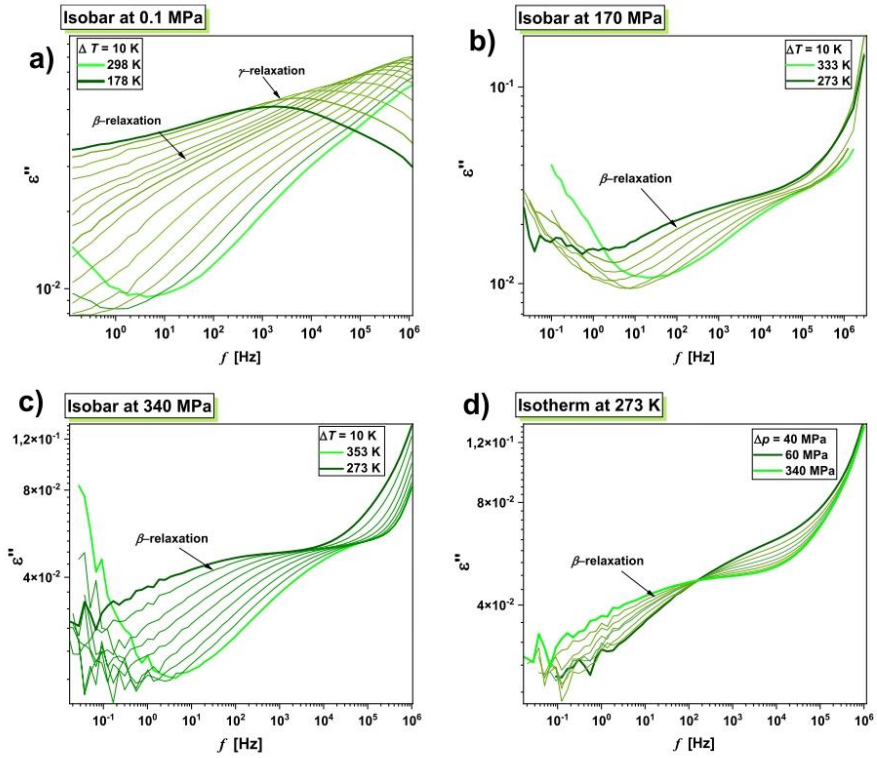

Figure 5. Dielectric spectra measured for TICA at 0.1 MPa (**a**), 170 MPa (**b**) and 340 MPa (**c**) and indicated $T < T_g$. Panel (**d**) represents isothermal data (T = 273 K) collected in the p range 60–340 MPa.

In the subsequent stage, we focused on characterizing the influence of high compression on the molecular dynamics of TICA in the glassy state. Representative dielectric loss spectra collected at isobaric conditions (i.e., at $p = 0.1$, 170 and 340 MPa), and indicated temperatures below T_g, as well as isothermal conditions ($T = 273$ K) and $p > p_g$ are illustrated in Fig. 5. As can be seen, in contrast to ambient p dielectric data (panel a), which revealed the presence of two secondary modes labeled as β and γ, at elevated p, only one well-resolved β-relaxation peak can be observed in the presented spectra. The maximum of γ-process is out of the experimental frequency window, which suggests its insensitivity to density changes.

In order to obtain relaxation times of secondary (β)-process at various thermodynamic conditions (as well as τ_γ at $p = 0.1$ MPa), the loss spectra presented in Fig. 5 were fitted to the HN formula, Eq. (2) (actually, we applied the superposition of two HN functions to describe the experimental data). The obtained τ_β and τ_γ ($p = 0.1$ MPa) together with τ_α from the previous analysis (Fig. 4a) have been plotted versus T_g/T; see Fig. 6. Next, these dependences (i.e., τ_β and τ_γ vs. T_g/T) were analyzed using the Arrhenius equation to determine the activation barrier (E_x) for the β and γ-modes:

$$\tau_x = \tau_\infty exp\left(\frac{E_x}{RT}\right), \quad x = \beta, \gamma \tag{6}$$

where τ_∞ is a pre-exponential factor, and R is a gas constant. In Fig. 6, the values of E_β and E_γ estimated with ± 5% uncertainty are presented. As can be observed, E_β increases with increasing compression ($E_\beta = 66$, 73, and 81 kJ/mol at 0.1 MPa, 170 MPa and 340 MPa, respectively). Moreover, the E_γ obtained at ambient p (= 38 kJ/mol) is clearly lower compared to E_β determined under the same conditions.

From Fig. 6, it is also well seen that τ_β obtained at $p = 0.1$, 170, 340 MPa and rescaled with respect to the T_g, nearly perfectly collapsed onto each other, forming one curve. Such behavior indicates a great sensitivity of the β-process to compression. Further confirmation of that is an enormously high value of the activation volume for this relaxation ($\Delta V_\beta = 43$ cm^3/mol), estimated from the analysis of isothermal data (dependences of τ_β obtained at 273 K versus p; see the upper inset to Fig. 6) using the following formula:

$$\Delta V_\beta = 2.303RT\left(\frac{dlog_{10}\tau_\beta}{dp}\right)_T \tag{7}$$

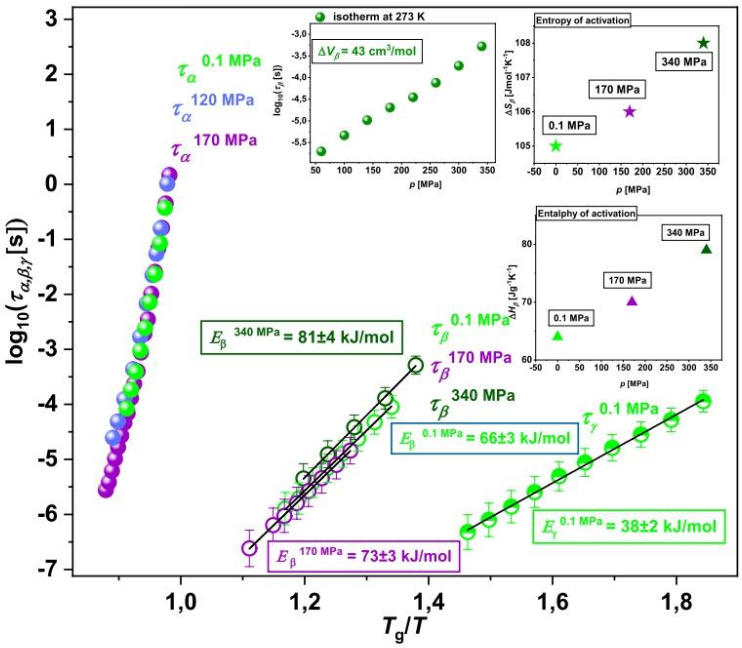

Figure 6. Dependences of relaxation times τ_α, τ_β, τ_γ versus T_g/T for TICA. The solid lines are Arrhenius fits (Eq. 6). In the insets, $\log_{10}\tau_\beta$ plotted versus p, as well as ΔS_β and ΔH_β calculated at ambient and elevated pressure conditions from the Eyring equation (Eq. 8) are presented.

Note that a slightly lower ΔV for this kind of secondary process has been reported for some other LMW compounds (e.g., posaconazole and itraconazole (23 and 35 cm^3/mol)[44], or phenolphthalein dimethyl ether (20–24 cm^3/mol)[45]), as well as polymers (e.g., polyethylene terephthalate (28–32 cm^3/mol)[45], and poly-[(phenyl glycidyl ether)-co-formaldehyde, PPGE (15–19 cm^3/mol)[45]).

Based on the above facts, including the high value of E_β, one can state that the β-process in the examined API is a true Johari–Goldstein (JG) relaxation (originating from the local motions of the whole API molecules)[46]. In turn, the faster γ-process with clearly lower E_γ has rather an intramolecular character—its source are reorientations of a small part of the molecule.

It is also worth adding that in the case of TICA, the constant ratio $\tau_\alpha/\tau_{JG-\beta}$ (data at 0.1 and 170 MPa) for the same τ_α indicates the fulfillment of the isochronal superpositioning of structural (α)- and secondary (JG-β)-relaxation times—a rule, whose validity has been shown in the literature for many glass-forming systems (including APIs) with different kinds of interactions[40,46–48].

Finally, we have used the Eyring formula[49]:

$$\ln(\tau_\beta T) = \left[\frac{\Delta H_\beta}{R}\frac{1}{T}\right] + \left[\ln\left(\frac{h}{k_B}\right) - \left(\frac{\Delta S_\beta}{R}\right)\right] \tag{8}$$

where k_B and h, are, respectively, the Boltzmann and Planck constants to calculate the entropy and enthalpy of activation for the β-relaxation process in TICA (ΔS_β and ΔH_β, respectively), at ambient and elevated p. For this purpose, dependences $\ln(\tau_\beta T)$ versus $1/T$ (see Fig. S3 in the SI) were fitted to the linear function. Further, we determined ΔS_β (a measure of the local molecular reorganization induced by the relaxation) from the point of interception with the y axis $\left[\ln\left(\frac{h}{k_B}\right) - \left(\frac{\Delta S_\beta}{R}\right)\right]$, while ΔH_β, which is identified with E_β in the Arrhenius equation (Eq. 6), from the slope of the line $\left[\frac{\Delta H_\beta}{R}\right]$. The obtained values of both parameters are presented versus pressure in the right insets in Fig. 6. As illustrated, both ΔS_β and ΔH_β (values comparable to E_β determined at the same thermodynamic conditions) increase with increasing compression. In the context of ΔS_β, the positive value of this parameter means the intermolecular cooperativity of the secondary (β)-relaxation in TICA, i.e., the correlation of molecular motions responsible for this process. Importantly, the increase of ΔS_β with p in the case of the examined pharmaceutical is not significant (from 105 J/mol·K at 0.1 MPa to 108 J/mol·K at 340 MPa). Similar behavior has been observed for some polymers, i.e., PPGE, and poly(vinyl acetate) (PVAc), however, the obtained values of activation entropy were clearly lower (21.3–21.6 J/mol·K and 6.2–14.6 J/mol·K for the former and latter systems, respectively)[50]. In turn, slightly greater changes of ΔS_β (from 94 J/mol·K at 0.1 MPa to 120 J/mol·K at 230 MPa)[44] have been reported by some of us for the β-mode in itraconazole and explained as resulting from some changes in the molecular special arrangement in the compressed sample. Moreover, we have also demonstrated a clear variation in ΔS_β (from 0.6 J/mol·K at 0.1 MPa to 78.1 J/mol·K at 115 MPa and 27.8 J/mol·K at 160 MPa) for probucol—an API forming weak O–H···S bonds at elevated p (which are absent at ambient p)[51]. In the case of TICA, the slight increase of ΔS_β with p is not associated with the changes in the H-bonding pattern due to compression, as can be deduced from the complementary FTIR studies on the pressure densified glass. One should suppose that it might be related to the solvation of ions (ionic impurities in the sample) around the TICA molecule. Herein, it is worth adding that this problem was well studied in the case of water, where the reorientation dynamics is strongly affected by ions even in strongly diluted solutions[52]. Furthermore, depending on the interaction strength, ions alter or slow down the water dynamics. However, it should be noted that in our system ion concentration was marginal as measured conductivity (σ_{dc}) changed with the examined T and p in the range of 10^{-10}–10^{-13} S/cm, while in the vicinity of the T_g, it was of the order of 10^{-15} S/cm; see Fig. S2 in the SI. Moreover, importantly, throughout dielectric measurements, the sample was enclosed in the capacitor, surrounded by an inert media (oil), so the concentration of impurities remained constant. In our experiments, the variation of the dc-conductivity was related only to the mobility changes induced by the viscosity alterations. Based on the above information, it seems that the solvation of ionic impurities has no effect on the value of activation entropy for the β-process in TICA. Hence, one can propose that the observed variation of this parameter might result from some small conformational/molecular variations of API molecules at high p.

Conclusions

In this paper, DSC, FTIR, and BDS techniques have been applied to investigate thermal properties, variation in the population of H-bonds, as well as molecular dynamics (in the liquid, supercooled liquid, and glassy states) at ambient and elevated pressure in ticagrelor. Interestingly, our comprehensive HP dielectric investigations demonstrated a strong sensitivity of the structural (α)-relaxation to compression (reflected in a high value of $dT_g/dp = 163$ K/GPa parameter) as well as the fulfillment of the TPS rule (a constant shape of the α-peak at various combinations of T and p, for the same τ_α). Further FTIR measurements on the ordinary and pressure densified glasses of TICA, as well as a comparison of the obtained data with those determined for another H-bonded API—RTV indicated that the lack of changes in the H-bonding pattern with compression is responsible for that. What is more, additional BDS measurements carried out on the examined substance at $T < T_g/p > p_g$ revealed that (1) at isochronal conditions, there is a constant ratio of structural and secondary (β-JG-type) relaxation time; (2) the activation entropy for the β-mode, ΔS_β, has a positive value (which suggests the intermolecular cooperativity of this process) and slightly increases with compression probably due to small conformational/molecular variations of API molecules at high p. Our studies open an interesting discussion on the issue concerning the connection between the changes in the H-bonding pattern and the shape of the structural relaxation process at various thermodynamic conditions, which can be probed indirectly by studying the properties of the pressure densified glass.

Methods

Materials. Ticagrelor (TICA) [the IUPAC name: (1*S*,2*S*,3*R*,5*S*)-3-[7-[[(1*R*,2*S*)-2-(3,4-difluorophenyl)cyclopropyl]amino]-5-propylsulfanyltriazolo[4,5-d]pyrimidin-3-yl]-5-(2-hydroxyethoxy)cyclopentane-1,2-diol] with molecular weight $M_w = 522.57$ g·mol^{-1} and purity ≥ 98% was supplied by Sigma Aldrich and used without further purification.

Preparation of the ordinary and pressure densified glasses of TICA. The ordinary glass (OG) of TICA was obtained by melting the crystalline sample at $T = 413$ K and rapid cooling the obtained liquid (vitrification method). The preparation of the pressure densified glass (PDG) of TICA included, respectively, (1) compressing the sample up to $p = 400$ MPa at $T = 385$ K; (2) cooling it down to $T = 283$ K, and (3) releasing the pressure. Infrared measurements on the OG and PDG (and dielectric studies on the OG) were performed immediately after their preparation.

DSC. Thermal properties of TICA were examined with the use of a Mettler–Toledo DSC apparatus equipped with a HSS8 ceramic sensor with 120 thermocouples as well as a liquid nitrogen cooling accessory. The instrument was calibrated for temperature and enthalpy using indium and zinc standards while for heat capacity (C_p)—using a sapphire disc. The crystalline sample of TICA was placed in an aluminum crucible (40 μL) and sealed. Next, it was heated above its melting temperature, quenched (with a rate of 20 K/min), and scanned over a T range of 170–430 K. A heating rate was equal to 10 K/min. The melting point was determined as the maximum of the peak, whereas the glass transition temperature as the midpoint of the heat capacity increment.

BDS. Dielectric measurements of TICA were performed using a dielectric spectrometer (Novo-Control Alpha, Hundsangen, Germany) in the frequency range from 10^{-1} to 10^{6} Hz at atmospheric pressure. The sample was placed between two stainless steel flat electrodes of the capacitor (diameter: 20 mm) with a 0.1 mm gap with a Teflon spacer and mounted on a cryostat. The temperatures were controlled by a Quatro System using a dry nitrogen gas cryostat with stability better than 0.1 K.

For BDS experiments at elevated p, a high-pressure Unipress setup (Warszawa, Poland) with a special home-made flat parallel capacitor (diameter: 20 mm; gap: 0.081 mm) was additionally employed. We applied a thin Teflon spacer to maintain a fixed distance between the plates. During the measurement, the sample capacitor was sealed and covered carefully by Teflon tape to separate it from the silicon oil. The pressure was measured using a Nova Swiss tensometric meter with a resolution of 1 MPa, while the temperature was adjusted with a precision of 0.1 K by a refrigerated and heating circulator (HUBER GmbH, Germany).

Comprehensive isothermal and isobaric measurements for the investigated API were performed in the following thermodynamic conditions: in the supercooled liquid state: isothermal measurements: $T = 347$ K ($p = 0.1$–120 MPa), $T = 381$ K ($p = 120$–300 MPa), isobaric measurements: $p = 0.1$ MPa ($T = 333$–363 K), $p = 120$ MPa ($T = 350$–383 K), $p = 170$ MPa ($T = 357$–381 K); in the glassy state: isothermal measurements: $T = 273$ K ($p = 60$–340 MPa), isobaric measurements: $p = 0.1$ MPa ($T = 173$–298 K), $p = 170$ MPa ($T = 273$–333 K), $p = 340$ MPa ($T = 273$–353 K).

Data availability

The datasets used and/or analyzed during the current study available from the corresponding author on reasonable request.

Received: 6 October 2022; Accepted: 23 May 2023
Published online: 01 June 2023

References

1. Ngai, K. L. *et al.* Recent advances in fundamental understanding of glass transition. *J. Non-Cryst. Solids* **354**, 5085–5088 (2008).
2. Zarzycki, J. *Glasses and the Vitreous State* (Cambridge University Press, 1991).
3. Debenedetti, P. G. & Stillinger, F. H. Supercooled liquids and the glass transition. *Nature* **410**, 259–267 (2001).
4. Floudas, G., Paluch, M., Grzybowski, A. & Ngai, K. L. *Molecular Dynamics of Glass-Forming Systems: Effects of Pressure* (Springer-Verlag, 2011).
5. Angell, C. A. Formation of glasses from liquids and biopolymers. *Science* **267**, 1924–1935 (1995).
6. Niss, K. & Hecksher, T. Perspective: Searching for simplicity rather than universality in glass-forming liquids. *J. Chem. Phys.* **149**, 230901 (2018).
7. Amann-Winkel, K. *et al.* Water's second glass transition. *PNAS* **110**, 17720–17725 (2013).
8. Levine, H. *Freeze-Drying of Pharmaceuticals and Biopharmaceuticals* (Royal Society of Chemistry, 2002).
9. Tong, H. & Tanaka, H. Structural order as a genuine control parameter of dynamics in simple glass formers. *Nat. Commun.* **10**, 5596 (2019).
10. Paluch, M., Knapik, J., Wojnarowska, Z., Grzybowski, A. & Ngai, K. L. Universal behavior of dielectric responses of glass formers: Role of dipole–dipole interactions. *Phys. Rev. Lett.* **116**, 025702 (2016).
11. Ngai, K. L., Casalini, R., Capaccioli, S., Paluch, M. & Roland, C. M. Do theories of the glass transition, in which the structural relaxation time does not define the dispersion of the structural relaxation, need revision?. *J. Phys. Chem. B* **109**, 17356–17360 (2005).
12. Minecka, A. *et al.* Studies on the internal medium-range ordering and high pressure dynamics in modified ibuprofens. *Phys. Chem. Chem. Phys.* **22**, 295–305 (2020).
13. Mierzwa, M., Pawlus, S., Paluch, M., Kaminska, E. & Ngai, K. L. Correlation between primary and secondary Johari–Goldstein relaxations in supercooled liquids: Invariance to changes in thermodynamic conditions. *J. Chem. Phys.* **128**, 044512 (2008).
14. Casalini, R. & Roland, C. M. Temperature and density effects on the local segmental and global chain dynamics of poly (oxybutylene). *Macromolecules* **38**, 1779–1788 (2005).

15. Niss, K., Dalle-Ferrier, C., Tarjus, G. & Alba-Simionesco, C. On the correlation between fragility and stretching in glass-forming liquids. *J. Phys. Condens. Matter* **19**, 076102 (2007).
16. Roed, L. A., Gundermann, D., Dyre, J. C. & Niss, K. Two measures of isochronal superposition. *J. Chem. Phys.* **139**, 101101 (2013).
17. Pawlus, S., Paluch, M., Kaminska, K. & Ngai, K. L. Anomalous narrowing of the structural relaxation dispersion of tris(dimethylsiloxy)phenylsilane at elevated pressures. *J. Phys. Chem. B* **110**, 7678–7681 (2006).
18. Heczko, D. *et al.* Anomalous narrowing of the shape of the structural process in derivatives of trehalose at high pressure. The role of the internal structure. *J. Mol. Liq.* **336**, 116321 (2021).
19. Hensel-Bielowka, S., Paluch, M. & Ngai, K. L. Emergence of the genuine Johari–Goldstein secondary relaxation in *m*-fluoroaniline after suppression of hydrogen-bonding induced clusters by elevating temperature and pressure. *J. Chem. Phys.* **123**, 014502 (2005).
20. Roland, C. M., Hensel-Bielowka, S., Paluch, M. & Casalini, R. Supercooled dynamics of glass-forming liquids and polymers under hydrostatic pressure. *Rep. Prog. Phys.* **68**, 1405–1478 (2005).
21. Casalini, R. & Roland, C. M. Excess wing in the dielectric loss spectra of propylene glycol oligomers at elevated pressure. *Phys. Rev. B* **69**, 094202 (2004).
22. Kaminska, E., Tarnacka, M., Jurkiewicz, K., Kaminski, K. & Paluch, M. High pressure dielectric studies on the structural and orientational glass. *J. Chem. Phys.* **144**, 054503 (2016).
23. Romanini, M. *et al.* Thermodynamic scaling of the dynamics of a strongly hydrogen bonded glass-former. *Sci. Rep.* **7**, 1346 (2017).
24. Kamińska, E., Minecka, A., Tarnacka, M., Kamiński, K. & Paluch, M. Breakdown of the isochronal structural (α) and secondary (JGβ) exact superpositioning in probucol—A low molecular weight. *J. Mol. Liq.* **299**, 112169 (2020).
25. Wojnarowska, Z., Hawelek, L., Paluch, M., Sawicki, W. & Ngai, K. L. Molecular dynamics at ambient and elevated pressure of the amorphous pharmaceutical: Nonivamide (pelargonic acid vanillylamide). *J. Chem. Phys.* **134**, 044517 (2011).
26. Skotnicki, M., Aguilar, J. A., Pyda, M. & Hodgkinson, P. Bisoprolol and bisoprolol-valsartan compatibility studied by differential scanning calorimetry, Nuclear magnetic resonance and X-ray powder diffractometry. *Pharm. Res.* **32**, 414–429 (2014).
27. Heczko, D. *et al.* The impact of chemical structure on the formation of the medium-range order and dynamical properties of selected antifungal APIs. *Phys. Chem. Chem. Phys.* **124**, 11949–11961 (2020).
28. Knapik, J. *et al.* Molecular dynamics and physical stability of coamorphous ezetimib and indapamide mixtures. *Mol. Pharm.* **12**, 3610–3619 (2015).
29. Hancock, B. C., Shamblin, S. L. & Zografi, G. Molecular mobility of amorphous pharmaceutical solids below their glass transition temperatures. *Pharm. Res.* **12**, 799–806 (1995).
30. Moura Ramos, J. J. & Diogo, H. P. Thermal behavior and molecular mobility in the glassy state of three anti-hypertensive pharmaceutical ingredients. *RSC Adv.* **7**, 10831–10840 (2017).
31. Madejczyk, O. *et al.* Studying the crystal growth of selected APIs from single and two-component systems above and below the glass transition temperature. *Cryst. Growth Des.* **19**, 1031–1040 (2019).
32. Heczko, D. *et al.* Variation in the local ordering, H-bonding pattern and molecular dynamics in the pressure densified ritonavir. *J. Mol. Liq.* **351**, 11866 (2022).
33. Williams, G. & Watts, D. C. Non-symmetrical dielectric relaxation behavior arising from a simple empirical decay function. *Trans Faraday Soc.* **66**, 80–85 (1970).
34. Kohlrausch, R. Nachtrag uber die elastiche nachwirkung beim cocon und glasladen. *Ann. Phys.* **72**, 353–405 (1847).
35. Mierzwa, M., Paluch, M., Rzoska, S. J. & Ziolo, J. The liquid–glass and liquid–liquid transitions of TPP at elevated pressure. *J. Phys. Chem. B* **112**, 10383–10385 (2008).
36. Rams-Baron, M. *et al.* The dielectric signature of glass density. *Appl. Phys. Lett.* **111**, 121902 (2017).
37. Havriliak, S. & Negami, S. A complex plane analysis of α-dispersions in some polymer systems. *J. Polym. Sci. Part C Polym. Symp.* **14**, 99–117 (1966).
38. Kremer, F. & Schönhals, A. *Broadband Dielectric Spectroscopy* (Springer, New York, 2003).
39. Avramov, I. Pressure dependence of viscosity of glassforming melts. *J. Non-Cryst. Solids* **262**, 258–262 (2000).
40. Avramov, I. Pressure and temperature dependence of viscosity of glassforming and of geoscientifically relevant systems. *J. Volcanol. Geotherm. Res.* **160**, 165–174 (2007).
41. Adrjanowicz, K. *et al.* Dielectric relaxation and crystallization kinetics of ibuprofen at ambient and elevated pressure. *J. Phys. Chem. B* **114**, 6579–6593 (2010).
42. Minecka, A. *et al.* Studying structural and local dynamics in model H-bonded active ingredient—Curcumin in the supercooled and glassy states at various thermodynamic conditions. *Eur. J. Pharm. Sci.* **135**, 38–50 (2019).
43. Becker, S. R., Poole, P. H. & Starr, F. W. Fractional Stokes–Einstein and Debye–Stokes–Einstein relations in a network forming liquid. *Phys. Rev. Lett.* **97**, 055901 (2006).
44. Heczko, D. *et al.* Influence of high pressure on the local order and dynamical properties of the selected azole antifungals. *J. Phys. Chem. B* **124**, 11949–21196 (2020).
45. Sharifi, S., Capaccioli, S., Lucchesi, M., Rolla, P. & Prevosto, D. Temperature and pressure dependence of secondary process in an epoxy system. *J. Chem. Phys.* **134**, 044510 (2011).
46. Ngai, K. L. & Paluch, M. Classification of secondary relaxation in glass-formers based on dynamic properties. *J. Chem. Phys.* **120**, 857–873 (2004).
47. Capaccioli, S., Ngai, K. L., Shahin Thayyil, M. & Prevosto, D. Coupling of caged molecule dynamics to JG β-relaxation: I. *J. Phys. Chem. B* **119**, 8800–8808 (2015).
48. Ngai, K. L., Capaccioli, S., Prevosto, D. & Wang, L. M. Coupling of caged molecule dynamics to JG β-relaxation III: van der Waals glasses. *J. Phys. Chem. B* **119**, 12519–12525 (2015).
49. Eyring, H. The activated complex in chemical reactions. *J. Chem. Phys.* **3**, 107 (1935).
50. Sharifi, S. & Asl, J. M. Secondary relaxation inside the glass. *ISRN Mater. Sci.* **201**, 764874 (2011).
51. Minecka, A., Hachuła, B., Kaminski, K., Paluch, M. & Kamińska, E. How does pressure affect the molecular dynamics, intramolecular interactions, and the relationship between structural (α) and secondary (JG-β) relaxation above and below the glass transition temperature in binary mixtures of H-bonded API—Probucol and acetylated saccharides?. *Eur. J. Pharm. Sci.* **164**, 105894 (2021).
52. Stirnemann, G., Wernersson, E., Jungwirth, P. & Laage, D. Mechanisms of acceleration and retardation of water dynamics by ions. *J. Am. Chem. Soc.* **135**, 11824–11831 (2013).

Acknowledgements

This research was funded in whole by the National Science Centre (Poland), Grant No.: Opus 21 No. 2021/41/B/NZ7/01654. For the purpose of Open Access, the author has applied a CC-BY public copyright license to any Author Accepted Manuscript (AAM) version arising from this submission.

Author contributions

P.J. carried out dielectric measurements, their analysis and visualization; D.H. participated partly in the BDS measurements and data analysis; B.H. performed FTIR experiments; K.K. and E.K. supervised the measurement, data analysis, and discussion of the results; P.J., and E.K. wrote and revised the article.

Competing interests

The authors declare no competing interests.

Additional information

Supplementary Information The online version contains supplementary material available at https://doi.org/10.1038/s41598-023-35772-7.

Correspondence and requests for materials should be addressed to P.J. or E.K.

Reprints and permissions information is available at www.nature.com/reprints.

Publisher's note Springer Nature remains neutral with regard to jurisdictional claims in published maps and institutional affiliations.

Open Access This article is licensed under a Creative Commons Attribution 4.0 International License, which permits use, sharing, adaptation, distribution and reproduction in any medium or format, as long as you give appropriate credit to the original author(s) and the source, provide a link to the Creative Commons licence, and indicate if changes were made. The images or other third party material in this article are included in the article's Creative Commons licence, unless indicated otherwise in a credit line to the material. If material is not included in the article's Creative Commons licence and your intended use is not permitted by statutory regulation or exceeds the permitted use, you will need to obtain permission directly from the copyright holder. To view a copy of this licence, visit http://creativecommons.org/licenses/by/4.0/.

© The Author(s) 2023

High-pressure studies in the supercooled and glassy state of the strongly associated active pharmaceutical ingredient - ticagrelor

Paulina Jesionek[1,2,✉], Dawid Heczko[3], Barbara Hachuła[1], Kamil Kamiński[4], Ewa Kamińska[2,✉]

[1] *Institute of Chemistry, Faculty of Science and Technology, University of Silesia in Katowice, Szkolna 9, 40-007 Katowice, Poland*
[2] *Department of Pharmacognosy and Phytochemistry, Faculty of Pharmaceutical Sciences in Sosnowiec, Medical University of Silesia in Katowice, Jagiellonska 4, 41-200 Sosnowiec, Poland*
[3] *Department of Statistics, Department of Instrumental Analysis, Faculty of Pharmaceutical Sciences in Sosnowiec, Medical University of Silesia in Katowice, Ostrogorska 30, 41-200 Sosnowiec, Poland*
[4] *Institute of Physics, Faculty of Science and Technology, University of Silesia in Katowice, 75 Pulku Piechoty 1, 41-500 Chorzow, Poland*

SUPPLEMENTARY INFORMATION

BDS DATA

The data shown in Fig. 4a in the manuscript were analyzed using the Avramov equation[1]:

$$\tau_\alpha = \tau_\infty exp\left[\ln(\tau_g/\tau_\infty)\left(\frac{T_r}{T}\right)^{\alpha_0\left(1-\frac{C}{C_{p_0}}\ln\left(1+\frac{p}{\Pi}\right)\right)}\left(1+\frac{p}{\Pi}\right)^{\beta}\right], \quad \text{(S1)}$$

where τ_∞ is a relaxation time at extremely high T, $\tau_g = \tau(T_g)$, T_r is a reference temperature lying close to the T_g, C_{p_0} is a specific heat capacity, C is an additional adjustable parameter, Π is a constant with the dimension of pressure, α_0 and β are exponential parameters, which are linked to the thermodynamic quantities via the following relations:

$$\alpha_0 = \frac{2C_{p_0}}{ZR}, \quad \text{(S2)}$$

$$\beta = \frac{2\alpha_p V_m}{ZR}\Pi, \quad \text{(S3)}$$

where Z represents the degeneracy of the system, α_p is a volume expansion coefficient at ambient p, and V_m is a molar volume. The parameters of equation S1 determined from the global numerical fitting (Fig. 4a) are presented in Table S1.

The separate isobars and isotherms together with the Avramov fitting curves are shown in Fig. S1.

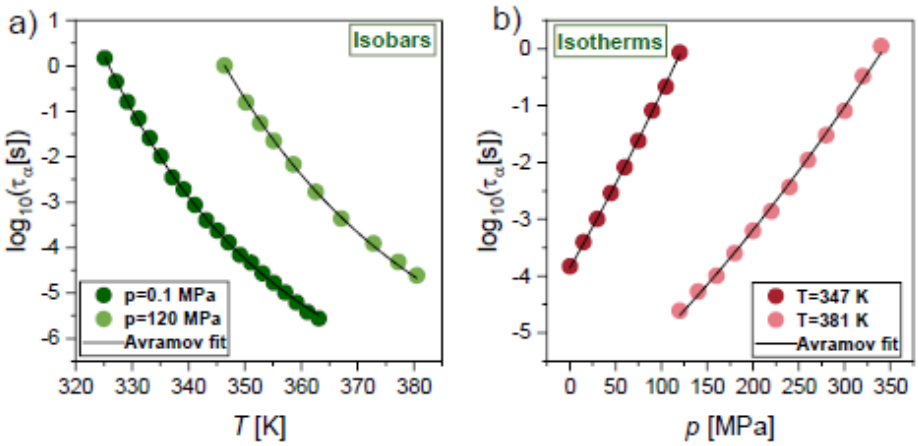

Figure S1. Temperature (a) and pressure (b) dependence of structural relaxation times obtained for TICA from isobaric and isothermal dielectric measurements. Black lines represent fits using the modified Avramov function.

Table S1. Parameters of the modified Avramov equation (equation S1) obtained from the analysis of $\tau_\alpha(T,p)$ dependencies for TICA.

	TICA
$\log_{10}(\tau_\infty[s])$	-8.19±0.17
T_r [K]	319.0±0.20
α_0	10.23±0.37
C/C_{p0}	0.27±0.009
Π [MPa]	217.96±13.05
β	1.189±0.068
Adj. R-Square	0.999

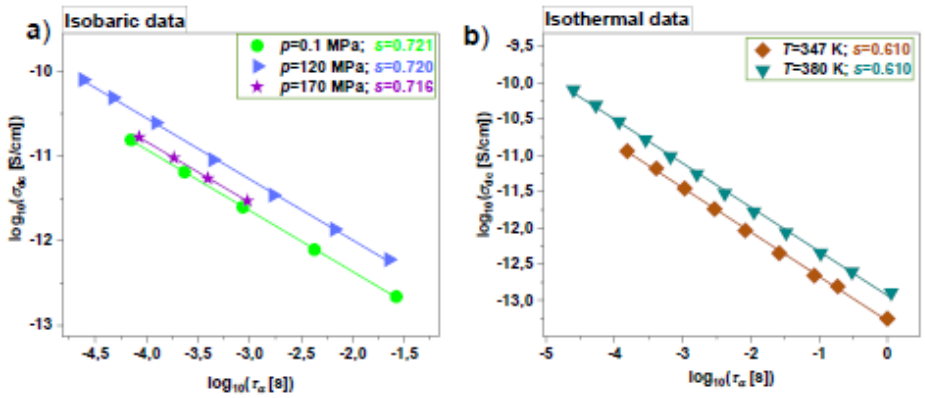

Figure S2. The logarithm of dc conductivity plotted versus the logarithm of structural relaxation times determined from the analysis of isobaric (a) and isothermal (b) dielectric data.

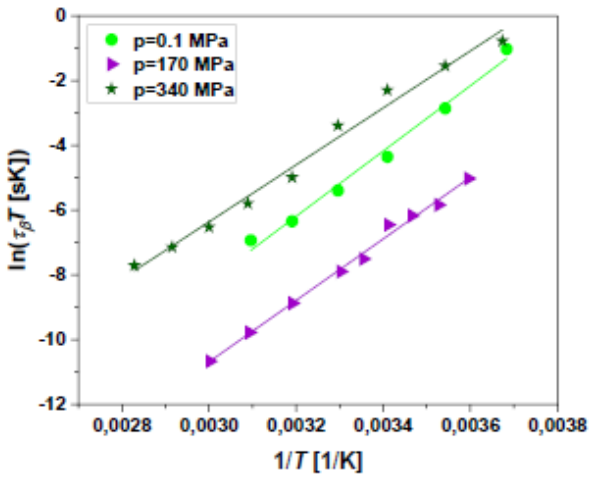

Figure S3. The dependences $\ln(\tau_\beta T)$ vs. $1/T$ obtained for TICA at p = 0.1, 170 and 340 MPa. Solid lines represent linear fits.

References

1. Avramov, I. Pressure dependence of viscosity of glass-forming melts. *J. Non-Cryst. Solids* **262**, 258–262 (2000).

3.2. **Publikacja 2 (P2):** *Variation of Activation Volume as an Indicator of the Difference in Clusterization Phenomenon Induced by H-Bonding and F−Π Stacking Interactions in Enantiomers and a Racemate of Flurbiprofen*, J. Phys. Chem. B. 128 (**2024**) 4021–4032.

Autorzy: P. Jesionek, B. Hachuła, K. Jurkiewicz, P. Włodarczyk, M. Hreczka, K. Kamiński, E. Kamińska.

DOI: 10.1021/acs.jpcb.4c00582

Impact Factor czasopisma z roku opublikowania pracy: 2.8

Liczba punktów ministerialnych MNiSW czasopisma z roku opublikowania pracy: 140

Mój udział w pracy polegał na przeglądzie literaturowym, współtworzeniu hipotezy badawczej, przygotowaniu próbek enancjomerów flurbiprofenu i ich mieszaniny racemicznej do badań, wykonaniu pomiarów dielektrycznych w ciśnieniu atmosferycznym i warunkach wysokiej kompresji, analizie otrzymanych danych, opracowaniu rysunków do pracy, uczestnictwie w dyskusji wyników. Ponadto brałam udział w redagowaniu tekstu manuskryptu, a także przygotowałam odpowiedzi do recenzentów i dokonałam niezbędnych poprawek w manuskrypcie.

THE JOURNAL OF PHYSICAL CHEMISTRY B
A JOURNAL OF THE AMERICAN CHEMICAL SOCIETY

Open Access
This article is licensed under CC-BY 4.0

pubs.acs.org/JPCB
Article

Variation of Activation Volume as an Indicator of the Difference in Clusterization Phenomenon Induced by H-Bonding and F–Π Stacking Interactions in Enantiomers and a Racemate of Flurbiprofen

Paulina Jesionek,* Barbara Hachuła, Karolina Jurkiewicz, Patryk Włodarczyk, Marek Hreczka, Kamil Kamiński, and Ewa Kamińska*

Cite This: *J. Phys. Chem. B* 2024, 128, 4021−4032
Read Online

ACCESS | Metrics & More | Article Recommendations | Supporting Information

ABSTRACT: In this paper, X-ray diffraction (XRD), differential scanning calorimetry (DSC), broadband dielectric (BDS), and Fourier transform infrared (FTIR) spectroscopy supported by molecular dynamics (MD) simulations and quantum chemical computations were applied to investigate the structural and thermal properties, molecular dynamics, and H-bonding pattern of *R*-, *S*-, and *RS*-flurbiprofen (FLP). Experimental data indicated various spatial molecular arrangements in crystalline forms of examined systems, which seemed to disappear in the liquid state. Surprisingly, deeper analysis of high-pressure dielectric data revealed unexpected variation in the activation volume of pure enantiomers and a racemate. MD simulations showed that it is an effect of the clusterization phenomenon and a higher population of small associates in the former samples. Moreover, theoretical consideration exposed the particular role of unspecific F–Π interactions as a driving force underlying local molecular arrangements of molecules in the liquid and the crystal lattice of *R*-, *S*-, and *RS*-FLP.

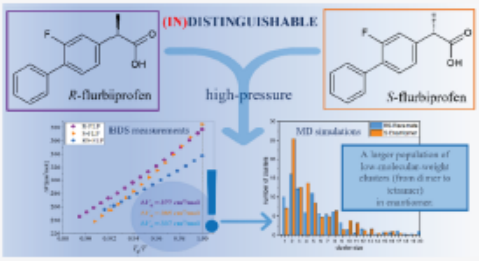

1. INTRODUCTION

In recent years, enantiomers, also called optical isomers or chiral molecules, have been the subject of intensive research in biology, chemistry, physics, and pharmaceutical sciences.[1−10] These systems are indistinguishable from each other regarding most physicochemical properties, such as chemical formula, melting points, or glass-transition temperature (T_g), except for the direction of their refraction of plane-polarized light[6] or circular dichroism.[11] Nevertheless, many papers have demonstrated that despite such strong similarity of enantiomers, they can vary significantly in their biological, toxicological, as well as pharmacodynamic, and pharmacokinetic properties.[6,8,12−23]

One of the groups of active pharmaceutical ingredients (APIs), where chirality seems to be an important aspect that is systematically and thoroughly studied from physical, chemical, and pharmaceutical perspectives, are 2-arylpropionic acids, the so-called profens.[24−36] The presence of a carboxylic moiety capable of forming hydrogen (H)-bonds in the close vicinity of the chiral carbon atom makes the situation very interesting since chirality can influence spatial molecular organization, self-assembly phenomenon, etc. This supposition was positively verified by studying, e.g., the H-bond pattern in the crystalline pure *R*- and *S*-enantiomers of flurbiprofen (FLP) and the racemic (*RS*) mixture. Namely, in the former systems, the chain-like organization of the molecules was found, while in the latter, dimeric structures were preferred.[27] Interestingly, the case seems to be much different in the supercooled liquid state. Molecular dynamic (MD) simulations carried out by Ottou Abe et al.[34] on ibuprofen (IBP) showed that the population of H-bonded (HB) aggregates, as well as the proportion of cyclic vs linear dimers, are comparable for pure *S*-enantiomer and the *RS*-racemate. Moreover, it is worth mentioning the investigations by Adrjanowicz et al., which revealed that structural (α)-relaxation times, as well as diffusion of pure *S*-enantiomer and *RS*-racemate of ketoprofen (KTP), are very similar around the T_g.[36] Herein, one can also briefly refer to the studies on the chiral compound from a different group, i.e., *N*-acetyl-α-methylbenzylamine (strictly R(+) and S(−) enantiomers, conglomerates at various enantiomeric excesses (ee) and the racemic mixture (ee = 0%)). It was presented that also the time scales of α-relaxation (and other processes detected in BDS spectra, i.e., Debye, β, and γ), as

Received: January 27, 2024
Revised: March 23, 2024
Accepted: March 29, 2024
Published: April 12, 2024

ACS Publications
© 2024 The Authors. Published by American Chemical Society

https://doi.org/10.1021/acs.jpcb.4c00582
J. Phys. Chem. B 2024, 128, 4021−4032

Downloaded via 89.64.109.38 on March 11, 2025 at 14:21:21 (UTC).
See https://pubs.acs.org/sharingguidelines for options on how to legitimately share published articles.

well as their temperature dependences, are insensitive to chirality. However, factors such as glass-forming ability and the recrystallization of heterochiral arrangements turned out to be chirality-dependent.[37]

The behavior of the enantiomers and racemates was also studied at high pressure. It was shown that it is possible to separate pure enantiomers from the racemic mixture after crystallization of the latter systems in the liquid phase at high compression.[38−40] However, such an approach can be effective only when both chiral molecules are denser than the racemate.[41] The other interesting high-pressure studies on racemates (profens) were performed by Adrjanowicz et al.[26,36] They indicated that there is only a small difference in the structural dynamics of the *S*-enantiomer of KTP and the racemic (*RS*) mixture under various temperature and pressure conditions. As a consequence, the pressure coefficient of the glass-transition temperature (dT_g/dp = 0.193 and 0.200 K/MPa, respectively), as well as the activation volume of both systems, were almost the same.[36] Furthermore, isochronal crystallization (τ_α = const) at high pressure revealed that the *S*-enantiomer of KTP forms crystals much faster with respect to the racemic mixture.[36] A different scenario was noted in the case of IBP. Koperwas et al.[42] assigned the observed discrepancy (i.e., a greater slowing down of crystallization in the case of pure *S*-isomer compared to the racemate) to a distinct impact of compression on the solid−liquid interfacial free energy of both systems.

This review presents the results of structural, spectroscopic, thermal, and dielectric studies carried out at ambient and elevated pressure on *R*- and *S*-enantiomers of FLP and their racemic mixture. The purpose of these studies, supported by molecular dynamics (MD) simulations and density functional theory (DFT) computations, was to answer the question of whether there are differences in molecular organization via H-bonds in pure enantiomers and the racemate in the crystalline and supercooled liquid states. If so, what do they result for? Moreover, the intention was to verify if the atomic structure, thermal properties, and ambient and high-pressure molecular dynamics of neat *R*- and *S*-FLP are similar to those of *RS*-FLP.

2. EXPERIMENTAL SECTION

2.1. Materials. *R*- and *S*-FLP, as well as their racemic mixture (*RS*-FLP) with a purity higher than 98%, were supplied by MedChemExpress and Acros Organics Chemicals, respectively, and used without further purification.

2.2. Methods. *2.2.1. X-ray Diffraction (XRD).* XRD patterns of crystalline and molten FLP samples were collected on a Rigaku Denki D/Max Rapid II diffractometer equipped with a 2D image plate detector and a rotating Ag anode. Incident radiation was monochromatized, and the wavelength of the beam was $\lambda_{K_{\alpha1+\alpha2}}$ = 0.5608 Å. The temperature was controlled by an Oxford Cryostrem system. Samples were measured in borosilicate glass capillaries, and the background from the empty capillary was subtracted.

2.2.2. Fourier Transform Infrared (FTIR) Spectroscopy. FTIR spectra of crystalline samples of racemic and chiral forms of FLP were recorded with a Nicolet iS50 spectrometer (Thermo Scientific) equipped with an attenuated total reflectance (ATR) accessory in the 4000−400 cm^{-1} region at 293 K. They were obtained with 16 scans and a resolution of 4 cm^{-1}. The spectra were also collected on a Nicolet iS50 spectrometer coupled with a Pike GladiATR module at 403 K. The measurements were taken with 16 scans and a resolution of 2 cm^{-1} in the wavenumber range of 4000−400 cm^{-1}.

2.2.3. Differential Scanning Calorimetry (DSC). Calorimetric experiments were performed using a Mettler-Toledo DSC apparatus equipped with a liquid nitrogen cooling accessory and an HSS8 ceramic sensor with 120 thermocouples. The instrument was calibrated for temperature and enthalpy using indium and zinc standards. The samples were placed in sealed aluminum crucibles (40 μL), then heated above their melting temperatures, quenched, and scanned at the rate of 10 K/min well above the respective melting points.

2.2.4. Broadband Dielectric Spectroscopy (BDS). Isobaric measurements of the complex dielectric permittivity $\varepsilon^*(\omega) = \varepsilon'(\omega) - i\varepsilon''(\omega)$ (frequency range from 10^{-2} to 10^6 Hz) were performed using a Novocontrol α dielectric spectrometer equipped with α impedance analyzer with an active sample cell. The samples were placed in a parallel-plate cell made of stainless steel (diameter: 15 mm; gap: 0.1 mm with Teflon spacer), mounted inside a cryostat, and kept under dry nitrogen gas flow during measurements. The temperature control was provided by a Quatro cryosystem with temperature stability better than 0.1 K. Measurements were carried out after fast cooling the liquid to the glassy state and were done in the temperature range from 298 to 203 K.

For dielectric studies at elevated pressure, a high-*p* chamber with a special homemade flat parallel capacitor was used. Thin Teflon spacers were employed to maintain a fixed distance between the plates. Each sample capacitor was sealed and mounted inside a Teflon capsule to separate it from the silicon liquid (a pressure-transmitting medium). Pressure was measured using a Nova Swiss tensometric meter with a resolution of 1 MPa. In turn, the temperature was adjusted with a precision of 0.1 K by means of a refrigerated and heated Huber circulator. Measurements of complex dielectric permittivity were performed in the same frequency range as in the case of measurements carried out at p = 0.1 MPa. It should be noted that each dielectric experiment (including sample preparation) was repeated three times. For more detailed information about the BDS technique (both ambient and high-pressure studies), see refs 43−45

2.2.5. Molecular Dynamics (MD) Simulations. Molecular dynamics simulations were performed in the Gromacs 2023 package[46−50] using a Gromos 54a7[51] force field. The topology for both FLP molecules was created by an online automated topology builder (ATB).[52−54] Starting geometry was generated by Packmol.[55] In the case of the *S*-enantiomer, it was 500 *S*-FLP molecules, while in the case of the racemate, it was 250 of *S*- and 250 of *R*-molecules. After the initial geometry optimization, two subsequent equilibrating simulations were performed. They were carried out in the NPT (constant temperature, constant pressure) ensemble, where the v-rescale and c-rescale were used as thermostat and barostat, respectively. The pressure was set in both simulations to 1 bar, while the temperature was set to 400 K in the first simulation and 293 K in the second simulation. The final production run was done as a 10 ns simulation in the NPT ensemble with p = 1 bar and T = 293 K using the same type of thermal and pressure control. The analysis of the production runs was performed using the Travis package,[56−58] which enabled the provision of all needed RDFs, ADFs, and HB topologies. The histogram of the cluster sizes was obtained by the use of the Gromacs "clustsize" routine.

2.2.6. Density Functional Theory (DFT) Calculations. DFT computations were carried out in the ORCA 5.0.4 package.[59−63]

https://doi.org/10.1021/acs.jpcb.4c00582
J. Phys. Chem. B 2024, 128, 4021−4032

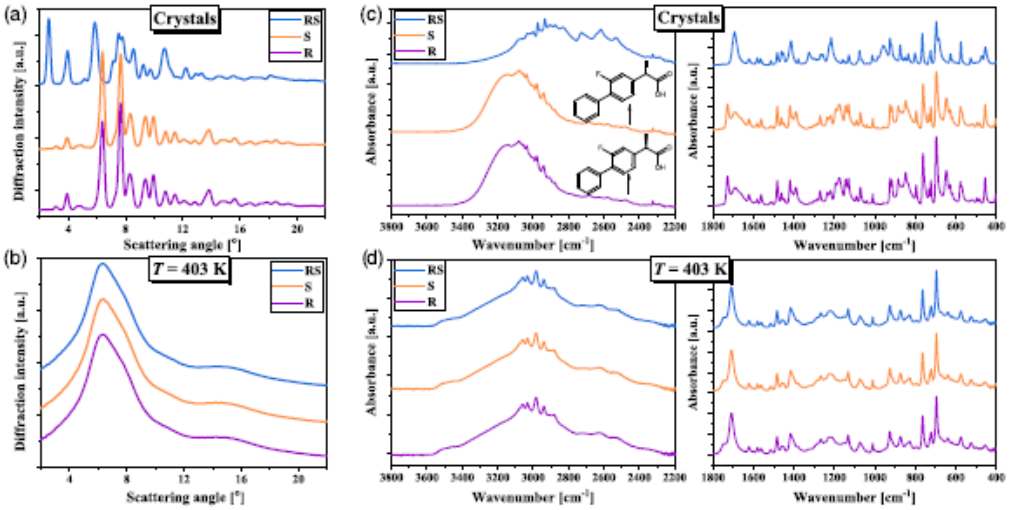

Figure 1. XRD patterns of racemic FLP and both (*R* and *S*) enantiomers in the (a) crystalline ($T = 293$ K) and (b) molten ($T = 403$ K) states. Panels (c, d) show the corresponding FTIR spectra of the same phases in the wavenumber region of 3800−400 cm^{-1}. In the insets of panel (c), the structures of *R*- and *S*-FLP are presented.

The starting geometry for calculating the *R*-*S* Π-stacking interaction was obtained from a cif file for the racemate. Then, the chirality of one molecule was changed by switching the H and OH group positions to form *S*−*S* Π-stacking interacting molecules. The geometry optimization was performed at the B97M-D4/6-31G(2d,2p) level of theory. The starting geometry of the dimers with linear HBs was created in a few steps. In the first step, the molecular dynamics algorithm in orca was employed to obtain 100 random dimeric structures by performing simulation at $T = 293$ K and saving xyz file after each 0.1 ps of simulation (where total time was 10 ps). All saved geometries were optimized in the xtb semiempirical method, and then, the 20 most energetically stable forms were optimized in the DFT method on the B97M-D4/6-31G(2d,2p) level of theory. The interaction energies were calculated as a difference between the energy of the optimized dimer and the sum of the energy of isolated molecules, according to the equation

$$E_{int} = E_T - \sum_{i=1}^{n} E_i \quad (1)$$

where E_{int} is the interaction energy, E_T is the total energy of the entire complex, and E_i is the energy of every isolated molecule forming the complex.

All of the energies were calculated at the B97/6-311G-(2df,2pd) level of theory using additional D4 corrections.

3. RESULTS AND DISCUSSION

The first stage of research was to characterize the atomic structure of the examined systems. According to previous studies, three polymorphic forms (I, II, and III) of *RS*-FLP have been reported. However, only the crystal structures of forms I and III have been solved.[64−66] In both polymorphs, the dimerization of enantiomers through the carboxylic acid group and a similar molecular conformation were recognized, except that in form III, the position of the F atom is disordered over two positions related by a 180° rotation of the F-substituted ring. Based on the diffraction pattern presented in Figure 1a, it was possible to identify the polymorphic form of crystalline racemic FLP as form I. It is characterized by triclinic *P*1 space group and unit cell parameters: 5.8164(2), 9.3136(4), 12.7480(5)Å, 73.136(4), 83.117(3), 72.982(4)° and is the thermodynamically stable form under ambient condition, and hence used in the clinic. In turn, the crystal structure of *R*- and *S*- enantiomers at the same conditions was identical but different from that of racemic FLP, which can be deduced from the following XRD patterns in Figure 1a. This crystal structure has also been reported for the *R*-isomer—as orthorhombic *P*212121 space group and unit cell lengths: 5.6535(3), 13.2097, 16.0709 (5)Å.[67] It was shown that in such crystal lattice, FLP molecules interacting via H-bonding create chains along the *a*-axis.[67,68] One can assume that an analogous structural motif occurs for the crystalline sample of the *S*-isomer based on a similar diffraction pattern. Thus, the main difference between the crystal structures of racemic mixture and *R*-, *S*-FLP may be related to the spatial organization of molecules and their interaction through H-bonds with neighboring molecules. In the case of the liquid structure upon melting, the diffraction patterns presented in Figure 1b did not exhibit apparent variations between the chiral and racemic forms.

The different spatial arrangement of the molecules in the crystalline lattice of racemate and pure enantiomers is also well captured in infrared spectra measured in a wide wavenumber range of 3800−400 cm^{-1} (please see Figure 1c). As can be seen, the spectra show the most significant differences in their band contours in the regions corresponding to the vibrations of the groups involved in the association process, i.e., stretching vibration of the H-bonded (HB) hydroxyl (ν_{O-H} 3500−3000 cm^{-1}), carbonyl ($\nu_{C=O}$ 1800−1640 cm^{-1}), carboxylic (ν_{C-O} 1280−1240 cm^{-1}), and aliphatic (ν_{C-H} 3000−2400 cm^{-1}) moieties as well as out-of-plane deformation of O−H group

https://doi.org/10.1021/acs.jpcb.4c00582
J. Phys. Chem. B 2024, 128, 4021−4032

(γ_{O-H} 980−930 cm^{-1}).[69] It should also be noted that the IR spectrum of racemic FLP exhibits a typical dimeric structure of the ν_{O-H} band consisting of the shorter-wave branch (3500−2750 cm^{-1}) of higher intensity and the longer-wave component (2750−2200 cm^{-1}) of lower intensity. In contrast, the ν_{O-H} band of *R*-FLP is essentially characterized by a single broad signal, shifted toward higher frequencies relative to *RS*-FLP. Moreover, in a lower wavenumber range of the *RS*-FLP spectrum, an intense and sharp peak at 1694 cm^{-1} due to the stretching vibration of the carbonyl group ($\nu_{C=O}$) is observed. On the other hand, the $\nu_{C=O}$ band of *R*- and *S*-FLP has a doublet structure consisting of two components (1728 and 1691 cm^{-1}). The peak at 1258 cm^{-1} in the infrared spectrum of the racemic FLP is assignable to the C−O stretching and C−O−H deformation vibrations, while for *R*- and *S*-FLP, no signal at this frequency occurs. Instead of that, a peak at 1270 cm^{-1} is detected. A broad, medium-intensity band due to out-of-plane O−H deformation in the *RS*-FLP spectrum can be observed at 957 cm^{-1}. In the case of both enantiomers, this peak has a very weak intensity.

As can be seen in Figure 1d, all of these spectral differences related to various spatial arrangements of the molecules in pure enantiomers and the racemate disappear after the sample's melting, and the spectra of the three examined systems are identical. Moreover, one can postulate that melting of *R*- or *S*-FLP destroys the chain-like arrangement of the molecules as the spectrum of liquid samples closely resembles that of the crystalline racemic FLP (Figure S1 in the Supporting Information). Thus, the broad structure and shape of the ν_{O-H} band after melting are maintained, and the positions of the peaks are similar to those in the racemic FLP crystals. Only the $\nu_{C=O}$ band is slightly shifted to the higher wavenumbers (1708 cm^{-1}) for molten samples relative to that in the crystalline *RS*-FLP (1694 cm^{-1}). This fact may suggest that the HB dimers, with a relatively similar geometry to those in the crystal lattice, exist in the liquid forms of studied *R*-, *S*-, and *RS*-FLP.

To verify the eventual differences or similarities in the phase transitions and thermal properties of the crystal and liquid samples, calorimetric measurements were performed. In Figure 2, DSC curves recorded on heating the crystalline (inset) and glassy (main panel) samples at the rate of 10 K/min are presented. As can be seen in the inset, there is one strong endothermic process at T = 384.6 K and T = 385.3 K for *R*- and *S*-enantiomer, respectively, as well as at T = 388.1 K for a racemate, related to the melting of the crystalline samples. It should be mentioned that the obtained values of the melting temperature (T_m) stay in good agreement with those published in the literature (T_m = 385 K for *S*-FLP[29] and T_m = 388 K for *RS*-FLP[70]). Further cooling without any sign of crystallization, followed by heating of the vitrified samples, reveals the presence of one visible glass transition as well as an exothermic peak at around 320 K (a racemate) or 325 K (both enantiomers), corresponding to the cold crystallization. Importantly, the glass-transition temperatures (T_g) of all examined samples are very similar (T_g = 267.9 ± 1.0, 268.1 ± 1.0, and 267.4 ± 1.0 K, for *R*-, *S*-, and *RS*-FLP, respectively). Moreover, the heat capacity jumps at the T_g are close to each other (ΔC_p = 0.373, 0.357, and 0.375 J g^{1-} K^{-1}, for *R*-, *S*-, and *RS*-FLP, respectively).

Subsequently, having the results of previous investigations in mind, the molecular dynamics of *R*-, *S*-, and *RS*-FLP at ambient and elevated pressure (p) conditions were followed using the BDS technique. Figure 3a−c presents dielectric loss spectra of all samples collected at p = 0.1 MPa and in a wide range of

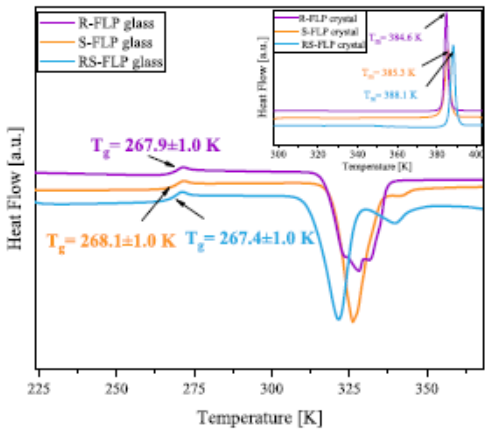

Figure 2. DSC thermograms obtained during heating of the crystalline (inset) and glassy (main panel) *R*-, *S*, and *RS*-FLP at a rate of 10 K/min. T_g values were determined as the midpoint of the heat capacity increment, while T_m values were obtained from the maximum of the endothermic peaks.

temperatures (T), both above and below the T_g. In the supercooled liquid phase ($T > T_g$), two characteristic processes can be identified in the spectra of pure FLP enantiomers and the racemic mixture. The first one, whose source is charge transport of ionic impurities, is the dc-conductivity (σ_{dc}), while the second one, located at higher frequencies (f), is a structural (α)-relaxation related to cooperative motions of all molecules in the examined samples. As illustrated, both processes shift toward lower values of f with a decreasing T. In turn, in the glassy state ($T < T_g$), one well-visible secondary relaxation, labeled β, is observed in dielectric loss spectra for all investigated systems.

To determine relaxation times of the structural (α) process, dielectric data collected at p = 0.1 MPa and $T > T_g$ were fitted using the Havriliak−Negami (HN) function[71]

$$\varepsilon(\varpi)^* = \frac{\sigma_{dc}}{\varepsilon_0 \varpi} + \mathrm{Im}\sum_{i=1}^{2}\left(\varepsilon_\infty + \frac{\Delta\varepsilon_i}{[1 + (i\varpi\tau_i)^{\alpha_i}]^{\beta_i}}\right) \quad (2)$$

where σ_{dc} is the dc-conductivity, ε_0 is the vacuum permittivity, ϖ is an angular frequency ($\varpi = 2\pi f$), ε_∞ is the high-frequency limit permittivity, $\Delta\varepsilon$ is the dielectric relaxation strength, τ is the HN relaxation times, and α and β are the shape parameters that represent the symmetric and asymmetric broadening of given relaxation peaks. Then, using the expression given in a book by Kremer and Schönhals,[43]

$$\tau_\alpha = \tau\left[\sin\left(\frac{\pi\alpha}{2 + 2\beta}\right)\right]^{-1/\alpha}\left[\sin\left(\frac{\pi\alpha\beta}{2 + 2\beta}\right)\right]^{1/\alpha} \quad (3)$$

τ_α have been recalculated from τ. To describe the T-dependencies of τ_α (see Figure S2 in the Supporting Information) at 0.1 MPa, the Vogel−Fulcher−Tammann (VFT) equation[72−74] was applied. Subsequently, based on the VFT fits, the T_g (defined as a T at which τ_α = 100 s) for pure enantiomers and the racemic mixture was estimated. It should be noted that the obtained values (T_g = 263.1 ± 1.0, 263.4 ± 1.0, and 261.9 ± 1.0 K for *R*-, *S*-, and *RS*-FLP, respectively) do not

https://doi.org/10.1021/acs.jpcb.4c00582
J. Phys. Chem. B 2024, 128, 4021−4032

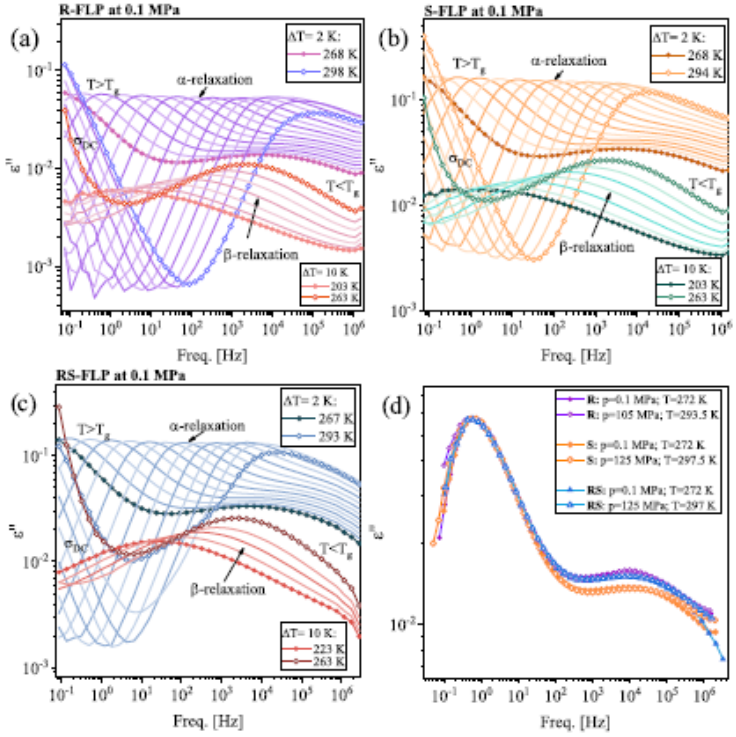

Figure 3. Dielectric loss spectra measured for *R*-FLP (a), *S*-FLP (b), and *RS*-FLP (c) at ambient pressure in a wide temperature range, above and below the T_g. A comparison of dielectric spectra obtained at different thermodynamic conditions (T, p), close to T_g, is shown for *R*, *S*, and *RS*-FLP (d). They were normalized with respect to the maximum of dielectric loss (ε''_{max}).

differ significantly from each other and are only a few Kelvins lower when compared to those estimated from the DSC technique (see Figure 2). At first sight, one can get the impression that the relaxation time at the vitrification point is different when we analyze dielectric and calorimetric data. However, it is a common observation reported in the literature for many systems that is predominantly related to a difference in the heating rates applied during both experiments.

Additionally, extensive high-pressure BDS investigations under isobaric and isothermal conditions were carried out. In Figure 4, representative dielectric loss spectra collected for pure enantiomers and a racemic FLP at constant p and various $T > T_g$ (panels a,c,e), as well as at constant T and indicated $p < p_g$, where p_g is a glass-transition pressure (panels b,d,f), are shown. Similar to the ambient pressure studies, except for the dc-conductivity, a structural (α)-relaxation peak (whose maximum moves toward lower f with decreasing T or increasing p), as well as one secondary (β)-relaxation, are observed in the spectra of all examined substances.

In Figure 3d, the normalized dielectric spectra measured for *R*-, *S*-FLP, and *RS*-FLP at ambient and high p, and T close to T_g (the maxima of α-peaks near 1 Hz) were compared. As can be seen, for all investigated samples, the position of α- and secondary (β)-relaxation peaks is the same at various combinations of T and p, which means the fulfillment of the isochronal α- and β-superpositioning (the rule, whose confirmation has been reported for many HB systems[75−78]). However, it can also be observed that for both FLP enantiomers, the left-hand side of α-dispersion broadens with compression, indicating the violation of the so-called temperature pressure superpositioning (TPS).[79] This effect is more pronounced for the *R*-isomer. Surprisingly, in the case of the racemic FLP, the TPS is satisfied (the width of the structural relaxation remains unchanged under various T and p conditions).

As the further part of the in-depth analysis of the molecular dynamics of *R*-, *S*-FLP, and *RS*-FLP, BDS data shown in Figure 4 were analyzed using the superposition of two HN functions (eq 2). Then, the obtained τ_α (also those determined from ambient-p experiments) were plotted as a function of T and p in Figure 5 and then analyzed with the use of the modified Avramov equation[80]

$$\tau_\alpha = \tau_{\infty} \exp\left[\ln(\tau_g/\tau_{\infty})\left(\frac{T_r}{T}\right)^{\alpha_0\left(1-\frac{C}{C_{p_0}}\ln\left(1+\frac{p}{\Pi}\right)\right)}\left(1+\frac{p}{\Pi}\right)^{\beta}\right] \tag{4}$$

where τ_∞ is a relaxation time at extremely high T, $\tau_g = \tau(T_g)$, T_r is a reference temperature lying close to the T_g, C_{p_0} is a specific heat capacity, C is an additional adjustable parameter, and Π is a

https://doi.org/10.1021/acs.jpcb.4c00582
J. Phys. Chem. B 2024, 128, 4021−4032

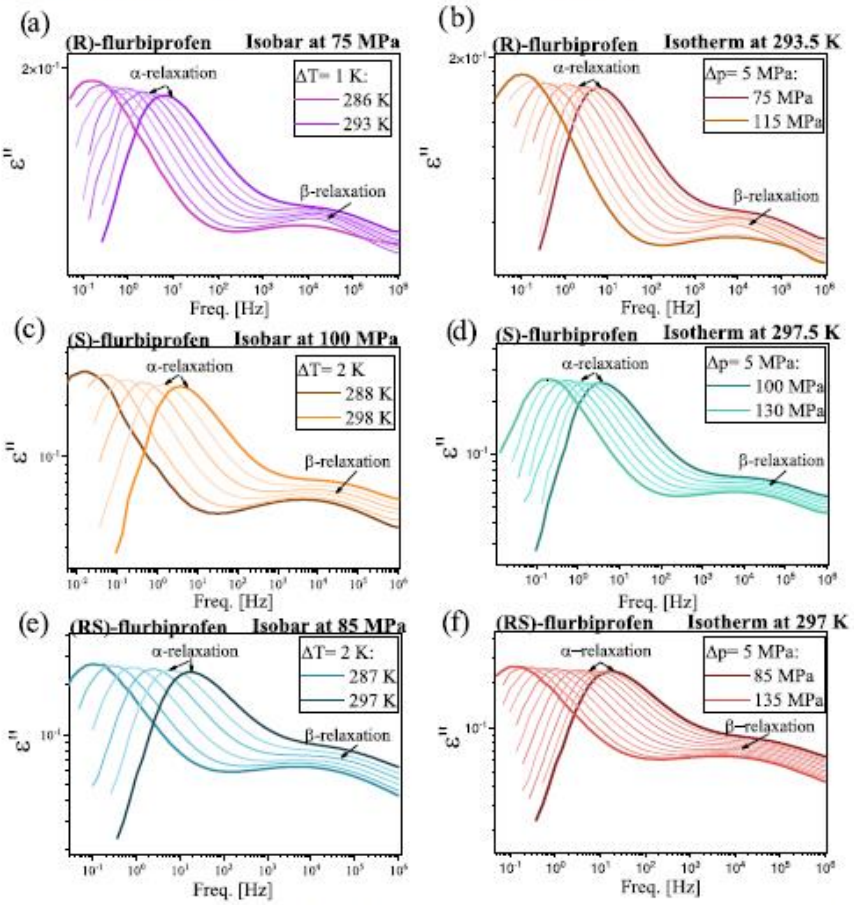

Figure 4. Representative dielectric loss spectra measured for *R*-, *S*-, and *RS*-FLP at isobaric (panels (a), (c), (e)) and isothermal (panels (b), (d), (f)) conditions.

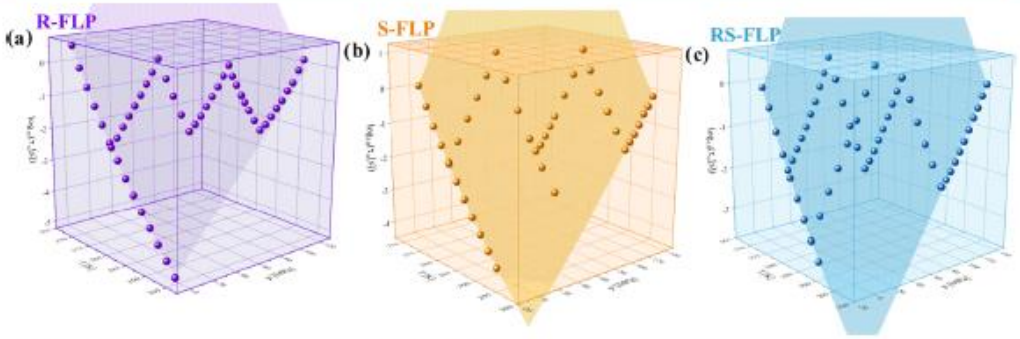

Figure 5. Structural relaxation times of *R*- (a), *S*- (b), and *RS*-FLP (c) plotted versus temperature (T) and pressure (p). Purple, orange, and blue areas represent surface fits to the modified Avramov eq (eq 4).

https://doi.org/10.1021/acs.jpcb.4c00582
J. Phys. Chem. B 2024, 128, 4021−4032

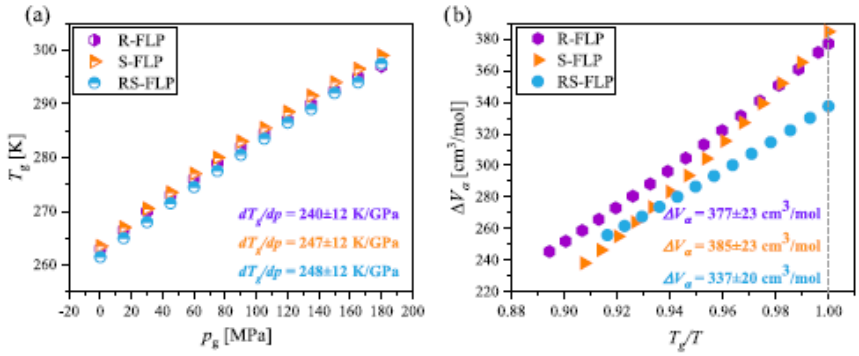

Figure 6. T_g plotted as a function of p_g (a). Dependence of the activation volume for the α-process (ΔV_α) versus T_g/T (b).

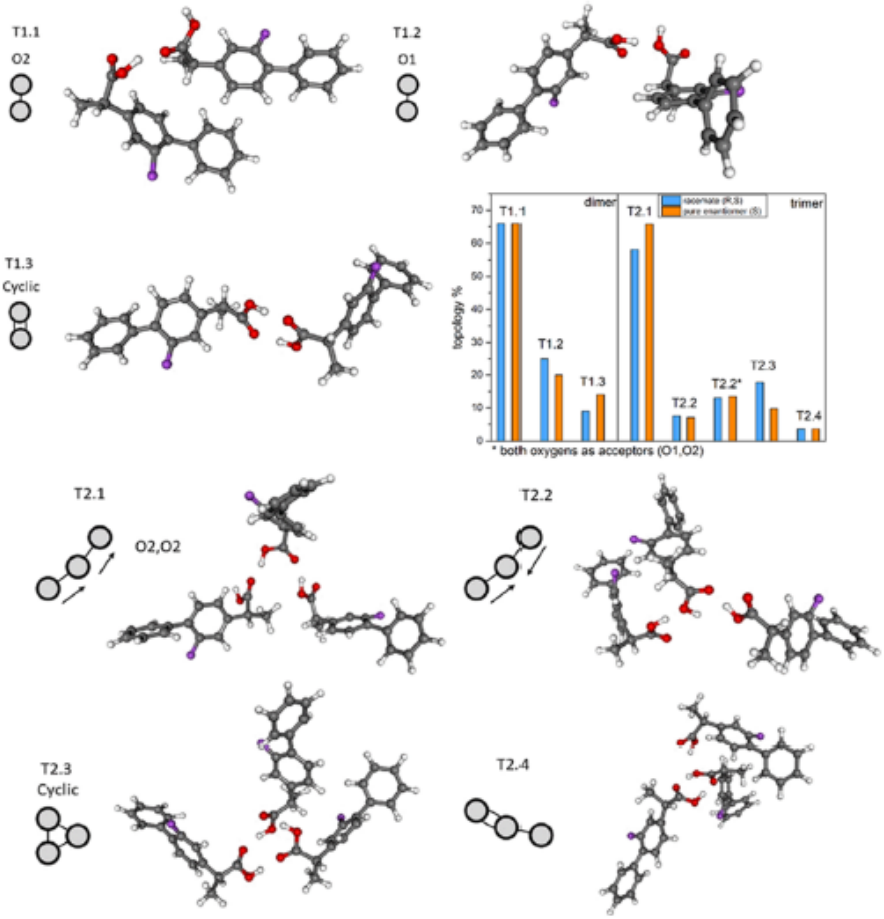

Figure 7. Topology of the most abundant H-bonds between two flurbiprofen molecules that can be found in the supercooled systems. T1.1, T1.2, and T1.3 are the most abundant dimer topologies, while T2.1−T2.4 are the most abundant trimer topologies.

https://doi.org/10.1021/acs.jpcb.4c00582
J. Phys. Chem. B 2024, 128, 4021−4032

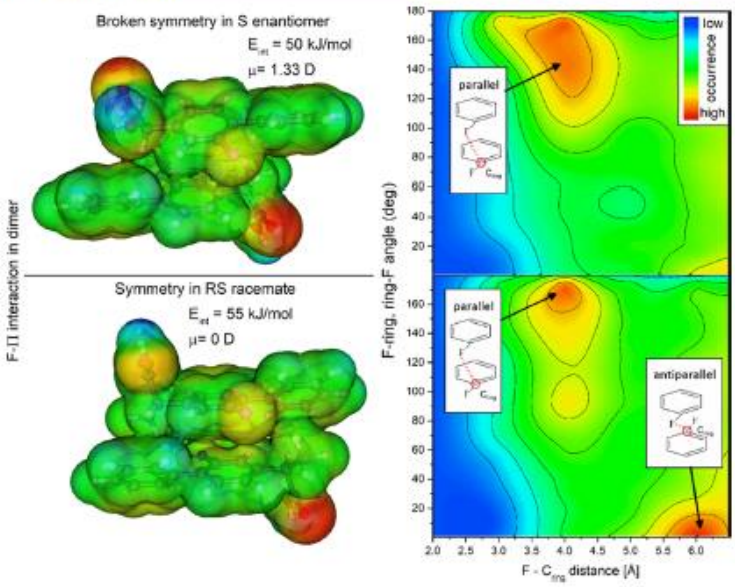

Figure 8. Visualization of the F−Π interactions in *RS*- and *S*-FLP systems. In the left panel, the geometry and electrostatic potential of R-S and S−S non-HB dimers are presented. In the right panel, RDF vs ADF 2D maps are illustrated to show the abundance of parallel and antiparallel Π-stacking formations.

constant with the dimension of pressure, while α_0 and β are exponential parameters defined as

$$\alpha_0 = \frac{2C_{p_0}}{ZR} \tag{5}$$

$$\beta = \frac{2\alpha_p V_m}{ZR}\Pi \tag{6}$$

where Z is the degeneracy of the system, α_p is a volume expansion coefficient at 0.1 MPa, and V_m is a molar volume. In Table S1 in the Supporting Information, the parameters of eq 4 determined from the global numerical fitting procedures (Figure 5) are presented.

Subsequently, two quantities, which define the sensitivity of the α-process to compression, i.e., the pressure coefficient of the glass-transition temperature (dT_g/dp) and the activation volume (ΔV_α), were estimated. To determine the former one, T_gs obtained for both enantiomers and the racemic FLP by applying the following expression proposed by Avramov[81]

$$T_g(p) = T_g(p_0)\left(1 + \frac{p}{\Pi}\right)^{\beta/\alpha_0\left(1-\frac{C}{C_{p0}}\left(\ln\left(1+\frac{p}{\Pi}\right)\right)\right)} \tag{7}$$

with the same values of the parameters C_{p_0}, Π, β, and α_0 as those appearing in eq 4, were presented as a function of pressure (Figure 6a). Interestingly, dT_g/dps obtained from this plot are almost the same for all examined systems ($dT_g/dp^{R\text{-}FLP} = 240 \pm 12$ K/GPa, $dT_g/dp^{S\text{-}FLP} = 247 \pm 12$, K/GPa, and $dT_g/dp^{RS\text{-}FLP} = 248 \pm 12$ K/GPa) and signify a high sensitivity of the structural relaxation to pressure. Note that somewhat lower values of this parameter have been previously reported for the two other APIs from the profens' group—ibuprofen ($dT_g/dp = 195$ K/GPa)[82] and ketoprofen ($dT_g/dp = 200$ K/GPa).[28]

On the other hand, ΔV_α for all examined systems (FLP enantiomers and the racemate), usually defined as[45]

$$\Delta V_\alpha = RT\left(\frac{d\ln \tau_\alpha}{dp}\right)_T \tag{8}$$

was determined at different T directly from the surface fit of the modified Avramov approach. The plot presenting ΔV_α versus T_g/T is shown in Figure 6b. Notably, the values of this parameter calculated for pure enantiomers at T_g ($T_g/T = 1$) were very close and equal to 377 ± 23 and 385 ± 23 cm^3/mol for *R*- and *S*-FLP. In turn, surprisingly, ΔV_α obtained for the racemic mixture is clearly lower ($\Delta V_\alpha = 337 \pm 20$ cm^3/mol) in comparison to the values obtained for both isomers. This unexpected variation in ΔV_α between pure FLP enantiomers and racemate indicates that the local spatial arrangement of the molecules in the liquid state of these systems may not be the same. Hence, some memory of the crystalline molecular arrangement, although not detectable with the experimental techniques applied in our studies, survived upon melting and in the vicinity of the T_g. To confirm this hypothesis, in-depth molecular dynamics (MD) simulations in the supercooled liquid state of *S*- and *RS*-FLP were performed.

The final simulations (after the initial equilibration) of FLP systems were taken at ambient pressure and a temperature of 293 K. The first analysis was related to the clusterization effect by H-bonds. It was found that hydrogen-bond-based clusters are more abundant in the enantiomeric system than in the racemate. Moreover, the difference in the total clusters, although noticeable, is relatively small. As presented in the histogram in Figure S3 in the Supporting Information, there is only a 0.5%

https://doi.org/10.1021/acs.jpcb.4c00582
J. Phys. Chem. B 2024, 128, 4021−4032

difference in the overall amount of HB clusters. Nevertheless, a more significant difference can be found in their distribution. In the case of the *S*-isomer, there is a higher population of low-molecular-weight clusters (dimer to tetramer). The percentage of low-molecular HB clusters (2−4 molecules) equals 56% in the enantiomer and 44% in the racemate.

In both systems, there is also a small population of cyclic dimers and trimers. As illustrated in Figure 7, showing the detailed topology of H-bonds, cyclic dimers constitute 13 and 9% of all dimers in the *S*-isomer and *RS*-racemate, respectively. In the case of trimers, more abundant cyclic structures occur in the racemic mixture (18% of all trimers in *RS* versus 9% of all trimers in the *S*-enantiomer).

Based on the data obtained from MD simulations, one can suppose that the higher activation volume obtained from dielectric investigations for the pure enantiomers with regard to the racemate is a manifestation of the difference in clusterization pattern and a higher population of the di-, tri-, and tetramers in the former systems. As a consequence of that, there is a larger average cluster size in the enantiomer. Having that in mind, one can ask the question, what is a driving force underlying the formation of extensive clusters in a pure isomer? To address this question, the OH···O hydrogen bond energy between *S*−*S* and *R*−*S* molecules was calculated. It was found that the interaction energies (E_{int}) between *S*−*S* and *R*−*S* molecules are similar. The obtained value was equal to 105 and 100 kJ/mol for the former and latter systems, respectively. The calculated E_{int} is unusually high if only a single OH···O hydrogen bond is considered. It became clear that the conformation of linearly H-bonded two FLP molecules has additional Π-stacking aromatic rings. Moreover, due to the fluorine (F) atom connected with the ring, the strength of such interaction can be higher because of the particular case of Π-stacking, i.e., F−Π interaction. As this was found to be a concurrent interaction with the H-bonds, MD simulations were analyzed to show possible differences in Π-stacking conformations. It was achieved by plotting 2D maps of the radial distribution function (RDF) of ring atoms versus the angular distribution function (ADF) of ring plane vectors. In the right panel of Figure 8, the 2D map of intermolecular RDF between F and C_{ring} (where C_{ring} is the ring atom connected with the F atom) versus the ADF between F−C_{ring} and F−C_{ring} vectors, indicating significant differences in the Π-stacked structures, are presented. As can be observed, there are two possible Π-stacking formations. The first one is when aromatic rings with fluorine atoms are parallel to each other. In this scenario, the angle on the map is close to 180°, and the distance between the F and C_{ring} atoms is approximately equal to 4 Å. The second possible arrangement is when both rings are antiparallel to each other. The angle on the map is then close to 0°, and the distance between F and C_{ring} is approximately equal to 6 Å. It is visible that in the case of the *RS*-racemate, both arrangements, i.e., ordered parallel and antiparallel structures, are abundant. For the *S*-enantiomer, only parallel structures are detected, but in this case, there is a broader angle distribution, which means that in these structures, rings are not so well parallel aligned. This finding corresponds very well with the crystalline patterns of the *R*-*S* and *S*−*S* structures. The antiparallel alignment found in the racemate is the precursor of the F−Π interacting conformation, which can be easily found in the unit cell of triclinic *R*-*S* crystals (see Figure S4 in the Supporting Information for details). In the left panel of Figure 8, two structures of *R*-*S* and *S*-*S* dimers bonded exclusively by Π-stacking forces are shown. These structures were optimized by the density functional theory (DFT) method and presented as electron density with mapped electrostatic potential on their surface. The *R*-*S* unit is the same as that found in the crystal cell. The *S*-*S* unit was optimized from the initial *R*-*S* structure after switching the chirality of the asymmetric carbon in one molecule. As one can see, the *R*-*S* structure is perfectly symmetric, which is manifested in the zero dipole moment ($\mu = 0$ D). In the case of the *S*-*S* conformation, there are visible distortions in the charge distribution and its symmetry. The dipole moment of *S*-*S* molecules is equal to 1.33 D. The F−Π stacking energy is equal to 55 and 50 kJ/mol in *R*-*S* and *S*-*S* systems, respectively. Therefore, in the case of *S*-FLP, as the enantiomeric molecules are unable to form symmetric F−Π structures, the system is dominated more by H-bonds, which further leads to the different crystalline structure (an orthorhombic structure in the case of the *S*-enantiomer). Moreover, as it was found that the energy of F−Π interaction is comparable to OH···O hydrogen bond, the bonding energy of linear dimer, where there are contributions of both types of interactions, is comparable to the bonding energy of cyclic dimer. This is the reason why both supercooled systems are dominated by the linear HB clusters and not seemingly more stable cyclic dimers.

4. CONCLUSIONS

To summarize, the studies indicated much different molecular organization via H-bonds in pure enantiomers (long chains) and racemate (cyclic dimers) in the crystalline samples of flurbiprofen. However, once the crystalline lattice is destroyed, these differences vanish, as can be deduced from the experimental data. According to the collected diffractograms, thermograms, infrared, and dielectric spectra, enantiomers have properties identical with those of the racemate. However, a deeper analysis of dielectric data revealed an unexpected variation in the activation volume, which may be related to changes in the local molecular arrangement of these compounds. In fact, MD simulations confirmed this supposition, indicating a higher population of smaller supramolecular clusters in *S*-FLP with regard to the *RS*-FLP. Finally, it was also found that there are very specific and enormously strong F−Π interactions in the studied systems that may control local molecular arrangement in the crystalline and supercooled samples. The presented data contribute to a better understanding of the correlation among the structure, intermolecular interactions, and basic physical properties of the enantiomers and racemates.

■ ASSOCIATED CONTENT

Supporting Information

The Supporting Information is available free of charge at https://pubs.acs.org/doi/10.1021/acs.jpcb.4c00582.

Comparison of FTIR spectra of crystalline and molten *RS*-FLP, relaxation map for FLP enantiomers, and a racemate obtained from the analysis of ambient pressure BDS data, parameters of the modified Avramov eq (eq 4), as well as additional outcomes of MD simulations and DFT calculations (PDF)

■ AUTHOR INFORMATION

Corresponding Authors

Paulina Jesionek − *Institute of Chemistry, Faculty of Science and Technology, University of Silesia in Katowice, 40-007 Katowice, Poland; Department of Pharmacognosy and Phytochemistry, Faculty of Pharmaceutical Sciences in*

Sosnowiec, Medical University of Silesia in Katowice, 41-200 Sosnowiec, Poland; Email: paulina.jesionek@us.edu.pl

Ewa Kamińska – *Department of Pharmacognosy and Phytochemistry, Faculty of Pharmaceutical Sciences in Sosnowiec, Medical University of Silesia in Katowice, 41-200 Sosnowiec, Poland*; orcid.org/0000-0001-9725-8654; Email: ekaminska@sum.edu.pl

Authors

Barbara Hachula – *Institute of Chemistry, Faculty of Science and Technology, University of Silesia in Katowice, 40-007 Katowice, Poland*; orcid.org/0000-0001-9886-1076

Karolina Jurkiewicz – *Institute of Physics, Faculty of Science and Technology, University of Silesia in Katowice, 41-500 Chorzow, Poland*; orcid.org/0000-0002-4289-7827

Patryk Wlodarczyk – *Łukasiewicz Research Network - Institute of Non-Ferrous Metals, 44-100 Gliwice, Poland*

Marek Hreczka – *Łukasiewicz Research Network - Institute of Non-Ferrous Metals, 44-100 Gliwice, Poland; Department of Mechatronics, Silesian University of Technology, 44-100 Gliwice, Poland*

Kamil Kamiński – *Institute of Physics, Faculty of Science and Technology, University of Silesia in Katowice, 41-500 Chorzow, Poland*; orcid.org/0000-0002-5871-0203

Complete contact information is available at: https://pubs.acs.org/10.1021/acs.jpcb.4c00582

Notes

The authors declare no competing financial interest.

■ ACKNOWLEDGMENTS

This research was funded in whole by the National Science Centre (Poland), grant number: Opus 21 No. 2021/41/B/NZ7/01654. For the purpose of open access, the author has applied a CC-BY public copyright license to any author accepted manuscript (AAM) version arising from this submission.

■ REFERENCES

(1) Naaman, R.; Paltiel, Y.; Waldeck, D. H. Chiral Induced Spin Selectivity and Its Implications for Biological Functions. *Annu. Rev. Biophys.* **2022**, *51*, 99−114.

(2) Zhao, X.; Zang, S. Q.; Chen, X. Stereospecific Interactions between Chiral Inorganic Nanomaterials and Biological Systems. *Chem. Soc. Rev.* **2020**, *49*, 2481−2503.

(3) Michaeli, K.; Naaman, R. Origin of Spin-Dependent Tunneling Through Chiral Molecules. *J. Phys. Chem. C* **2019**, *123*, 17043−17048.

(4) Naaman, R.; Paltiel, Y.; Waldeck, D. H. Chiral Molecules and the Electron Spin. *Nat. Rev. Chem.* **2019**, *3*, 250−260.

(5) Greenfield, J. L.; Wade, J.; Brandt, J. R.; Shi, X.; Penfold, T. J.; Fuchter, M. J. Pathways to Increase the Dissymmetry in the Interaction of Chiral Light and Chiral Molecules. *Chem. Sci.* **2021**, *12*, 8589−8602.

(6) Muñoz, J.; González-Campo, A.; Riba-Moliner, M.; Baeza, M.; Mas-Torrent, M. Chiral Magnetic-Nanobiofluids for Rapid Electrochemical Screening of Enantiomers at a Magneto Nanocomposite Graphene-Paste Electrode. *Biosens. Bioelectron.* **2018**, *105*, 95−102.

(7) Fernández-García, J. M.; Evans, P. J.; Filippone, S.; Herranz, M. Á.; Martín, N. Chiral Molecular Carbon Nanostructures. *Acc. Chem. Res.* **2019**, *52*, 1565−1574.

(8) Abram, M.; Jakubiec, M.; Kamiński, K. Chirality as an Important Factor for the Development of New Antiepileptic Drugs. *ChemMedChem* **2019**, *14*, 1744−1761.

(9) Ribeiro, A. R.; Castro, P. M. L.; Tiritan, M. E. Chiral Pharmaceuticals in the Environment. *Environ. Chem. Lett.* **2012**, *10*, 239−253.

(10) Higuchi, A.; Tamai, M.; Ko, Y.-A.; Tagawa, Y.-I.; Wu, Y.-H.; Freeman, B. D.; Bing, J.-T.; Chang, Y.; Ling, Q.-D. Polymeric Membranes for Chiral Separation of Pharmaceuticals and Chemicals. *Polym. Rev.* **2010**, *50*, 113−143.

(11) Coquerel, G.; Tamura, R. "Enantiomeric Disorder" Pharmaceutically Oriented. *Disord. Pharm. Mater.* **2016**, 135−160.

(12) Tokunaga, E.; Yamamoto, T.; Ito, E.; Shibata, N. Understanding the Thalidomide Chirality in Biological Processes by the Self-Disproportionation of Enantiomers. *Sci. Rep.* **2018**, *8*, No. 17131.

(13) Blaschke, G.; Kraft, H. P.; Fickentscher, K.; Köhler, F. Chromatographic separation of racemic thalidomide and teratogenic activity of its enantiomers (author's transl). *Arzneimittel-forschung* **1979**, *29*, 1640−1642.

(14) Rulcova, A.; Prokopova, I.; Krausova, L.; Bitman, M.; Vrzal, R.; Dvorak, Z.; Blahos, J.; Pavek, P. Stereoselective Interactions of Warfarin Enantiomers with the Pregnane X Nuclear Receptor in Gene Regulation of Major Drug-Metabolizing Cytochrome P450 Enzymes. *J. Thromb. Haemostasis* **2010**, *8*, 2708−2717.

(15) Miyazaki, K.; Kaiho, F.; Inagaki, A.; Dohi, M.; Hazemoto, N.; Haga, M.; Hara, H.; Kato, Y. Enantiomeric Difference in Percutaneous Penetration of Propranolol Through Rat Excised Skin. *Chem. Pharm. Bull.* **1992**, *40*, 1075−1076.

(16) Kamalzadeh, Z.; Babanezhad, E.; Ghaffari, S.; Mohseni Ezhiyeh, A.; Mohammadnejad, M.; Naghibfar, M.; Bararjanian, M.; Attar, H. Determination of Bortezomib in API Samples Using HPLC: Assessment of Enantiomeric and Diastereomeric Impurities. *J. Chromatogr. Sci.* **2017**, *55*, 697−705.

(17) Kakumanu, V. K.; Arora, V.; Bansal, A. K. Investigation on Physicochemical and Biological Differences of Cefpodoxime Proxetil Enantiomers. *Eur. J. Pharm. Biopharm.* **2006**, *64*, 255−259.

(18) Waldeck, B. Biological Significance of the Enantiomeric Purity of Drugs. *Chirality* **1993**, *5*, 350−355.

(19) Younes, A. A.; Ates, H.; Mangelings, D.; Heyden, Y. V. A Separation Strategy Combining Three HPLC Modes and Polysaccharide-Based Chiral Stationary Phases. *J. Pharm. Biomed. Anal.* **2013**, *75*, 74−85.

(20) Ward, T. J.; Ward, K. D. Chiral Separations: A Review of Current Topics and Trends. *Anal. Chem.* **2012**, *84*, 626−635.

(21) Younes, A. A.; Mangelings, D.; Heyden, Y. V. Chiral Separations in Normal-Phase Liquid Chromatography: Enantioselectivity of Recently Commercialized Polysaccharide-Based Selectors. Part II. Optimization of Enantioselectivity. *J. Pharm. Biomed. Anal.* **2011**, *56*, 521−537.

(22) Thunberg, L.; Hashemi, J.; Andersson, S. Comparative Study of Coated and Immobilized Polysaccharide-Based Chiral Stationary Phases and Their Applicability in the Resolution of Enantiomers. *J. Chromatogr. B* **2008**, *875*, 72−80.

(23) Phadnis, N. V.; Suryanarayanan, R. Simultaneous Quantification of an Enantiomer and the Racemic Compound of Ibuprofen by X-Ray Powder Diffractometry. *Pharm. Res.* **1997**, *14*, 1176−1180.

(24) Yuan, X.; Li, X.; Guo, P.; Xiong, Z.; Zhao, L. Simultaneous Enantiomeric Analysis of Chiral Non-Steroidal Anti-Inflammatory Drugs in Water, River Sediment, and Sludge Using Chiral Liquid Chromatography-Tandem Mass Spectrometry. *Anal. Methods* **2018**, *10*, 4404−4413.

(25) Caldwell, J.; Hutt, A. J.; Fournel-Gigleux, S. The Metabolic Chiral Inversion and Dispositional Enantioselectivity of the 2-Arylpropionic Acids and Their Biological Consequences. *Biochem. Pharmacol.* **1988**, *37*, 105−114.

(26) Adrjanowicz, K.; Kaminski, K.; Paluch, M.; Niss, K. Crystallization Behavior and Relaxation Dynamics of Supercooled S-Ketoprofen and the Racemic Mixture along an Isochrone. *Cryst. Growth Des.* **2015**, *15*, 3257−3263.

(27) Hachula, B. The Nature of Hydrogen-Bonding Interactions in Nonsteroidal Anti-Inflammatory Drugs Revealed by Polarized IR Spectroscopy. *Spectrochim. Acta, Part A* **2018**, *188*, 189−196.

(28) Cao, S.; Zhou, Y.; Ma, Q.; Zhang, J.; Wang, Z. Experimental and Computational Studies of Enantioseparation of Three Profen Enantiomers with a Focus on Quantification of the Enantiomeric

Impurities Present in the Corresponding Enantiopure S-Profen Drugs. *J. Chromatogr. A* **2022**, *1673*, No. 463095.
(29) Rodrigues, A. C.; Viciosa, M. T.; Danède, F.; Affouard, F.; Correia, N. T. Molecular Mobility of Amorphous S-Flurbiprofen: A Dielectric Relaxation Spectroscopy Approach. *Mol. Pharmaceutics* **2014**, *11*, 112−130.
(30) Rigoni, L.; Venti, S.; Bevilacqua, M.; Bucci, R.; Magrì, A. D.; Magrì, A. L.; Marini, F. Quantification of the Enantiomeric Excess of Two APIs by Means of near Infrared Spectroscopy and Chemometrics. *Chemom. Intell. Lab. Syst.* **2014**, *133*, 149−156.
(31) Hao, H.; Wang, G.; Sun, J. Enantioselective Pharmacokinetics of Ibuprofen and Involved Mechanisms. *Drug Metab. Rev.* **2005**, *37*, 215−234.
(32) Sonawane, H. R.; Bellur, N. S.; Kulkarni, D. G.; Ayyangar, N. R. Photochemical Rearrangement of α-Chloro-Propiophenones to α-Arylpropanoic Acids: Studies on Chirality Transfer and Synthesis of (S)-(+)-Ibuprofen and (S)-(+)-Ketoprofen. *Tetrahedron* **1994**, *50*, 1243−1260.
(33) Caballo, C.; Sicilia, M. D.; Rubio, S. Enantioselective Determination of Representative Profens in Wastewater by a Single-Step Sample Treatment and Chiral Liquid Chromatography−Tandem Mass Spectrometry. *Talanta* **2015**, *134*, 325−332.
(34) Ottou Abe, M. T.; Viciosa, M. T.; Correia, N. T.; Affouard, F. Impact of Chirality on Peculiar Ibuprofen Molecular Dynamics: Hydrogen Bonding Organization and Syn vs. Anti Carboxylic Group Conformations. *Phys. Chem. Chem. Phys.* **2018**, *20*, 29528−29538.
(35) Emel'Yanenko, V. N.; Stange, P.; Feder-Kubis, J.; Verevkin, S. P.; Ludwig, R. Dissecting Intermolecular Interactions in the Condensed Phase of Ibuprofen and Related Compounds: The Specific Role and Quantification of Hydrogen Bonding and Dispersion Forces. *Phys. Chem. Chem. Phys.* **2020**, *22*, 4896−4904.
(36) Adrjanowicz, K.; Kaminski, K.; Tarnacka, M.; Szutkowski, K.; Popenda, L.; Bartkowiak, G.; Paluch, M. The Effect of Hydrogen Bonding Propensity and Enantiomeric Composition on the Dynamics of Supercooled Ketoprofen - Dielectric, Rheological and NMR Studies. *Phys. Chem. Chem. Phys.* **2016**, *18*, 10585−10593.
(37) Atawa, B.; Couvrat, N.; Affouard, F.; Correia, N. T.; Coquerel, G.; Saiter-Fourcin, A. Impact of Chirality on the Amorphous State of Conglomerate Forming Systems: A Case Study of N-Acetyl-α-Methylbenzylamine. *Phys. Chem. Chem. Phys.* **2021**, *23*, 24282−24293.
(38) Roszak, K.; Katrusiak, A. High-Pressure Crystallization and Thermodynamic Stability Study on the Resolution of High-Density Enantiomers from Low-Density Racemates. *Org. Lett.* **2023**, *25*, 37−41.
(39) Rietveld, I. B.; Barrio, M.; Tamarit, J.-L.; Do, B.; Céolin, R. Enantiomer Resolution by Pressure Increase: Inferences from Experimental and Topological Results for the Binary Enantiomer System (R)- and (S)-Mandelic Acid. *J. Phys. Chem. B* **2011**, *115*, 14698−14703.
(40) Ostrowska, K.; Kropidłowska, M.; Katrusiak, A. High-Pressure Crystallization and Structural Transformations in Compressed R,S-Ibuprofen. *Cryst. Growth Des.* **2015**, *15*, 1512−1517.
(41) Jacques, J.; Collet, A.; Wilen, S. H. *Enantiomers, Racemates, and Resolutions*; Wiley: New York, 1981.
(42) Koperwas, K.; Tu, W.; Affouard, F.; Adrjanowicz, K.; Kaskosz, F.; Paluch, M. Pressure Dependence of the Crystallization Rate for the S-Enantiomer and a Racemic Mixture of Ibuprofen. *Cryst. Growth Des.* **2021**, *21*, 7075−7086.
(43) Kremer, F.; Schönhals, A. *Broadband Dielectric Spectroscopy*; Springer: Berlin, 2003.
(44) Roland, C. M.; Hensel-Bielowka, S.; Paluch, M.; Casalini, R. Supercooled Dynamics of Glass-Forming Liquids and Polymers under Hydrostatic Pressure. *Rep. Prog. Phys.* **2005**, *68*, 1405−1478.
(45) Floudas, G.; Paluch, M.; Ngai, K. *Molecular Dynamics of Glass-Forming Systems: Effects of Pressure*; Springer: Berlin, 2011.
(46) Bekker, H.; Berendsen, H. J. C.; Dijkstra, E. J.; Achterop, S.; Vondrumen, R.; Vanderspoel, D.; Sijbers, A.; Keegstra, H.; Renardus, M. K. R. *GROMACS - a Parallel Computer for Molecular-Dynamics Simulations*; World Scientific Publishing: Singapore, 1993.
(47) Lindahl, E.; Hess, B.; van der Spoel, D. GROMACS 3.0: A Package for Molecular Simulation and Trajectory Analysis. *J. Mol. Model.* **2001**, *7*, 306−317.
(48) Van Der Spoel, D.; Lindahl, E.; Hess, B.; Groenhof, G.; Mark, A. E.; Berendsen, H. J. C. GROMACS: Fast, Flexible, and Free. *J. Comput. Chem.* **2005**, *26*, 1701−1718.
(49) Hess, B.; Kutzner, C.; van der Spoel, D.; Lindahl, E. GROMACS 4: Algorithms for Highly Efficient, Load-Balanced, and Scalable Molecular Simulation. *J. Chem. Theory Comput.* **2008**, *4*, 435−447.
(50) Abraham, M. J.; Murtola, T.; Schulz, R.; Páll, S.; Smith, J. C.; Hess, B.; Lindahl, E. GROMACS: High Performance Molecular Simulations through Multi-Level Parallelism from Laptops to Supercomputers. *SoftwareX* **2015**, *1−2*, 19−25.
(51) Schmid, N.; Eichenberger, A. P.; Choutko, A.; Riniker, S.; Winger, M.; Mark, A. E.; van Gunsteren, W. F. Definition and Testing of the GROMOS Force-Field Versions 54A7 and 54B7. *Eur. Biophys. J.* **2011**, *40*, 843−856.
(52) Malde, A. K.; Zuo, L.; Breeze, M.; Stroet, M.; Poger, D.; Nair, P. C.; Oostenbrink, C.; Mark, A. E. An Automated Force Field Topology Builder (ATB) and Repository: Version 1.0. *J. Chem. Theory Comput.* **2011**, *7*, 4026−4037.
(53) Canzar, S.; El-Kebir, M.; Pool, R.; Elbassioni, K.; Malde, A. K.; Mark, A. E.; Geerke, D. P.; Stougie, L.; Klau, G. W. Charge Group Partitioning in Biomolecular Simulation. *J. Comput. Biol.* **2013**, *20*, 188−198.
(54) Koziara, K. B.; Stroet, M.; Malde, A. K.; Mark, A. E. Testing and Validation of the Automated Topology Builder (ATB) Version 2.0: Prediction of Hydration Free Enthalpies. *J. Comput.-Aided Mol. Des.* **2014**, *28*, 221−233.
(55) Martinez, L.; Andrade, R.; Birgin, E. G.; Martinez, J. M. PACKMOL: A Package for Building Initial Configurations for Molecular Dynamics Simulations. *J. Comput. Chem.* **2009**, *30*, 2157−2164.
(56) Brehm, M.; Thomas, M.; Gehrke, S.; Kirchner, B. TRAVIS—A Free Analyzer for Trajectories from Molecular Simulation. *J. Chem. Phys.* **2020**, *152*, No. 164105.
(57) Brehm, M.; Kirchner, B. TRAVIS - A Free Analyzer and Visualizer for Monte Carlo and Molecular Dynamics Trajectories. *J. Chem. Inf. Model.* **2011**, *51*, 2007−2023.
(58) Hollóczki, O.; Macchiagodena, M.; Weber, H.; Thomas, M.; Brehm, M.; Stark, A.; Russina, O.; Triolo, A.; Kirchner, B. Triphilic Ionic-Liquid Mixtures: Fluorinated and Non-Fluorinated Aprotic Ionic-Liquid Mixtures. *ChemPhysChem* **2015**, *16*, 3325−3333.
(59) Grimme, S. Density functional theory with London dispersion corrections. *WIREs Comput. Mol. Sci.* **2011**, *1*, 211−228.
(60) Neese, F. The ORCA Program System. *WIREs Comput. Mol. Sci.* **2012**, *2*, 73−78.
(61) Neese, F. Software Update: The ORCA Program System, Version 4.0. *WIREs Comput. Mol. Sci.* **2018**, *8*, No. e1327.
(62) Neese, F. Software Update: The ORCA Program System—Version 5.0. *WIREs Comput. Mol. Sci.* **2022**, *12*, No. e1606.
(63) Bannwarth, C.; Caldeweyher, E.; Ehlert, S.; Hansen, A.; Pracht, P.; Seibert, J.; Spicher, S.; Grimme, S. Extended Tight-Binding Quantum Chemistry Methods. *WIREs Comput. Mol. Sci.* **2021**, *11*, No. e1493.
(64) Betlejewska-Kielak, K.; Bednarek, E.; Budzianowski, A.; Michalska, K.; Maurin, J. K. Comprehensive Characterisation of the Flurbiprofen/β-Cyclodextrin Inclusion Complex Using X-Ray Techniques and NMR Spectroscopy. *J. Mol. Struct.* **2023**, *1285*, No. 135450.
(65) Tian, B.; Feng, Y.; Li, X.; Yang, J.; Ding, Z.; Huang, X.; Yin, Q.; Xie, C.; Hao, H. Solution Thermodynamic Properties of Flurbiprofen in Twelve Solvents from 283.15 to 323.15 K. *J. Mol. Liq.* **2019**, *296*, No. 111744.
(66) Grzesiak, A. L.; Matzger, A. J. New Form Discovery for the Analgesics Flurbiprofen and Sulindac Facilitated by Polymer-induced Heteronucleation. *J. Pharm. Sci.* **2007**, *96*, 2978−2986.
(67) Tumanova, N.; Tumanov, N.; Robeyns, K.; Fischer, F.; Fusaro, L.; Morelle, F.; Ban, V.; Hautier, G.; Filinchuk, Y.; Wouters, J.; et al. Opening Pandora's Box: Chirality, Polymorphism, and Stoichiometric

Diversity in Flurbiprofen/Proline Cocrystals. *Cryst. Growth Des.* **2018**, *18*, 954−961.
(68) Liu, D.; Liu, Z.-R.; Wang, Z.-H.; Ma, C.; Herbert, S.; Schirok, H.; Mei, T.-S. Paired Electrolysis-Enabled Nickel-Catalyzed Enantioselective Reductive Cross-Coupling between α-Chloroesters and Aryl Bromides. *Nat. Commun.* **2022**, *13*, No. 7318.
(69) Sagdinc, S.; Pir, H. Spectroscopic and DFT Studies of Flurbiprofen as Dimer and Its Cu(II) and Hg(II) Complexes. *Spectrochim. Acta, Part A* **2009**, *73*, 181−194.
(70) Essa, E. A.; Elmarakby, A. O.; Donia, A. M. A.; El Maghraby, G. M. Controlled Precipitation for Enhanced Dissolution Rate of Flurbiprofen: Development of Rapidly Disintegrating Tablets. *Drug Dev. Ind. Pharm.* **2017**, *43*, 1430−1439.
(71) Havriliak, S.; Negami, S. A Complex Plane Analysis of α-Dispersions in Some Polymer Systems. *J. Polym. Sci., Part C: Polym. Symp.* **1966**, *14*, 99−117.
(72) Vogel, H. Das Temperaturabhangigkeitsgesetz Der Viskositat von Flussigkeiten. *Phys. Z.* **1921**, *22*, 645−646.
(73) Fulcher, G. S. Analysis of Recent Measurements of the Viscosity of Glasses. *J. Am. Ceram. Soc.* **1925**, *8*, 339−355.
(74) Tammann, G. A.; Hesse, W. Die Abhängigkeit Der Viscosität von Der Temperatur Bie Unterkühlten Flüssigkeiten. *Z. Anorg. Allg. Chem.* **1926**, *156*, 245−257.
(75) Ngai, K. L.; Wang, L.-M. Relations between the Structural α-Relaxation and the Johari−Goldstein β-Relaxation in Two Monohydroxyl Alcohols: 1-Propanol and 5-Methyl-2-Hexanol. *J. Phys. Chem. B* **2019**, *123*, 714−719.
(76) Wojnarowska, Z.; Adrjanowicz, K.; Wlodarczyk, P.; Kaminska, E.; Kaminski, K.; Grzybowska, K.; Wrzalik, R.; Paluch, M.; Ngai, K. L. Broadband Dielectric Relaxation Study at Ambient and Elevated Pressure of Molecular Dynamics of Pharmaceutical: Indomethacin. *J. Phys. Chem. B* **2009**, *113*, 12536−12545.
(77) Ngai, K. L.; Casalini, R.; Capaccioli, S.; Paluch, M.; Roland, C. M. Do Theories of the Glass Transition, in Which the Structural Relaxation Time Does Not Define the Dispersion of the Structural Relaxation, Need Revision? *J. Phys. Chem. B* **2005**, *109*, 17356−17360.
(78) Adrjanowicz, K.; Pionteck, J.; Paluch, M. Isochronal Superposition and Density Scaling of the Intermolecular Dynamics in Glass-Forming Liquids with Varying Hydrogen Bonding Propensity. *RSC Adv.* **2016**, *6*, 49370−49375.
(79) Jesionek, P.; Heczko, D.; Hachula, B.; Kamiński, K.; Kamińska, E. High-Pressure Studies in the Supercooled and Glassy State of the Strongly Associated Active Pharmaceutical Ingredient—Ticagrelor. *Sci. Rep.* **2023**, *13*, No. 8890.
(80) Avramov, I. Pressure Dependence of Viscosity of Glassforming Melts. *J. Non-Cryst. Solids* **2000**, *262*, 258−263.
(81) Avramov, I. Pressure and Temperature Dependence of Viscosity of Glassforming and of Geoscientifically Relevant Systems. *J. Volcanol. Geotherm. Res.* **2007**, *160*, 165−174.
(82) Adrjanowicz, K.; Kaminski, K.; Wojnarowska, Z.; Dulski, M.; Hawelek, L.; Pawlus, S.; Paluch, M.; Sawicki, W. Dielectric Relaxation and Crystallization Kinetics of Ibuprofen at Ambient and Elevated Pressure. *J. Phys. Chem. B* **2010**, *114*, 6579−6593.

https://doi.org/10.1021/acs.jpcb.4c00582
J. Phys. Chem. B 2024, 128, 4021−4032

Variation of Activation Volume as an Indicator of the Difference in Clusterization Phenomenon Induced by H-bonding and F – Π stacking Interactions in Enantiomers and a Racemate of Flurbiprofen

Paulina Jesionek[a,b,*], Barbara Hachuła[a], Karolina Jurkiewicz[c], Patryk Włodarczyk[d], Marek Hreczka[d,e] Kamil Kamiński[c], Ewa Kamińska[b,*]

[a] *Institute of Chemistry, Faculty of Science and Technology, University of Silesia in Katowice, Szkolna 9, 40-007 Katowice, Poland*
[b] *Department of Pharmacognosy and Phytochemistry, Faculty of Pharmaceutical Sciences in Sosnowiec, Medical University of Silesia in Katowice, Jagiellonska 4, 41-200 Sosnowiec, Poland*
[c] *Institute of Physics, Faculty of Science and Technology, University of Silesia in Katowice, 75 Pulku Piechoty 1, 41-500 Chorzow, Poland*
[d] *Lukasiewicz Research Network - Institute of Non-Ferrous Metals, Sowinskiego 5 St., 44-100, Gliwice, Poland*
[e] *Department of Mechatronics, Silesian University of Technology, Akademicka 10A St., 44-100, Gliwice, Poland*

SUPPORTING INFORMATION

Results:

FTIR Spectroscopy data

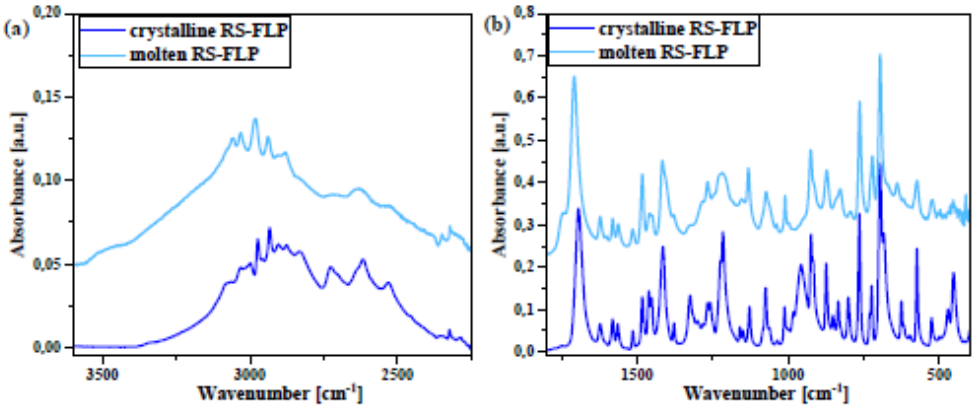

Figure S1. Comparison of FTIR spectra of crystalline and melted racemic FLP in the wavenumber regions of (a) 3600-2250 cm^{-1} and (b) 1800-400 cm^{-1}.

BDS data

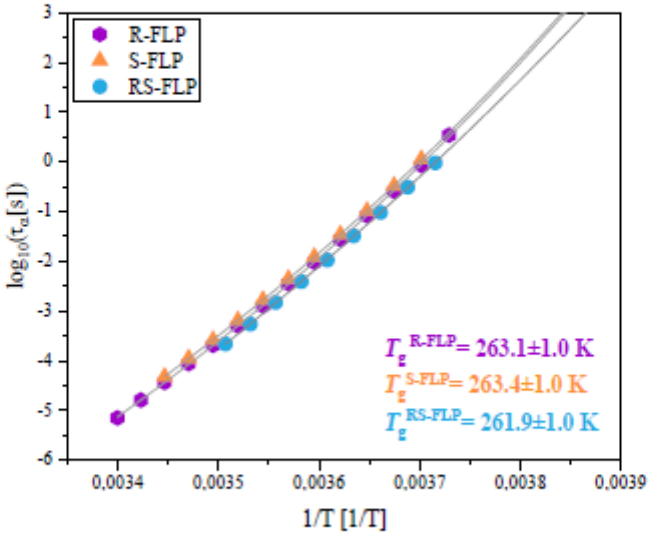

Figure S2. Temperature dependence of structural relaxation times determined from ambient pressure BDS measurements for *R*-, *S*-, and *RS*-FLP. The solid lines represent fits using the Vogel–Fulcher–Tammann (VFT) equation: $\tau_\alpha = \tau_{VFT}\exp\left(\frac{D_T T_0}{T - T_0}\right)$, where τ_{VFT} is the time scale of vibrational movements, D_T is the strength parameter, and T_0 represents the temperature at which relaxation times tend to infinity). The values of T_g correspond to the structural relaxation time of 100 s.

Table S1. Parameters of the modified Avramov equation (eq. 4) obtained from the analysis of $\tau_\alpha(T, p)$ dependencies for *R*-FLP, *S*-FLP, and *RS*-FLP.

	***R*-FLP**	***S*-FLP**	***RS*-FLP**
$\log_{10}(\tau_\infty[s])$	-14.02±1.16	-13.56 ± 1.27	-15.84 ± 2.03
T_r [K]	263.20±0.23	263.50 ± 0.23	261.49 ± 0.47
α_0	5.276±0.535	5.379 ± 0.602	4.372 ± 0.562
C/C_{p0}	0.082±0.007	0.001 ± 0.0001	0.062 ± 0.002
Π [MPa]	212.47±39.60	410.74 ± 86.22	354.97 ± 88.53
β	0.991±0.154	1.969 ± 0.292	1.338 ± 0.329
Adj. R-Square	0.998	0.999	0.999

Results of MD simulations and DFT computations

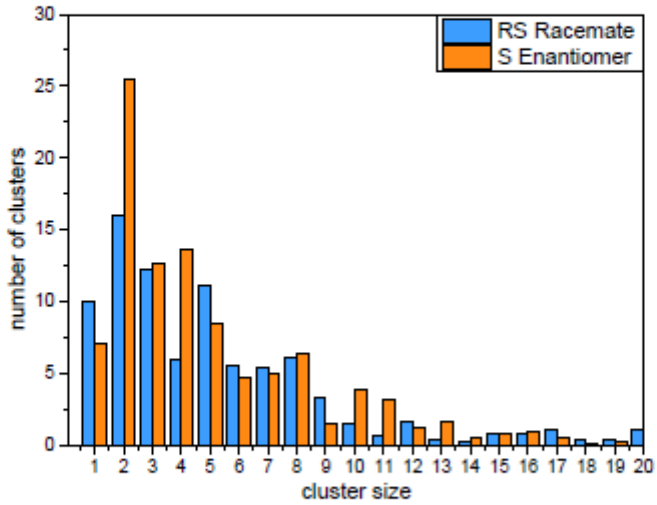

Figure S3. Histogram of HB clusters distribution in *RS*- and *S*-FLP systems.

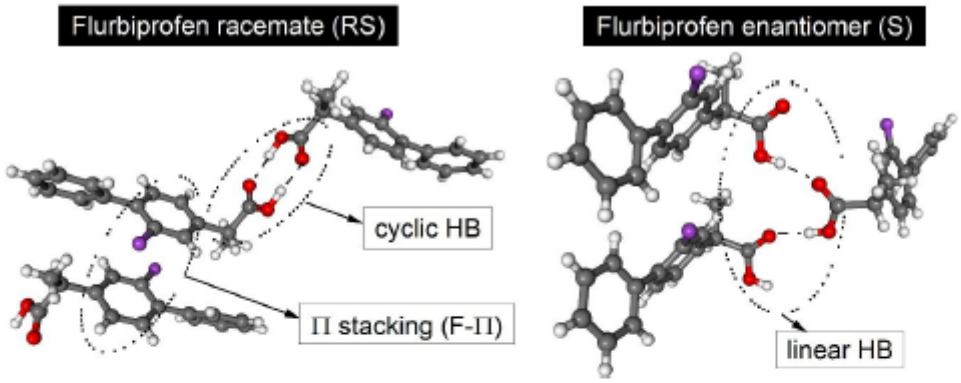

Figure S4. Comparison of flurbiprofen mer repeating units in the crystal structures. In the racemate, the (cHB ··· Π ··· cHB) pattern, while in the enantiomer, the (HB···HB···HB) pattern can be found in their crystalline states.

3.3. **Publikacja 3 (P3):** *Studies on the nature and pressure evolution of phase transitions in 1-adamantylamine and 1-adamantanol,* Spectrochim. Acta Part A Mol. Biomol. Spectrosc. 299 (**2023**) 122794.

Autorzy: P. Jesionek, B. Hachuła, D. Heczko, T. Lamrani, K. Jurkiewicz, M. Tarnacka, M. Książek, K. Kamiński, E. Kamińska.

DOI: 10.1016/j.saa.2023.122794

Impact Factor czasopisma z roku opublikowania pracy: 4.3

Liczba punktów ministerialnych MNiSW czasopisma z roku opublikowania pracy: 140

Mój udział w pracy polegał na przeglądzie literaturowym, współtworzeniu hipotezy badawczej, przygotowaniu próbek 1-adamantylaminy i 1-adamantanolu do badań, przeprowadzeniu pomiarów dynamiki molekularnej w ciśnieniu atmosferycznym oraz podwyższonym, analizie danych dielektrycznych, opracowaniu rysunków do pracy, uczestnictwie w dyskusji wyników, redagowaniu tekstu artykułu, a także przygotowaniu odpowiedzi do recenzentów i poprawek w manuskrypcie.

Spectrochimica Acta Part A: Molecular and Biomolecular Spectroscopy 299 (2023) 122794

Contents lists available at ScienceDirect

Spectrochimica Acta Part A: Molecular and Biomolecular Spectroscopy

journal homepage: www.journals.elsevier.com/spectrochimica-acta-part-a-molecular-and-biomolecular-spectroscopy

Studies on the nature and pressure evolution of phase transitions in 1-adamantylamine and 1-adamantanol

Paulina Jesionek [a,b], Barbara Hachuła [a,*], Dawid Heczko [c], Taoufik Lamrani [d], Karolina Jurkiewicz [d,*], Magdalena Tarnacka [d], Maria Książek [d], Kamil Kamiński [d], Ewa Kamińska [b]

[a] Institute of Chemistry, Faculty of Science and Technology, University of Silesia in Katowice, Sokolna 9, 40-007 Katowice, Poland
[b] Department of Pharmacognosy and Phytochemistry, Faculty of Pharmaceutical Sciences in Sosnowiec, Medical University of Silesia in Katowice, Jagiellonska 4, 41-200 Sosnowiec, Poland
[c] Department of Statistics, Department of Instrumental Analysis, Faculty of Pharmaceutical Sciences in Sosnowiec, Medical University of Silesia in Katowice, ul. Ostrogorska 30, 41-200 Sosnowiec, Poland
[d] Institute of Physics, Faculty of Science and Technology, University of Silesia in Katowice, 75 Pułku Piechoty 1, 41-500 Chorzow, Poland

HIGHLIGHTS

- H-bond strength influences the nature of phase transitions in 1-NH_2-OH and 1-OH-ADM.
- There are three transitions between various plastic crystal (PC) phases in 1-NH_2-OH.
- Only one transition between PC and ordinary crystal phases occurs in 1-OH-ADM.
- Compression has a strong impact on phase transitions in both examined compounds.

GRAPHICAL ABSTRACT

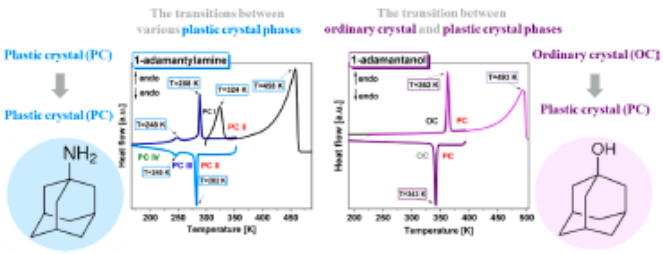

ARTICLE INFO

Keywords:
1-Adamantylamine
1-Adamantanol
Phase transition
Plastic crystal
High-pressure
Dielectric measurements

ABSTRACT

In this paper, several experimental techniques, i.e., differential scanning calorimetry, X-ray diffraction, Fourier transform infrared, Raman, and broadband dielectric spectroscopy were applied to study the nature of the phase transitions in 1-adamantylamine (1-NH_2-ADM, $C_{10}H_{17}N$) and 1-adamantanol (1-OH-ADM, $C_{10}H_{16}O$). Calorimetric measurements showed one and three endothermic peaks in thermograms for the latter and the former substance, respectively. Indeed, results of spectroscopic investigations indicated that the observed thermal events in 1-NH_2-ADM correspond to transitions between various plastic crystal (PC) phases (I, II, III, IV), while the endothermic process in 1-OH-ADM can be assigned to a phase transition between the PC and the ordinary crystal (OC). Especially interesting were the outcomes of dielectric studies carried out both at ambient and high-pressure conditions, during heating and cooling cycles. They showed: *i)* noticeable changes in the frequency dependencies of the imaginary (ε'') and real (ε') parts of the complex dielectric permittivity that occurred around temperatures of the characteristic endothermic events detected by the calorimetry, and *ii)* significant fluctuations of ε'' and ε' at pressures attributed to the respective phase transitions. Moreover, the pressure coefficients of the phase

* Corresponding authors.
E-mail addresses: barbara.hachula@us.edu.pl (B. Hachuła), karolina.jurkiewicz@us.edu.pl (K. Jurkiewicz).

https://doi.org/10.1016/j.saa.2023.122794
Received 23 January 2023; Received in revised form 1 April 2023; Accepted 26 April 2023
Available online 3 May 2023
1386-1425/© 2023 The Authors. Published by Elsevier B.V. This is an open access article under the CC BY license (http://creativecommons.org/licenses/by/4.0/).

transition temperatures were estimated to be approximately equal to 0.2 K/MPa for both compounds. In turn, volume variation (ΔV) at the PC (II)-PC (III) and PC (III)-PC (IV) transition temperatures for 1-NH_2-ADM was essentially different than ΔV for the PC-OC transition in 1-OH-ADM.

1. Introduction

In recent years, Orientationally Disordered Crystals (ODICs), sharing properties of liquids and regular crystals, commonly referred to as plastic crystals (PCs), have been the subject of intensive research [1–11]. Previous studies have indicated that this state of matter can be formed by globular molecules with nearly spherical shape [1], where the average position of the molecular centers of mass has translational order, forming regular lattices. However, in contrast to ordinary crystals (OCs), molecules in PCs have orientational degrees of freedom [12,13].

One of the best-known examples of materials forming the ODIC phase is adamantane (ADM) [14–18]. In the literature, there are numerous research papers on derivatives of this compound, where one or two hydrogen atoms were substituted by, e.g., chlorine [19–21], or bromine [22–24] atoms, as well as hydroxyl [25,26], amine [27,28] or cyano [1,29–31] groups. It turns out that such chemical modifications of the ADM structure do not suppress the transition from the OC to the ODIC. At most, it changes the crystal lattice, the symmetry of the unit cell, as well as temperature (T) at which the transition takes place. It was reported that for ADM, 1-bromoadamantane (1-Br-ADM) and 1-adamantanol (1-OH-ADM), the OC-ODIC transition occurs at $T = 209$, 310, and 357 K, respectively, with corresponding entropy changes $\Delta S = 16.2$, 23.9, and 31.62 J/mol·K [14,24,25]. Other investigations have revealed the dependence of the OC-ODIC transition temperature on the atomic number (Z) of the halogen atom (X) attached to the ADM molecule, i.e., the increase of this temperature with the increasing Z of X (such as F, Cl, Br) in 1-X-ADM [32]. Furthermore, it should be mentioned about the papers concentrating on the H-bonding pattern in the OCs and PCs. In this context, one can refer to the infrared (IR) spectroscopic studies on 1-OH-ADM indicating that the degree of association in the ODIC phase is smaller with respect to the OC [33]. The other interesting features of PCs revealed broadband dielectric spectroscopy (BDS) investigations. It was shown that, generally, these materials exhibit features, which are typical for disordered supercooled liquids, e.g., a non-exponential dielectric response function as well as non-Arrhenius behaviour of structural relaxation times [1].

As far as there is an abundance of research on either the thermodynamic or spectroscopic properties of ADM derivatives at ambient pressure (p), only a few studies were carried out under high compression [32,34–38]. These investigations were mainly focused on the nature of the phase transitions in the examined compounds, as well as their elastic properties. For example, Gromnitskaya *et al.* [34] reported apparent differences in elastic moduli for ADM and 1-Cl-ADM. In particular, for the halogen derivative, both elastic moduli (bulk and shear) turned out to be substantially lower compared to ADM. Additionally, the Poisson coefficient for 1-Cl-ADM exceeded that determined for ADM, which indicated a much softer plastic phase in the former compound. Moreover, very recent investigations on the elastic properties of 1-X-ADM series (X = H, F, Cl, Br) have revealed a monotonic dependence of the bulk modulus at low pressures as a function of Z of the halogen substituent. The bulk modulus was the highest for ADM and decreased with an increasing Z of the X [32]. One can also mention the results of high-pressure (HP) Fourier transform infrared (FTIR) studies carried out by Pracsyk *et al.* [37] on 1-Cl-ADM, which demonstrated significant changes in the vibrational spectrum, where the splitting of several bands (in the CH deformation and stretching, and CH_2 deformation regions) was detected as a result of compression, indicating a disordered-ordered phase transition at $p = 5$ kbar. Notably, the same splitting phenomenon was observed in low temperatures at the transition from phase I to phase II. Based on the above, it was suggested that the HP phase transition in this ADM derivative is identical to that detected during temperature reduction to 244.2 K at ambient pressure. A similar observation was also reported for ADM [39] and 2-adamantanone [40]. Finally, it is worth mentioning the paper by Hedoux *et al.* [38], where HP Raman investigations on 1-CN-ADM have shown noticeable differences between the spectra measured for the ordered HP and low-temperature (LT) phases. The authors concluded that the occurrence of these two different ordered phases in 1-CN-ADM may be responsible for the glass formation in the examined system.

In this paper, we combined the results of differential scanning calorimetry (DSC), X-ray diffraction (XRD), FTIR, Raman, and BDS measurements, performed at ambient and elevated pressure, on the two ADM derivatives: 1-adamantylamine (1-NH_2-ADM, molecular formula: $C_{10}H_{17}N$) and 1-adamantanol (1-OH-ADM, molecular formula: $C_{10}H_{16}O$). Our main aim was to determine the nature of the phase transitions as well as their pressure evolutions in both compounds. These data, aside from the scientific value contributing to the whole discussion on the ODICs, may have also significant implications on the formulations of 1-NH_2-ADM – the drug known under the name 'amantadine', commonly used to treat Parkinson's disease and its symptoms, e.g., stiffness, shaking, and repetitive, uncontrolled muscle movements caused by certain medicines. The HP dielectric experiments allowed us to construct a simple phase diagram of this compound, which can be valuable for the prediction of the possible transitions between various ODIC phases during the tableting process. Hence, this knowledge might be useful in controlling both thermodynamic variables (i.e., temperature and pressure) to obtain formulations of this active substance with well-defined physico-chemical and pharmacokinetic properties.

2. Materials and methods

Neat 1-NH_2-ADM (molecular weight $M_w = 151.25$ g/mol) and 1-OH-ADM ($M_w = 152.23$ g/mol), with purity > 97% and > 99%, respectively, were supplied from Sigma Aldrich and used as received. The chemical structures of the investigated compounds are presented in the insets in panels (a) and (b) of Fig. 1, respectively.

2.1. Differential scanning calorimetry (DSC)

Thermal properties of both ADM derivatives were examined by using a Mettler-Toledo DSC apparatus (Mettler–Toledo International, Inc., Greifensee, Switzerland) equipped with a liquid nitrogen cooling accessory as well as an HSS8 ceramic heat flux sensor with 120 thermocouples. The instrument was calibrated for temperature and enthalpy using indium and zinc standards. The investigated compounds were placed in aluminum crucibles (40 mL) and sealed. The samples of 1-NH_2-ADM and 1-OH-ADM were heated from room temperature up to 493 and 503 K, respectively. Due to the fact that there were no substances in the crucibles after the completion of measurements, we prepared new samples of both substances, which initially were heated from 293 to 353 K (1-NH_2-ADM) or 393 K (1-OH-ADM), then cooled down, to 160 or 123 K, and heated again up to 353 or 393 K, respectively. All measurements were recorded with a heating/cooling rate of 10 K/min.

2.2. X-ray diffraction (XRD)

X-ray diffraction studies of commercial powder samples were performed using a D/MAX RAPID II-R diffractometer (Rigaku Denki Co., Tokyo, Japan) in the Debye – Scherrer geometry, equipped with a rotating Ag anode, a graphite (0 0 2) monochromator, and an image

plate detector. The wavelength of the incident beam was 0.5608 Å. The powders were measured in glass capillaries with a diameter of 1.5 mm and a wall thickness of 0.01 mm, in the temperature range of 173–373 K. The 800 Series Cryostream Cooler (Oxford Cryosystems Ltd., Oxford, United Kingdom) was used to control the temperature.

X-ray quality single crystals of ethanol solvate of 1-NH_2-ADM were formed during slow evaporation of the substance, where ethanol was used for crystallization. The crystal structure of 1-NH_2-ADM ethanol solvate was solved. For details, see the Supplementary Material (SM). However, attempts to grow pure 1-NH_2-ADM single crystals with this method failed.

2.3. Fourier transform infrared (FTIR) spectroscopy

FTIR spectra were measured on the Nicolet iS50 spectrometer (Thermo Fisher Scientific, Massachusetts, USA), at a spectral resolution of 4 cm^{-1}, taking 16 scans. The spectra of commercial 1-OH-ADM and 1-NH_2-ADM were first recorded in the ATR mode, in the range of 4000–400 cm^{-1} at 293 K. Moreover, FTIR data of 1-OH-ADM as a function of temperature were measured using a GladiATR accessory (Pike Technologies), in the 4000–400 cm^{-1} region and at 2 cm^{-1} spectral resolution. The temperature-dependent FTIR data of 1-NH_2-ADM were collected in the transmission mode. The limited spectral range (4000–1000 cm^{-1}) of these experiments was due to the absorption of CaF_2 window discs, which were used for the preparation of thin films (3,5 μm) of 1-NH_2-ADM. For this ADM derivative, the temperature was monitored with a Linkam heating/cooling stage (Linkam Scientific Instruments Ltd., Surrey, UK, model THMS600) with a stability of ± 0.01 K. The temperature investigations were performed in two sequences: (i) upon heating from 293 to 343 K for 1-NH_2-ADM and from 293 to 403 K for 1-OH-ADM, and (ii) upon cooling from 343 to 203 K for 1-NH_2-ADM and from 403 to 293 K for 1-OH-ADM, with a rate of 4 K min^{-1}. During the measurements, the spectrometer was purged with liquid nitrogen.

2.4. Raman spectroscopy

Raman spectra of 1-NH_2-ADM were recorded with a DXRxi Raman spectrometer (Thermo Fisher Scientific) equipped with an Olympus microscope at the following conditions: 785 nm laser source with a power of 24 mW at the sample; 3300–65 cm^{-1} range; full range grating; 10 × objective; 50 μm slit, 6 cm^{-1} spectral resolution (FWHM), the exposure time 1 s, 20 scans. Since at excitation wavelength of 785 nm the stretching vibrations of the NH groups were beyond the long wavelength response limit of the detector, an alpha300 R Raman microscope (WITec Wissenschaftliche Instrumente und Technologie GmbH, Ulm, Germany) with a laser of 532 nm (10 mW power at the sample) was additionally used to measure the spectra in this region. Data were collected with a 1.5–2 cm^{-1} spectral resolution (the diffraction grating of 600 lines/mm), and 32 expositions of 2 s each were averaged. The THMS600 heating/cooling stage (Linkam Scientific Instruments Ltd., Surrey, UK) was used to monitor the temperature changes in the spectra upon heating from 293 to 343 K and cooling from 343 to 203 K, with a constant rate of 4 K min^{-1}.

2.5. Broadband dielectric spectroscopy (BDS)

Ambient and elevated-pressure measurements of the complex dielectric permittivity, $\varepsilon^*(\omega) = \varepsilon'(\omega) - i\,\varepsilon''(\omega)$ over a frequency (f) range of 10^{-1} - 10^6 Hz, were taken using a Novo-Control Alpha dielectric spectrometer (Novocontrol Technologies GmbH & Co. KG, Hundsangen, Germany). The temperature control during the experiments at $p = 0.1$ MPa was provided by Quatro System using a nitrogen gas cryostat, with stability better than 0.1 K. The samples (powder forms) of investigated compounds were placed between two stainless-steel electrodes, separated by a thin Teflon spacer (diameter of 20 mm, gap of 0.18 mm). Measurements (upon heating and cooling procedures) were performed in the following temperature ranges: 225–333 K (for 1-NH_2-ADM) and 323–383 K (for 1-OH-ADM). For dielectric experiments under compression, a HP chamber was used. The sample capacitor was sealed, as well as covered thoroughly by Teflon tape to separate it from the silicon oil. The pressure was measured using a Nova Swiss tensometric meter with a resolution of 1 MPa. Moreover, the temperature was regulated within 0.1 K by means of a Huber circulator (HUBER GmbH, Germany). Isothermal measurements for both investigated ADM derivatives were performed in the pressure ranges given in Table S1 in the SM. It should be noted that in the case of 1-NH_2-ADM, two (or one) phase transitions were detected in the ε' vs. f and ε'' vs. f dependences obtained at given thermodynamic conditions (T, p).

3. Results and discussion

3.1. DSC data

At first, we carried out calorimetric measurements to characterise

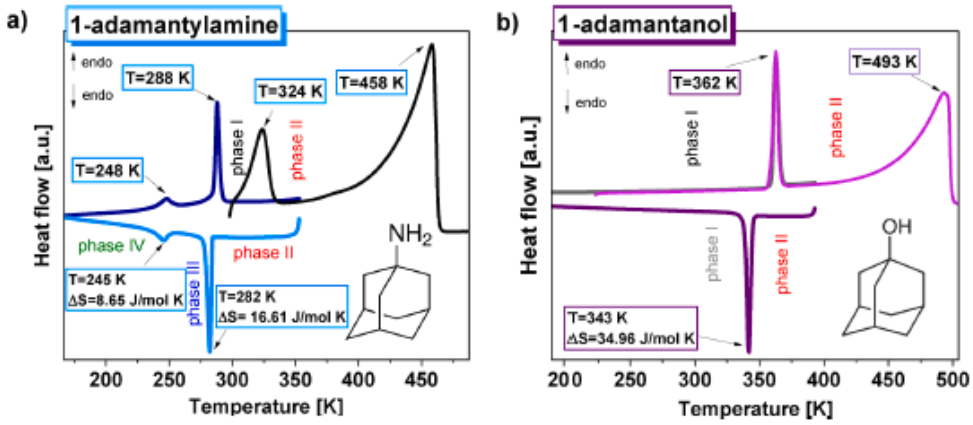

Fig. 1. DSC thermograms obtained during heating and cooling of the two ADM derivatives: 1-NH_2-ADM (a) and 1-OH-ADM (b), with the rate of 10 K/min. In the insets, the chemical structures of the examined compounds are presented.

the thermal properties of two ADM derivatives: 1-NH_2-ADM and 1-OH-ADM. In Fig. 1(a,b), DSC thermograms of both systems, recorded on heating and cooling, with a rate of 10 K/min, are shown. For 1-NH_2-ADM, two strong endothermic events, at $T = 324$ and $T = 458$ K, were observed during the first heating run (black line). Importantly, after the measurements were finished, there was no substance in the alumina crucible. Based on the above, we concluded that the thermal event at 458 K is related to the sublimation phenomenon. Therefore, a second 1-NH_2-ADM sample was prepared and, after initial heating from room temperature to 353 K, it was measured on cooling (down to 160 K, blue line), and subsequently on heating (up to 353 K, navy blue line). The thermograms obtained on cooling revealed the presence of two endothermic processes corresponding to two phase transitions, at $T = 245$ and $T = 282$ K, with the entropy change ΔS of 8.65 and 16.61 J/mol·K, respectively. A similar scenario of the appearance of two endothermic events was observed during the subsequent heating. However, they occurred at slightly higher temperatures, i.e., 248 and 288 K. Additionally, no thermal event at 324 K was detected, indicating that the initial phase has not been restored after heating/cooling cycles. It should be mentioned that the presence of the two phase transitions in 1-NH_2-ADM at temperatures close to those obtained from the DSC studies (strictly at 241.4 and 284.6 K) was reported also by Bazyleva et al. [27]. Note that the sum of entropies ($\sum \Delta S$) determined by the authors for both transitions ($\sum \Delta S = 25.8$ J/mol·K) was very similar to that obtained from our experiments ($\sum \Delta S = 25.3$ J/mol·K). Importantly, considering the estimated value of $\sum \Delta S$ and pronounced plasticity of 1-NH_2-ADM at mechanical load (pressing), Bazyleva et al. suggested the formation of the ODIC phase in this compound.

In the case of 1-OH-ADM, the DSC curve collected on first heating (fuchsia line) showed two well-visible endothermic processes at $T = 362$ and $T = 493$ K. By analogy with 1-NH_2-ADM, the latter one can be assigned to the sample sublimation. In the thermogram collected upon cooling of a fresh 1-OH-ADM sample (previously heated from 293 to 393 K), only one phase transition at 343 K, with entropy change equal to 34.96 J/mol·K, was detected. Notably, this thermal event was also observed during further heating (dark grey line), however, at much higher temperature, $T = 362$ K (identical to that determined during the initial heating run). It should be mentioned that DSC data obtained herein for 1-OH-ADM are in good agreement with those reported previously by Charapennikau et al. [25]. It is also worth emphasizing that, according to Ref. [25], the thermal event at around 360 K (during the sample heating) is due to a transition from the OC to the ODIC phase. Hence, at first sight, it is visible that the entropy changes associated with the phase transitions in 1-NH_2-ADM are much lower than in 1-OH-ADM, suggesting that they originate from the changes between different PC phases, in agreement with Bazyleva et al. [27].

In order to follow the structural transformation in 1-OH-ADM, as well as to gain a deeper insight into the nature of the transitions recorded in thermograms of 1-NH_2-ADM, further XRD studies were performed.

3.2. XRD data

From the powder XRD data presented in Fig. 2(b), one can see that the room-temperature phase I of 1-OH-ADM transforms into another structure – phase II at 362 K that agrees with the temperature of the endothermic process observed in thermograms measured on heating. The structure of form I was resolved by Amoureux et al. as a tetragonal $P42/n$ system with 8 molecules per unit cell of volume around 1726 $Å^{-3}$ [41]. The structure of phase II exhibits a higher symmetry of the unit cell than phase I, with the pattern of Bragg peaks typical for the cubic lattice system. Such a transformation to a higher symmetry is typical when dealing with a transition from a crystalline to a plastic state and has been recognized in 1-OH-ADM by Charapennikau et al. [25]. They also established that the plastic phase II of 1-OH-ADM belongs to the $F43c$ space group with 4 molecules per cubic unit cell of volume around 973 $Å^{-3}$. After cooling the 1-OH-ADM sample from the temperature above 362 K down to 343 K, the reverse transition from phase II to phase I was registered on the XRD patterns, which was stable upon further cooling. This scenario is in line with the presented above DSC data. It is worth mentioning that the phase behaviour of 1-OH-ADM mimics that reported for pristine ADM, which forms low-temperature ordered tetragonal system and orientationally disordered cubic crystals at higher temperature. However, it differs from 1-OH-ADM in the temperature of this transition – it is much lower, around 208 K [42].

The phase behaviour of 1-NH_2-ADM is more complex than that of ADM and 1-OH-ADM. The room temperature form of 1-NH_2-ADM was labeled as phase I, in accordance with the caption on DSC thermograms. Although attempts to obtain X-ray quality single crystals of 1-NH_2-ADM from different solvents (water, methanol, ethanol, acetone, carbon tetrachloride, chloroform) have been made, they failed and the crystal structure of this compound has not yet been solved. It was due to the poor solubility of this compound in the majority of the mentioned solvents. The sample was successfully dissolved only in methanol and

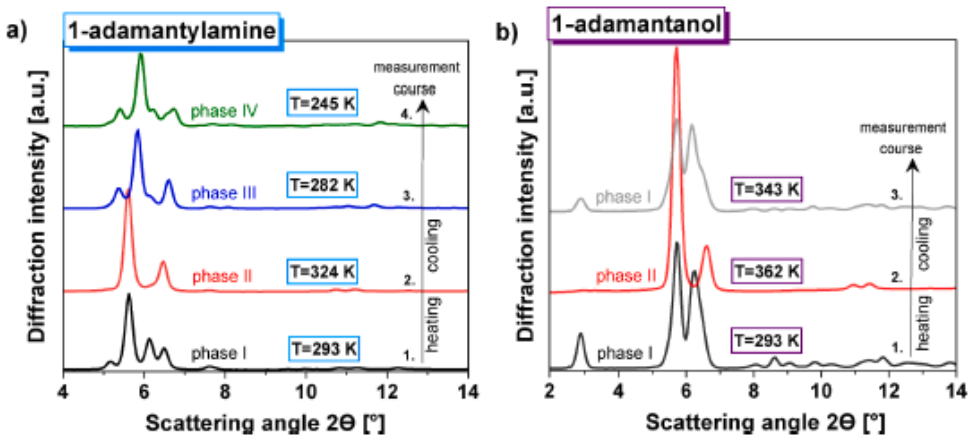

Fig. 2. XRD patterns of the two ADM derivatives: 1-NH_2-ADM (a) and 1-OH-ADM (b), measured at different temperatures, in the sequence indicated by numbers 1–4 in the figure.

ethanol. However, only single crystals of ethanol solvate of 1-NH_2-ADM were grown. Their crystal structure was determined as the trigonal $P\bar{3}c1$ space group (please see the SM).

As shown in Fig. 2(a), the XRD pattern of 1-NH_2-ADM phase I is typical for spherical molecules forming ODIC (PC) phases, with only some strong Bragg reflections at small scattering angles and much attenuated high-angle peaks. From the diffractogram, it can be deduced that the unit cell symmetry is lower than tetragonal for 1-OH-ADM phase I. However, after heating, 1-NH_2-ADM undergoes a transition to a cubic unit cell at around 324 K that corresponds to the endothermic process on the DSC curve at this temperature. One may expect, therefore, that above 324 K, 1-NH_2-ADM forms ODIC state, referred here to as phase II. Then, after cooling the sample from the temperature above 324 K down to 282 K, another phase transition is observed. However, unlike 1-OH-ADM, it is not a reverse change to phase I but to a system with other Bragg peak positions and intensities, having a lattice with another space group, marked as phase III. Upon further cooling down, at 245 K (where an additional transition was revealed by the thermogram), we uncovered another very subtle structural change manifested by, e.g., splitting of the peak around 6.6° and a slight decrease in the intensity of the two first peaks. This new form, with the unit cell very similar to that for phase III, was marked as phase IV. The changes in the diffraction patterns for 1-NH_2-ADM at different temperatures can be also clearly seen in Fig. S1 in the SM, where they have been superimposed. Interestingly, below 245 K, the diffraction patterns of 1-NH_2-ADM still evolve with temperature, down to the measurement limit of 173 K, as can be seen in Fig. S1(c) in the SM. These changes are visible as variations in peak intensities and their broadening, e.g., the most pronounced diffraction peak at around 5.9° drops and broadens with the decrease of temperature that cannot be associated with the freezing of the thermal vibrations of atoms. This finding indicates that the 1-NH_2-ADM molecules retain considerable molecular mobility, even at temperatures below 200 K. In other words, it suggests that 1-NH_2-ADM is in a plastic phase, where molecules have still some degree of orientational freedom. However, this hypothesis will be further verified by other experimental methods.

3.3. FTIR and Raman data

In the next step, we performed complementary FTIR and Raman studies, which are widely applied to investigate the structure and related phase transitions in diverse types of materials [43–46], in order to obtain more information about the molecular reorganization processes related to the phase transitions in ADM derivatives. First, we collected FTIR spectra of 1-OH-ADM and 1-NH_2-ADM at 293 K (Figs. S2 and S3) and made assignments of the visible bands to the given kind of molecular vibrations (for further information, please see the SM). Then, to verify the nature of the phase transition occurring in 1-OH-ADM, FTIR spectra as a function of temperature, upon heating and cooling runs, were recorded. The representative data are presented in Fig. 3. Furthermore, it should be mentioned that the temperature dependences of the spectral parameters (peak position, integrated intensity (area), and the full width at half maximum (FWHM)) of selected bands are depicted in Figs. S4 and S5 in the SM. One can see that the IR spectrum of room-temperature phase I, characterized by the band splitting typical for the OC phase (highlighted in Fig. 3), transforms around 362 K into pattern typical for the ODIC, where the bands become broader and blurred. The effect of the phase transition between the OC and the ODIC is especially well visible for the bands observed in the higher wavenumber range (Fig. 3 (a)). Namely, a considerable broadening of the shape of the OH stretching band (3700–3000 cm^{-1}) occurs and splitting of the CH stretching band (3000–2750 cm^{-1}) is lost. After following cooling down the sample to 349 K, the reverse scenario (the transition from the PC to the OC phase) is observed and the obtained spectrum clearly resembles the one measured for the phase I at room temperature.

Subsequently, we tried to elucidate the changes accompanying the phase transitions in 1-NH_2-ADM on the microscopic/molecular level. It should be emphasized that the structural variations occurring under temperature disturbance affect the vibrational dynamics and, consequently, the spectral parameters of the absorption bands (i.e., their wavenumbers, FWHMs, and areas). For this reason, we analyzed temperature-dependent FTIR spectra of 1-NH_2-ADM, measured during heating from 293 to 343 K, and then cooling from 343 to 203 K, in the wavenumber range of 3600–1050 cm^{-1} (see Figs. S6 and S7 in the SM). The representative data recorded at T = 293, 343, 263 and 203 K are shown in Fig. 4. Moreover, to better visualize the temperature-dependent evolution of the vibrational spectra, the plots of selected peak positions, integrated intensities, and FWHM values vs. temperature, showing the most significant variations of these parameters during heating and cooling were presented in Figs. S8 and S9 in the SM.

The comparison of the FTIR data in Figs. 4, S8 and S9 revealed that the most prominent changes appear in four wavenumber ranges: 3500–3100, 1463–1413, 1160–1118, and 1118–1075 cm^{-1}. The first region is associated with the vibrations of H-bonded NH groups. The peaks in this region are red-shifted and narrower at lower temperatures that indicates the strengthening of H-bonds (HBs) and the increase of homogeneity of the HB strength. Next, the peak occurring in the range of 1463–1413 cm^{-1} shows the noticeable variations of the profile with temperature, connected with the disorder of CH_2 units. The bands detected in other spectral regions, related to the stretching and bending vibrations of CN, CH, and CC groups, are also sensitive to the orientational order of ADM skeleton.

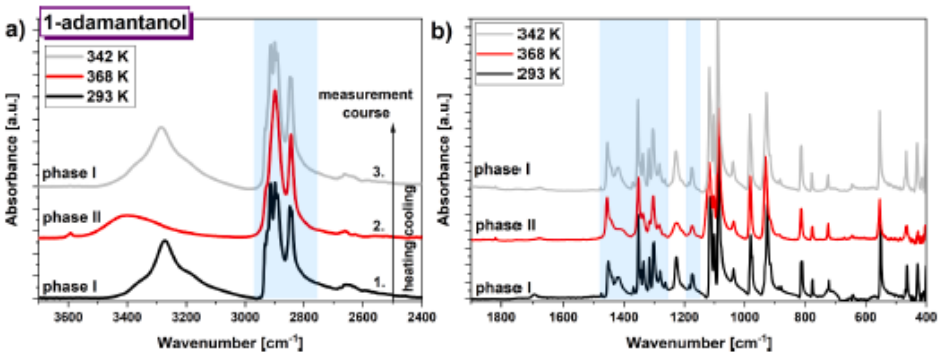

Fig. 3. FTIR spectra of 1-OH-ADM measured at different temperatures, in the sequence indicated by numbers 1–3 in the figure, in two wavenumber regions of (a) 3700–2400 cm^{-1} and (b) 1900–400 cm^{-1}.

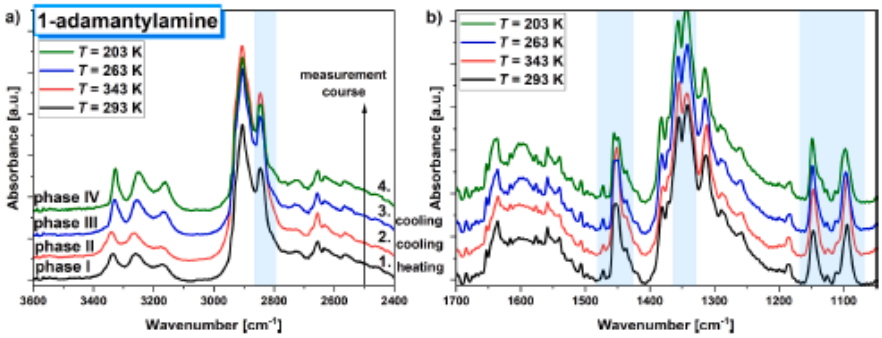

Fig. 4. FTIR spectra of 1-NH_2-ADM measured at different temperatures, in the sequence indicated by numbers 1–4 in the figure, in two wavenumber regions of (a) 3600–2400 cm^{-1} and (b) 1700–1050 cm^{-1}. The spectral ranges analysed in the plots were highlighted for clarity.

As illustrated in Fig. S8, upon heating of 1-NH_2-ADM sample to around 330 K, some anomalies in the IR spectra arise that manifest themselves in the changes of the temperature dependences of the peak position, integrated intensity, and FWHM for the analysed bands. This clearly indicates the intramolecular reorganization of 1-NH_2-ADM molecules, which is in agreement with DSC data. The values of the phase transition temperatures were estimated as the first derivatives of the temperature-functions of the given spectral parameters (Fig. S10). It can be also noticed that IR bands located at 1450 cm^{-1} (CH_2 scissoring), 1316 cm^{-1} (CN stretching; NH_2, CH_2 and CH bending), 1146 cm^{-1} (CN stretching, NH_2 wagging, CH_2 wagging, CH bending, CC stretching), 1096 cm^{-1} (CH_2 wagging, CH_2 twisting, CH bending), are shifted to higher (1450 cm^{-1}, 1316 cm^{-1}) and lower (1146 cm^{-1}, 1096 cm^{-1}) wavenumbers, respectively. Thus, some bonds shorten, and others get longer during heating. The shifts in the positions of the analysed peaks are also accompanied by a significant change in their integral intensity and width (Fig. S8). The broadening of the bands corresponding to the stretching vibrations of CH (3100–2750 cm^{-1}) and CN (1160–1118 cm^{-1}) groups suggests the increase in hydrocarbon chain conformational disorder and mobility that occurs upon heating. Importantly, the peaks located at 3100–2750 cm^{-1} and 1468–1413 cm^{-1} regions exhibit no splitting at 293 and 343 K, which, according to literature [37,47], may indicate the disorder-disorder phase transition (phase I to phase II) in 1-NH_2-ADM at around 331 K (Fig. S8). It can therefore be assumed that 1-NH_2-ADM forms an ODIC (PC) phase at room temperature (phase I). This is in accordance with the suggestions of Bazyleva et al. [27].

A detailed analysis of the temperature-dependences of the spectral parameters for the selected IR bands during cooling of 1-NH_2-ADM revealed their discontinuous character also at around 277 K (Figs. S9 and S11). In more detail, the position, area, and FWHM values of the studied bands showed visible changes at $T = 277$ K, suggesting the formation of another plastic phase – phase III. It should be noted that this temperature is close to that estimated from DSC measurements for the II to III phase transition in 1-NH_2-ADM. Moreover, a gradual increase of the wavenumber for the bands occurring in the range of 1118–1075, 1160–1118, and 1325–1295 cm^{-1} was observed, which means the shortening of the corresponding bond distances at lower temperatures. Interestingly, below 277 K, the subtle splitting of the mode located at 1450 cm^{-1}, corresponding to the CH_2 scissoring, was observed on further cooling down to 203 K. Such a feature may fingerprint the formation of spatially different CH_2 units in the low-temperature phase. Thus, the changes in the CH vibrations provide information about the conformational mobility of the alkyl skeleton at low temperatures. It is also observed that there is a reduction in the intensity of the analysed bands, as well as a broadening of absorption bands at 1450 and 1096 cm^{-1} on cooling, which might be due to a rearrangement of the molecular cores, leading to a transformation of conformational isomers. It should be noted that no additional anomalies in the FTIR spectra were observed, especially near $T = 245$ K, where DSC and XRD outcomes revealed the additional phase transition - from phase III to phase IV. The lack of sensitivity of FTIR bands on this low-temperature phase transition can be due to very small differences in the crystal lattices and general structural organization of molecules between the phases III and IV, as well as disorder of CH_2 units in these two phases. Overall, there is a significant similarity between the IR spectra recorded for the four phases of 1-NH_2-ADM. In particular, the abrupt changes in the spectra during the temperature evolution, such as those visible in 1-OH-ADM, are not observed. This leads us once again to assume that in the amine derivative of ADM we are dealing only with phase transitions between ODICs having different symmetry, unit cell parameters, etc. Importantly, a spectrum of the room-temperature phase I of 1-NH_2-ADM strongly resembles that of a plastic phase II of 1-OH-ADM. It is essentially visible in the region of stretching and bending vibrations of CH groups of ADM skeleton (Fig. 5). This fact may additionally confirm a plasticity of 1-NH_2-ADM.

The complementary Raman spectroscopy experiment was carried out only for 1-NH_2-ADM compound, at the same temperature conditions as FTIR measurements. The representative spectra collected at 343, 293, 273, and 203 K, in the 3000–200 cm^{-1} region, are presented in Fig. S12 in the SM. Moreover, the spectra measured in a higher wavenumber region, up to 3500 cm^{-1}, for analogical temperature conditions, are shown in Fig. 6. The data illustrated in Fig S12, similarly to the FTIR investigations, revealed only small spectral variations with the temperature, occurring in the lower wavenumber regions (the highlighted areas). Therefore, in Fig. S13, we presented the temperature dependences of the selected peaks, located at around 422, 716, 987, and 1200 cm^{-1}, measured upon heating (from 293 to 343 K) and cooling (from 343 to 203 K). The analysis of this data enabled us to determine the phase transition temperatures, see Figs. S13, S14 and S15 in the SM. Especially, we found visible changes in the wavenumber at around 303 K on heating. This temperature does not agree well with that observed for the endothermic process in thermograms – 324 K. Nevertheless, it coincides with the onset of calorimetric phase transition between ODIC phases I and II, which extends over a wide temperature range (please see Fig. 1(a)). In the case of the spectra measured on cooling, a variance in the position of the selected peaks was detected at $T = 281$ K, very close to $T = 282$ K of the phase II – phase III transition determined from the calorimetry. Such a result was also consistent with the outcome of FTIR analysis for 1-NH_2-ADM. Moreover, after further cooling of the sample from 281 to 203 K, no significant variations in the Raman spectra were noted that would suggest the transition between phases III and IV. The subtle shifts of the Raman bands at low temperatures may be mainly

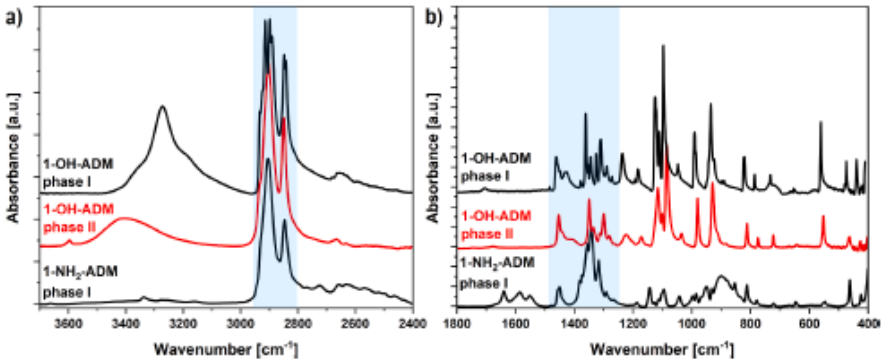

Fig. 5. FTIR spectra of 1-OH-ADM (phases I and II) and 1-NH_2-ADM (phase I) measured in two wavenumber regions of (a) 3700–2400 cm^{-1} and (b) 1800–400 cm^{-1}.

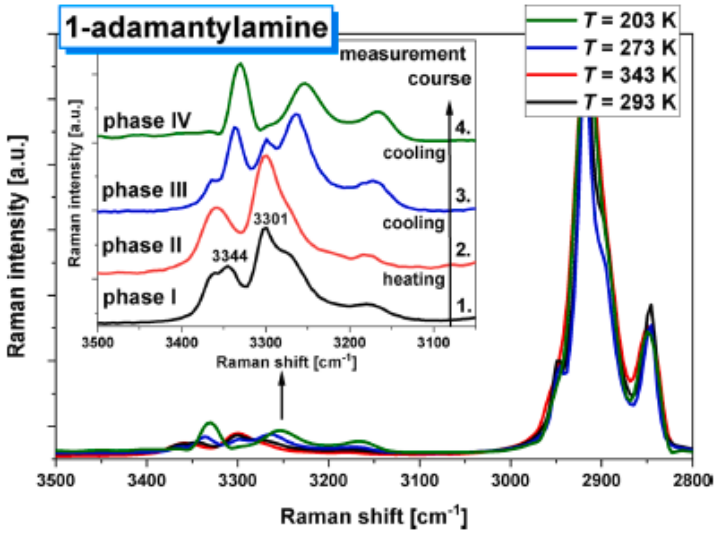

Fig. 6. Raman spectra of 1-NH_2-ADM measured at four consecutive temperatures: 293, 343, 273, and 203 K, in the sequence indicated by numbers 1–4 in the figure, in the 3500–2800 cm^{-1} region.

related to the temperature effect.

Analyzing the Raman spectra presented in Fig. 6, one can state that there is a shift of the NH band to lower wavenumbers with decreasing temperature, which indicates a lengthening of the NH distance and weakening of the NH bond in the amine group caused by shortening of the N···H and N···N intermolecular H-bonds. Importantly, the shape of the NH band slightly varies with temperature. In the spectrum measured in the phase III at 273 K, the peaks at 3344 and 3301 cm^{-1} split into two components (3363 and 3336 cm^{-1}, as well as 3299 and 3263 cm^{-1}, respectively). This suggests a reorganization of HBs accompanying the transition from phase II to phase III. Interestingly, below 273 K, the Raman spectra still change upon cooling, up to the measurement limit of 203 K. The peaks shift to lower wavenumbers that can be associated with the standard temperature effect (the strengthening of HBs). However, another finding is more interesting. Namely, the splitting in the NH vibrations disappears, which can be due to the formation of a new, low-temperature ODIC phase. This inference coincides with the XRD data, making the assumption of the existence of four various plastic phases of 1-NH_2-ADM more reliable.

Summarizing the FTIR and Raman spectroscopy results, one can claim that, except for the spectral regions connected to the vibrations of NH (stretching) and CH (stretching and bending) groups, there were only minor variations in the spectra at temperatures of phase transitions between the different ODIC forms. In this context, it is worth stressing that in the case of various materials forming the ODIC state, only very small differences between the vibrational spectra of their ODIC and liquid phases are observed [48,49,50]. Moreover, a similar scenario occurs also for the transitions between two plastic phases as demonstrated in the case of 1,12-dicarbacloso0dodecaboran, where isotropic or anisotropic molecular reorientation is detected in both phases [51]. These findings are related to the orientational disorder of molecules in PC phases, which is responsible for the peak-broadening and blurring in FTIR and Raman spectra. Therefore, it is not surprising that the spectra collected from both experimental techniques at different PC states of 1-

NH_2-ADM show very similar profiles.

3.4. Ambient and high-pressure BDS data

After FTIR and Raman investigations, we performed ambient pressure ($p = 0.1$ MPa) BDS measurements for 1-NH_2-ADM and 1-OH-ADM. In Fig. 7(a,b), dielectric loss spectra collected for the examined compounds in a wide temperature range are illustrated. As can be seen, the dielectric response evolves with temperature, on both heating and cooling cycles. In the case of 1-NH_2-ADM, the loss spectra measured on heating from 295 to 333 K revealed the presence of a single relaxation process, most likely originating from the fluctuations within the amine moiety. Intriguingly, above $T = 323$ K, which corresponds to the maximum of the endothermic peak in the registered thermograms (Fig. 1(a)), and indicates the transition from phase I to phase II, this loss peak is systematically covered by the contribution of the dc conductivity (DC), connected to the transport of ionic impurities. The value of the exponent, characterizing the slope of the DC line in 1-NH_2-ADM, approaches 1 ($\log \omega \approx f^{-1}$) at higher temperatures. Nevertheless, upon cooling, at around 280 K (see the lower panel in Fig. 7(a)), a relaxation process that shifts to lower frequencies with decreasing temperature, can be again observed in the spectra. At $T = 249$ K (related to the second endothermic process in the thermogram, see Fig. 1(a)), variations in the loss spectra are too small to be discussed.

In the case of 1-OH-ADM, the dielectric behaviour is somewhat different (see Fig. 7(b)). There is no trace of a relaxation process in the collected loss spectra. Above 363 K on heating, one can identify the DC that dominates the dielectric response of the sample. Upon cooling, there is a clear characteristic variation in the slope of the $\varepsilon''(f)$ suggesting the formation of the OC phase below 347 K.

Additionally, we have performed an in-depth analysis of frequency dependences of the real part of complex dielectric permittivity, ε', for both investigated compounds. Fig. 8(a,b) presents the results obtained upon cooling for 1-NH_2-ADM and 1-OH-ADM. In both cases, one can observe significant changes of ε' at temperatures corresponding to the phase transitions. The abrupt decrease in the real dielectric permittivity is especially visible at 249 K for 1-NH_2-ADM and at 347 K for 1-OH-ADM. To verify these observations, we have plotted ε' measured at a constant frequency, $f = 10^5$ Hz (the Plateau area), as a function of temperature; see Fig. 8(c,d). It can be seen that for the amine derivative, ε' ($f = 10^5$ Hz) increases with cooling down to −275 K, then it remains almost constant down to − 249 K, and next it decreases rapidly at the end. A slightly different behaviour is observed for the hydroxyl derivative of ADM, where ε' ($f = 10^5$ Hz) first increases during cooling, at around 347 K it sharply decreases, and subsequently remains nearly constant up to 325 K (Fig. 8(d)). Note that during heating, the situation was similar, but an abrupt increase in ε' occurred at around 363 K. Importantly, the changes in the dielectric permittivity of the material due to the phase transitions are also visible in the insets of Fig. 8(c,d), illustrating the derivatives $d\varepsilon'/dT$ as a function of temperature. Importantly, from these plots, it was possible to estimate directly the temperatures of the phase transitions. A similar procedure was also performed for the permittivity ε' measured at $f = 10^3$ and 10^4 Hz for both ADM derivatives (see Fig. S16 in the SM). We found that the character of $\varepsilon'(T)$ evolution, as well as temperatures determined from the inflection points designated in the main panels, at which ODIC-ODIC and ODIC-OC transitions occur, are almost identical and do not depend on the frequency. Importantly, these characteristic temperatures were very similar to those estimated from DSC, XRD, FTIR, and Raman measurements (please see Table S2 in the SM). One can comment that

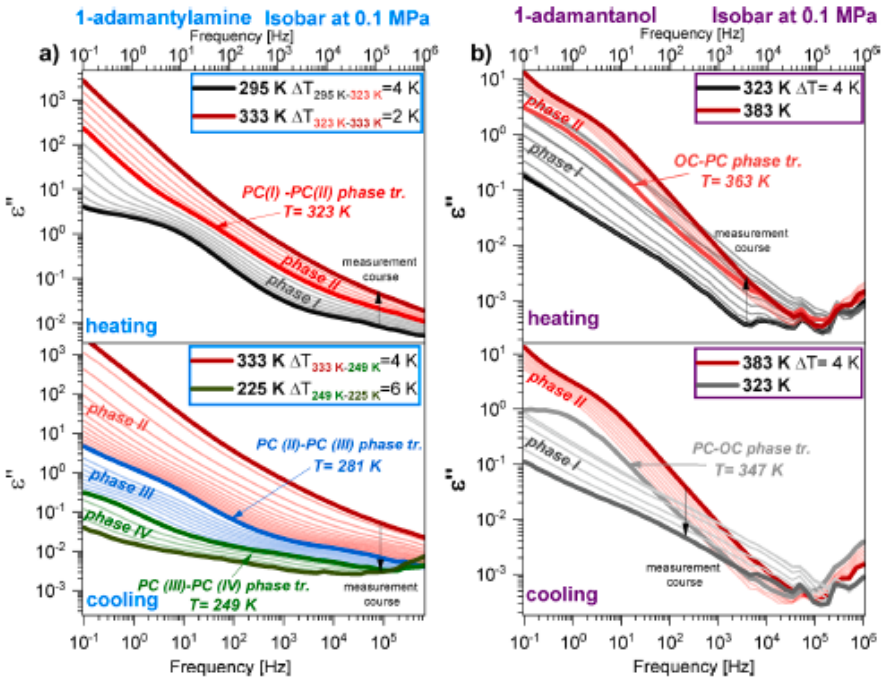

Fig. 7. Representative dielectric loss spectra measured for 1-NH_2-ADM (a) and 1-OH-ADM (b) at ambient pressure, in a wide temperature range, during heating and cooling cycles.

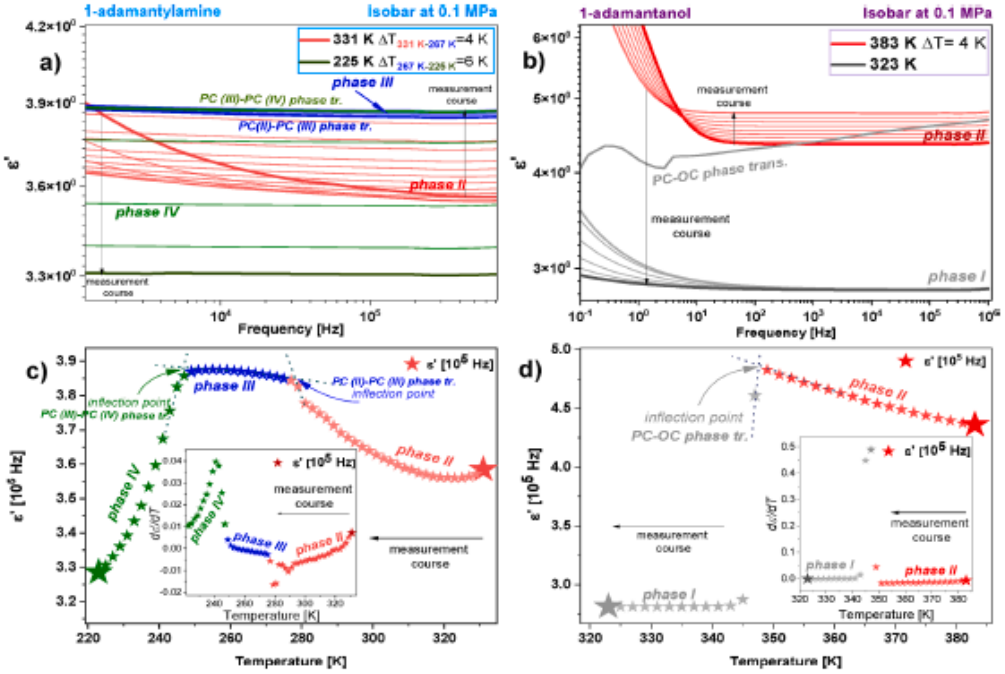

Fig. 8. Frequency dependence of the real part of the complex dielectric permittivity, ε', for 1-NH_2-ADM (a) and 1-OH-ADM (b) at ambient pressure, upon cooling. In panels (c) and (d) temperature dependencies of ε', taken at constant f (=10^5 Hz) are presented. The insets in panels (c) and (d) show the derivatives of the experimental data given in the main panels.

besides one exception addressed earlier, the observed small differences in temperatures of the phase transitions can be easily assigned to the various heating/cooling rates applied in these different experimental techniques, as well as the temperature calibration of the instruments.

Additionally, it is worth emphasizing that the permittivity changes reflecting the variation in the mobility of the sample might be a suitable indication of the character of the phases (crystalline vs. plastic) in the probed system. First, for 1-NH_2-ADM it is well-visible that, in contrast to 1-OH-ADM, the permittivity increases on cooling, reaching the inflection point around 280 K. Then, it slightly grows up to ~245 K. Such a pattern of behaviour suggests the PC (II)-PC (III) phase transition at ~280 K, while a systematic decrease of permittivity below 245 K indicates freezing out of molecular mobility. Considering the data obtained from DSC measurements (a low entropy change associated with the transition between phases III and IV), as well as FTIR and XRD investigations, one can postulate that at around 245 K, also a transition between plastic phases occurs.

Having in mind the results of calorimetric, diffraction, infrared, Raman, and ambient pressure dielectric investigations, in the subsequent stage, we have focused on characterizing the influence of compression on the phase transitions in both examined compounds. All isothermal experiments were carried out starting from temperatures above 323 K for 1-NH_2-ADM and 363 K for 1-OH-ADM. It should be noted that prior to high-pressure (HP) experiments for the latter compound, the sample was first heated up above 363 K at $p = 0.1$ MPa. Fig. 9 (a,b) shows representative dielectric spectra collected for 1-NH_2-ADM and 1-OH-ADM at isothermal conditions, in wide pressure ranges. As in the case of ambient pressure data, the loss spectra are dominated by the contribution of the dc-conductivity. For 1-NH_2-ADM, the slope of the DC part (i.e., the exponent value) reaches 1 at lower pressures and the dielectric response evolves with compression. A relaxation process, originating probably from fluctuations within the amine moiety, becomes more prominent at some pressure. Moreover, near $p = 60$ MPa and $p = 220$ MPa at 291 K, there are some changes in the shape of the loss spectra, which, similar to the results at $p = 0.1$ MPa, can be attributed to the two PC-PC phase transitions, designated as PC (II)-PC (III) and PC (III)-PC (IV).

For 1-OH-ADM, a slightly different scenario was observed during HP BDS studies. As illustrated in Fig. 9(b), there is no trace of the relaxation process in the loss spectra. Only a pronounced DC part is evident. It should be noted that for this compound, a strong variation in the dielectric response, which can be related to the PC-OC phase transition, occurs at $p = 160$ MPa and 371 K.

Moreover, by the analogy to the ambient pressure BDS data, we have performed the analysis of HP frequency dependences of the real part of the complex dielectric permittivity, ε'. Fig. 9(c,d) show the representative data obtained for both studied substances at constant temperature conditions (291 and 371 K for 1-NH_2-ADM and 1-OH-ADM, respectively). In each case, the variations of ε' at pressures corresponding to the phase transitions can be noticed. The rapid decrease of the real part of dielectric permittivity at $p = 220$ MPa and $p = 160$ MPa for amine and hydroxyl derivative of ADM, respectively, resembles those observed at around 249 and 347 K (see Fig. 8(a,b)). Similarly to the data presented at 0.1 MPa, in Fig. 9(e,f), we have plotted ε' measured at constant frequency, $f = 10^5$ Hz, versus pressure. As can be seen, for 1-NH_2-ADM, the permittivity rapidly increases with compression from $p = 30$ MPa up to about $p = 60$ MPa. Next, in the pressure range from 60 MPa to 220 MPa, the rise slows down and then, ε' sharply decreases up to $p = 300$ MPa. In the case of 1-OH-ADM, a somewhat different behaviour can be noted.

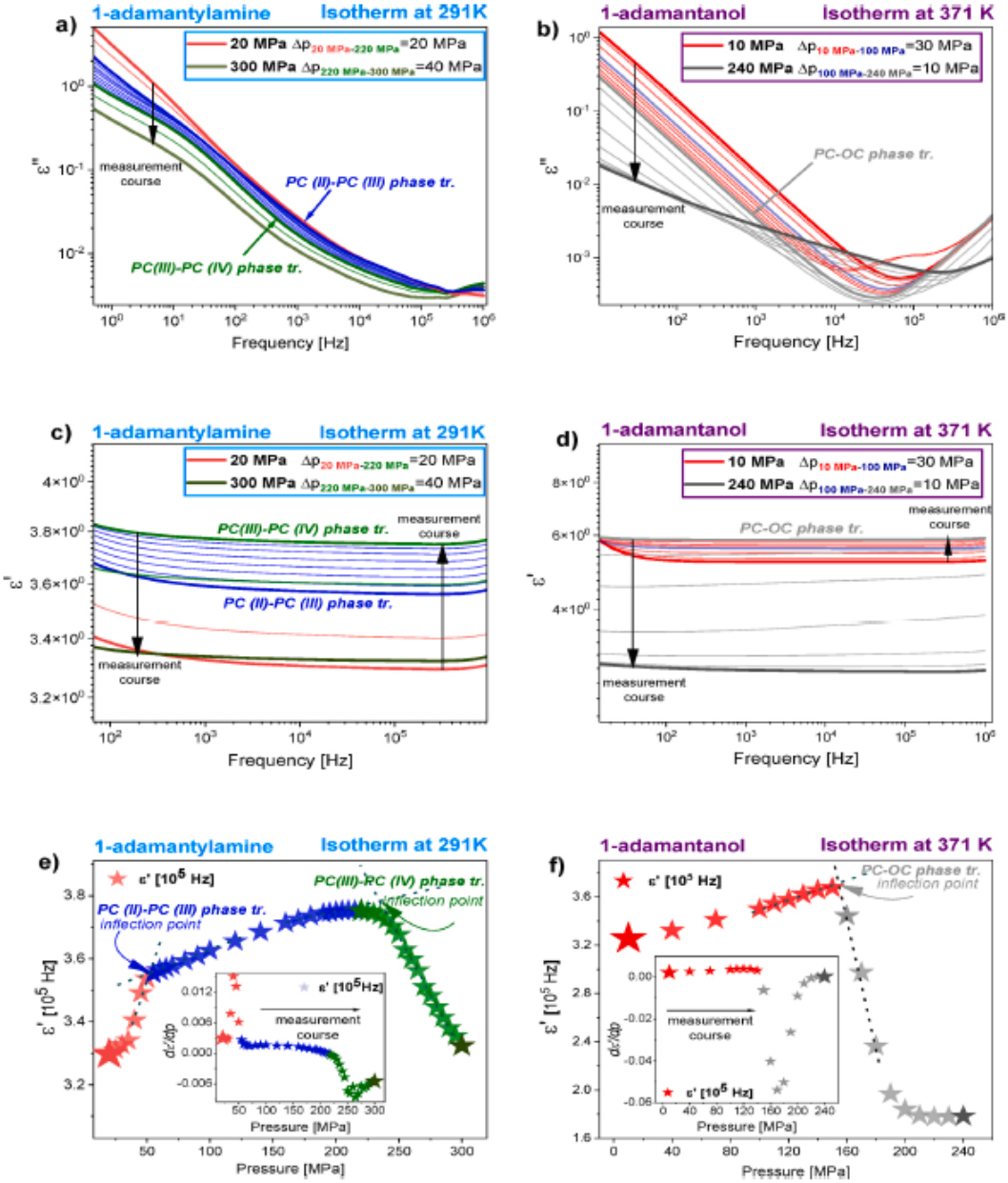

Fig. 9. Representative dielectric loss spectra measured for 1-NH_2-ADM (a) and 1-OH-ADM (b) at isothermal conditions. Frequency dependence of the dielectric real part, ε', for 1-NH_2-ADM (c) and 1-OH-ADM (d) at isothermal conditions. In panels (e) and (f) pressure dependencies of ε', taken at constant f (=10^5 Hz), are presented. The insets in panels (e) and (f) show the derivatives of the experimental data given in the main panels.

Namely, ε' ($f = 10^5$ Hz) slightly increases with compression from 0.1 MPa and then, from $p = 160$ MPa rapidly decreases with pressure. Importantly, in the insets of Fig. 9(e,f), we illustrated the derivatives of the permittivity ($d\varepsilon'/dp$) as a function of pressure, which enabled us a straightforward determination of the pressure values, at which phase transitions occur. They were close to the inflection points indicated in the main panels of Fig. 9(e,f). It should be added that similar analyses were performed for the data (ε' and ε'' vs. f dependencies) obtained from other isothermal measurements carried out at various pressure ranges (details are included in the *Materials and methods* section and the SM). Importantly, these experiments also showed the presence of two PC-PC (PC (II)-PC III), PC (III)-PC (IV)) and one PC-OC phase transitions in 1-NH_2-ADM and 1-OH-ADM, respectively.

To evaluate the impact of compression on the detected phase transitions, in Fig. 10 (a–c) we presented the pressure dependences of the phase transition temperatures determined from the analysis of ambient and HP data. The plot of $T_{PC(II)\text{-}PC(III)}$ (i.e., which occurs at higher temperature or lower pressure) vs. pressure for 1-NH_2-ADM was linear, hence, it was fitted using the linear function (blue dashed line in Fig. 10 (a)). In turn, to fit the pressure dependences of $T_{PC(III)\text{-}PC(IV)}$ (1-NH_2-ADM) and $T_{PC\text{-}OC}$ (1-OH-ADM), which have logarithmic character, the Andersson-Andersson formula [52] was applied (green and grey dashed lines in Fig. 10(b,c), respectively):

$$T_{PC-PC(PC-OC)} = k_1\left(1+\frac{k_2}{k_3}p\right)^{1/k_2} \quad (1)$$

where k_1, k_2 and k_3 are material constants. Subsequently, from the slope of the line in Fig. 10(a), and from the ratio k_1/k_3 ($k_1 = 247.12$ and $k_3 = 1128.84$ for 1-NH_2-ADM; $k_1 = 346.39$, and $k_3 = 1797.68$ for 1-OH-ADM), we estimated the pressure coefficient of the temperature of the two PC-PC and the one PC-OC phase transitions. The values obtained for 1-NH_2-ADM ($dT_{PC(II)\text{-}PC(III)}/dp = 0.236$ K/MPa and $dT_{PC(III)\text{-}PC(IV)}/dp = 0.219$ K/MPa) indicate that the PC(II)-PC(III) phase transition in this compound is a little more sensitive to compression than the transition between PC(III) and PC(IV) phases. Moreover, $dT_{PC\text{-}OC}/dp = 0.193$ K/MPa for 1-OH-ADM is slightly lower in comparison to those calculated for both PC-PC transitions in 1-NH_2-ADM. It is worth mentioning that the value of the $dT_{PC\text{-}OC}/dp$ parameter for 1-OH-ADM is, in turn, significantly higher than 0.093–0.113 K/MPa reported for another plastic crystal - neopentylglycol (NPG) [53]. Interestingly, the values of $dT_{PC(II)\text{-}PC(III)}/dp$, $dT_{PC(III)\text{-}PC(IV)}/dp$, and $dT_{PC\text{-}OC}/dp$ obtained for both examined compounds also significantly exceed the pressure coefficient of the PC-glassy crystal (GC) transition temperature ($dT_{PC\text{-}GC}/dp$) calculated for two PCs: anhMAN [8] and anhGLU [9], as well as that determined for mixed PC formed by NPG and neopentyl alcohol (NPA) [54]: $dT_{PC\text{-}GC}/dp = 0.056$, 0.060, and 0.028 K/MPa for anhMAN, anhGLU, as well as NPG and NPA mixture, respectively.

Additionally, we compared the changes in the volume at the phase transition point (ΔV) for both compounds using the Clausius-Clapeyron equation [55]:

$$dp/dT_{PC-PC(PC-OC)} = \Delta S(\Delta V)^{-1} \quad (2)$$

where ΔS represents the entropy variation during phase transition (its values were taken from DSC measurements - the cooling cycle, Fig. 1). The calculated ΔV were equal to 0.0259 cm^3/g and 0.0125 cm^3/g for the PC (II)-PC (III) and PC (III)-PC(IV) transitions in 1-NH_2-ADM (Fig. 10(a, b)), as well as 0.0443 cm^3/g for the PC-OC transition in the hydroxyl derivative of ADM (Fig. 10(c)). Thus the second (PC (III)-PC (IV)) phase transition in 1-NH_2-ADM is accompanied by a two-fold decrease of ΔV with respect to the first one (PC (II)-PC (III)). Interestingly, for 1-OH-ADM, the variation in volume during the PC-OC phase transition is much greater, even in comparison to ΔV accompanying the PC (II)-PC (III) phase transition in 1-NH_2-ADM.

Therefore, considering all the data, one can postulate that all phase transitions observed for 1-NH_2-ADM are between various ODIC states, while in 1-OH-ADM the transition between PC and OC phases occurs. Moreover, HP BDS studies allowed us to construct a simple phase diagram for both ADM derivatives. This is especially important in the case of 1-NH_2-ADM, which is an active substance used to treat Parkinson's disease and its symptoms. Knowledge about the pressure-evolution of the transition between various ODIC phases in this pharmaceutical may be useful to predict eventual phase transitions upon the tableting process, which requires compression and obtain formulations with well-defined pharmacokinetic properties.

4. Conclusions

In this work, we have performed DSC, XRD, FTIR, Raman, and BDS measurements on two ADM derivatives: 1-NH_2-ADM and 1-OH-ADM, differing by the strength of H-bonds due to the type of the substituent attached to the molecule (NH_2 vs. OH). The main purpose was to examine the impact of this variation in the molecular structure on temperature and pressure dependences of the phase transitions in both systems. We have assigned three and one characteristic endothermic peaks observed in thermograms of 1-NH_2-ADM and 1-OH-ADM, respectively, to the PC-PC (i.e., PC (I)-PC (II), PC (II)-PC (III), PC (III)-PC (IV)) and PC-OC phase transitions. Three of the mentioned transitions (except for the PC (III)-PC (IV)) were reflected in variations of the FTIR and Raman spectra. We have also found significant changes in the dielectric spectra (ε'' vs. f), as well as frequency dependencies of the dielectric permittivity (ε' vs. f), which were noticeable at temperatures for which the characteristic endothermic events in the DSC curves were visible. Importantly, HP BDS studies indicated that there are variations of ε'' and ε', which, depending on the temperature, occurred at two or

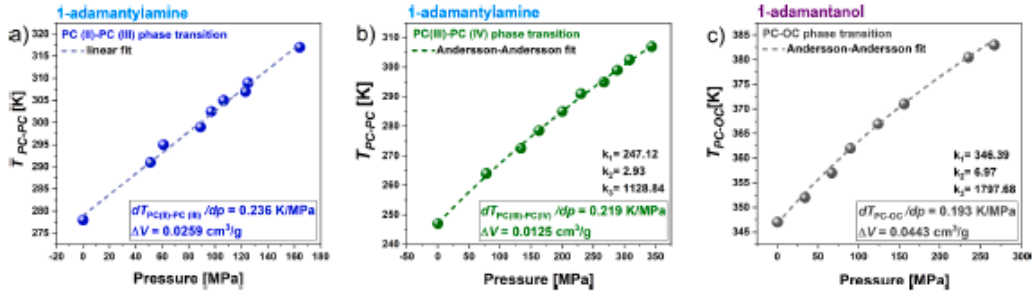

Fig. 10. Pressure dependences of (a,b) temperature of two plastic crystal-plastic crystal ($T_{PC(II)\text{-}PC(III)}$ and $T_{PC(III)\text{-}PC(IV)}$) phase transitions for 1-NH_2-ADM, and (c) temperature of plastic crystal-ordinary crystal ($T_{PC\text{-}OC}$) phase transition for 1-OH-ADM. The dashed lines are fits to the data using a linear function (panel a) or the Andersson-Andersson equation (panels b,c).

one characteristic pressures in the amine and hydroxyl derivative of ADM, respectively. Additionally, the analysis of the pressure dependences of $T_{PC(II)\text{-}PC(III)}$, $T_{PC(III)\text{-}PC(IV)}$ for 1-NH_2-ADM, and $T_{PC\text{-}OC}$ for 1-OH-ADM enabled us to determine the pressure coefficients of temperatures of these phase transitions, i.e., $dT_{PC(II)\text{-}PC(III)}/dp$, $dT_{PC(III)\text{-}PC(IV)}/dp$, and $dT_{PC\text{-}OC}/dp$. The obtained values of −0.2 K/MPa for each case showed the substantial impact of the compression on the mentioned transitions. Moreover, the comparison of changes in the volume at the phase transition point (ΔV) revealed the essential differences between this parameter for the PC (II)-PC (III) and the PC (III)-PC (IV) phase transitions in 1-NH_2-ADM (ΔV = 0.0259 cm^3/g and 0.0125 cm^3/g, respectively). For 1-OH-ADM, the obtained ΔV value (0.0443 cm^3/g) was considerably higher even than that determined for the PC (II)-PC (III) transition in 1-NH_2-ADM.

We are convinced that aside from the contribution to the important discussion on plastic crystals, our data might be valuable for the development of improved and more conscious pharmaceutical formulations of 1-NH_2-ADM.

CRediT authorship contribution statement

Paulina Jesionek: Investigation, Formal analysis, Visualization, Methodology, Writing – original draft. **Barbara Hachuła:** Conceptualization, Writing – review & editing, Investigation. **Dawid Heczko:** Investigation. **Taoufik Lamrani:** Investigation. **Karolina Jurkiewicz:** Investigation, Writing – review & editing, Funding acquisition. **Magdalena Tarnacka:** Investigation. **Maria Książek:** Investigation. **Kamil Kamiński:** Conceptualization, Supervision. **Ewa Kamińska:** Conceptualization, Supervision, Writing – original draft, Writing – review & editing, Funding acquisition.

Declaration of Competing Interest

The authors declare that they have no known competing financial interests or personal relationships that could have appeared to influence the work reported in this paper.

Data availability

Data will be made available on request.

Acknowledgments

This research was funded in whole by the National Science Centre (Poland), grant number: Opus 21 No. 2021/41/B/NZ7/01654. For the purpose of Open Access, the author has applied a CC-BY public copyright licence to any Author Accepted Manuscript (AAM) version arising from this submission.

Appendix A. Supplementary material

Supplementary data to this article can be found online at https://doi.org/10.1016/j.saa.2023.122794.

References

[1] R. Brand, P. Lunkenheimer, A. Loidl, Relaxation dynamics in plastic crystals, J. Chem. Phys. 116 (2002) 10386–10401, https://doi.org/10.1063/1.1477186.
[2] S. Das, A. Mondal, C.M. Reddy, Harnessing molecular rotations in plastic crystals: a holistic view for crystal engineering of adaptive soft materials, Chem. Soc. Rev. 49 (2020) 8878–8896, https://doi.org/10.1039/d0cs00475b.
[3] J. Timmermans, Un nouvel état mésomorphe les cristaux organiques plastiques, J. Chim. Phys. 35 (1938) 331–344, https://doi.org/10.1051/jcp/1938350331.
[4] A. Vispa, M. Romanini, M.A. Ramos, L.C. Pardo, F.J. Bermejo, M. Hassaine, A. I. Krivchikov, J.W. Taylor, J.L. Tamarit, Thermodynamic and kinetic fragility of freon 113: the most fragile plastic crystal, Phys. Rev. Lett. 118 (2017) 1–6, https://doi.org/10.1103/PhysRevLett.118.105701.
[5] M. Michl, T. Bauer, P. Lunkenheimer, A. Loidl, Cooperativity and heterogeneity in plastic crystals studied by nonlinear dielectric spectroscopy, Phys. Rev. Lett. 114 (2015) 67601, https://doi.org/10.1103/PhysRevLett.114.067601.
[6] L.C. Pardo, P. Lunkenheimer, A. Loidl, α and β relaxation dynamics of a fragile plastic crystal, J. Chem. Phys. 124 (2006), https://doi.org/10.1063/1.2180786.
[7] B. Riechers, K. Samwer, R. Richert, Structural recovery in plastic crystals by time-resolved non-linear dielectric spectroscopy, J. Chem. Phys. 142 (2015), 154504, https://doi.org/10.1063/1.4918280.
[8] D. Heczko, E. Kamińska, A. Minecka, A. Drzienia, K. Jurkiewicz, M. Tarnacka, A. Talik, K. Kamiński, M. Paluch, High-pressure dielectric studies on 1,6-anhydro-β-D-mannopyranose (plastic crystal) and 2,3,4-tri-O-acetyl-1,6-anhydro-β-D-glucopyranose (canonical glass), J. Chem. Phys. 148 (2018), 204510, https://doi.org/10.1063/1.5032209.
[9] E. Kaminska, M. Tarnacka, K. Jurkiewicz, K. Kaminski, M. Paluch, High pressure dielectric studies on the structural and orientational glass, J. Chem. Phys. 144 (2016) 54503, https://doi.org/10.1063/1.4940776.
[10] G.J. Kabo, A.A. Kozyro, M. Frenkel, A.V. Blokhin, Solid phase transitions of the cyclohexane derivatives and the model of energy states of molecules in plastic crystals, Mol. Cryst. Liq. Cryst. Sci. Technol. Sect. A. Mol. Cryst. Liq. Cryst. 326 (1999) 333–355, https://doi.org/10.1080/10587259908025424.
[11] J.J. Moura Ramos, H.P. Diogo, Orientational glass, orientationally disordered crystal and crystalline polymorphism: a further study on the thermal behavior and molecular mobility in levoglucosan, J. Mol. Liq. 286 (2019), 110914, https://doi.org/10.1016/j.molliq.2019.110914.
[12] F. Simon, C.V. Simson, Die kristallstruktur des chlorwasserstoffs, Z. Phys. 21 (1924) 168–177, https://doi.org/10.1007/BF01328260.
[13] W.G. Haase, J.N. Sherwood (Eds.), The Plastically Crystalline State, John Wiley & Sons Limited, New York, 1979.
[14] G.J. Kabo, A.V. Blokhin, M.B. Charapennikau, A.G. Kabo, V.M. Sevruk, Thermodynamic properties of adamantane and the energy states of molecules in plastic crystals for some cage hydrocarbons, Thermochim. Acta. 345 (2000) 125–133, https://doi.org/10.1016/S0040-6031(99)00393-7.
[15] J.P. Amoureux, M. Bee, A cubic harmonic analysis of the plastic crystal structures of adamantane, $C_{10}H_{16}$, and adamantanone, $C_{10}H_{14}O$, at room temperature, Acta Crystallogr. Sect. B. 36 (1980) 2636–2642, https://doi.org/10.1107/S0567740880009582.
[16] J.P. Amoureux, M. Bee, J.C. Damien, Structure of adamantane, $C_{10}H_{16}$, in the disordered phase, Acta Crystallogr. Sect. B. 36 (1980) 2633–2636, https://doi.org/10.1107/S0567740880009570.
[17] S. Chang, E.F.J. Westrum, Heat capacities and thermodynamic properties of globular molecules. adamantane and hexamethylenetetramine, J. Phys. Chem. 64 (1960) 1547–1551.
[18] T.E. Jenkins, J. Lewis, A Raman study of adamantane ($C_{10}H_{16}$), diamantane ($C_{14}H_{20}$) and triamantane ($C_{18}H_{24}$) between 10 K and room temperatures, Spectrochim. Acta Part A Mol. Spectrosc. 36 (1980) 259–264, https://doi.org/10.1016/0584-8539(80)80128-0.
[19] M. Foulon, T. Belgrand, C. Gors, M. More, Structural phase transition in 1-chloroadamantane ($C_{10}H_{15}Cl$), Acta Crystallogr. Sect. B. 45 (1989) 404–411, https://doi.org/10.1107/S0108768189002739.
[20] J.L. Adcock, H. Luo, S.S. Zuberi, Aerosol fluorination of 1-chloroadamantane, 2-chloroadamantane, and methyl 1-adamantylacetate: a novel synthetic approach to 1- and 2-substituted hydryl-, methyl-, and difluoromethyl-F-adamantanes, J. Org. Chem. 57 (2002) 4749–4752, https://doi.org/10.1021/jo00043a039.
[21] J.P. Amoureux, M. Bée, J.L. Sauvajol, Crystal structure of 1-chloroadamantane, $C_{10}H_{15}Cl$, in its plastic phase, Mol. Phys. 45 (1982) 709–719, https://doi.org/10.1080/00268978200100551.
[22] I.V. Danilov, E.L. Gromnitskaya, V.V. Brazhkin, Phase transitions in 1-bromoadamantane compared to 1-chloroadamantane: similarities and unique features, Phys. Chem. Chem. Phys. 23 (2021) 23274–23279, https://doi.org/10.1039/D1CP03080A.
[23] P.M. Ivanov, D. Salvatierra, C. Jaime, Experimental (NMR) and computational (MD) studies on the inclusion complexes of 1-bromoadamantane with α-, β-, and γ-cyclodextrin, J. Org. Chem. 61 (1996) 7012–7017, https://doi.org/10.1021/jo960526v.
[24] M. Kosmowska, J. Tarasiewicz, H.A. Kołodziej, Dielectric relaxation of 1-bromoadamantane, J. Mol. Struct. 1016 (2012) 8–12, https://doi.org/10.1016/j.molstruc.2012.02.030.
[25] M.B. Charapennikau, A.V. Blokhin, A.G. Kabo, G.J. Kabo, The heat capacities and parameters of solid phase transitions and fusion for 1- and 2-adamantanols, J. Chem. Thermodyn. 35 (2003) 145–157, https://doi.org/10.1016/S0021-9614(02)00317-8.
[26] M. Kosmowska, J. Tarasiewicz, M.J. Adamczyk, Dielectric relaxation of 1-hydroxyadamantane, Chem. Phys. Lett. 579 (2013) 64–67, https://doi.org/10.1016/j.cplett.2013.06.032.
[27] A.B. Bazyleva, A.V. Blokhin, A.G. Kabo, G.J. Kabo, V.N. Emel'yanenko, S.P. Verevkin, Thermodynamic properties of 1-aminoadamantane, J. Chem. Thermodyn. 40 (2008) 509–522, https://doi.org/10.1016/j.jct.2007.08.002.
[28] O.V. Dorofeeva, M.A. Filimonova, Sublimation enthalpy of 1-aminoadamantane: comparison of theory and experiment, Chem. Phys. Lett. 711 (2018) 231–235, https://doi.org/10.1016/j.cplett.2018.09.044.
[29] J.P. Amoureux, G. Noyel, M. Foulon, M. Bée, L. Jorat, Low frequency dielectric properties of 1-cyanoadamantane $C_{10}H_{15}CN$, Mol. Phys. 52 (1984) 161–171, https://doi.org/10.1080/00268978400101121.
[30] J.P. Amoureux, M. Bee, Crystal structure of 1-cyanoadamantane, $C_{10}H_{15}CN$, in its plastic phase, Acta Crystallogr. Sect. B. 35 (1979) 2957–2962, https://doi.org/10.1107/S0567740879011043.

[31] J.L. Sauvajol, M. Bee, J.P. Amoureux, The Raman spectra of the 1-cyanoadamantane plastic phase at T = 295 K, Mol. Phys. 46 (1982) 811–826, https://doi.org/10.1080/00268978200101601.
[32] E.L. Gromnitskaya, I.V. Danilov, V.V. Brazhkin, Ultrasonic study of 1-X adamantane (X = F, Cl, Br) compounds at high pressure and at order–disorder transitions, Phys. Chem. Chem. Phys. 24 (2022) 18022–18027, https://doi.org/10.1039/D2CP02720H.
[33] P.D. Harvey, D.F.R. Gilson, I.S. Butler, Phase transitions and molecular motions in adamantane derivatives: 1-adamantanol, Can. J. Chem. 65 (1987) 1757–1760, https://doi.org/10.1139/v87-296.
[34] E.L. Gromnitskaya, I.V. Danilov, V.V. Brazhkin, Comparative study of the elastic properties of adamantane and 1-chloroadamantane at high pressure and different temperatures and at order–disorder transitions, Phys. Chem. Chem. Phys. 23 (2021) 2349–2354, https://doi.org/10.1039/D0CP04550K.
[35] N.T. Kawai, D.F.R. Gilson, I.S. Butler, Phase transitions in adamantane derivatives: 1-fluoroadamantane, Can. J. Chem. 69 (1991) 1758–1765, https://doi.org/10.1139/v91-258.
[36] P. Negrier, M. Barrio, J. Ll, D.M. Tamarit, Polymorphism in 2-X-Adamantane Derivatives (X = Cl, Br), J. Phys. Chem. B. 118 (2014) 9595–9603, https://doi.org/10.1021/jp505280d.
[37] L.A. Fraczyk, Y. Huang, A high pressure FT-IR spectroscopic study of phase transitions in 1-chloro- and 1-bromoadamantane, Spectrochim, Acta Part A Mol. Biomol. Spectrosc. 57 (2001) 1061–1071, https://doi.org/10.1016/S1386-1425(00)00423-6.
[38] A. Hédoux, Y. Guinet, J.-F. Willart, F. Capet, M. Descamps, Pressure-induced ordering in cyanoadamantane plastic crystal, Solid State Commun. 128 (2003) 267–272, https://doi.org/10.1016/S0038-1098(03)00656-2.
[39] G. Burns, F.H. Dacol, B. Welber, Lattice vibrational study of the phase transition in the plastic crystal adamantane ($C_{10}H_{16}$), Solid State Commun. 32 (1979) 151–155, https://doi.org/10.1016/0038-1098(79)91077-9.
[40] P.D. Harvey, I.S. Butler, D.F.R. Gilson, Raman study of the effect of high pressure on the order-disorder phase transition in 2-adamantanone, J. Phys. Chem. 90 (2002) 4546–4549, https://doi.org/10.1021/j100410a014.
[41] J.P. Amoureux, M. Bee, C. Gors, V. Warin, F. Baert, 1-Adamantanol, Cryst. Struct. Commun. 8 (1979) 449–454.
[42] C.E. Nordman, D.L. Schmitkons, Phase transition and crystal structures of adamantane, Acta Crystallogr. 18 (1965) 764–767, https://doi.org/10.1107/S0365110X65001755.
[43] R. Kalthoum, M.B. Bechir, A.B. Rhaiem, M.H. Dhaou, Optical properties of new organic-inorganic hybrid perovskites $(CH_3)_2NH_2CdCl_3$ and $CH_3NH_3CdCl_3$ for solar cell applications, Opt. Mater. (Amst). 125 (2022), 112084, https://doi.org/10.1016/J.OPTMAT.2022.112084.
[44] K. Trabelsi, K. Karoui, F. Hajlaoui, M. Zaghrioui, F. Jomni, A.B. Rhaiem, An organic-inorganic hybrid cadmium chloride with face-sharing $CdCl_6$ octahedral chains: synthesis, crystal structure, optical and conduction mechanisms: $[NH_2(CH_3)_2]_5Cd_3Cl_{11}$, Opt. Mater. (Amst). 134 (2022), 113100, https://doi.org/10.1016/J.OPTMAT.2022.113100.
[45] H. Tiernan, B. Byrne, S.G. Kazarian, ATR-FTIR spectroscopy and spectroscopic imaging for the analysis of biopharmaceuticals, Spectrochim, Acta Part A Mol. Biomol. Spectrosc. 241 (2020), 118636, https://doi.org/10.1016/J.SAA.2020.118636.
[46] Y. Yamamoto, H. Hoshina, H. Sato, Differences in intermolecular interactions and flexibility between poly(ethylene terephthalate) and poly(butylene terephthalate) studied by far-infrared/terahertz and low-frequency raman spectroscopy, Macromolecules. 54 (2021) 1052–1062, https://doi.org/10.1021/acs.macromol.0c02049.
[47] A. Hédoux, Y. Guinet, F. Capet, F. Affouard, M. Descamps, Raman effects under pressure in chloroadamantane plastic crystal, J. Phys. Condens. Matter. 14 (2002) 8725–8741, https://doi.org/10.1088/0953-8984/14/37/309.
[48] E. Kamińska, O. Madejczyk, M. Tarnacka, K. Jurkiewicz, K. Wolnica, W.E. Śmiszek-Lindert, K. Kamiński, M. Paluch, Anhydrosaccharides—a new class of the fragile plastic crystals, J. Chem. Phys. 148 (2018), 074501, https://doi.org/10.1063/1.5011672.
[49] B. Granzow, Hydrogen bonding and phase transitions of a group of alcohols derived from 2,2-dimethylpropane, J. Mol. Struct. 381 (1996) 127, https://doi.org/10.1016/0022-2860(96)09232-0.
[50] Y. Ren, X. Cheng, K. Yang, X. Zhu, H. Li, Y. Wang, Raman study of plastic crystal phase of cyclooctanol under high pressure with different compression rate, J. Mol. Struct. 1102 (2015) 6, https://doi.org/10.1016/j.molstruc.2015.08.006.
[51] L.A. Leites, S.S. Bukalov, Raman study of phase transitions in plastic solid 1,12 dicarbaclosododecaborane (para-carborane), J. Raman Spectrosc. 7 (1978) 235, https://doi.org/10.1002/jrs.1250070502.
[52] S.P. Andersson, O. Andersson, Relaxation studies of poly(propylene glycol) under high pressure, Macromolecules. 31 (1998) 2999–3006, https://doi.org/10.1021/ma971282z.
[53] P. Lloveras, A. Aznar, M. Barrio, P. Negrier, C. Popescu, A. Planes, L. Mañosa, E. Stern-Taulats, A. Avramenko, N.D. Mathur, X. Moya, J.-L. Tamarit, Colossal barocaloric effects near room temperature in plastic crystals of neopentylglycol, Nat. Commun. 10 (2019) 1803, https://doi.org/10.1038/s41467-019-09730-9.
[54] A. Drozd-Rzoska, S.J. Rzoska, S. Pawlus, J.L. Tamarit, Dielectric relaxation in compressed glassy and orientationally disordered mixed crystals, Phys. Rev. B. 74 (2006) 64201, https://doi.org/10.1103/PhysRevB.74.064201.
[55] T. Takigawa, J. Horinaka, Application of a clapeyron-type equation to the volume phase transition of polymer gels, Gels 6 (2020) 25, https://doi.org/10.3390/gels6030025.

Supplementary Material

Studies on the nature and pressure evolution of phase transitions in 1-adamantylamine and 1-adamantanol

Paulina Jesionek[a,b], Barbara Hachuła[a,*], Dawid Heczko[c], Taoufik Lamrani[d], Karolina Jurkiewicz[d,*], Magdalena Tarnacka[d], Maria Książek[d], Kamil Kamiński[d], Ewa Kamińska[b]

[a] *Institute of Chemistry, Faculty of Science and Technology, University of Silesia in Katowice, Szkolna 9, 40-007 Katowice, Poland*
[b] *Department of Pharmacognosy and Phytochemistry, Faculty of Pharmaceutical Sciences in Sosnowiec, Medical University of Silesia in Katowice, Jagiellonska 4, 41-200 Sosnowiec, Poland*
[c] *Department of Statistics, Department of Instrumental Analysis, Faculty of Pharmaceutical Sciences in Sosnowiec, Medical University of Silesia in Katowice, ul. Ostrogorska 30, 41-200 Sosnowiec, Poland*
[d] *Institute of Physics, Faculty of Science and Technology, University of Silesia in Katowice, 75 Pulku Piechoty 1, 41-500 Chorzow, Poland*

* Corresponding authors: e-mails: (B.H.) barbara.hachula@us.edu.pl; (K.J.) karolina.jurkiewicz@us.edu.pl

XRD data

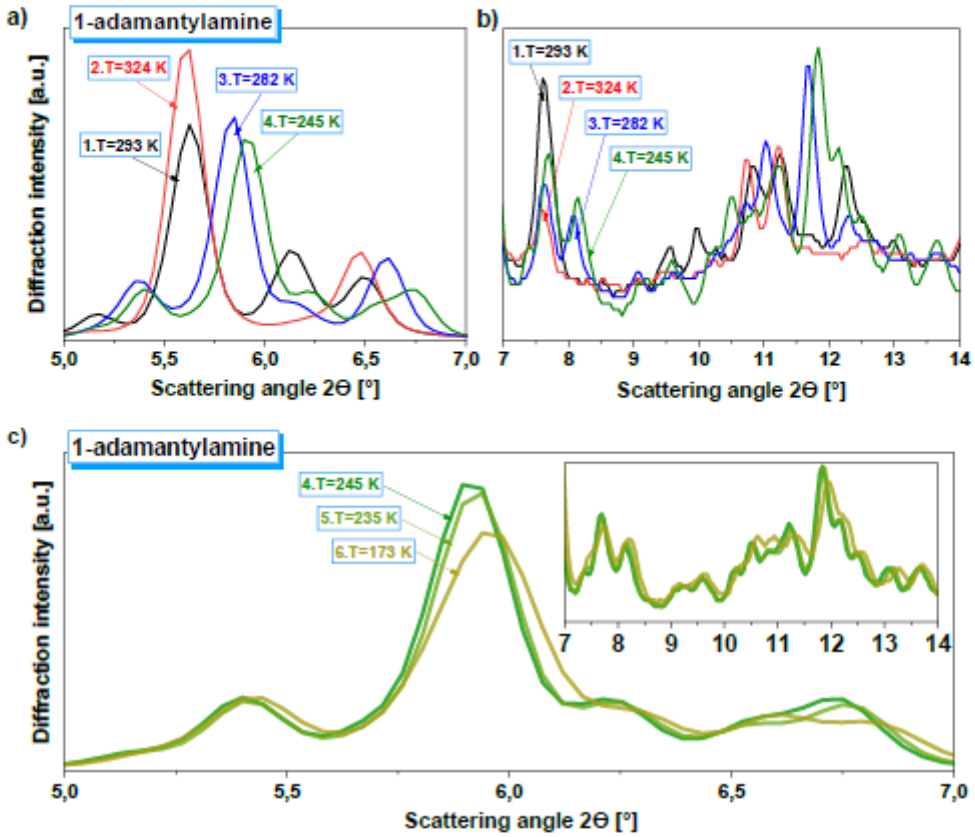

Fig. S1. XRD patterns of 1-NH_2-ADM at various temperatures (1. 293 K, 2. 324 K upon heating from 293 K, 3. 282 K upon cooling from 324 K, 4. 245 K upon cooling from 282 K) at scattering angle range of 5–7° (a) and 7–14° (b). Panel (c) shows the comparison of XRD patterns at cooling from 245 K down to 173 K.

FTIR data

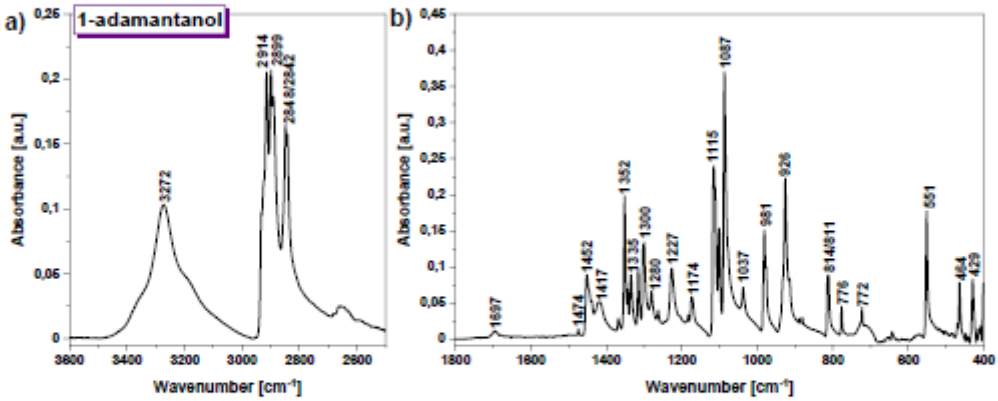

Fig. S2. ATR-FTIR spectrum of commercial 1-OH-ADM in the wavenumber region of (a) 3600-2500 cm^{-1} and (b) 1800-400 cm^{-1}.

As illustrated in Figure S2(a), the spectrum of the commercial 1-OH-ADM exhibits a broad band at 3272 cm^{-1}, assigned to the stretching vibration of hydrogen-bonded OH groups, and strong peaks in the wavenumber region 3000-2800 cm^{-1} (2914, 2899, 2848 and 2842 cm^{-1}) related to the CH stretching vibrations. According to the literature [1], the deformation vibrations of CH units are observed at lower wavenumber regions, between 1480 cm^{-1} and 1100 cm^{-1} (1474, 1368, 1352, 1344, 1335, and 1115 cm^{-1}) (Figure S2(b)). The signals at 1452 and 1417 cm^{-1} originate from the OH deformation vibrations. The stretching of the CO group is observed at 1227 cm^{-1}. The band at 1174 cm^{-1} is connected with the CH_2 twist. An intense peak at 1087 cm^{-1} and weak signal at 1037 cm^{-1} correspond to the CC stretching and CH_2 twisting vibrations. The CC stretching vibrations occur at 926, 814, 811, 776, and 722 cm^{-1}. The CCC deformation vibrations are visible in the range from 670 to 400 cm^{-1}.

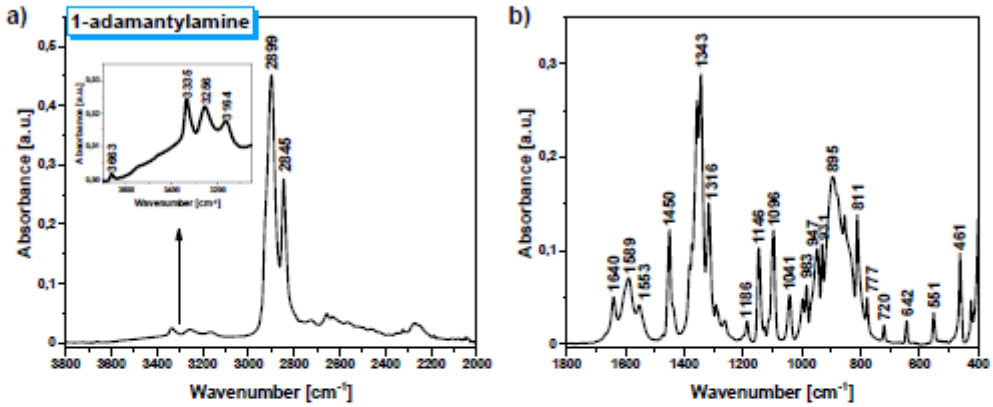

Fig. S3. ATR-FTIR spectrum of commercial 1-NH_2-ADM in the wavenumber region of (a) 3800-2000 cm^{-1} and (b) 1800-400 cm^{-1}.

As reported in the literature [2,3], the broad and complex band located in the higher wavenumber range, from 3700 cm^{-1} to 3050 cm^{-1}, is assigned to the stretching vibrations of NH bonds (**Figure S3**(a)). In detail, the weak absorption signal at 3663 cm^{-1} corresponds to the free (non-hydrogen-bonded) NH moieties (ν_{N-H}^{free}), whereas the three peaks occurring at 3335, 3256, and 3164 cm^{-1} are associated with the hydrogen-bonded (HB) NH units (ν_{N-H}^{HB}). The asymmetric and symmetric CH stretching vibrations of the adamantane skeleton (four cyclohexane rings) are observed at 2899 and 2845 cm^{-1}. A band of medium intensity due to the deformation (scissoring) vibration of the NH bonds of the amine (NH_2) group is visible in the range of 1700-1500 cm^{-1} (1640 cm^{-1}, 1589 cm^{-1}, 1553 cm^{-1}) (**Figure S3**(b)). The CN stretching absorption of the amine group is weak and occurs in the region 1090-1020 cm^{-1} (1041 cm^{-1}). The peaks observed in the lower wavenumber range (below 1500 cm^{-1}) are mainly associated with the CH deformation vibrations. The signal at 1450 cm^{-1} corresponds to the CH_2 scissoring vibration band, whereas the CH_2 wagging, rocking and twisting vibrations are noticeable in the region 1430-715 cm^{-1} [2,3]. The CC stretching absorptions occur in the region 1260-700 cm^{-1}.

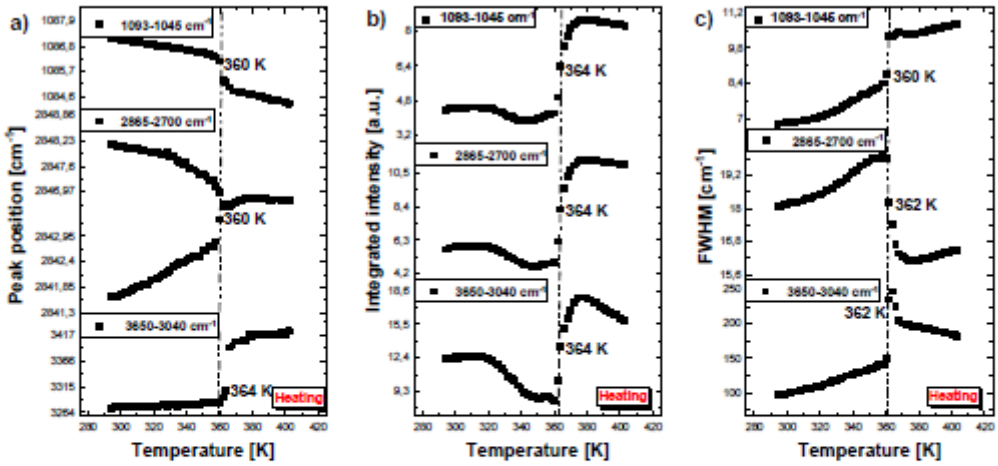

Fig. S4. Temperature dependence of peak position (a), integrated intensity (b), and FWHM (c) of the bands occurring in the regions: 1093-1045 cm^{-1}, 2895-2700 cm^{-1}, and 3650-3040 cm^{-1}, measured for 1-OH-ADM under heating.

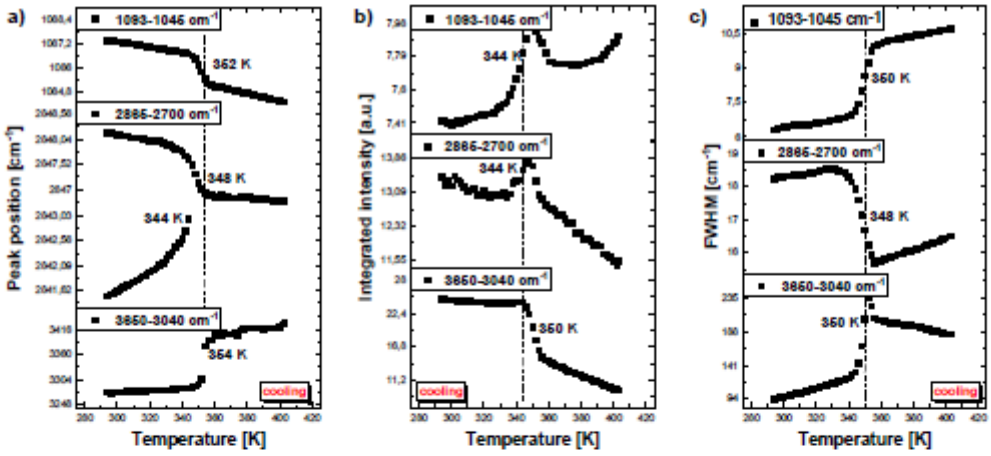

Fig. S5. Temperature dependence of peak position (a), integrated intensity (b), and FWHM (c) of the bands occurring in the regions: 1093-1045 cm^{-1}, 2895-2700 cm^{-1}, and 3650-3040 cm^{-1}, measured for 1-OH-ADM under cooling.

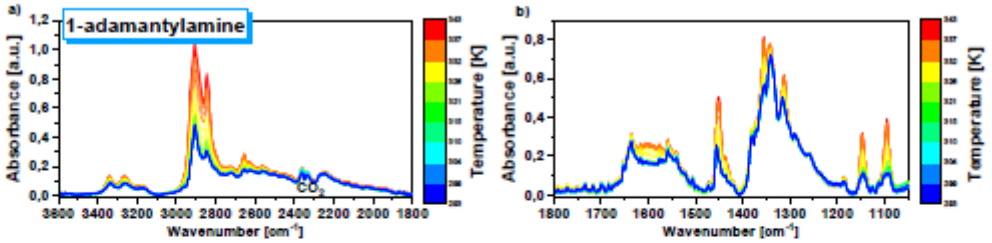

Fig. S6. FTIR spectra of 1-NH_2-ADM upon heating from 293 K to 343 K in the wavenumber regions of (a) 3600-1800 cm^{-1} and (b) 1800-1050 cm^{-1}

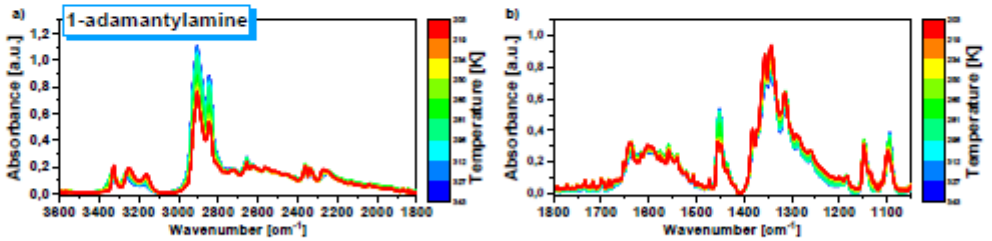

Fig. S7. FTIR spectra of 1-NH_2-ADM upon cooling from 343 K to 203 K in the wavenumber regions of (a) 3600-1800 cm^{-1} and (b) 1800-1050 cm^{-1}.

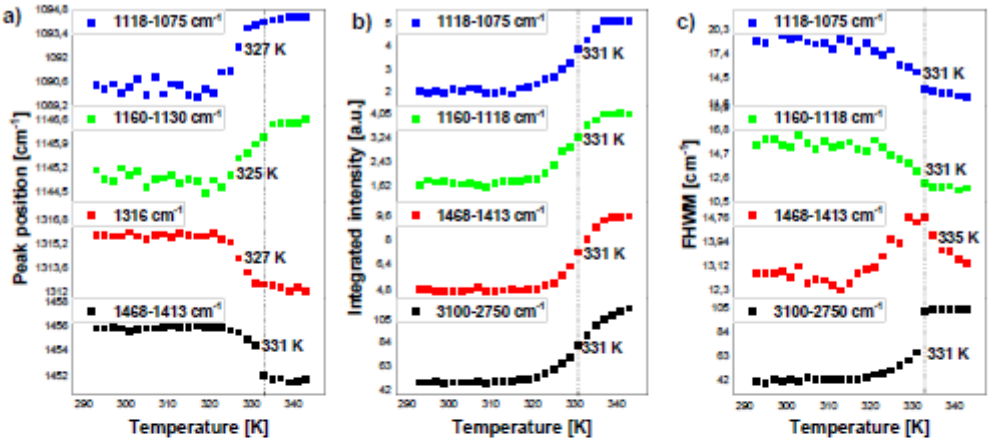

Fig. S8. The dependence of (a) the peak position, (b) the integrated intensity, and (c) the FWHM of the selected bands as a function of *T* upon heating. The vertical lines indicate the temperature at which 1-NH_2-ADM undergoes the phase transition.

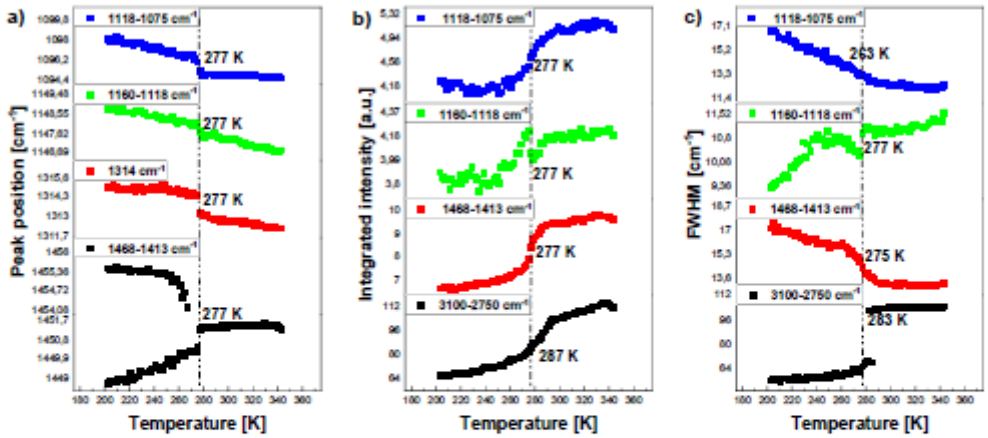

Fig. S9. The dependence of (a) the peak position, (b) the integrated intensity and (c) FWHM of the selected bands as a function of temperature upon cooling. The vertical lines indicate the temperature at which 1-NH_2-ADM undergoes the phase transition.

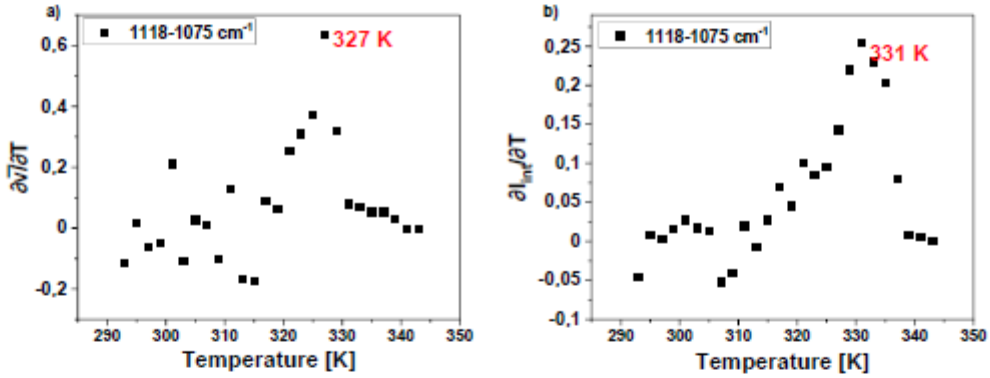

Fig. S10. The plots of first derivative of (a) the peak position (wavenumber) and (b) the integrated intensity of the band in the 1118-1075 cm^{-1} region of FTIR spectra of 1-NH_2-ADM ($\frac{\partial \nu}{\partial T}$ and $\frac{\partial I_{int}}{\partial T}$, respectively) versus temperature upon heating.

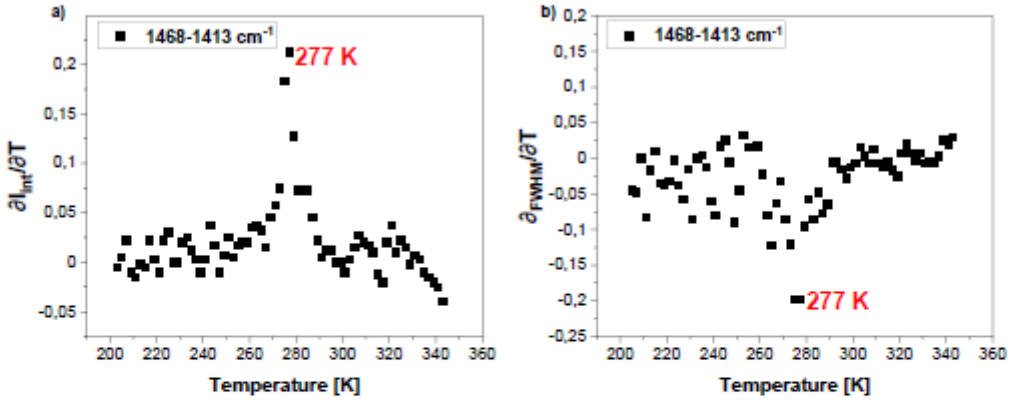

Fig. S11. The plots of first derivative of (a) the integrated intensity and (b) FWHM of the band in the 1118-1075 cm^{-1} region of FTIR spectra of 1-NH_2-ADM ($\frac{\partial I_{int}}{\partial T}$ and $\frac{\partial FWHM}{\partial T}$, respectively) versus temperature upon cooling.

Raman data

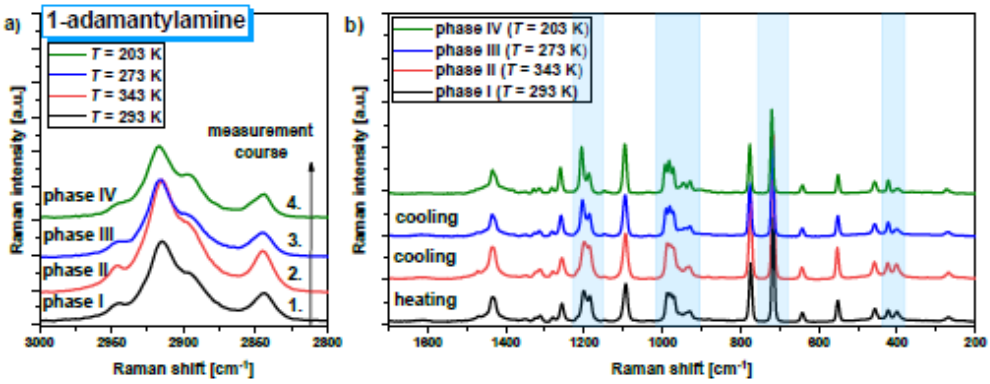

Fig. S12. Raman spectra of 1-NH_2-ADM measured at different temperatures, in the sequence indicated by numbers 1-4 in the figure, in two regions: (a) 3000-2800 cm^{-1} and (b) 1700-200 cm^{-1}. The spectral ranges analysed in the plots were highlighted for clarity.

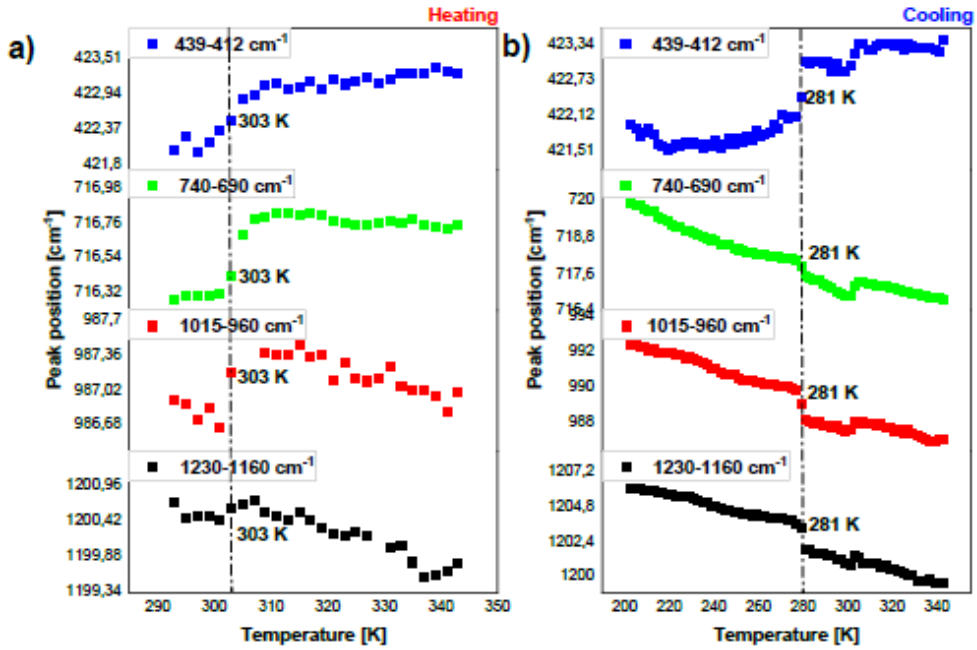

Fig. S13. The dependences of the peak position of the selected bands in Raman spectra of 1-NH_2-ADM as a function of *T* upon (a) heating and (b) cooling. The vertical lines indicate the temperature at which 1-NH_2-ADM undergoes the phase transition.

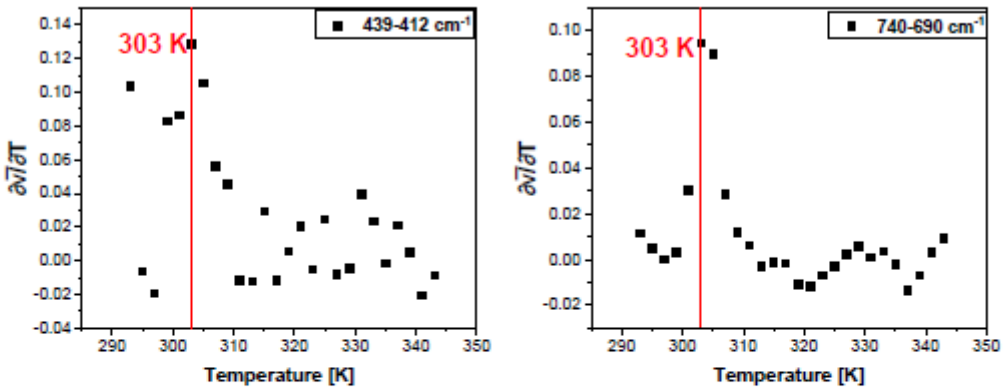

Fig. S14. The plots of first derivative of the peak position (wavenumber) of the bands ($\frac{\partial \bar{\nu}}{\partial T}$) in the 439-412 and 740-690 cm^{-1} regions of Raman spectra of 1-NH_2-ADM versus temperature upon heating.

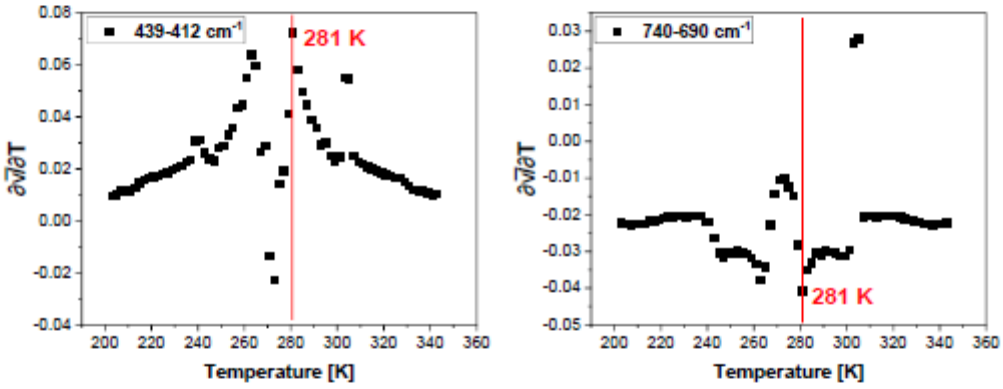

Fig. S15. The plots of first derivative of the peak position (wavenumber) of the bands ($\frac{\partial \bar{\nu}}{\partial T}$) in the 439-412 and 740-690 cm^{-1} regions of Raman spectra of 1-NH_2-ADM versus temperature upon cooling.

BDS data

Table S1. The ranges of pressures at which isothermal measurements for 1-NH_2-ADM and 1-OH-ADM were carried out.

1-NH_2-ADM		1-OH-ADM	
T [K]	p-range [MPa]	T [K]	p-range [MPa]
264	10-160	352	10-100
272.5	20-200	357	10-140
278.5	40-220	362	10-180
285	30-285	367	10-180
291	20-300	371	10-240
295	10-295	380.5	20-300
299	10-400	383	20-330
302.5	15-440		
305	10-160		
307	10-440		
309	30-170		
317	50-200		

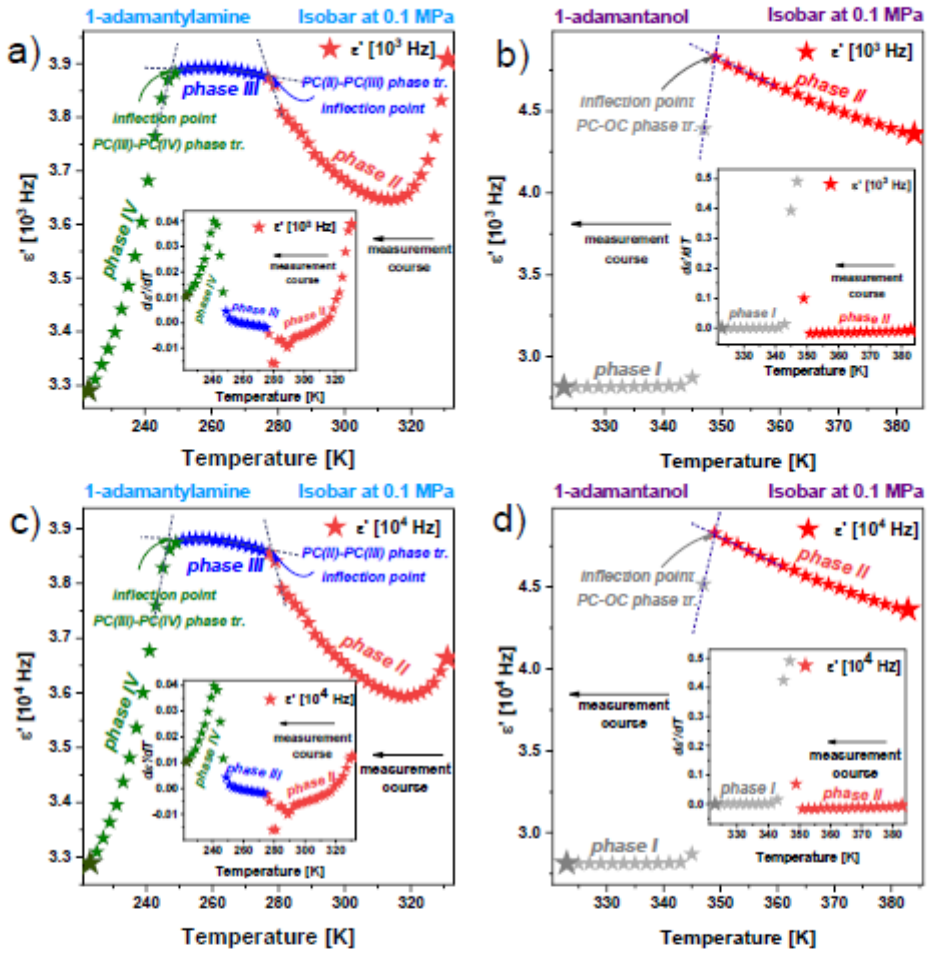

Fig. S16. Temperature dependence of the real part of the complex dielectric permittivity, ε', for 1-NH_2-ADM (a,c) and 1-OH-ADM (b,d) taken at constant f (=10^3 and 10^4 Hz) and ambient pressure, upon cooling. The insets show the derivatives of the experimental data given in the main panels.

Table S2. Temperatures of phase transitions obtained from different experimental methods for both ADM derivatives.

Experimental method	1-NH_2-ADM			1-OH-ADM
	$T_{PC(I)-PC(II)}$ [K]	$T_{PC(II)-PC(III)}$ [K]	$T_{PC(III)-PC(IV)}$ [K]	T_{PC-OC} [K]
DSC	324	282	245	343
XRD	324	282	245	343
FTIR	(325-335)	(263-287)	-	(344-354)
Raman	303	281	-	-
BDS	-	278	247	347

Crystal structure determination and analysis of an ethanol solvate of 1-NH_2-ADM

The single crystals of an ethanol solvate of 1-NH_2-ADM, suitable for the X-ray measurements, were selected under the stereoscopic microscope Stemi 2000-C (Zeiss). The measurement was performed using the four-circle SuperNova X-ray diffractometer with graphite-monochromated Mo-Kα radiation. CrysAlis^{Pro} software [4] was used for controlling the measurement procedure and data reduction.

The structure of the ethanol solvate of 1-NH_2-ADM was solved using the SHELXS-2013 program and refined with the SHELXL-2019/2 program [5]. Non-hydrogen atoms were refined with anisotropic displacement parameters. Hydrogen atoms were introduced to the structure by appropriate rigid body constraints (AFIX 13, 23 or AFIX 137) with displacement parameters $U_{iso}(H) = 1.2U_{eq}(C)$.

CCDC-2237036 contains supplementary crystallographic data for this paper. These data can be obtained free of charge from The Cambridge Crystallographic Data Centre *via*: www.ccdc.cam.ac.uk/data_request/cif.

The ethanol solvate of 1-NH_2-ADM crystallizes in the trigonal $\bar{P}3c1$ space group with half of the adamantylamine molecule in the asymmetric unit cell. The hydrogen atoms from the

amine group are disordered. Also, the ethanol molecule, used as solvent, is disordered. The molecular structure of the ethanol solvate of 1-NH_2-ADM is presented in Figure S17, while the crystal packing is shown in Figure S18. Table S3 contains the most important crystallographic information.

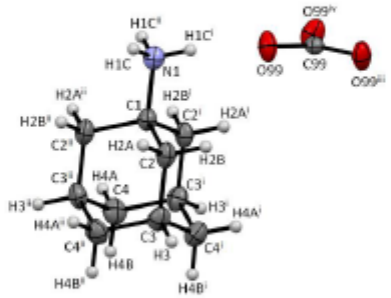

Fig. S17. Molecular structure of 1-NH_2-ADM. Displacement ellipsoids for non-H atoms are shown with 50% probability. i: 1-*y*, *x*-*y*, *z*; ii: 1-*x*+*y*, 1-*x*, *z*; iii: 1-*y*, -1+*x*-*y*, *z*; iv: 2-*x*+*y*, 1-*x*, *z*.

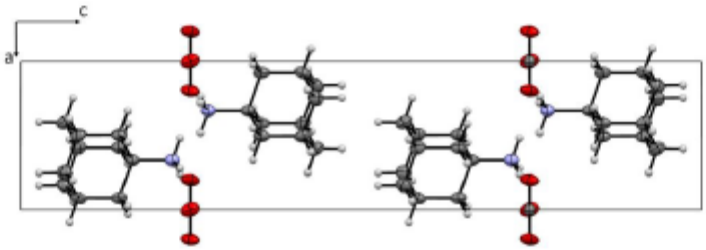

Fig. S18. Packing diagram of the structure of an ethanol solvate of 1-NH_2-ADM.

Table S3. Crystallographic information for ethanol solvate of 1-NH_2-ADM.

Empirical formula	$C_{21}H_{36}N_2O_3$
Formula weight	364.52
Temperature / K	293(2)
Wavelength / Å	0.71073
Crystal system	Trigonal
Space group	$P\bar{3}c1$
Unit cell dimensions / Å	a = 6.4335(3)
	c = 25.4901(18)
Volume / Å^3	913.69(11)
Z	2
Density (calculated) / Mg/m^3	1.325
Absorption coefficient / mm^{-1}	0.088
F(000)	400
Theta range for data collection / °	3.197 to 26.351
Index ranges	$-6 \leq h \leq 8$

	$-8 \leq k \leq 8$
	$-31 \leq l \leq 31$
Reflections collected	5267
Independent reflections	628
R(int)	0.0351
Completeness to theta = 25.242° / %	99.8
Data / restraints / parameters	628 / 0 / 42
Goodness-of-fit on F^2	1.095
Final R indices [I>2σ(I)]	R1 = 0.0383
	wR2 = 0.1016
R indices (all data)	R1 = 0.0443
	wR2 = 0.1057
Largest diff. peak and hole / $eÅ^{-3}$	0.220 and -0.180

The molecules of the ethanol solvate of 1-NH_2-ADM interact with solvent molecules *via* hydrogen bonds of the type N-H···H (Figure S19). The detailed characteristic of such intermolecular interactions is given in Table S4.

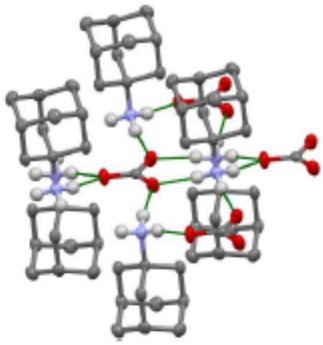

Fig. S19. Hydrogen bond network between molecules of ethanol solvate of 1-NH_2-ADM.

Table S4. Hydrogen bonds for ethanol solvate of 1-NH_2-ADM

D-H···A	d(D-H) / Å	d(H···A) / Å	d(D···A) / Å	<(DHA) / °
N1-H1A···O99	0.89	1.88	2.7650(10)	169.9
N1-H1A···O99^{i}	0.89	1.88	2.7650(10)	169.9
N1-H1A···O99^{ii}	0.89	1.88	2.7650(10)	169.9

Symmetry operators: (i) 1-*x*+*y*, 1-*x*, *z*; (ii) 1-*y*, *x*-*y*, *z*.

References

[1] P.D. Harvey, D.F.R. Gilson, I.S. Butler, Phase transitions and molecular motions in adamantane derivatives : 1-adamantanol, Can. J. Chem. 65 (1987) 1757–1760.
[2] A.B. Bazyleva, A.V. Blokhin, A.G. Kabo, G.J. Kabo, V.N. Emel'yanenko, S.P. Verevkin, Thermodynamic properties of 1-aminoadamantane, J. Chem. Thermodyn. 40 (2008) 509–522.
[3] G. Socrates, (2004) Infrared and Raman Characteristic Group Frequencies: Tables and Charts. 3rd Edition, Wiley & Sons, Chichester.
[4] Rigaku Oxford Diffraction, CrysAlis^{Pro} Software system, version 1.171.38.41q, Rigaku Corporation, Wroclaw, Poland (2015).
[5] G.M. Sheldrick, Crystal structure refinement with *SHELXL*. Acta Cryst. C71 (2015) 3-8.

3.4. **Publikacja 4 (P4):** *Comparative studies on the nature and kinetics of phase transitions in plastic crystals: Hydrogen-bonded adamantane derivatives*, J. Mol. Liq. 413 (**2024**) 125907.

Autorzy: P. Jesionek, B. Hachuła, M. Tarnacka, K. Jurkiewicz, K. Kamiński, E. Kamińska.

DOI: 10.1016/j.molliq.2024.125907

Impact Factor czasopisma z roku opublikowania pracy: 5.3

Liczba punktów ministerialnych MNiSW czasopisma z roku opublikowania pracy: 100

Mój udział w pracy polegał na zebraniu danych literaturowych, współtworzeniu hipotezy badawczej, przygotowaniu próbek 3-amino-1-adamantanolu i 1-adamantylaminy do badań, przeprowadzeniu pomiarów dielektrycznych, analizie uzyskanych wyników, opracowaniu rysunków do pracy, uczestnictwie w dyskusji wyników, redagowaniu tekstu artykułu, a także przygotowaniu odpowiedzi do recenzentów i poprawek w manuskrypcie.

Journal of Molecular Liquids 413 (2024) 125907

Contents lists available at ScienceDirect

Journal of Molecular Liquids

journal homepage: www.elsevier.com/locate/molliq

Comparative studies on the nature and kinetics of phase transitions in plastic crystals: Hydrogen-bonded adamantane derivatives

Paulina Jesionek [a,b,*], Barbara Hachuła [a], Magdalena Tarnacka [c], Karolina Jurkiewicz [c], Kamil Kamiński [c], Ewa Kamińska [b,**]

[a] Institute of Chemistry, Faculty of Science and Technology, University of Silesia in Katowice, Szkolna 9, 40-007 Katowice, Poland
[b] Department of Pharmacognosy and Phytochemistry, Faculty of Pharmaceutical Sciences in Sosnowiec, Medical University of Silesia in Katowice, Jagiellonska 4, 41-200 Sosnowiec, Poland
[c] Institute of Physics, Faculty of Science and Technology, University of Silesia in Katowice, 75 Pułku Piechoty 1, 41-500 Chorzow, Poland

ARTICLE INFO

Keywords:
3-amino-1-adamantanol
1-adamantylamine
Phase transition
Plastic crystal
Dielectric spectroscopy
Time-dependent measurements

ABSTRACT

In this paper, the results of thermal, structural, and spectroscopic studies on 3-amino-1-adamantanol (3-NH_2-1-OH-ADM) were discussed with those recently published for 1-hydroxyl and 1-amine derivatives of adamantane (1-OH-ADM, 1-NH_2-ADM). Calorimetric measurements showed that the examined compound, like 1-NH_2-ADM, is characterized by multiple thermal events in the thermogram measured on heating and cooling. Further X-ray diffraction, Fourier-transform infrared, and Raman spectroscopy investigations suggested that two of them correspond to the transition from the ordinary crystal (OC) to the plastic crystal (PC) phase I and the transition between two PC phases (PC(I) and PC(II)), while the third subtle one is rather not related to a phase transition. Interestingly, ambient pressure dielectric studies performed during heating and cooling cycles revealed changes in the imaginary and real parts of the complex dielectric permittivity at temperatures close to the temperatures of phase transitions detected by the calorimetry. Such behavior resembled that reported for 1-NH_2-ADM. Finally, isothermal time-dependent dielectric and infrared studies, supported by the analysis of asynchronous 2D-IR correlation spectra, indicated that the first endothermic peak, visible in the thermogram of 3-NH_2-1-OH-ADM over an enormously large temperature interval and related to the OC-PC(I) phase transition, similarly to the one, assigned to the PC(I)-PC(II) transition in 1-NH_2-ADM, has a character of the kinetic process. Importantly, during the annealing of 3-NH_2-1-OH-ADM at $T = 328$–343 K, we observed a clear change in the dc-conductivity as well as intramolecular dynamics related to the vibrations of CH, NH_2, and OH moieties that occur at different rates.

1. Introduction

The nature of phase transitions in disordered materials has been a unique area of research in recent decades [1–4]. This is motivated by a quest to determine the variations in the system's structure or intermolecular interactions accompanying the phase transitions. A literature survey shows a particular concern in systems undergoing pressure/temperature transitions from a phase with randomly distributed atoms/molecules to a state with a periodic pattern and long-range correlations (disorder–order phase transition) [2,5–11]. Consequently, based on experimental studies and theoretical/computational models, it is possible to gain insight into the microscopic nature of these phenomena and the unique changes in the physical properties of examined systems.

Special attention in the context of disorder–order/order–disorder phase transitions is focused on Orientationally Disordered Crystals (ODICs), also known as plastic crystals (PCs), combining solid (i.e., regular crystal) and liquid-like properties [5,12]. On the one hand, in ODICs, centers of the mass of nearly spherical molecules are translationally ordered (tend to form space groups from the higher-symmetry crystal systems) [5,13]. However, the formation of lattice defects and a lower density compared to the ordinary crystals (OCs) accompanies the dynamic orientational disorder, as in a liquid state. Furthermore, it is worth mentioning that the relaxation dynamics and thermodynamic properties of PCs are quite similar to those typical for disordered glass-forming liquids [2,11,14–16].

Among the systems forming the ODIC phases, cyclic/aromatic

* Corresponding author at: Institute of Chemistry, Faculty of Science and Technology, University of Silesia in Katowice, Szkolna 9, 40-007 Katowice, Poland.
** Corresponding author.
E-mail addresses: paulina.jesionek@us.edu.pl (P. Jesionek), ekaminska@sum.edu.pl (E. Kamińska).

https://doi.org/10.1016/j.molliq.2024.125907
Received 4 July 2024; Received in revised form 27 August 2024; Accepted 30 August 2024
Available online 7 September 2024
0167-7322/© 2024 The Author(s). Published by Elsevier B.V. This is an open access article under the CC BY license (http://creativecommons.org/licenses/by/4.0/).

compounds, such as *hexa*-substituted benzenes [17,18], *ortho*- and *meta*-carboranes [19], or adamantane (ADM) [20–22] and its derivatives (obtained by substituting one or two hydrogen atoms by e.g., halogen atoms [22–25], as well as hydroxyl [26,27], cyano [2], or amine groups [28–30]) have been intensively studied. The latter group is especially interesting due to the presence of thermally/or pressure induced OC-ODIC/PC or ODIC-ODIC phase transitions. According to the literature data, the phase behavior of ADM derivatives varies according to the substituent. As demonstrated, most of these substances (e.g., 1-chloroadamantane, 1-cyanoadamantane, and 1-bromoadamantane) during heating reveal the OC-PC phase transition before the melting point (at T = 244, 293, and 310 K, respectively) [23,31]. The exception is 1-iodoadamantane, where the high-temperature phase is not orientationally disordered [32]. One can also mention the studies on two ADM derivatives differing in the strength of hydrogen bonds (HBs), i.e., 1-adamantanol (1-OH-ADM) and 1-adamantylamine (1-NH_2-ADM), which showed one OC-PC and four PC-PC transitions (i.e., PC (I)-PC (II), PC (II)-PC (III), PC (III)-PC (IV)) in the former and the latter substance, respectively [29]. Thus, it was indicated that the nature of the side group significantly affects the character and quantity of the phase transitions. Furthermore, it is worth noting that the substituent position may influence the properties of plastic crystals. In this context, one can refer to the thermodynamic and structural studies on 1-OH-ADM and 2-OH-ADM, demonstrating that the first derivative, as mentioned above, is characterized by the presence of one transition from the OC to PC phase at T = 360 K [29], while for the second one – three phase transitions (two OC-OC and one OC-PC at T = 238.4, 322.3, and 389.3 K, respectively) are detected [26,27]. In both cases, the high-temperature phases exhibited X-ray diffraction pattern characteristic for the plastic crystals. Similar behavior, i.e., one and three phase transitions, has been observed during investigations of 1-chloroadamantane [33], (OC-PC at T = 246 K) and 2-chloroadamantane [34] (OC-OC, OC-PC, and PC-PC, at T = 224.4, 240.9, and 244.0 K, respectively). It should also be added that depending on the substitution, the plastic phase can even be suppressed, as for 1-adamantane-methanol [35] or 1,3-dibromo-adamantane [25]. Finally, one can mention the papers focusing on HBs in OC and PC phases of ADM derivatives. For example, Harvey et al., based on the results of spectroscopic studies performed on 1-OH-ADM, confirmed the presence of free hydroxyl groups in the high-temperature PC phase. That means the degree of molecular association was reduced in the ODIC compared to the OC [36]. Moreover, other investigations on 2-methyl-2-adamantanol indicated that the molecules of this compound in the crystalline state are bounded/associated due to the formation of strongly H-bonded dimeric structures [37]. However, the energy of H-bonds decreases at the OC-PC phase transition because of the low symmetry of 2-methyl-2-adamantanol molecules and the existence of orientational ensembles formed by H-bonded dimers as well as monomers in the PC phase [37].

As can be seen, the complementary thermodynamic, structural, and spectroscopic studies on the ODICs enable insight into the phase behavior as well as the hydrogen bond pattern of these molecular systems. In this paper, we combined the results of differential scanning calorimetry (DSC), X-ray diffraction (XRD), Fourier transform infrared (FTIR) spectroscopy, Raman spectroscopy, and broadband dielectric spectroscopy (BDS) measurements carried out on the 3-amino-1-adamantanol (3-NH_2-1-OH-ADM). The obtained data were compared to those previously determined for two other ADM derivatives: 1-NH_2-ADM and 1-OH-ADM [29].

2. Experimental section

2.1. Material

Neat 3-NH_2-1-OH-ADM (molecular weight M_w = 167.25 g/mol) and 1-NH_2-ADM (M_w = 151.25) with purity greater than 96 % and 97 %, respectively, were supplied from Sigma Aldrich. Due to the hygroscopicity of both investigated materials, they were dried under vacuum conditions before the experiments.

2.2. Differential scanning calorimetry (DSC)

Thermal properties of 3-NH_2-1-OH-ADM were examined using a Mettler–Toledo DSC apparatus equipped with an HSS8 ceramic sensor with 120 thermocouples and a liquid nitrogen cooling accessory. The instrument was calibrated for temperature and enthalpy using indium and zinc standards. The sample of 3-NH_2-1-OH-ADM was placed in an aluminum crucible (volume 40 mL) and sealed. Next, it was heated from room temperature up to 371 K, then cooled down to 123 K, and heated again to 353 K. A heating/cooling rate during the experiment was equal to 10 K/min.

2.3. X-ray diffraction (XRD)

Powder X-ray diffraction (XRD) studies of 3-NH_2-1-OH-ADM were performed using a D/MAX RAPID II-R diffractometer (Rigaku Denki) in the Debye – Scherrer geometry, equipped with a rotating Ag anode, a graphite (002) monochromator and an image plate detector. The wavelength of the incident beam was 0.5608 Å. The sample was probed in a glass capillary with a diameter of 1.5 mm and a wall thickness of 0.01 mm. The temperature was controlled by the 800 Series Cryostream Cooler system (Oxford Cryosystems).

2.4. Fourier transform infrared (FTIR) spectroscopy

FTIR spectra were recorded with a Nicolet iS50 spectrometer (Thermo Scientific) in the attenuated total reflectance (ATR) mode using the Low Temperature Golden Gate™ ATR accessory (Specac) with 16 scans and a resolution of 2 cm^{-1}. FTIR data of 3-NH_2-1-OH-ADM as a function of temperature were measured in the wavenumber range of 4000–400 cm^{-1} in three sequences: (i) upon heating from 293 to 353 K, (ii) upon cooling from 353 to 253 K, and (iii) upon reheating from 253 to 293 K. During the measurements, the FTIR spectrometer was purged with liquid nitrogen to effectively remove water vapor and carbon dioxide from the instrument. Time-dependent FTIR spectra were collected at a temperature of 343 K at 10-minute intervals during the phase transition process (for 1320 min; 22 h) by co-adding 16 scans at a 2 cm^{-1} resolution. OriginPro graphing software (OriginPro, Version 2022; OriginLab Corporation, Northampton, MA, USA) was used to calculate two-dimensional infrared (2D-IR) correlation spectra. The average spectrum (reference) was applied for each analysis.

2.5. Raman spectroscopy

Raman spectra were collected on a DXRxi Raman spectrometer (Thermo Fisher Scientific) equipped with an Olympus microscope with the measurement parameters: 24 mW of the 780 nm laser power at the sample, 3300–50 cm^{-1} range, full-range grating, 5 cm^{-1} spectral resolution (FWHM), 50 μm slit, the exposure time 1 s, 10 scans. Temperature was controlled by a Linkam heating/cooling stage (Linkam Scientific Instruments Ltd., Surrey, UK, model THMS600) with a stability of ± 0.01 K. The temperature changes in Raman spectra were recorded in the same sequence as during FTIR measurements, i.e., *i)* from 293 to 343 K, *ii)* from 343 to 253 K, and *iii)* from 253 to 293 K with a constant rate of 4 K/min.

2.6. Broadband dielectric spectroscopy (BDS)

Measurements of the complex dielectric permittivity, $\varepsilon^*(\omega) = \varepsilon'(\omega) - i\varepsilon''(\omega)$ of 3-NH_2-1-OH-ADM were performed using a dielectric spectrometer (Novo-Control Alpha, Hundsangen, Germany) in the frequency range from 10^{-1} to 10^6 Hz at atmospheric pressure. The powder sample

was placed between two stainless steel flat electrodes of the capacitor (diameter: 10 mm) with a 0.23 mm gap mounted on a cryostat. The temperatures were controlled by a Quatro System using a dry nitrogen gas cryostat with stability better than 0.1 K. Measurements were taken in the following temperature ranges: 296–364 K upon heating and 364–282 K upon cooling.

Time-dependent BDS experiments for 3-NH_2-1-OH-ADM were carried out at $T = 328$, 333, 338, and 343 K, while for 1-NH_2-ADM at $T =$ 308, 311, 316, and 319 K.

3. Results and discussion

3.1. DSC data

At first, we performed calorimetric measurements to entirely characterize the thermal properties of 3-NH_2-1-OH-ADM and compare them with those previously reported for 1-NH_2-ADM and 1-OH-ADM. In Fig. 1 (a), DSC curves of the examined compound, recorded on heating and cooling (with a rate of 10 K/min), are presented. As can be seen, during the first DSC scan (dark green line), there is one strong, broad endothermic peak at $T = 352$ K in the thermogram. Interestingly, the temperature of this thermal event is between the temperature of **phase I** (PC(I))-**phase II** (PC(II)) transition in 1-NH_2-ADM (at $T = 324$) and **phase I** (OC)-**phase II** (PC) transition 1-OH-ADM (at $T = 362$ K). It is worth mentioning that in contrast to 1-NH_2-ADM and 1-OH-ADM, where an additional endothermic peak at $T = 458$ and 493 K, associated with the sublimation phenomenon, was detected (see Fig. 1 (b,c)) [29], there is no such peak upon heating in the case of 3-NH_2-1-OH-ADM. It is due to the sample flash point at $T = 383$ K, which made it impossible to carry out DSC measurements at high temperatures. Subsequently, 3-NH_2-1-OH-ADM was measured on cooling (down to 123 K, blue line) and heating (up to 353 K, light green line). As shown in Fig. 1 (a), the DSC curve recorded on cooling shows the presence of the two thermal (exothermic) events at $T = 309$ and 293 K, while on heating, only one thermal event at $T = 341$ K is visible. Such a scenario suggests the presence of multiple phase transitions in this compound. It can also be stated that some phases are metastable with respect to others, emphasizing/indicating their monotropic character at ambient pressure [38]. Notably, a similar behavior upon cooling, i.e., two exothermic peaks related to the transitions between **phases II** (PC(II)) and **III** (PC(III)) at $T = 282$ K as well as **III** (PC(III)) and **IV** (PC(IV)) at $T = 245$ K, was observed for 1-NH_2-ADM (see Fig. 1 (b)). However, in this case, both thermal events were also detected during further heating (herein, just one is observed) but at slightly higher temperatures (at $T = 248$ and 288 K) [29]. On the other hand, the thermograms measured for 1-OH-ADM revealed only one: **phase II** (PC)-**phase I** (OC) transition at $T = 343$ K (on cooling) and $T = 362$ K (on heating), see Fig. 1 (c). Having that in mind, further diffraction, FTIR, Raman, and dielectric studies were performed to verify, what is the true nature of thermal events observed in DSC curves of 3-NH_2-1-OH-ADM.

3.2. XRD data

The XRD pattern of commercial 3-NH_2-1-OH-ADM at 293 K exhibits Bragg peaks typical for the crystalline OC phase (indicated as **phase I** in Fig. 2 (a)). However, according to our knowledge, the crystal structure of 3-NH_2-1-OH-ADM has not yet been resolved. On heating, around 353 K, a transition was observed to **phase II**, which exhibits typical features for the transformation from OC to PC phase. The crystal lattice changes towards a higher symmetry system, and the diffraction maxima for wider scattering angles are more damped than the peaks for OC. Similar behavior was observed on heating for 1-OH-ADM and 1-NH_2-ADM [29], which also form PC phases. On cooling of **phase II** from 363 K, another phase transition was observed at 313 K, analogously to 1-OH-ADM and 1-NH_2-ADM (Fig. 2 (b,c)). However, contrary to 1-OH-ADM, 3-NH_2-1-OH-ADM did not revert to the starting **phase I**. The system evolved to a

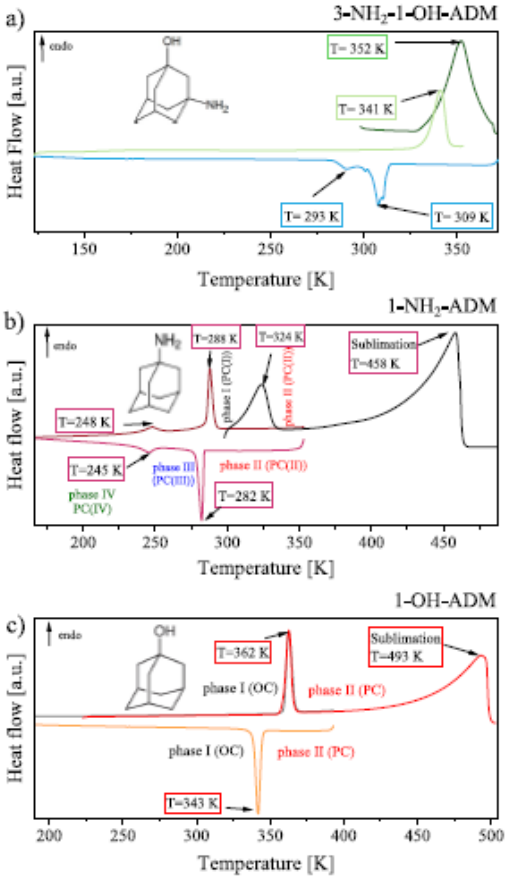

Fig. 1. DSC thermograms obtained during the heating and cooling of the three ADM derivatives: 3-NH_2-1-OH-ADM (a), 1-NH_2-ADM (b) [29], and 1-OH-ADM (c) [29], with the rate of 10 K/min. 3-NH_2-1-OH-ADM (a) was heated from 293 K to 371 K (dark green line), then cooled down to 123 K (blue line), and reheated to 353 K (light green line). 1-NH_2-ADM (b) and 1-OH-ADM (c) were heated from 293 K to 493 and 503 K (black and red lines)), respectively, then new samples were heated from 293 to 353 K (1-NH_2-ADM) or 393 K (1-OH-ADM), then cooled down to 160 K (pink line) or 123 K (orange line), and heated again up to 353 K (burgundy line) or 393 K (grey line). The arrows indicate temperatures of respective phase transitions. In the insets, the chemical structures of these compounds are presented.

space group with lower symmetry, but the wide-angle peaks remained suppressed, with an analogy to 1-NH_2-ADM. Thus, we hypothesized that this may indicate the formation of another PC system, which was denoted as **phase III**. This phase was stable on further cooling from $T =$ 313 K down to $T = 288$ K and even much below this T, where the same sequence of diffraction maxima suggested the presence of the same translational order of molecules. However, we noted peculiar behavior of the amplitude of the most intense maximum around 5.7° that decreased with a drop in temperature (see the inset in Fig. 2 (a)) in the T-range, where a small exothermic peak was observed in the thermogram recorded on cooling ($T = 293$ K). It should also be added that **phase III** was stable upon further cooling to 173 K and reheating the sample to room temperature.

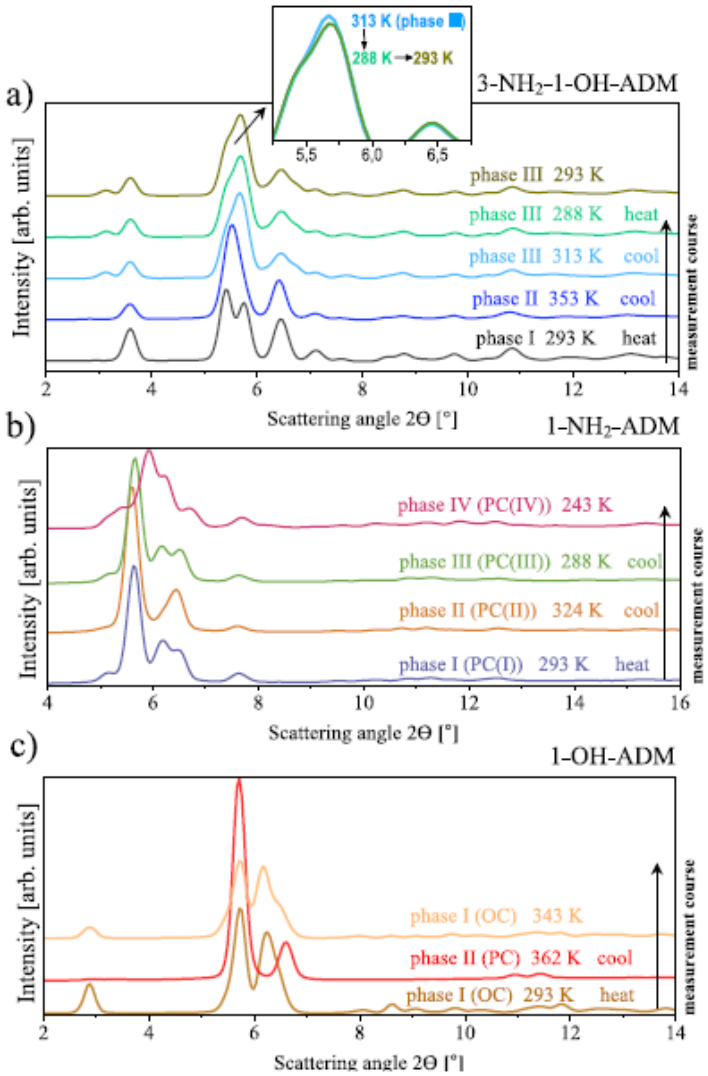

Fig. 2. XRD patterns of the three ADM derivatives: 3-NH_2-1-OH-ADM (a), 1-NH_2-ADM (b), and 1-OH-ADM (c) measured at indicated temperatures (in various phases). Data for the two latter compounds were taken from Ref. [29]. In the case of 3-NH_2-1-OH-ADM (a), the sample was heated from 293 to 353 K, then cooled down to 288 K, and heated again up to 293 K. 1-NH_2-ADM (b), and 1-OH-ADM (c) were initially heated to 324 K and 362 K, respectively, and then cooled down to 243 K (1-NH_2-ADM) and 343 K (1-OH-ADM). The inset in panel (a) presents a comparison of the amplitude of the most intense peak at around 5.7° obtained for 3-NH_2-1-OH-ADM at T = 313, 288, and 293 K.

3.3. FTIR and Raman data

Subsequently, to obtain more information about the molecular reorientation processes related to the phase transitions in this compound, complementary FTIR and Raman measurements on the commercial crystalline samples of 3-NH_2-1-ADM-OH have been carried out. We started our study by assigning the vibrational bands in the spectra measured at 293 K to the bending or stretching of a specific bond (Fig. S1; for further information, please see the Supplementary Material, SM). Next, FTIR and Raman spectra of 3-NH_2-1-ADM-OH were measured as a function of temperature upon heating and cooling runs. As shown in Fig. 3 (a,b), the FTIR spectrum of room-temperature phase I is typical for molecules in the fully ordered crystalline phase, where the numerous splitting of the bands arising from the intermolecular dipolar interactions between molecules is observed. One can see that the most visible splitting occurs for the bands located in the following wavenumber regions: ~2950–2865 cm^{-1} (C—H stretching), ~1650–1550 cm^{-1} (N—H deformation), 1400–1290 cm^{-1} (CH_2 wagging) and

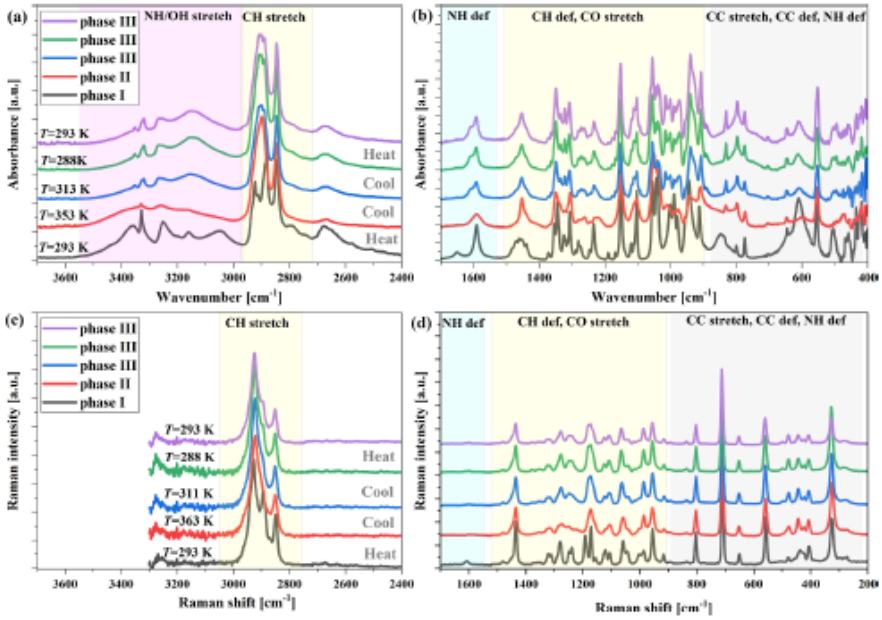

Fig. 3. FTIR (a,b) and Raman (c,d) spectra of 3-NH_2-1-OH-ADM measured at different temperatures in the regions of (a) 3700–2400 cm^{-1}, (c) 3300-2400 cm^{-1} and (b,d) FTIR: 1700–400 (Raman: 1700–200) cm^{-1}. FTIR and Raman spectra were collected during the initial heating samples from room temperature to 353 K and 363 K, respectively, then cooling down to 288 K and reheating to 293 K.

1080–960 cm^{-1} (CH_2 twisting, C—C stretching). It should be added that similar splitting is noticed for the bands occurring in the Raman spectrum, i.e., 1335–1300 cm^{-1}, 1260–1220 cm^{-1}, 1210–1150 cm^{-1}; 1135–1085 cm^{-1} (C—H deformation) (Fig. 3 (e,d)). Importantly, as the temperature increases, both FTIR and Raman spectra strongly change; the peaks become broader and blurred, and the band splitting disappears, i.e., each doublet gradually merges into a single broad band. It indicates that the highly ordered low-temperature **phase I** undergoes a solid–solid phase transition to the orientationally disordered high-temperature **phase II** at 353 K. Interestingly, after the lowering temperature from 353 to 313 K, slight differences in FTIR and Raman spectra (with maintained the overall profile of the analyzed bands) are noticeable. Namely, the shape of the complex OH/NH stretching band occurring in the higher frequency region (3600–3000 cm^{-1}) of the IR spectrum changes a little, i.e., the intensity of the lower frequency component of this band increases (the peak maximum at 3153 cm^{-1}), while the higher frequency one decreases relative to those measured at 353 K, and the peak at ca. 3330 cm^{-1} splits into doublet (3328 and 3321 cm^{-1}). Then, the CH stretching peak at 2899 cm^{-1} weakly splits into a triplet (2907, 2902, and 2891 cm^{-1}), and the other signals located at 1590 cm^{-1} (N—H deformation), 1349 cm^{-1} (CH_2 bending), or 1011 cm^{-1} (CH_2 twisting) split into two components at 313 K (1608 and 1592 cm^{-1}; 1349 and 1337 cm^{-1}; 1015 and 1002 cm^{-1}), respectively, probably due to the coupling of vibration modes of molecules differing in the orientational order in a unit cell (showing random small angle rotations). Further lowering the temperature to 288 K reveals very subtle anomalies in FTIR or Raman spectra, i.e., a variation in the intensity ratio of the OH/NH band components and the splitting of the CH stretching band. Nevertheless, one can state that generally, the spectra collected around $T = 288$ K and much below this temperature resemble the one measured for **phase III** at 313 K, suggesting considerable similarity in terms of the crystal lattices, the structural organization of molecules, and the disorder of CH_2 units in these two phases. This result is fully consistent with XRD investigations, where no change in the translational order of molecules is noted around the thermal event observed at $T = 293$ K. Finally, it should also be stressed that the cooling and reheating of the sample from 253 to 293 K also does not cause significant variations in the spectra. Thus, **phase III** is stable after the whole measurement course (heating/cooling cycles), and the initial **phase I** is not restored.

The above experimental data indicate some similarity in the behavior of 3-NH_2-1-OH-ADM with that of 1-OH-ADM and 1-NH_2-ADM (Fig. S2 in the SM). At room temperature, the spectra of 3-NH_2-1-OH-ADM are typical for the OC phase, which transforms into the PC phase upon heating. This transition is evident from the characteristic splitting of bands in **phase I**, which disappears upon the conversion to PC **phase II**, indicating variations in the sample mobility and the phase nature (crystalline vs. plastic) under temperature changes (most remarkable changes are visible in the CH stretching band region highlighted in Fig. S2). Such a scenario resembles the one observed for 1-OH-ADM, as it also exists as an ordered crystal (OC **phase I**) at 293 K and transforms into a PC **phase II** at elevated T. However, for this ADM derivative, a reversible PC–OC phase transition is detected upon cooling. On the other hand, the spectra of the low-temperature **phase III** of 3-NH_2-1-OH-ADM look very similar to those of PC **phase II**, not the initial OC **phase I** in 1-OH-ADM. Generally, abrupt changes in the spectra during temperature reduction are not detected, suggesting the plastic nature of 3-NH_2-1-OH-ADM in **phases II and III**. Note that nearly the same spectral behavior was observed in the case of 1-NH_2-ADM, exhibiting four PC phases with very similar IR spectral profiles.

3.4. BDS data

After the FTIR and Raman studies, we performed BDS measurements

of 3-NH_2-1-OH-ADM. Experiments were done at ambient pressure in a wide temperature range. In Fig. 4, the loss spectra (frequency dependences of ε'', i.e., the imaginary part of the complex dielectric permittivity, ε^*) of the investigated compound are shown. As can be seen, the dielectric response evolves with temperature both during heating and cooling cycles. The data obtained during heating the sample from 298 to 364 K (see Fig. 4 (a)) indicate the presence of a subtle relaxation process (originating probably from the spatio-temporal thermal fluctuations of the —OH group, connected to the hydrogen mobility due to the dynamical character of interaction within the disordered phase), which becomes apparent with increasing T. Interestingly, at around $T = 352$ K, corresponding to the maximum of the endothermic event (related to the I–II, i.e., OC–PC(I) phase transition) in DSC thermogram (Fig. 1 (a)), this loss peak is nearly entirely suppressed by the contribution of the dc-conductivity (a process, which can be related to the charge transport of ionic impurities as well as proton hopping along H bonded molecules connected via hydroxyl and amine groups). However, as illustrated in Fig. 4 (b), during subsequent cooling, at around $T = 316$ K (close to the temperature at which the thermal event connected to the II-III phase transition is detected in the DSC thermogram, Fig. 1 (a)), the relaxation process can be again observed in the spectra. It is also worth mentioning that at $T = 294$ K, which corresponds to the T of the maximum of a subtle peak in the DSC curve, only slight variations in dielectric loss spectra are visible.

Subsequently, we analyzed frequency dependences of the real part of dielectric permittivity, ε', for 3-NH_2-1-OH-ADM. In Fig. 5 (a), the results obtained upon cooling are presented. As can be seen, ε' varies significantly at the temperature corresponding to the transition between phases II and III (the rapid decrease in ε' is particularly visible at around $T = 320$ K). To verify these observations, as well as to estimate the temperature of this phase transition directly, we have plotted ε' measured at a constant frequency, $f = 10^5$ Hz, as a function of temperature (see Fig. 5 (b)). It can be seen that $\varepsilon'(f = 10^5$ Hz) first increases during cooling, and at around 320 K, it sharply decreases. Then, at $T \sim 300$ K, there is a slight variation (drop) in ε' vs. T dependence, and subsequently, dielectric permittivity remains nearly constant up to 284 K. Importantly, the changes in ε' of the investigated compound are also visible in Fig. 5 (c), illustrating the derivative of experimental data (i.e., ε' measured at $f = 10^5$ Hz) presented versus T.

It should be mentioned that a similar procedure has been performed for 1-NH_2-ADM and 1-OH-ADM [29]. In the case of the amine derivative, we found that ε' ($f = 10^5$ Hz) increases with cooling down to ~275 K (PC (II)-PC(III)), then it remains almost constant up to 249 K (PC(III) to PC (IV)), and, on further cooling it decreased. Note also that for 1-OH-ADM, a sharp decrease in ε' at the phase II (PC)-phase I (OC) transition temperature ($T_{PC\text{-}OC}$=347 K) was detected. The phase behavior of 3-NH_2-1-OH-ADM resembles that reported for 1-NH_2-ADM [29]. However, it should be stressed that in contrast to 1-NH_2-ADM, evident changes in temperature dependences of ε' ($f = 10^5$ Hz) are visible only at one temperature – corresponding to the phase transition at $T \sim 320$ K, which slightly exceeded that determined from the calorimetry, $T = 309$ K. At the T region, where the second, small thermal peak was detected in the thermogram measured on cooling – Fig. 1 (a), the variations in ε' vs. T plot are very subtle. Taking into account the outcomes of XRD and FTIR/Raman methods, one can state that the dielectric permittivity fluctuations at $T = 320$ K (Figs. 4 and 5), which reflect changes in the mobility of the sample, correspond most likely to the transitions between two PC phases, i.e., PC(I)-PC(II) in 3-NH_2-1-OH-ADM.

Aside from analyzing the real part of dielectric permittivity, we also plotted the dc- conductivity (σ) as a function of temperature for 3-NH_2-1-OH-ADM (see Fig. S9 in the SM). Note that to determine the values of σ, dielectric data collected during cooling cycles (Fig. 4 (b)) were fitted using the Havriliak-Negami (HN) function [39]:

$$\varepsilon(\varpi)^* = \frac{\sigma}{\varepsilon_0 \varpi} + \varepsilon_\infty + \frac{\Delta\varepsilon}{[1 + (i\omega\tau_{HN})^\alpha]^\beta}, \quad (1)$$

where ε_0 is the vacuum permittivity, ϖ is an angular frequency ($\varpi = 2\pi f$), ε_∞ is the high-frequency limit permittivity, $\Delta\varepsilon$ is the dielectric relaxation strength, τ_{HN} is the HN relaxation time, α and β are the shape parameters that represent the symmetric and asymmetric broadening of a relaxation peak. Importantly, σ vs T plot (Fig. S9) showed visible changes in the dc-conductivity values in the vicinity of the temperature of calorimetric phase transition at $T \sim 320$ K. Hence, one can state that based on BDS data, we could easily capture the transition between phases II and III. Unfortunately, we were not able to measure the dc-conductivity around the T of the exothermal event at 293 K recorded in the DSC curve

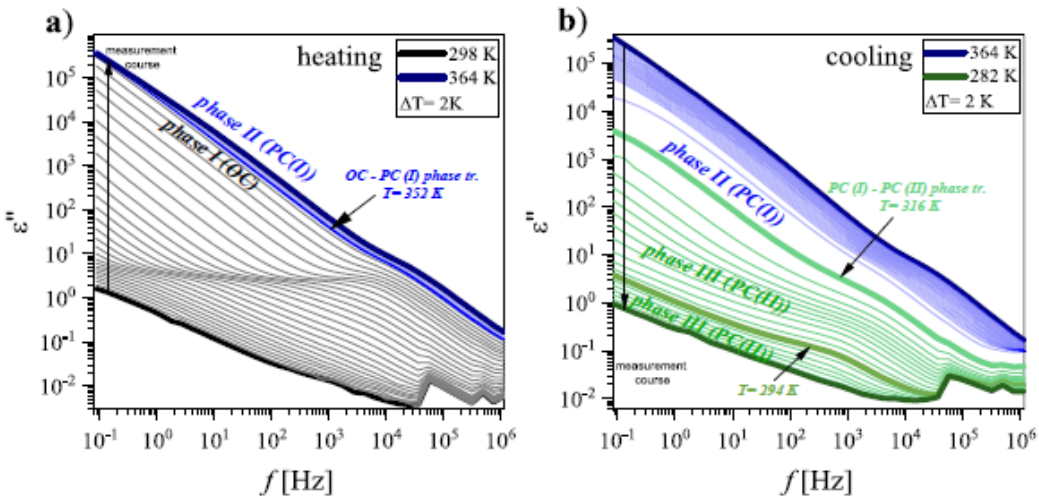

Fig. 4. Dielectric spectra measured for 3-NH_2-1-OH-ADM at ambient pressure, in a wide temperature range, during heating from 298 K to 364 K (a) and subsequent cooling to 282 K (b). Arrows denote temperatures of respective phase transitions. Various phases are marked with different colors.

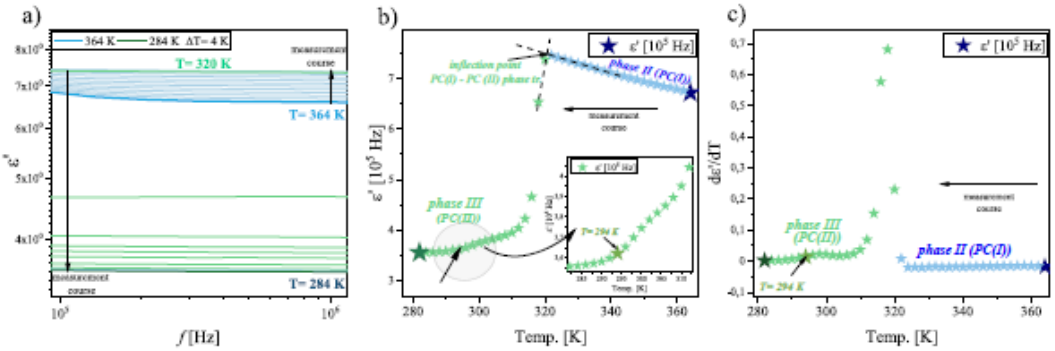

Fig. 5. (a) Frequency dependence of the real part of the complex dielectric permittivity, ε', for 3-NH_2-1-OH-ADM at ambient pressure upon cooling. In panel (b), the temperature dependence of ε', taken at constant f (=10^5 Hz), is presented. Panel (c) shows the derivatives of the experimental data given in the panel (b).

measured on cooling (Fig. 1 (a)). However, the analysis of the temperature evolution of the real part of the permittivity revealed subtle changes around this *T*. Considering the results of temperature-dependent XRD studies supported by further FTIR and Raman investigations, it should be stressed that the transitions between phases I and II as well as II and III in 3-NH_2-1-OH-ADM are due to OC-PC(I) and PC(I)-PC(II) transformations. On the other hand, the presence of a thermal peak at $T = 293$ K must be due to some variation in the orientational disorder within the sample since there was a noticeable fluctuation in the permittivity in dielectric investigations that reflects the molecular mobility of the studied sample. Herein, it is worth mentioning that subtle variations in the orientational order can exist without any change in the symmetry of the lattice (for example, in the case of 1-Cl-ADM, it has been shown that changes in the asymmetry of the orientational diffusion coefficient give rise to a change in the specific heat [33,40]).

3.5. Time-dependent BDS and FTIR data

In the final stage of our investigations, we conducted a series of isothermal BDS measurements at four temperatures below $T = 352$ K for 3-NH_2-1-OH-ADM. The motivation of these time-dependent experiments was to gain insight into the character of the OC-PC (I) phase transition in this compound (which, according to DSC data, occurs over enormously large temperature intervals, Fig. 1 (a)). Note that due to the same scenario observed for 1-NH_2-ADM (a broad peak in the DSC curve at $T = 324$ K denoting the PC(I)-PC(II) transition), we decided to carry out similar experiments at four different *T* below 324 K also for this

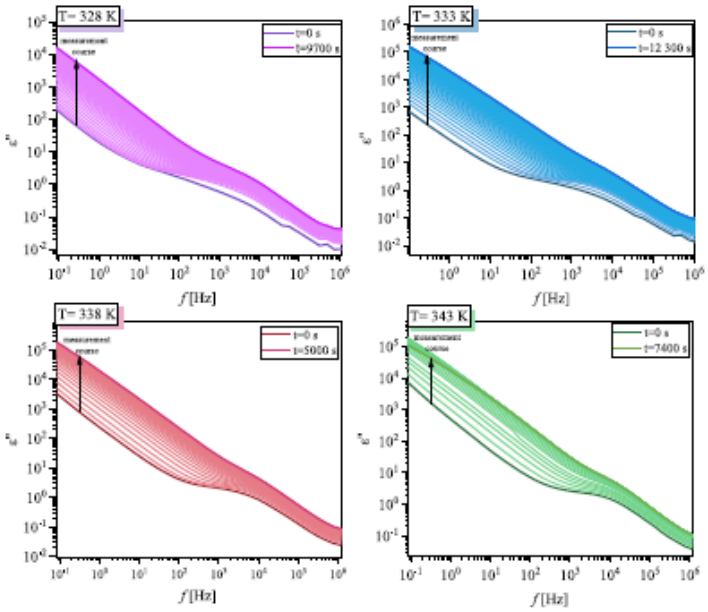

Fig. 6. Time evolution of the imaginary part of the complex permittivity at constant temperatures for 3-NH_2-1-OH-ADM.

compound. Herein, one can mention that nearly 20 years ago, a wide thermal peak in the DSC curve with a maximum at $T = 363$ K was reported for another plastic crystal, caffeine [41]. Descamps et al., based on the results of isothermal time-dependent structural studies (strictly time dependence of X-ray intensity of one characteristic peak of form I and one of form II) carried out at T close to the maximum of this very broad thermal event, suggested the kinetic nature of the transformation from metastable, undercooled form I towards form II in this compound. The same outcomes were drawn from isothermal dielectric spectroscopy measurements performed at the same T [41]. It was shown that at $T = 363$ K, the maximum of dielectric loss peak of caffeine gradually decreases with time, indicating that the rotating dipoles contribute less to the polarization as the transformation to phase II progresses. Hence, the authors confirmed that the transition between phases I (PC) and II (OC) at $T = 363$ K is a physical phenomenon, which, however, has the character of the kinetic process. In Fig. 6 and Fig. S10 in the SM, time dependences of ε'' collected for 3-NH_2-1-OH-ADM and 1-NH_2-ADM, respectively, at indicated T, are presented. As illustrated in both figures, similar to caffeine, the dielectric response of the examined ADM derivatives evolves with the time of the experiment. This effect is, however, more noticeable in the case of 3-NH_2-1-OH-ADM. Moreover, for this ADM derivative, dielectric spectra shift towards higher frequencies with time, which is the opposite scenario than that observed for 1-NH_2-ADM (the shift towards lower f, see Fig. S10). It can also be noted that the subtle relaxation process, visible at the beginning of annealing measurements performed for 3-NH_2-1-OH-ADM, is gradually suppressed by the contribution of dc-conductivity. Taking all this into account, one can suppose that as for caffeine, also the OC-PC(I) transition in 3-NH_2-1-OH-ADM and the PC(I)-PC(II) transition in 1-NH_2-ADM have features of the kinetic process.

To explore in detail the kinetics of these phase transformations, the dc-conductivity (σ) measured upon the annealing procedure of both ADM derivatives was renormalized using the following equation:

$$\sigma_n = \frac{\sigma(0) - \sigma(t)}{\sigma(0) - \sigma(\infty)} \quad (2)$$

where $\sigma(0)$ is the value of dc-conductivity at the beginning of the phase transition (at phase I: OC), $\sigma(\infty)$ is the value, which refers to the final state (phase II: PC(I)), and $\sigma(t)$ is the value at the time, t. In panels (a) and (b) of Fig. 7, log σ_n for both samples have been plotted versus time. As can be seen, the OC-PC(I) (3-NH_2-1-OH-ADM) and PC(I)-PC(II) (1-NH_2-ADM) transitions slow down with decreasing temperature. To quantify this effect and determine the rate constant (k) for the OC-PC(I) phase transition in 3-NH_2-1-OH-ADM, the exponential decay function was used:

$$\sigma_n = \sigma_0 \exp(-kt) \quad (3)$$

As can be seen in the main panel of Fig. 7 (a), Eq. (3) describes very well the presented kinetic curves (solid grey lines), indicating the first-order kinetics of this phase transition. The same fitting procedure was also attempted to apply for the analysis of isothermal data determined for 1-NH_2-ADM (see Fig. 7 (b)). Unfortunately, in this case, Eq. (3) turned out to be insufficient to describe the experimental data. Considering this, we utilized the Avrami equation [42]:

$$1 - \sigma_n = \exp(-kt^n) \quad (4)$$

where n is the Avrami exponent (herein, $n = 1.6$ was obtained). Subsequently, the rate constants (k) determined for 3-NH_2-1-OH-ADM and 1-NH_2-ADM were plotted as a function of inverse temperature in the insets in Fig. 7 (a,b). The analysis of these dependencies using the Arrhenius equation:

$$k = k_0 \exp\left(\frac{E_a}{RT}\right) \quad (5)$$

where k_0 is the pre-exponential factor and R is a gas constant, enabled us to estimate the activation barrier (E_a) for the respective phase transitions. Interestingly, the value obtained for the OC-PC(I) transition in 3-NH_2-1-OH-ADM ($E_a = 88$ kJ/mol) was higher compared to that determined for the PC(I)-PC(II) transition in 1-NH_2-ADM ($E_a = 62$ kJ/mol).

Additionally, to support the outcomes of isothermal dielectric studies, we performed time-dependent ATR-FTIR measurements of 3-NH_2-1-OH-ADM at $T = 343$ K. In Fig. 8, the spectral changes of 3-NH_2-1-OH-ADM in two regions of (FTIR) 3700–2400 and 1700–400 cm^{-1} are presented as a function of the isothermal annealing time (22 h). They are well visible in Fig. S3 in the SM, which presents a comparison of the IR spectra recorded at the beginning of the measurement and after 22 h. Note that we also calculated the difference FTIR spectra by the subtraction of the initial spectrum from the time-dependent spectra, as well as the synchronous and asynchronous 2D-IR correlation spectra, to identify the specific sequence of the bands during the isothermal annealing process of 3-NH_2-1-OH-ADM (for more details, please see Figs. S4–S8 in the SM and the description). It can be mentioned that the

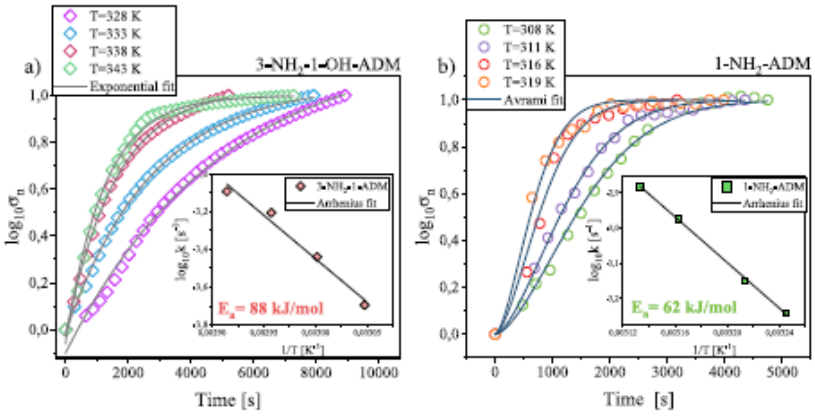

Fig. 7. Time evolution of the normalized dc-conductivity for the measurements carried out at selected T for 3-NH_2-1-OH-ADM (a) and 1-NH_2-ADM (b). Grey and navy blue solid lines are exponential and Avrami fits, respectively. In the insets, the temperature dependences of the logarithm of rate constant (k) are presented. The black solid lines denote the Arrhenius fits.

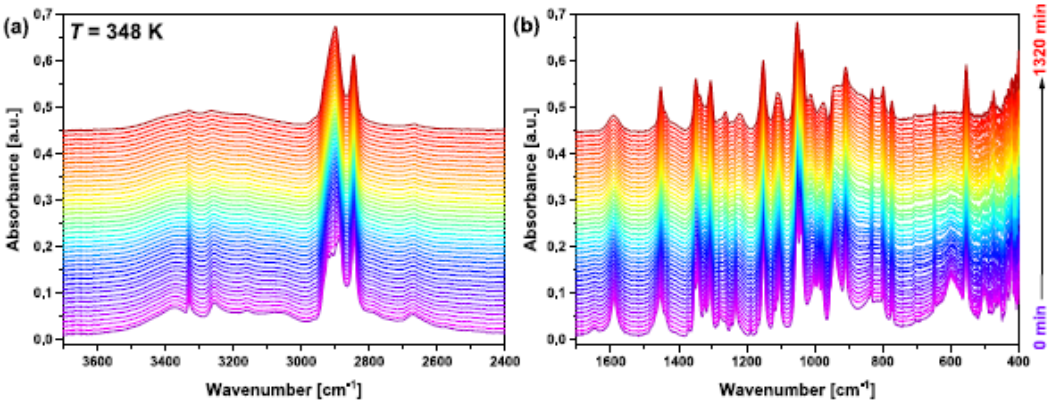

Fig. 8. Time-dependent IR spectra of 3-NH_2-1-OH-ADM measured at 348 K over 22 h in the wavenumber regions of (a) 3700–2400 cm^{-1} and (b) 1700–400 cm^{-1}, shown with 30 min intervals for clarity.

synchronous spectrum represents the intramolecular interactions or correlation of groups corresponding to spectral intensity, whereas the asynchronous spectrum represents sequential or successive changes of spectral intensities measured at different peak positions [43–46]. From the time-dependent spectroscopic measurements and the 2D correlation analysis of the IR spectra, it can be stated that the significant changes in the higher wavenumber region of the spectra, observed during isothermal annealing, mainly occur for the CH stretching vibration bands (please see the 2950–2850 cm^{-1} range, in which the peak at 2883 cm^{-1} diminishes, while that of around 2903 cm^{-1} intensifies), Fig. 8 (a) and Figs. S4–S6. These variations are due to the transition from the OC phase I to the PC phase II. Moreover, the intensity of the broad OH/NH stretching band occurring in the 3600–3000 cm^{-1} region decreases over time, and this band becomes blurred. The asynchronous correlation maps indicate that the changes in the CH stretching vibration bands occur faster than those resulting from vibrations of NH/OH groups (Fig. S5 (b)). This fact may be explained by intermolecular interactions involving the NH/OH groups, which decrease the mobility of these groups compared to the CH groups. Additionally, conclusions can be deduced from the analysis of IR spectra in the lower frequency region, in which the deformation vibrations of NH, OH, and CH bonds are visible (see Figs. S7 and S8). More specifically, the intensity of the bands at 1589 and 1649 cm^{-1} changes before that of 1452 cm^{-1}, indicating that the vibrations of NH groups vary earlier than those of OH groups. Another significant region associated with CH deformations occurs in the 1380–1180 cm^{-1} range. Here, a combination of positive and negative cross peaks is evident, likely reflecting the structural disorder of CH groups during the phase transformation. Thus, the presented results confirmed the outcomes of isothermal BDS studies, i.e., they showed the kinetic character of the OC-PC phase transition in 3-NH_2-1-OH-ADM. Moreover, the analysis of asynchronous 2D spectra clearly indicated that aside from the change in the dc-conductivity (determined from dielectric investigations), also the variation in the intramolecular dynamics of CH, NH, and OH units is observed during the OC-PC phase transition. Importantly, there is a notable difference in the rates of change in the vibration of these moieties. The fluctuations within the CH groups are the fastest motions – they precede any changes in reorientations of the polar OH and NH_2 units. However, finding any correlation between the intramolecular dynamics of these characteristic units is very difficult since they are strictly due to the increasing orientational disorder during the OC-PC transition in 3-NH_2-1-OH-ADM.

4. Conclusions

In this work, several experimental techniques: DSC, XRD, FTIR, and Raman spectroscopy, as well as BDS, were applied to characterize thermal and structural properties, molecular reorientation processes, and dielectric response accompanying the phase transitions in 3-NH_2-1-OH-ADM. The obtained results were discussed with those published recently for 1-NH_2-ADM and 1-OH-ADM. Calorimetric studies revealed multiple thermal events in the DSC curves recorded on heating and cooling of the examined compound, which resembled the scenario observed for 1-NH_2-ADM. Based on the outcomes of structural measurements, as well as FTIR and Raman studies (which indicated some variations in the organization of molecules), two thermal events were assigned to the OC-PC(I) and PC(I)-PC(II) transitions at $T = 352$ K and $T = 309$ K, respectively. In turn, the lack of visible changes in the XRD pattern, as well as FTIR and Raman spectra, suggested that the third subtle exothermal peak at $T = 293$ K is not related to the phase transition. Notably, the analysis of dielectric data allowed us to suppose that the thermal event at $T = 293$ K could be connected to the change in the orientational disorder. Additionally, we performed isothermal BDS and FTIR investigations as well as the analysis of the synchronous and asynchronous 2D-IR correlation spectra, to get deeper insight into the character of the OC-PC(I) transition in 3-NH_2-1-OH-ADM, which, as the PC(I)-PC(II) transition in 1-NH_2-ADM, was visible in the DSC thermogram over an enormously large temperature interval. It was found that although these phase transitions in both ADM derivatives are physical phenomena, they have kinetic character. Our data clearly indicated that upon the OC-PC(I) transition in 3-NH_2-1-OH-ADM the dc-conductivity increases. Moreover, this process is accompanied by a change in the intramolecular dynamics related to the vibrations of CH, NH, and OH units that occur at different rates.

CRediT authorship contribution statement

Paulina Jesionek: Writing – original draft, Writing – review & editing, Visualization, Methodology, Investigation, Formal analysis. **Barbara Hachuła:** Visualization, Investigation. **Magdalena Tarnacka:** Investigation. **Karolina Jurkiewicz:** Investigation, Funding acquisition. **Kamil Kamiński:** Supervision, Conceptualization. **Ewa Kamińska:** Writing – original draft, Writing – review & editing, Supervision, Funding acquisition, Conceptualization.

Declaration of competing interest

The authors declare that they have no known competing financial interests or personal relationships that could have appeared to influence the work reported in this paper.

Data availability

Data will be made available on request.

Acknowledgments

This research was funded in whole by the National Science Centre (Poland), grant number: Opus 21 No. 2021/41/B/NZ7/01654. For the purpose of Open Access, the author has applied a CC-BY public copyright license to any Author Accepted Manuscript (AAM) version arising from this submission.

Appendix A. Supplementary material

Supplementary data to this article can be found online at https://doi.org/10.1016/j.molliq.2024.125907.

References

[1] S. Das, A. Mondal, C.M. Reddy, Harnessing molecular rotations in plastic crystals: a holistic view for crystal engineering of adaptive soft materials, Chem. Soc. Rev. 49 (2020) 8878–8896.
[2] R. Brand, P. Lunkenheimer, A. Loidl, Relaxation dynamics in plastic crystals, J. Chem. Phys. 116 (2002) 10386–10401.
[3] M. Michl, T. Bauer, P. Lunkenheimer, A. Loidl, Nonlinear dielectric spectroscopy in a fragile plastic crystal, J. Chem. Phys. 144 (2016) 114506.
[4] E. Kaminska, M. Tarnacka, K. Jurkiewicz, K. Kaminski, M. Paluch, High pressure dielectric studies on the structural and orientational glass, J. Chem. Phys. 144 (2016) 54503.
[5] J.N. Sherwood, The Plastically Crystalline State, John Wiley & Sons Ltd, Chichester, New York, Brisbane, Toronto, 1979.
[6] I.E. Collings, M. Bykov, E. Bykova, M. Hanfland, S. van Smaalen, L. Dubrovinsky, N. Dubrovinskaia, Disorder-order transitions in the perovskite metal-organic frameworks $[(CH_3)_2NH_2][M(HCOO)_3]$ at high pressure, CrstEngComm 20 (2018) 3512–3521.
[7] B. Park, B. Philippe, T. Gustafsson, K. Sveinbjörnsson, A. Hagfeldt, E.M. J. Johansson, G. Boschloo, Enhanced crystallinity in organic-inorganic lead halide perovskites on mesoporous TiO2 via disorder-order phase transition, Chem. Mater. 26 (2014) 4466–4471.
[8] A.B. Cairns, A.L. Goodwin, Structural disorder in molecular framework materials, Chem. Soc. Rev. 42 (2013) 4881–4893.
[9] A.A. Bakulin, O. Selig, H.J. Bakker, Y.L.A. Rezus, C. Müller, T. Glaser, R. Lovrincic, Z. Sun, Z. Chen, A. Walsh, J.M. Frost, T.L.C. Jansen, Real-time observation of organic cation reorientation in methylammonium lead iodide perovskites, J. Phys. Chem. Lett. 6 (2015) 3663–3669.
[10] V.K. Dolganov, M. Gal, N. Kroo, L. Rosta, E.F. Sheka, Evolution of the coherence of vibrational states in a gradual disorder-order phase transition, J. Mol. Struct. 114 (1984) 325–328.
[11] F. Affouard, M. Descamps, Is there something of mode coupling theory in orientationally disordered crystals? Phys. Rev. Lett. 87 (2001) 35501.
[12] J. Timmermans, Un nouvel état mésomorphe les cristaux organiques plastiques, J. Chim. Phys. 35 (1938) 331–344.
[13] B. Parat, L.C. Pardo, M. Barrio, J.L. Tamarit, P. Negrier, J. Salud, D.O. López, D. Mondieig, Polymorphism of $CBrCl_3$, Chem. Mater. 17 (2005) 3359–3365.
[14] A. Vispa, M. Romanini, M.A. Ramos, L.C. Pardo, F.J. Bermejo, M. Hassaine, A. I. Krivchikov, J.W. Taylor, J.L. Tamarit, Thermodynamic and kinetic fragility of Freon 113: the most fragile plastic crystal, Phys. Rev. Lett. 118 (2017) 105701.
[15] I.S. Gutzow, B.P. Petroff, S.V. Todorova, J.W.P. Schmelzer, Thermodynamics of amorphous solids, glasses and disordered crystals. Glasses and the Glass Transition, Wiley-VCH Verlag GmbH & Co. KGaA, 2011.
[16] K.L. Ngai, Relaxation and Diffusion in Complex Systems, Springer, New York, 2011.
[17] J.F. Gebbia, A.H. Aristizabal, P. Negrier, D. Aguilà, J.L. Tamarit, L.C. Pardo, Dynamics and local ordering of pentachloronitrobenzene: a molecular-dynamics investigation, PCCP 25 (2023) 30553–30562.
[18] M. Shahin, S.S.N. Murthy, L.P. Singh, Glass transition phenomena in two-component plastic crystals: study of hexasubstituted benzenes, J. Phys. Chem. B 110 (2006) 18573–18582.
[19] H.P. Diogo, N.T. Correia, J.J. Moura Ramos, Molecular mobility, phase transitions and phase transformations in crystalline ortho- and meta-carboranes, J. Phys. Chem. Solid 66 (2005) 832–838.
[20] P. Wu, L. Hsu, D.A. Dows, Spectroscopic study of the phase transition in crystalline adamantane, J. Chem. Phys. 54 (2003) 2714–2721.
[21] N.A. Murugan, S. Yashonath, Pressure-induced ordering in adamantane: a Monte Carlo simulation study, J. Phys. Chem. B 109 (2005) 2014–2020.
[22] E.L. Gromnitskaya, I.V. Danilov, V.V. Brazhkin, Comparative study of the elastic properties of adamantane and 1-chloroadamantane at high pressure and different temperatures and at order–disorder transitions, PCCP 23 (2021) 2349–2354.
[23] I.V. Danilov, E.L. Gromnitskaya, V.V. Brazhkin, Phase transitions in 1-bromoadamantane compared to 1-chloroadamantane: similarities and unique features, PCCP 23 (2021) 23274–23279.
[24] M. Kosmowska, J. Tarasiewicz, H.A. Kołodziej, Dielectric relaxation of 1-bromoadamantane, J. Mol. Struct. 1016 (2012) 8–12.
[25] P. Negrier, B. Ben Hassine, M. Barrio, M. Romanini, D. Mondieig, J.L. Tamarit, Polymorphism of 1,3-X-adamantanes (X = Br, OH, CH3) and the crystal plastic phase formation ability, CrstEngComm 22 (2020) 1230–1238.
[26] M.B. Charapennikau, A.V. Blokhin, A.G. Kabo, G.J. Kabo, The heat capacities and parameters of solid phase transitions and fusion for 1- and 2-adamantanols, J. Chem. Thermodyn. 35 (2003) 145–157.
[27] A. Salvatori, P. Negrier, S. Massip, A. Muñoz-Duque, P. Lloveras, M. Barrio, J. L. Tamarit, Polymorphism and solid-solid phase transitions of hydrogen bonded 2-adamantanol and 2-methyl-2-adamantanol compounds, CrstEngComm 24 (2022) 3692–3700.
[28] A.B. Bazyleva, A.V. Blokhin, A.G. Kabo, G.J. Kabo, V.N. Emel'yanenko, S. P. Verevkin, Thermodynamic properties of 1-aminoadamantane, J. Chem. Thermodyn. 40 (2008) 509–522.
[29] P. Jesionek, B. Hachuła, D. Heczko, T. Lamrani, K. Jurkiewicz, M. Tarnacka, M. Książek, K. Kamiński, E. Kamińska, Studies on the nature and pressure evolution of phase transitions in 1-adamantylamine and 1-adamantanol, Spectrochim. Acta A: Mol. Biomol. Spectrosc. (2023) 122794.
[30] O.V. Dorofeeva, M.A. Filimonova, Sublimation enthalpy of 1-aminoadamantane: comparison of theory and experiment, Chem. Phys. Lett. 711 (2018) 231–235.
[31] J.C. Martinez-Garcia, J.L. Tamarit, S. Capaccioli, M. Barrio, N. Veglio, L.C. Pardo, α -relaxation dynamics of orientationally disordered mixed crystals composed of Cl-adamantane and CN-adamantane, J. Chem. Phys. 132 (2010) 164516.
[32] O. Al Rahal, B.M. Kariuki, C.E. Hughes, P.A. Williams, X. Xu, S. Gaisford, D. Iuga, K.D.M. Harris, Unraveling the complex solid-state phase transition behavior of 1-iodoadamantane, a material for which ostensibly identical crystals undergo different transformation pathways, Cryst. Growth Des. 23 (2023) 3820–3833.
[33] A. Vispa, D. Monserrat, G.J. Cuello, F. Fernandez-Alonso, S. Mukhopadhyay, F. Demmel, J.L. Tamarit, L.C. Pardo, On the microscopic mechanism behind the purely orientational disorder-disorder transition in the plastic phase of 1-chloroadamantane, PCCP 19 (2017) 20259–20266.
[34] P. Negrier, M. Barrio, J. Li, D.M. Tamarit, Polymorphism in 2-X-adamantane derivatives (X = Cl, Br), J. Phys. Chem. B 118 (2014) 9595–9603.
[35] B. Ben Hassine, P. Negrier, M. Barrio, D. Mondieig, S. Massip, J.L. Tamarit, Phase transition in hydrogen-bonded 1-adamantane-methanol, Cryst. Growth Des. 15 (2015) 4149–4155.
[36] P.D. Harvey, D.F.R. Gilson, I.S. Butler, Phase transitions and molecular motions in adamantane derivatives: 1-adamantanol, Can. J. Chem. 65 (1987) 1757–1760.
[37] M.B. Charapennikau, A.V. Blokhin, G.J. Kabo, A.G. Kabo, V.V. Diky, A.G. Gusakov, Thermodynamic properties and the plastic crystal state of 2-methyl-2-adamantanol, Thermochim Acta 382 (2002) 109–118.
[38] P. Negrier, M. Barrio, M. Romanini, J.L. Tamarit, D. Mondieig, A.I. Krivchikov, L. Kępiński, A. Jezowski, D. Szewczyk, Polymorphism of 2-adamantanone, Cryst. Growth Des. 14 (2014) 2626–2632.
[39] S. Havriliak, S. Negami, A complex plane analysis of α-dispersions in some polymer systems, J. Polym. Sci., Part C: Polym. Symp. 14 (1966) 99–117.
[40] K. Kobashi, T. Kyōmen, M. Oguni, Construction of an adiabatic calorimeter in the temperature range between 13 and 505 K, and thermodynamic study of 1-chloroadamantane, J. Phys. Chem. Solid 59 (1998) 667–677.
[41] M. Descamps, N.T. Correia, P. Derollez, F. Danede, F. Capet, Plastic and glassy crystal states of caffeine, J. Phys. Chem. B 109 (2005) 16092–16098.
[42] M. Avrami, Kinetics of phase change. II transformation-time relations for random distribution of nuclei, J. Chem. Phys. 8 (1940) 212–224.
[43] P. Lasch, I. Noda, Two-dimensional correlation spectroscopy (2D-COS) for analysis of spatially resolved vibrational spectra, Appl. Spectrosc. 73 (2019) 359–379.
[44] I. Noda, A.E. Dowrey, C. Marcott, G.M. Story, Y. Ozaki, Generalized two-dimensional correlation spectroscopy, Appl. Spectrosc. 54 (2000) 236A–248A.
[45] K. Zheng, R. Liu, Y. Huang, A two-dimensional IR correlation spectroscopic study of the conformational changes in syndiotactic polypropylene during crystallization, Polym. J. 42 (2010) 81–85.
[46] I. Noda, Two-dimensional infrared spectroscopy two-dimensional infrared spectroscopy, Spectroscopy 111 (1989) 8116–8118.

Comparative studies on the nature and kinetics of phase transitions in plastic crystals: Hydrogen-bonded adamantane derivatives

Paulina Jesionek[a,b], Barbara Hachuła[a], Magdalena Tarnacka[c], Karolina Jurkiewicz[c], Kamil Kamiński[c], Ewa Kamińska[b]

[a] *Institute of Chemistry, Faculty of Science and Technology, University of Silesia in Katowice, Szkolna 9, 40-007 Katowice, Poland*
[b] *Department of Pharmacognosy and Phytochemistry, Faculty of Pharmaceutical Sciences in Sosnowiec, Medical University of Silesia in Katowice, Jagiellonska 4, 41-200 Sosnowiec, Poland*
[c] *Institute of Physics, Faculty of Science and Technology, University of Silesia in Katowice, 75 Pulku Piechoty 1, 41-500 Chorzow, Poland*

Supplementary material

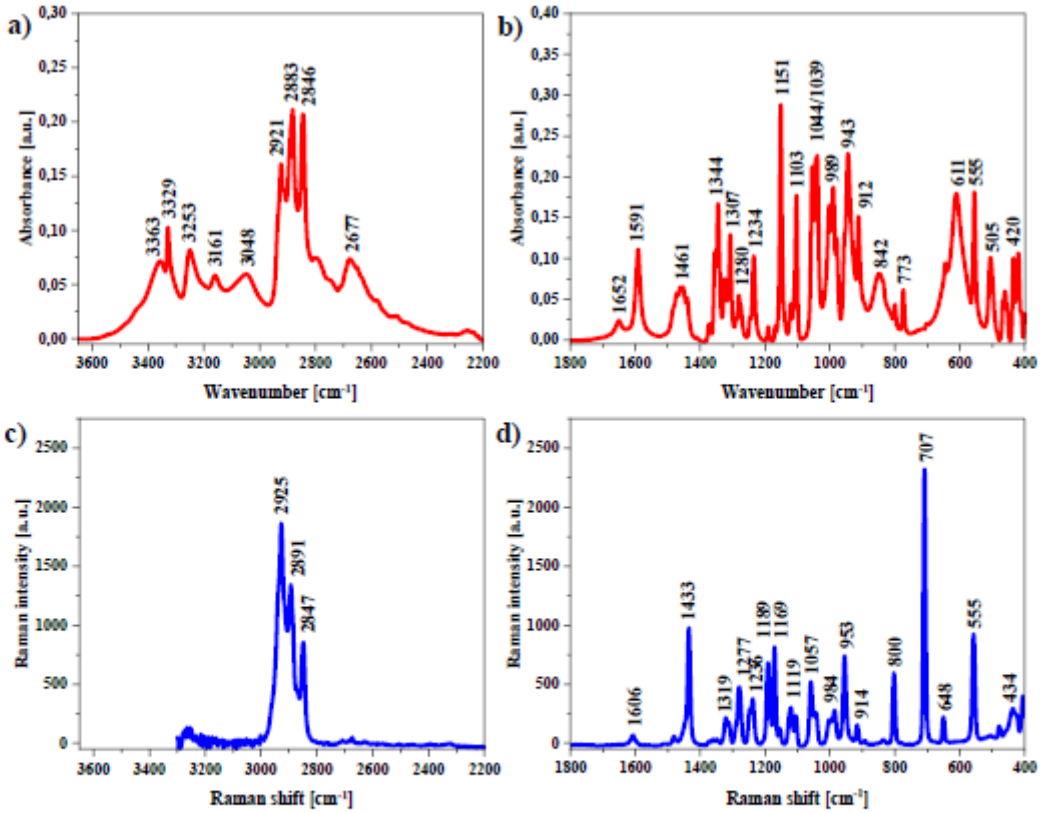

S1

Fig. S1. FTIR (a) and Raman (b) spectra of 3-NH_2-1-OH-ADM measured at room temperature in two frequency ranges of (left) 3700-2400 cm^{-1} and (right) 1800-400 cm^{-1}.

As shown in **Fig. S1 (a)**, the broad and complex band observed in the higher wavenumber range (from 3600 cm^{-1} to 3000 cm^{-1}) of the IR spectrum of the commercial 3-NH_2-1-OH-ADM is related to the stretching vibrations of H-bonded NH and OH groups. It should be mentioned that no band at ca. 3650-3600 cm^{-1} occurs in this spectrum, which indicates that nearly all OH and NH groups are linked in the H-bonded clusters. The intense peaks located between 3000 and 2800 cm^{-1} (IR: 2923, 2882, and 2843 cm^{-1}; Raman 2928, 2894, and 2850 cm^{-1}) correspond to the asymmetric and symmetric CH stretching vibrations of the adamantane skeleton (four cyclohexane rings). The absorption signals at 1649 and 1591 cm^{-1} in the IR spectrum (Raman: 1607 cm^{-1}) are assigned to the deformation (scissoring) vibrations of NH bonds of the amine (NH_2) group (**Fig. S1 (b)**). The CH_2 scissoring, wagging, rocking, and twisting vibrations occur in the region 1430-715 cm^{-1} in both IR and Raman spectra, whereas the CC skeletal vibrations of cyclohexane derivatives of variable intensity appear as a set of several peaks in 1055-1000, 1015-950, ~900, 570-435 cm^{-1} ranges.[1–5] A broad band located from 1520 to 1400 cm^{-1} is assigned to the CH_2 scissoring and the OH deformation vibrations.[1–5] The absorption signals at 1280 and 1235 cm^{-1} are related to the CH_2 twist vibrations. The OH in-plane deformation occurs at ca. 1260 cm^{-1}. The CN stretching absorption of the amine group occurs at 1151 and 1103 cm^{-1}. At 1044/1039 cm^{-1}, a doublet assigned to the CO stretching is observed.[1–5] The N-H out-of-plane wagging and CH_2 rocking vibrations are visible at 611 cm^{-1} (Raman: 648 cm^{-1}). A strong peak at 707 cm^{-1} in the Raman spectrum is associated with the CC stretching vibrations of adamantane skeletal.

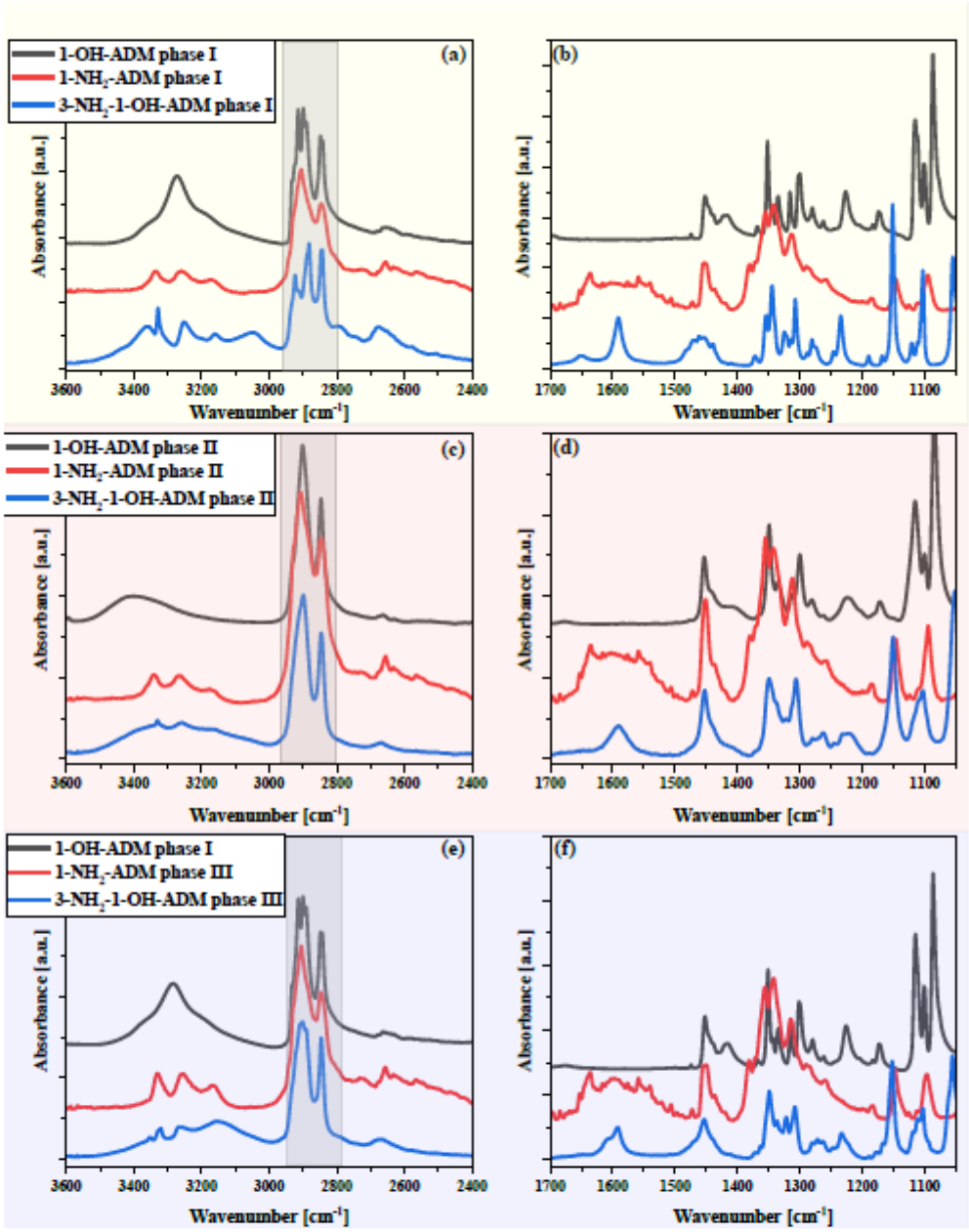

Fig. S2. The comparison of FTIR spectra of 1-OH-ADM, 1-NH_2-ADM, and 3-NH_2-1-OH-ADM at different phases in the wavenumber range of (a,c,e) 3600-2400 cm^{-1} and (b,d,f) 1700-1050 cm^{-1}; (a,b) the room temperature phases; (c,d) the high-temperature phases; (e,f) the low-temperature phases (the phases after cooling from high temperatures).

Time-dependent IR spectra of 3-NH_2-1-OH-ADM

As can be seen in Figs. S3-S8, the most significant variations in the higher wavenumber region of the spectra of 3-NH_2-1-OH-ADM, measured as a function of the isothermal annealing time, take place to the bands associated with the CH stretching vibrations, i.e., the peak located at ca. 2889 cm^{-1} decreases in intensity, and a second band at ca. 2894 cm^{-1} grows with isothermal annealing. It can be correlated with the disappearance of the component related to the OC **phase I** and an increase in the component assigned to PC **phase II**. For such types of overlapping bands, whose intensities are changing in the opposite direction, the 2D synchronous correlation spectrum shows a pattern consisting of two cross peaks, both of which are negative (blue areas; Figs. S5 (a), S6 (a)). In the asynchronous correlation spectrum (Figs. S5 (b), S6 (b)), two cross-peaks are visible, one of which is positive (red area) and the other negative (blue area), consistent with the changes in peak intensity associated with the transformation being linked together one increasing and the other decreasing. The analysis of this asynchronous map suggests that the CH stretching vibrations visible at 2894 cm^{-1} changed before the CH stretching vibrations detected at 2889 cm^{-1}. We were also interested in analyzing the high-wavenumber range associated with the stretching vibrations of OH and NH groups to recognize whether these bonds are also sensitive to the OC-PC phase transition. As shown in Fig. S4, this $\nu_{OH/NH}$ band shows only small changes in subtle structure with time (the intensity of the higher wavenumber component increases, and the lower one decreases). Moreover, the intensity of this whole band essentially decreases during the transformation process. As a result, the cross-peaks are weak and show only a small magnitude compared with the strong main cross-peaks of CH stretching bands. The analysis of asynchronous correlation maps suggests that the CH stretching vibrations are accelerated relative to those of the NH/OH groups. Thus, the absorption band characteristics of the last parts of the molecule (OH/NH groups) are less sensitive to the studied phase transition than the CH group.

Then, we turn our attention to the changes in spectral properties of the bands assigned to the deformation vibrations of NH, OH, and CH bonds (1700-1380 cm^{-1}) as a function of time (Fig. S7). In this region, the positive cross peaks are present (ν_1 = 1465, 1589, 1649 cm^{-1}); these represent simultaneous changes in the peak intensities at different wavenumbers. As they decrease in intensity, they are due to the development of the PC **phase II**. Moreover, there are also negative cross peaks in this synchronous 2D correlation spectrum consistent with the increase in intensity of the signal at 1452 cm^{-1} (the region of 1400-1450 cm^{-1}) relative to the other bands. As shown in Fig. S7 **(b)**, the asynchronous spectrum has intense cross peaks – the positive and other negative indicative of the intensities changing in opposite directions. In detail, the intensity change of bands at 1589 and 1649 cm^{-1} occurs predominantly before that at 1452 cm^{-1} in the sequential order of time. Thus, the deformation vibrations of NH groups change earlier than that of OH groups. Another interesting region where the positive and negative peaks are observed is the 1380-1180 cm^{-1} range, mainly related to the CH deformations (Fig. S8). Here, a mix of positive and negative cross-peaks can be related to the structural disorder of the CH groups during the phase transformation. Accurately, the signals at ca. 1353, 1343, 1306, 1280, 1230, and 1188 cm^{-1} disappear, while those at about 1348, 1332, 1262, and 1220 cm^{-1} enhance their intensity (Fig. S4 **(b)**). Below 1180 cm^{-1}, most peaks show the reduction of intensity associated with the change of mobility of hydrocarbon rings due to the phase transformation. For example, the intensity of the broad signal located at ca. 600 cm^{-1} (the NH out-of-plane wagging and CH_2 rocking vibrations), as well as the intensities of the peaks at ca. 1150, 1100, and 940 cm^{-1} (the CO stretching, CC stretching and CH deformation vibrations), decrease with time. Therefore, the observed changes in the analyzed spectra may be explained by different sensitivity of CH, OH, and NH vibrations to the short-range order of molecules, i.e., the vibrations of the CH groups in the hydrocarbon core respond stronger than that of hydroxyl and amine groups.

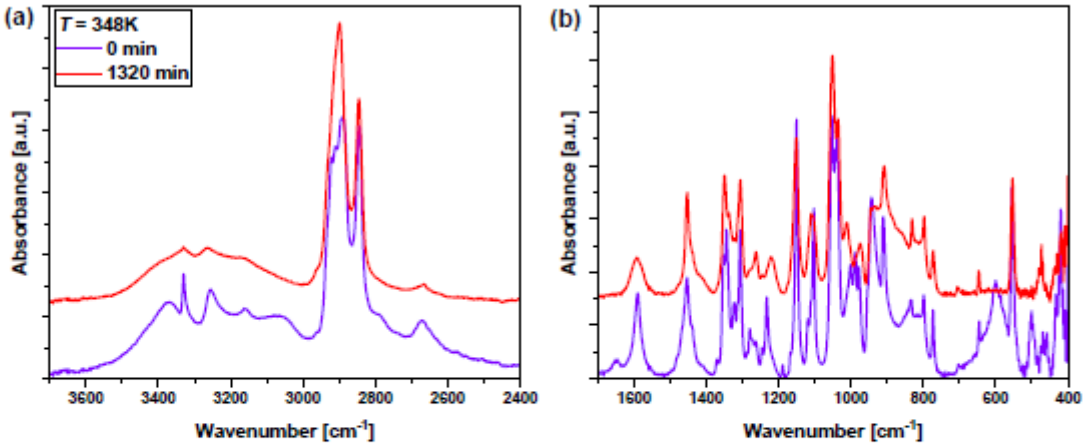

Fig. S3. The comparison of FTIR spectra of 3-NH_2-1-OH-ADM measured at 348 K at 0 and 1320 min in the wavenumber ranges of (a) 3700-2400 cm^{-1} and (b) 1700-400 cm^{-1}.

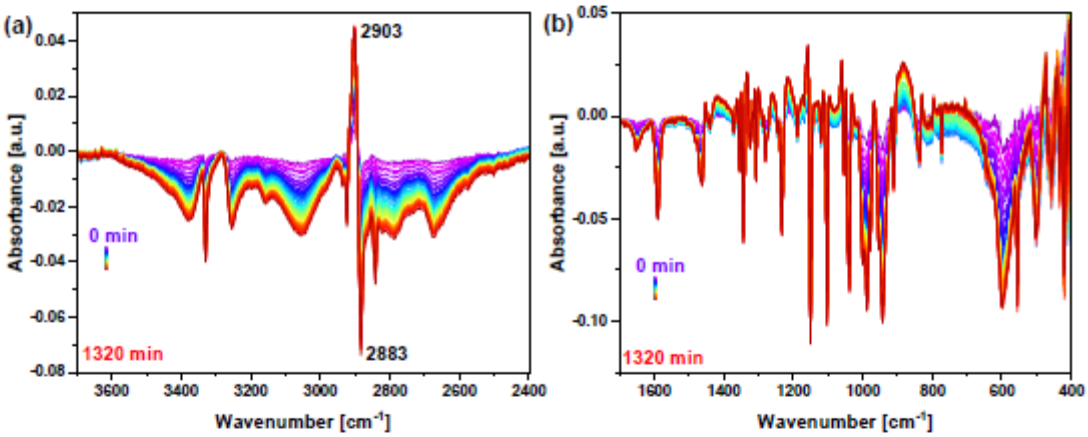

Fig. S4. The difference FTIR spectra obtained by subtracting the initial spectrum from the spectra shown in Fig. 8 in the wavenumber regions of (a) 3700-2400 cm^{-1} and (b) 1700-400 cm^{-1}.

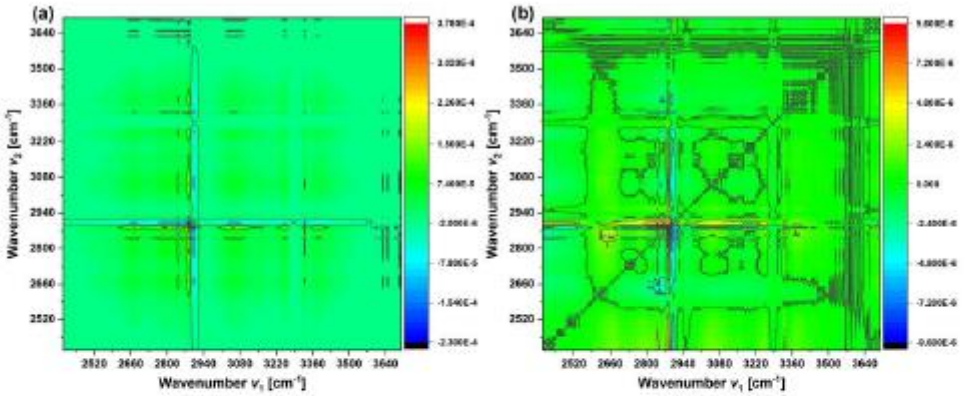

Fig. S5. Synchronous (a) and asynchronous (b) two-dimensional (2D) infrared correlation spectra of 3-NH_2-1-OH-ADM in the wavenumber region of 3700-2400 cm^{-1} calculated from spectra obtained during the isothermal annealing process at 348 K. The red and blue areas in contour maps represent positive and negative peaks, respectively.

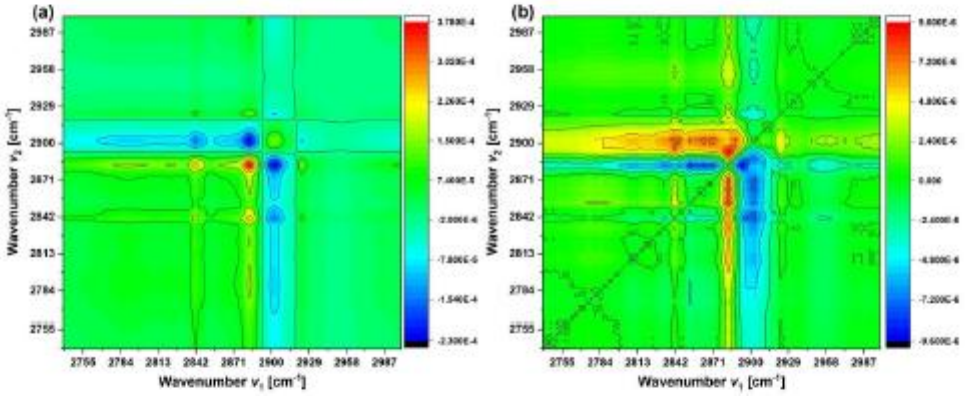

Fig. S6. Synchronous (a) and asynchronous (b) two-dimensional (2D) infrared correlation spectra of 3-NH_2-1-OH-ADM in the wavenumber region of 3000-2740 calculated from spectra obtained during the isothermal annealing process at 348 K.

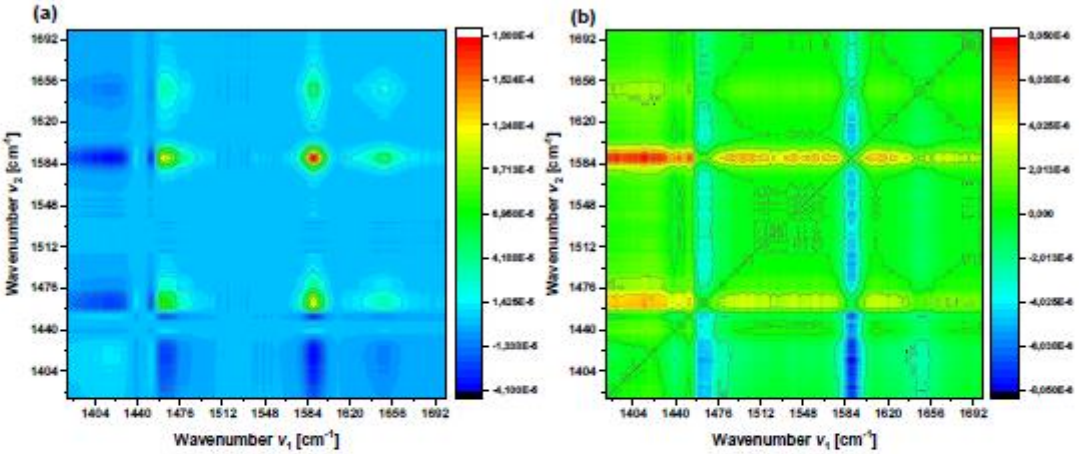

Fig. S7. Synchronous (a) and asynchronous (b) two-dimensional (2D) infrared correlation spectra of 3-NH_2-1-OH-ADM in the wavenumber region of 1700-1380 cm^{-1} calculated from spectra obtained during the isothermal annealing process at 348 K.

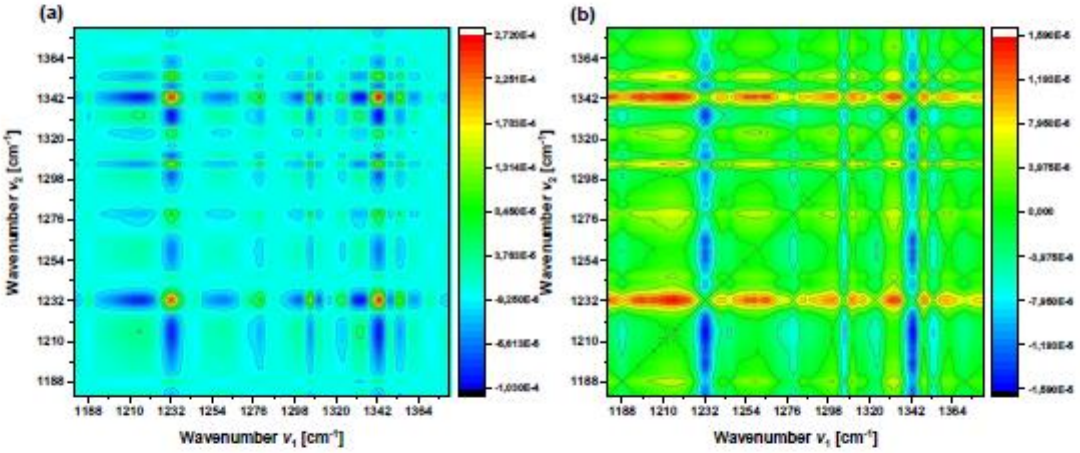

Fig. S8. Synchronous (a) and asynchronous (b) two-dimensional (2D) infrared correlation spectra of 3-NH_2-1-OH-ADM in the wavenumber region of 1380-1180 cm^{-1} calculated from spectra obtained during the isothermal annealing process at 348 K.

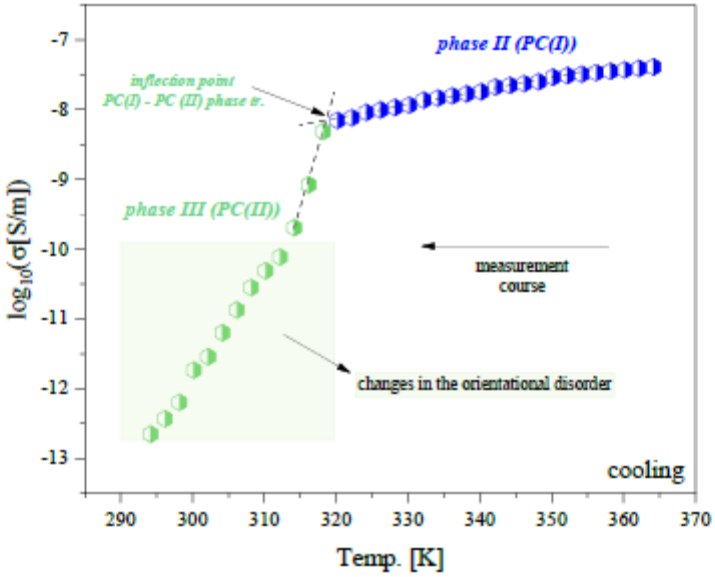

Fig. S9. Temperature evolution of the dc-conductivity (σ) for 3-NH_2-1-OH-ADM during cooling cycle.

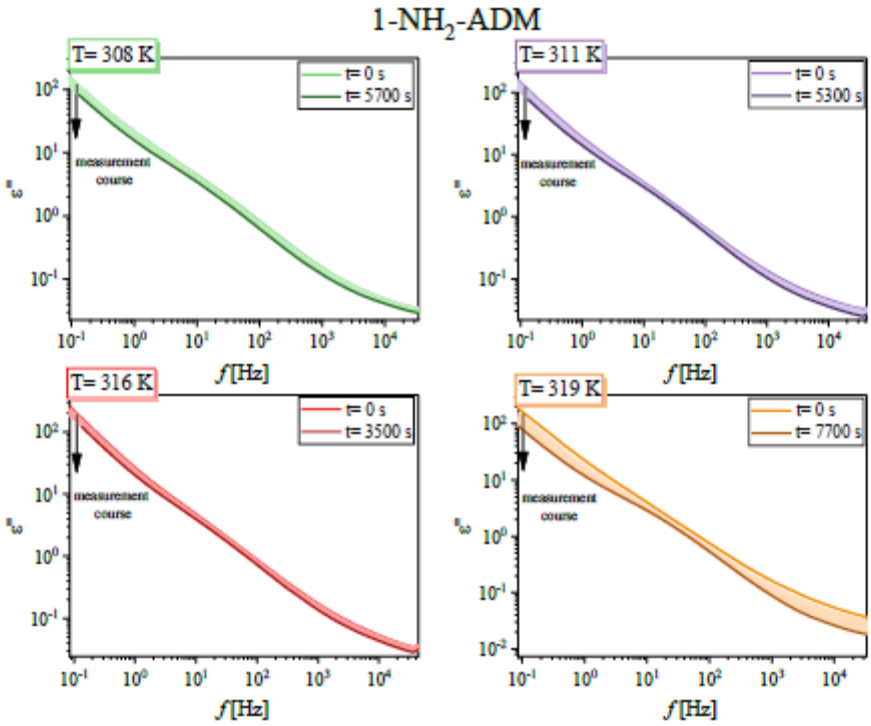

Fig. S10. Time evolution of the imaginary part of the complex permittivity at constant temperatures for 1-NH_2-ADM.

Chorzów, 08.05.2025r.

Prof. dr hab. n. farm. Ewa Ozimina-Kamińska
Katedra i Zakład Farmakognozji i Fitochemii
Wydział Nauk Farmaceutycznych w Sosnowcu
Śląskiego Uniwersytetu Medycznego w Katowicach
ul. Jagiellońska 4
41-200 Sosnowiec

OŚWIADCZENIE

Oświadczam, że w pracach:

P1. P. Jesionek, D. Heczko, B. Hachuła, K. Kamiński, E. Kamińska, ***High-pressure studies in the supercooled and glassy state of the strongly associated active pharmaceutical ingredient—ticagrelor***, Sci. Rep. 13 (**2023**) 8890.

P2. P. Jesionek, B. Hachuła, K. Jurkiewicz, P. Włodarczyk, M. Hreczka, K. Kamiński, E. Kamińska, ***Variation of Activation Volume as an Indicator of the Difference in Clusterization Phenomenon Induced by H-Bonding and F−π Stacking Interactions in Enantiomers and a Racemate of Flurbiprofen***, J. Phys. Chem. B. 128 (**2024**) 4021–4032.

P3. P. Jesionek, B. Hachuła, D. Heczko, T. Lamrani, K. Jurkiewicz, M. Tarnacka, M. Książek, K. Kamiński, E. Kamińska, ***Studies on the nature and pressure evolution of phase transitions in 1-adamantylamine and 1-adamantanol***, Spectrochim. Acta Part A Mol. Biomol. Spectrosc. 299 (**2023**) 122794.

P4. P. Jesionek, B. Hachuła, M. Tarnacka, K. Jurkiewicz, K. Kamiński, E. Kamińska, ***Comparative studies on the nature and kinetics of phase transitions in plastic crystals: Hydrogen-bonded adamantane derivatives***, J. Mol. Liq. 413 (**2024**) 125907.

mój wkład polegał na udziale w formułowaniu hipotez badawczych, nadzorowaniu przeprowadzonych analiz, dyskusji wyników, współtworzenia i korekcji manuskryptu wraz z odpowiedziami na uwagi recenzentów oraz finansowaniu badań w ramach projektu NCN OPUS.

Ewa Ozimina-Kamińska
.....
Podpis współautora publikacji

Chorzów, 08.05.2025r.

Prof. dr hab. Kamil Kamiński
Instytut Fizyki im. Augusta Chełkowskiego
Wydział Nauk Ścisłych i Technicznych
Uniwersytet Śląski w Katowicach
ul. 75 Pułku Piechoty 1
41-500 Chorzów

OŚWIADCZENIE

Oświadczam, że w pracach:

P1. P. Jesionek, D. Heczko, B. Hachuła, K. Kamiński, E. Kamińska, ***High-pressure studies in the supercooled and glassy state of the strongly associated active pharmaceutical ingredient—ticagrelor***, Sci. Rep. 13 (**2023**) 8890.

P2. P. Jesionek, B. Hachuła, K. Jurkiewicz, P. Włodarczyk, M. Hreczka, K. Kamiński, E. Kamińska, ***Variation of Activation Volume as an Indicator of the Difference in Clusterization Phenomenon Induced by H-Bonding and F−Π Stacking Interactions in Enantiomers and a Racemate of Flurbiprofen***, J. Phys. Chem. B. 128 (**2024**) 4021–4032.

P3. P. Jesionek, B. Hachuła, D. Heczko, T. Lamrani, K. Jurkiewicz, M. Tarnacka, M. Książek, K. Kamiński, E. Kamińska, ***Studies on the nature and pressure evolution of phase transitions in 1-adamantylamine and 1-adamantanol,*** Spectrochim. Acta Part A Mol. Biomol. Spectrosc. 299 (**2023**) 122794.

P4. P. Jesionek, B. Hachuła, M. Tarnacka, K. Jurkiewicz, K. Kamiński, E. Kamińska, ***Comparative studies on the nature and kinetics of phase transitions in plastic crystals: Hydrogen-bonded adamantane derivatives***, J. Mol. Liq. 413 (**2024**) 125907.

mój wkład polegał na nadzorowaniu przeprowadzonych badań i analiz oraz dyskusji uzyskanych wyników.

.....

Podpis współautora publikacji

Chorzów, 08.05.2025r.

dr hab. Barbara Hachuła, prof. UŚ
Instytut Chemii
Wydział Nauk Ścisłych i Technicznych
Uniwersytet Śląski w Katowicach
ul. Szkolna 9
40-006 Katowice

OŚWIADCZENIE

Oświadczam, że w pracach:

P1. P. Jesionek, D. Heczko, B. Hachuła, K. Kamiński, E. Kamińska, ***High-pressure studies in the supercooled and glassy state of the strongly associated active pharmaceutical ingredient—ticagrelor***, Sci. Rep. 13 (**2023**) 8890.

P2. P. Jesionek, B. Hachuła, K. Jurkiewicz, P. Włodarczyk, M. Hreczka, K. Kamiński, E. Kamińska, ***Variation of Activation Volume as an Indicator of the Difference in Clusterization Phenomenon Induced by H-Bonding and F−Π Stacking Interactions in Enantiomers and a Racemate of Flurbiprofen***, J. Phys. Chem. B. 128 (**2024**) 4021–4032.

P3. P. Jesionek, B. Hachuła, D. Heczko, T. Lamrani, K. Jurkiewicz, M. Tarnacka, M. Książek, K. Kamiński, E. Kamińska, ***Studies on the nature and pressure evolution of phase transitions in 1-adamantylamine and 1-adamantanol***, Spectrochim. Acta Part A Mol. Biomol. Spectrosc. 299 (**2023**) 122794.

P4. P. Jesionek, B. Hachuła, M. Tarnacka, K. Jurkiewicz, K. Kamiński, E. Kamińska, ***Comparative studies on the nature and kinetics of phase transitions in plastic crystals: Hydrogen-bonded adamantane derivatives***, J. Mol. Liq. 413 (**2024**) 125907.

mój wkład polegał na wykonaniu pomiarów spektroskopowych (FTIR i Raman) i ich analizie oraz dyskusji otrzymanych wyników.

Barbara Hachuła
.....
Podpis współautora publikacji

Chorzów, 08.05.2025r.

dr inż. Karolina Jurkiewicz, prof. UŚ
Instytut Fizyki im. Augusta Chełkowskiego
Wydział Nauk Ścisłych i Technicznych
Uniwersytet Śląski w Katowicach
ul. 75 Pułku Piechoty 1
41-500 Chorzów

OŚWIADCZENIE

Oświadczam, że w pracach:

P2. P. Jesionek, B. Hachuła, K. Jurkiewicz, P. Włodarczyk, M. Hreczka, K. Kamiński, E. Kamińska, ***Variation of Activation Volume as an Indicator of the Difference in Clusterization Phenomenon Induced by H-Bonding and F–π Stacking Interactions in Enantiomers and a Racemate of Flurbiprofen***, J. Phys. Chem. B. 128 (**2024**) 4021–4032.

P3. P. Jesionek, B. Hachuła, D. Heczko, T. Lamrani, K. Jurkiewicz, M. Tarnacka, M. Książek, K. Kamiński, E. Kamińska, ***Studies on the nature and pressure evolution of phase transitions in 1-adamantylamine and 1-adamantanol***, Spectrochim. Acta Part A Mol. Biomol. Spectrosc. 299 (**2023**) 122794.

P4. P. Jesionek, B. Hachuła, M. Tarnacka, K. Jurkiewicz, K. Kamiński, E. Kamińska, ***Comparative studies on the nature and kinetics of phase transitions in plastic crystals: Hydrogen-bonded adamantane derivatives***, J. Mol. Liq. 413 (**2024**) 125907.

mój wkład polegał na wykonaniu badań dyfrakcyjnych i ich analizie oraz dyskusji otrzymanych wyników.

.....Jurkiewicz.....

Podpis współautora publikacji

Chorzów, 08.05.2025r.

dr hab. Magdalena Tarnacka, prof. UŚ
Instytut Fizyki im. Augusta Chełkowskiego
Wydział Nauk Ścisłych i Technicznych
Uniwersytet Śląski w Katowicach
ul. 75 Pułku Piechoty 1
41-500 Chorzów

OŚWIADCZENIE

Oświadczam, że w pracach:

P3. P. Jesionek, B. Hachuła, D. Heczko, T. Lamrani, K. Jurkiewicz, M. Tarnacka, M. Książek, K. Kamiński, E. Kamińska, ***Studies on the nature and pressure evolution of phase transitions in 1-adamantylamine and 1-adamantanol***, Spectrochim. Acta Part A Mol. Biomol. Spectrosc. 299 (**2023**) 122794.

P4. P. Jesionek, B. Hachuła, M. Tarnacka, K. Jurkiewicz, K. Kamiński, E. Kamińska, ***Comparative studies on the nature and kinetics of phase transitions in plastic crystals: Hydrogen-bonded adamantane derivatives***, J. Mol. Liq. 413 (**2024**) 125907.

mój wkład polegał na wykonaniu pomiarów kalorymetrycznych oraz dyskusji otrzymanych wyników.

Magdalena Tarnacka
.....
Podpis współautora publikacji

Chorzów, 08.05.2025r.

dr Patryk Włodarczyk
Instytut Metali Nieżelaznych
Sieć Badawcza Łukasiewicz
ul. Sowińskiego 5
44-100 Gliwice

OŚWIADCZENIE

Oświadczam, że w pracy:

P2. P. Jesionek, B. Hachuła, K. Jurkiewicz, P. Włodarczyk, M. Hreczka, K. Kamiński, E. Kamińska, ***Variation of Activation Volume as an Indicator of the Difference in Clusterization Phenomenon Induced by H-Bonding and F−π Stacking Interactions in Enantiomers and a Racemate of Flurbiprofen***, J. Phys. Chem. B. 128 (**2024**) 4021–4032.

mój wkład polegał na wykonaniu obliczeń DFT, analizie, wizualizacji i dyskusji otrzymanych wyników, jak również interpretacji wyników symulacji dynamiki molekularnej.

.....Patryk Włodarczyk.....

Podpis współautora publikacji

Sosnowiec, 13.05.2025r.

dr Dawid Heczko
Zakład Statystyki Medycznej
Wydział Nauk Farmaceutycznych
Śląskiego Uniwersytetu Medycznego w Katowicach
ul. Ostrogórska 30
41-200 Sosnowiec

OŚWIADCZENIE

Oświadczam, że w pracach:

P1. P. Jesionek, D. Heczko, B. Hachuła, K. Kamiński, E. Kamińska, ***High-pressure studies in the supercooled and glassy state of the strongly associated active pharmaceutical ingredient—ticagrelor***, Sci. Rep. 13 (**2023**) 8890.

P3. P. Jesionek, B. Hachuła, D. Heczko, T. Lamrani, K. Jurkiewicz, M. Tarnacka, M. Książek, K. Kamiński, E. Kamińska, ***Studies on the nature and pressure evolution of phase transitions in 1-adamantylamine and 1-adamantanol***, Spectrochim. Acta Part A Mol. Biomol. Spectrosc. 299 (**2023**) 122794.

mój wkład polegał na pomocy w wykonaniu części pomiarów dielektrycznych (BDS) i ich analizie.

PUNKT BADAWCZO-DYDAKTYCZNY
Zakładu Statystyki Medycznej
Śląskiego Uniwersytetu Medycznego w Katowicach

dr n. farm. Dawid Heczko

.....Dawid Heczko.....

Podpis współautora publikacji

Chorzów, 08.05.2025r.

Taoufik Lamrani, MSc
Institute of Physics
Faculty of Science and Technology
University of Silesia in Katowice
75 Pułku Piechoty 1
41-500 Chorzów

STATEMENT

I declare that for the following work:

P3. P. Jesionek, B. Hachuła, D. Heczko, T. Lamrani, K. Jurkiewicz, M. Tarnacka, M. Książek, K. Kamiński, E. Kamińska, ***Studies on the nature and pressure evolution of phase transitions in 1-adamantylamine and 1-adamantanol,*** Spectrochim. Acta Part A Mol. Biomol. Spectrosc. 299 **(2023)** 122794.

my participation consisted of performing part of the diffraction experiments and analyzing the obtained results.

.....Lamrani.....

Signature of the co-author of the publication

Chorzów, 08.05.2025r.

mgr inż. Marek Hreczka
Instytut Metali Nieżelaznych
Sieć Badawcza Łukasiewicz
ul. Sowińskiego 5
44-100 Gliwice

Katedra Mechatroniki
Wydział Elektryczny
Politechnika Śląska
ul. Akademicka 10A
44-100 Gliwice

OŚWIADCZENIE

Oświadczam, że w pracy:

P2. P. Jesionek, B. Hachuła, K. Jurkiewicz, P. Włodarczyk, M. Hreczka, K. Kamiński, E. Kamińska, ***Variation of Activation Volume as an Indicator of the Difference in Clusterization Phenomenon Induced by H-Bonding and F−π Stacking Interactions in Enantiomers and a Racemate of Flurbiprofen***, J. Phys. Chem. B. 128 (**2024**) 4021–4032.

mój wkład polegał na wykonaniu symulacji dynamiki molekularnej.

.....Marek Hreczka.....

Podpis współautora publikacji

Chorzów, 08.05.2025r.

dr Maria Książek
Instytut Fizyki im. Augusta Chełkowskiego
Wydział Nauk Ścisłych i Technicznych
Uniwersytet Śląski w Katowicach
ul. 75 Pułku Piechoty 1
41-500 Chorzów

OŚWIADCZENIE

Oświadczam, że w pracach:

P3. P. Jesionek, B. Hachuła, D. Heczko, T. Lamrani, K. Jurkiewicz, M. Tarnacka, M. Książek, K. Kamiński, E. Kamińska, ***Studies on the nature and pressure evolution of phase transitions in 1-adamantylamine and 1-adamantanol,*** Spectrochim. Acta Part A Mol. Biomol. Spectrosc. 299 (**2023**) 122794.

mój wkład polegał na wykonaniu części pomiarów dyfrakcyjnych.

Maria Książek
.....

Podpis współautora publikacji

IV. Podsumowanie i wnioski

Podsumowując, w rozprawie doktorskiej, obejmującej cykl czterech publikacji naukowych, przedstawiono wyniki badań, których głównym celem była dogłębna charakterystyka własności termicznych, struktury wewnętrznej, oddziaływań międzycząsteczkowych, dynamiki molekularnej, jak również natury przejść fazowych na przykładzie wybranych zasocjowanych, tworzących wiązania wodorowe APIs i ich pochodnych o różnym stopniu nieuporządkowania (tj. tikagreloru, enancjomerów flurbiprofenu i ich racemicznej mieszaniny, 1-adamantylaminy, 1-adamantanolu, oraz 3-amino-1-adamantanolu) w szerokim zakresie T i p. Kluczową rolę odegrały wysokociśnieniowe eksperymenty dielektryczne, które dostarczyły informacji na temat struktury atomowej, pośrednio siły i populacji wiązań wodorowych (na podstawie kształtu dyspersji α oraz parametru ΔV), dynamiki globalnej i lokalnej, jak również wpływu wysokiej kompresji na przejścia fazowe w układach o zbliżonej budowie, tworzących fazy PC.

Przeprowadzone przeze mnie badania wykazały:

1) silną wrażliwość relaksacji strukturalnej (α) TICA na kompresję, co miało swe odzwierciedlenie w wysokiej wartości parametru dT_g/dp równemu 163 K/GPa;
2) spełnienie reguły TPS (zachowanie kształtu α-procesu TICA w różnych warunkach T i p), co wynikało z faktu niezmienności populacji wiązań wodorowych w podwyższonym ciśnieniu;
3) stały stosunek czasów relaksacji strukturalnej oraz drugorzędowej (typu β-JG) w warunkach izochronicznych dla TICA;
4) dodatnią wartość entropii aktywacji dla β-relaksacji (co sugerowało międzycząsteczkową kooperatywność tego procesu) oraz jej nieznaczny wzrost wraz z kompresją, co powiązano z niewielkimi fluktuacjami konformacyjnymi/molekularnymi cząsteczek TICA w podwyższonym ciśnieniu;
5) wyraźne różnice w organizacji molekuł połączonych wiązaniami wodorowymi między krystalicznymi próbkami czystych enancjomerów FLP (długie łańcuchy) a ich racematem (cykliczne dimery), które po stopieniu i przechłodzeniu całkowicie zanikały, co potwierdziły wyniki pomiarów XRD, DSC, FTIR oraz BDS;
6) niespodziewaną fluktuację w objętości aktywacji α-procesu (uzyskane wartości ΔV_α wyniosły odpowiednio 377 i 385 cm^3/mol dla R- i S-FLP oraz 337 cm^3/mol dla racematu) w warunkach wysokiego p, którą, w oparciu o przeprowadzone symulacje dynamiki molekularnej, powiązano ze zmianami w lokalnym układzie molekularnym tych

związków, wskazując na większą populację niskocząsteczkowych klastrów supramolekularnych w *S*-FLP w odniesieniu do *RS*-FLP;

7) istnienie specyficznych i wyjątkowo silnych oddziaływań F-Π w *RS*-FLP i *S*-FLP, które wpływają na lokalne uporządkowanie molekuł (struktury równoległe i antyrównoległe) w przechłodzonej fazie ciekłej oraz fazie krystalicznej;
8) występowanie przejść między czterema fazami PC: PC(I)-PC(II), PC(II)-PC(III), PC(III)-PC(IV) w 1-NH_2-ADM, przejścia fazowego OC-PC w 1-OH-ADM oraz przejść OC-PC i PC(I)-PC(II) w 3-NH_2-1-OH-ADM;
9) taką samą sekwencję i charakter przejść fazowych na drodze chłodzenia, jak i kompresowania w przypadku 1-NH_2-ADM oraz 1-OH-ADM;
10) charakter kinetyczny przejść OC-PC(I) w 3-NH_2-1-OH-ADM oraz PC(I)-PC(II) w 1-NH_2-ADM;
11) modyfikacje dynamiki wewnątrzcząsteczkowej powiązanej z drganiami grup CH, NH_2 i OH podczas przejścia OC-PC(I) w 3-NH_2-1-OH-ADM, przy czym najszybsze fluktuacje zachodziły w obrębie ugrupowań CH, wyprzedzając tym samym reorientację polarnych grup OH oraz NH_2.

Warto podkreślić, że obserwowane zachowanie TICA (wysoka wartość parametru *dTg/dp*, spełnienie reguły TPS oraz izochronicznej superpozycji czasów relaksacji α i JG-β) w różnych warunkach termodynamicznych wyraźnie odbiega od typowego scenariusza obserwowanego dla innych silnie zasocjowanych układów molekularnych. Aby zweryfikować, czy T i p wpływają na zmianę siły oraz populacji wiązań wodorowych, zasadne byłoby zastosowanie badań FTIR w wysokim ciśnieniu, aby lepiej zinterpretować uzyskane wyniki dielektryczne. Wobec ograniczeń technicznych uniemożliwiających realizację takich eksperymentów w ramach niniejszej rozprawy, zastosowano podejście alternatywne, polegające na analizie PDG, które pozwoliło częściowo obejść powyższe trudności. Należy jednak wspomnieć, że podczas dekompresji może dochodzić do relaksacji badanego układu, co w konsekwencji prowadzi do utraty istotnych informacji o jego strukturze czy dynamice molekularnej. Dlatego dla pełniejszego zrozumienia zachowania silnie zasocjowanych układów oraz wpływu organizacji przestrzennej cząsteczek poprzez sieć wiązań wodorowych na kształt α-procesu, niezwykle cenne byłoby uzupełnienie w przyszłości badań BDS o eksperymenty dyfrakcyjne lub podczerwone w warunkach wysokiej kompresji. Ponadto, z punktu widzenia kompleksowej charakterystyki właściwości fizykochemicznych pochodnych ADM, kluczowe znaczenie miałoby także uzyskanie monokryształu 1-NH_2-ADM. Pozwoliłoby to nie tylko na jednoznaczne określenie struktury krystalicznej układu, ale również na pogłębioną analizę oraz

lepsze zrozumienie zależności pomiędzy organizacją przestrzenną cząsteczek a dynamiką molekularną. Niestety pomimo wielu przeprowadzonych prób, nie udało się tego zrobić. Niemniej jednak, w świetle uzyskanych wyników oraz pojawiających się pytań, planowane są dalsze badania w kierunku dokładniejszego poznania natury przejść fazowych oraz mechanizmów, które nimi sterują, jak również dynamiki molekularnej w układach plastycznych, z uwzględnieniem kolejnych pochodnych ADM, takich jak adapromina czy memantyna.

Wyniki przedstawione w niniejszej pracy dostarczają cennych informacji na temat dynamiki molekularnej oraz natury przejść fazowych w zasocjowanych układach o różnym stopniu nieuporządkowania. Poruszane aspekty, takie jak związek między zmianą w populacji wiązań wodorowych a kształtem dyspersji α, który można śledzić poprzez badanie właściwości PDG (przykład TICA), zależności między strukturą wewnętrzną, oddziaływaniami i właściwościami fizycznymi izomerów optycznych i ich mieszaniny (przykład *R*-, *S*-, i *RS*-FLP), jak również właściwości substancji tworzących fazy orientacyjnie nieuporządkowane (przykład trzech pochodnych ADM) wnoszą duży wkład do dyskusji nad amorficznymi substancjami aktywnymi jak również kryształami plastycznymi.

V. Literatura

[1] C.A. Angell, Formation of Glasses from Liquids and Biopolymers, Science 267 (1995) 1924–1935.

[2] K. Niss, T. Hecksher, Perspective: Searching for simplicity rather than universality in glass-forming liquids, J. Chem. Phys. 149 (2018) 230901.

[3] F. Franks, T. Auffret, Freeze-drying of Pharmaceuticals and Biopharmaceuticals, Royal Society of Chemistry, 2008.

[4] H. Tong, H. Tanaka, Structural order as a genuine control parameter of dynamics in simple glass formers, Nat. Commun. 10 (2019) 4–6.

[5] K. Amann-Winkel, C. Gainaru, P.H. Handle, M. Seidl, H. Nelson, R. Böhmer, T. Loerting, Water's second glass transition, Proc. Natl. Acad. Sci. 110 (2013) 17720–17725.

[6] P.G. Debenedetti, F.H. Stillinger, Supercooled liquids and the glass transition, Nature. 410 (2001) 259–267.

[7] P.W. Bridgman, P.W. Bridgman, P.W. Bridgman, P.W. Bridgman, Collected experimental papers, Harvard University Press Cambridge, 1964.

[8] G. Floudas, M. Paluch, K. Ngai, Molecular Dynamics of Glass-Forming Systems: Effects of pressure, Springer, Berlin, 2011.

[9] R. Zallen, Fizyka ciał amorficznych, Phil. Mag. 6 (1994) 1013.

[10] H. Tanaka, Two-order-parameter description of liquids. I. A general model of glass transition covering its strong to fragile limit, J. Chem. Phys. 111 (1999) 3163–3174.

[11] A.K. Doolittle, D.B. Doolittle, Studies in Newtonian flow. V. Further verification of the free-space viscosity equation, J. Appl. Phys. 28 (1957) 901–905.

[12] G. Adam, J.H. Gibbs, On the temperature dependence of cooperative relaxation properties in glass-forming liquids, J. Chem. Phys. 43 (1965) 139–146.

[13] M. Rams-Baron, Z. Wojnarowska, J. Knapik-Kowalczuk, K. Jurkiewicz, A. Burian, M. Wojtyniak, J. Pionteck, M. Jaworska, C. Rodríguez-Tinoco, M. Paluch, The dielectric signature of glass density, Appl. Phys. Lett. 111 (2017) 121902.

[14] F. Cipcigan, V. Sokhan, G. Martyna, J. Crain, Structure and hydrogen bonding at the limits of liquid water stability, Sci. Rep. 8 (2018) 1–8.

[15] V.M. Egorov, V.A. Marikhin, L.P. Myasnikova, Phase transitions in molecular crystals of n-alkane alcohols, Phys. Solid State. 50 (2008) 126–132.

[16] T. Atake, C.A. Angell, Pressure dependence of the glass transition temperature in molecular liquids and plastic crystals, J. Phys. Chem. 83 (1979) 3218–3223.

[17] G. Szklarz, K. Adrjanowicz, M. Dulski, J. Knapik, M. Paluch, Dielectric Relaxation Study at Ambient and Elevated Pressure of the Modeled Lipophilic Drug Fenofibrate, J.

Phys. Chem. B. 120 (2016) 11298–11306.

[18] K. Adrjanowicz, K. Kaminski, Z. Wojnarowska, M. Dulski, L. Hawelek, S. Pawlus, M. Paluch, W. Sawicki, Dielectric Relaxation and Crystallization Kinetics of Ibuprofen at Ambient and Elevated Pressure, J. Phys. Chem. B. 114 (2010) 6579–6593.

[19] K. Adrjanowicz, K. Kaminski, M. Tarnacka, K. Szutkowski, L. Popenda, G. Bartkowiak, M. Paluch, The effect of hydrogen bonding propensity and enantiomeric composition on the dynamics of supercooled ketoprofen - Dielectric, rheological and NMR studies, Phys. Chem. Chem. Phys. 18 (2016) 10585–10593.

[20] C.M. Roland, M. Paluch, T. Pakula, R. Casalini, Volume and temperature as control parameters for the dielectric α relaxation of polymers and molecular glass formers, Philos. Mag. 84 (2004) 1573–1581.

[21] K.L. Ngai, M. Paluch, Classification of secondary relaxation in glass-formers based on dynamic properties, J. Chem. Phys. 120 (2004) 857–873.

[22] R. Casalini, C.M. Roland, Excess wing in the dielectric loss spectra of propylene glycol oligomers at elevated pressure, Phys. Rev. B. 69 (2004).

[23] T. Okuchi, G.D. Cody, H. Mao, R.J. Hemley, Hydrogen bonding and dynamics of methanol by high-pressure diamond-anvil cell NMR, J. Chem. Phys. 122 (2005) 244509.

[24] M. Mierzwa, M. Paluch, S.J. Rzoska, J. Zioło, The Liquid−Glass and Liquid−Liquid Transitions of TPP at Elevated Pressure, J. Phys. Chem. B. 112 (2008) 10383–10385.

[25] M. Romanini, M. Barrio, R. Macovez, M.D. Ruiz-Martin, S. Capaccioli, J.L. Tamarit, Thermodynamic Scaling of the Dynamics of a Strongly Hydrogen-Bonded Glass-Former, Sci. Rep. 7 (2017) 1346.

[26] B.C. Hancock, M. Parks, What is the true solubility advantage for amorphous pharmaceuticals?, Pharm. Res. 17 (2000) 397–404.

[27] M. Rams-Baron, R. Jachowicz, E. Boldyreva, D. Zhou, W. Jamroz, M. Paluch, M. Rams-Baron, R. Jachowicz, E. Boldyreva, D. Zhou, others, Amorphous drug solubility and absorption enhancement, Amorph. Drugs Benefits Challenges. (2018) 41–68.

[28] T. Einfalt, O. Planinšek, K. Hrovat, Methods of amorphization and investigation of the amorphous state, Acta Pharm. 63 (2013) 305–334.

[29] V. V Boldyrev, Mechanochemical modification and synthesis of drugs, J. Mater. Sci. 39 (2004) 5117–5120.

[30] S.B. Murdande, M.J. Pikal, R.M. Shanker, R.H. Bogner, Solubility advantage of amorphous pharmaceuticals: I. A thermodynamic analysis, J. Pharm. Sci. 99 (2010) 1254–1264.

[31] T.A. Ezquerra, A. Nogales, Crystallization as studied by broadband dielectric spectroscopy, Springer, 2020.

[32] R. Paus, Y. Ji, L. Vahle, G. Sadowski, Predicting the solubility advantage of amorphous pharmaceuticals: a novel thermodynamic approach, Mol. Pharm. 12 (2015) 2823–2833.

[33] S.P. Bhardwaj, K.K. Arora, E. Kwong, A. Templeton, S.-D. Clas, R. Suryanarayanan, Correlation between molecular mobility and physical stability of amorphous itraconazole, Mol. Pharm. 10 (2013) 694–700.

[34] A.T.M. Serajuddin, Solid dispersion of poorly water-soluble drugs: Early promises, subsequent problems, and recent breakthroughs, J. Pharm. Sci. 88 (1999) 1058–1066.

[35] R. Brand, P. Lunkenheimer, A. Loidl, Relaxation dynamics in plastic crystals, J. Chem. Phys. 116 (2002) 10386–10401.

[36] S. Das, A. Mondal, C.M. Reddy, Harnessing molecular rotations in plastic crystals: A holistic view for crystal engineering of adaptive soft materials, Chem. Soc. Rev. 49 (2020) 8878–8896.

[37] Timmermans, J., Un nouvel état mésomorphe les cristaux organiques plastiques, J. Chim. Phys. 35 (1938) 331–344.

[38] A. Vispa, M. Romanini, M.A. Ramos, L.C. Pardo, F.J. Bermejo, M. Hassaine, A.I. Krivchikov, J.W. Taylor, J.L. Tamarit, Thermodynamic and Kinetic Fragility of Freon 113: The Most Fragile Plastic Crystal, Phys. Rev. Lett. 118 (2017) 1–6.

[39] M. Michl, T. Bauer, P. Lunkenheimer, A. Loidl, Cooperativity and Heterogeneity in Plastic Crystals Studied by Nonlinear Dielectric Spectroscopy, Phys. Rev. Lett. 114 (2015) 67601.

[40] L.C. Pardo, P. Lunkenheimer, A. Loidl, A and ß Relaxation Dynamics of a Fragile Plastic Crystal, J. Chem. Phys. 124 (2006) 124911.

[41] B. Riechers, K. Samwer, R. Richert, Structural recovery in plastic crystals by time-resolved non-linear dielectric spectroscopy, J. Chem. Phys. 142 (2015) 154504.

[42] D. Heczko, E. Kamińska, A. Minecka, A. Dzienia, K. Jurkiewicz, M. Tarnacka, A. Talik, K. Kamiński, M. Paluch, High-pressure dielectric studies on 1,6-anhydro-β-D-mannopyranose (plastic crystal) and 2,3,4-tri-O-acetyl-1,6-anhydro-β-D-glucopyranose (canonical glass), J. Chem. Phys. 148 (2018) 204510.

[43] E. Kaminska, M. Tarnacka, K. Jurkiewicz, K. Kaminski, M. Paluch, High pressure dielectric studies on the structural and orientational glass, J. Chem. Phys. 144 (2016) 54503.

[44] G.J. Kabo, A.A. Kozyro, M. Frenkel, A. V Blokhin, Solid Phase Transitions of the Cyclohexane Derivatives and the Model of Energy States of Molecules in Plastic Crystals, Mol. Cryst. Liq. Cryst. Sci. Technol. Sect. A. Mol. Cryst. Liq. Cryst. 326 (1999) 333–355.

[45] J.N. Sherwood, The Plastically Crystalline State, John Wiley & Sons, Ltd, Chichester, New York, Brisbane, Toronto, 1979.

[46] B. Parat, L.C. Pardo, M. Barrio, J.L. Tamarit, P. Negrier, J. Salud, D.O. López, D. Mondieig, Polymorphism of $CBrCl_3$, Chem. Mater. 17 (2005) 3359–3365.

[47] G.W. Gray, P.A. Winsor, Liquid crystals \& plastic crystals. Editors, 1974.

[48] K.L. Ngai, Relaxation and diffusion in complex systems, Springer, New York, 2011.

[49] K. Adachi, H. Suga, S. Seki, Phase changes in crystalline and glassy-crystalline cyclohexanol, Bull. Chem. Soc. Jpn. 41 (1968) 1073–1087.

[50] R. Kohlrausch, Ueber das dellmann'sche elektrometer, Ann. Phys. 148 (1847) 353–405.

[51] G. Williams, D.C. Watts, Non-symmetrical dielectric relaxation behaviour arising from a simple empirical decay function, Trans. Faraday Soc. 66 (1970) 80–85.

[52] H.P. Diogo, N.T. Correia, J.J. Moura Ramos, Molecular mobility, phase transitions and phase transformations in crystalline ortho- and meta-carboranes, J. Phys. Chem. Solids. 66 (2005) 832–838.

[53] K. Zhang, R. Song, J. Qi, Z. Zhang, Z. Zhang, C. Yu, K. Li, Z. Zhang, B. Li, Colossal Barocaloric Effect in Carboranes as a Performance Tradeoff, Adv. Funct. Mater. 32 (2022) 1–10.

[54] E. Kamińska, O. Madejczyk, M. Tarnacka, K. Jurkiewicz, K. Wolnica, W.E. Śmiszek-Lindert, K. Kamiński, M. Paluch, Anhydrosaccharides—A new class of the fragile plastic crystals, J. Chem. Phys. 148 (2018) 074501.

[55] Y. Ren, X. Cheng, K. Yang, X. Zhu, H. Li, Y. Wang, Raman study of plastic crystal phase of cyclooctanol under high pressure with different compression rate, J. Mol. Struct. 1102 (2015) 6–10.

[56] A. Drozd-Rzoska, S. Starzonek, S.J. Rzoska, J. Łoś, Z. Kutnjak, S. Kralj, Pretransitional Effects of the Isotropic Liquid–Plastic Crystal Transition, Molecules. 26 (2021) 429.

[57] M. Shahin, S.S.N. Murthy, L.P. Singh, Glass Transition Phenomena in Two-Component Plastic Crystals: Study of Hexasubstituted Benzenes, J. Phys. Chem. B. 110 (2006) 18573–18582.

[58] J.F. Gebbia, A.H. Aristizabal, P. Negrier, D. Aguilà, J.L. Tamarit, L.C. Pardo, Dynamics and local ordering of pentachloronitrobenzene: a molecular-dynamics investigation, Phys. Chem. Chem. Phys. 25 (2023) 30553–30562.

[59] A. Salvatori, P. Negrier, S. Massip, A. Muñoz-Duque, P. Lloveras, M. Barrio, J.L. Tamarit, Polymorphism and solid-solid phase transitions of hydrogen bonded 2-adamantanol and 2-methyl-2-adamantanol compounds, CrystEngComm. 24 (2022) 3692–3700.

[60] P. Negrier, M. Barrio, J. Ll. Tamarit, D. Mondieig, Polymorphism in 2-X-Adamantane Derivatives (X = Cl, Br), J. Phys. Chem. B. 118 (2014) 9595–9603.

[61] P. Negrier, B. Ben Hassine, M. Barrio, M. Romanini, D. Mondieig, J.L. Tamarit, Polymorphism of 1,3-X-adamantanes (X = Br, OH, CH_3) and the crystal plastic phase formation ability, CrystEngComm. 22 (2020) 1230–1238.

[62] E.L. Gromnitskaya, I. V Danilov, V. V Brazhkin, Ultrasonic study of 1-X adamantane (X = F, Cl, Br) compounds at high pressure and at order–disorder transitions, Phys. Chem. Chem. Phys. 24 (2022) 18022–18027.

[63] E.L. Gromnitskaya, I. V Danilov, V. V Brazhkin, Comparative study of the elastic properties of adamantane and 1-chloroadamantane at high pressure and different temperatures and at order–disorder transitions, Phys. Chem. Chem. Phys. 23 (2021) 2349–2354.

[64] G.J. Kabo, A. V Blokhin, M.B. Charapennikau, A.G. Kabo, V.M. Sevruk, Thermodynamic properties of adamantane and the energy states of molecules in plastic crystals for some cage hydrocarbons, Thermochim. Acta. 345 (2000) 125–133.

[65] J.P. Amoureux, M. Bee, A cubic harmonic analysis of the plastic crystal structures of adamantane, $C_{10}H_{16}$, and adamantanone, $C_{10}H_{14}O$, at room temperature, Acta Crystallogr. Sect. B. 36 (1980) 2636–2642.

[66] J.P. Amoureux, M. Bee, J.C. Damien, Structure of adamantane, $C_{10}H_{16}$, in the disordered phase, Acta Crystallogr. Sect. B. 36 (1980) 2633–2636.

[67] S. Chang, E.F.J. Westrum, Heat capacities and thermodynamic properties of globular molecules. I. adamantane and hexamethylenetetramine, J. Phys. Chem. 64 (1960) 1547–1551.

[68] T.E. Jenkins, J. Lewis, A Raman study of adamantane ($C_{10}H_{16}$), diamantane ($C_{14}H_{20}$) and triamantane ($C_{18}H_{24}$) between 10 K and room temperatures, Spectrochim. Acta Part A Mol. Spectrosc. 36 (1980) 259–264.

[69] M. Kosmowska, J. Tarasiewicz, H.A. Kołodziej, Dielectric relaxation of 1-bromoadamantane, J. Mol. Struct. 1016 (2012) 8–12.

[70] I. V Danilov, E.L. Gromnitskaya, V. V Brazhkin, Phase transitions in 1-bromoadamantane compared to 1-chloroadamantane: similarities and unique features, Phys. Chem. Chem. Phys. 23 (2021) 23274–23279.

[71] O. Al Rahal, B.M. Kariuki, C.E. Hughes, P.A. Williams, X. Xu, S. Gaisford, D. Iuga, K.D.M. Harris, Unraveling the Complex Solid-State Phase Transition Behavior of 1-Iodoadamantane, a Material for Which Ostensibly Identical Crystals Undergo Different Transformation Pathways, Cryst. Growth Des. 23 (2023) 3820–3833.

[72] K. Kobashi, T. Kyômen, M. Oguni, Construction of an adiabatic calorimeter in the temperature range between 13 and 505 K, and thermodynamic study of 1-chloroadamantane, J. Phys. Chem. Solids. 59 (1998) 667–677.

[73] A. Vispa, D. Monserrat, G.J. Cuello, F. Fernandez-Alonso, S. Mukhopadhyay, F. Demmel, J.L. Tamarit, L.C. Pardo, On the microscopic mechanism behind the purely orientational disorder-disorder transition in the plastic phase of 1-chloroadamantane, Phys. Chem. Chem. Phys. 19 (2017) 20259–20266.

[74] M.B. Charapennikau, A. V Blokhin, A.G. Kabo, G.J. Kabo, The heat capacities and parameters of solid phase transitions and fusion for 1- and 2-adamantanols, J. Chem. Thermodyn. 35 (2003) 145–157.

[75] O. V Dorofeeva, M.A. Filimonova, Sublimation enthalpy of 1-aminoadamantane: Comparison of theory and experiment, Chem. Phys. Lett. 711 (2018) 231–235.

[76] A.B. Bazyleva, A. V Blokhin, A.G. Kabo, G.J. Kabo, V.N. Emel'yanenko, S.P. Verevkin, Thermodynamic properties of 1-aminoadamantane, J. Chem. Thermodyn. 40 (2008) 509–522.

[77] Y. Huang, R.M. Paroli, D.F.R. Gilson, I.S. Butler, Order–disorder transitions in adamantane derivatives: vibrational spectroscopic and 13C NMR studies of 1-chloroadamantane, Can. J. Chem. 71 (1993) 1890–1897.

[78] B. Ben Hassine, P. Negrier, M. Romanini, M. Barrio, R. Macovez, A. Kallel, D. Mondieig, J.L. Tamarit, Structure and reorientational dynamics of 1-F-adamantane, Phys. Chem. Chem. Phys. 18 (2016) 10924–10930.

[79] A.B. Bazyleva, A. V Blokhin, G.J. Kabo, A.G. Kabo, Y.U. Paulechka, Thermodynamic properties of 1-bromoadamantane in the condensed state and molecular disorder in its crystals, J. Chem. Thermodyn. 37 (2005) 643–657.

[80] P.D. Harvey, D.F.R. Gilson, I.S. Butler, Phase transitions and molecular motions in adamantane derivatives: 1-adamantanol, Can. J. Chem. 65 (1987) 1757–1760.

[81] M.B. Charapennikau, A. V. Blokhin, G.J. Kabo, A.G. Kabo, V. V. Diky, A.G. Gusakov, Thermodynamic properties and the plastic crystal state of 2-methyl-2-adamantanol, Thermochim. Acta. 382 (2002) 109–118.

[82] F. Affouard, J.F. Willart, M. Descamps, Orientationally disordered crystals: From the onset of slow dynamics to the glass transition, J. Non. Cryst. Solids. 307–310 (2002) 9–15.

[83] J.C. Garcia, J.F. Justo, W.V.M. Machado, L.V.C. Assali, Structural, Electronic, and Vibrational Properties of Amino-adamantane and Rimantadine Isomers, J. Phys. Chem. A. 114 (2010) 11977–11983.

[84] J.C. Martinez-Garcia, J.L. Tamarit, S. Capaccioli, M. Barrio, N. Veglio, L.C. Pardo, α -relaxation dynamics of orientanionally disordered mixed crystals composed of Cl-adamantane and CN-adamantane, J. Chem. Phys. 132 (2010) 164516.

[85] N.T. Kawai, D.F.R. Gilson, I.S. Butler, Phase transitions in adamantane derivatives: 1-fluoroadamantane, Can. J. Chem. 69 (1991) 1758–1765.

[86] L.A. Fraczyk, Y. Huang, A high pressure FT-IR spectroscopic study of phase transitions in 1-chloro- and 1-bromoadamantane, Spectrochim. Acta Part A Mol. Biomol. Spectrosc. 57 (2001) 1061–1071.

[87] A. Hédoux, Y. Guinet, J. F. Willart, F. Capet, M. Descamps, Pressure-induced ordering in cyanoadamantane plastic crystal, Solid State Commun. 128 (2003) 267–272.

[88] P. D. Harvey, I. S. Butler, D. F. R. Gilson, Raman study of the effect of high pressure on the order-disorder phase transition in 2-adamantanone, J. Phys. Chem. 90 (2002) 4546–4549.

[89] D. Heczko, P. Jesionek, B. Hachuła, K. Jurkiewicz, J. Grelska, M. Tarnacka, K. Kamiński, M. Paluch, E. Kamińska, Variation in the local ordering, H-bonding pattern and molecular dynamics in the pressure densified ritonavir, J. Mol. Liq. 351 (2022)

118666.

[90] I. Avramov, Pressure dependence of viscosity of glassforming melts, J. Non. Cryst. Solids. 262 (2000) 258–263.

[91] J. Muñoz, A. González-Campo, M. Riba-Moliner, M. Baeza, M. Mas-Torrent, Chiral magnetic-nanobiofluids for rapid electrochemical screening of enantiomers at a magneto nanocomposite graphene-paste electrode, Biosens. Bioelectron. 105 (2018) 95–102.

[92] M. Abram, M. Jakubiec, K. Kamiński, Chirality as an Important Factor for the Development of New Antiepileptic Drugs, ChemMedChem. 14 (2019) 1744–1761.

[93] E. Tokunaga, T. Yamamoto, E. Ito, N. Shibata, Understanding the Thalidomide Chirality in Biological Processes by the Self-disproportionation of Enantiomers, Sci. Rep. 8 (2018) 17131.

[94] A. Hédoux, Y. Guinet, F. Capet, F. Affouard, M. Descamps, Raman effects under pressure in chloroadamantane plastic crystal, J. Phys. Condens. Matter. 14 (2002) 8725–8741.

[95] M. Descamps, N.T. Correia, P. Derollez, F. Danede, F. Capet, Plastic and Glassy Crystal States of Caffeine, J. Phys. Chem. B. 109 (2005) 16092–16098.